Search for Gaugino Mediation Non-Universal Higgs Masses Model with $\tilde{\nu}_\tau$ NLSP with the ATLAS Detector in Final States with Jets and Missing Transverse Momentum and 20.3 fb^{-1} of $\sqrt{s}$ = 8 TeV Proton-Proton Collision Data

D I S S E R T A T I O N

zur Erlangung des akademischen Grades

doctor rerum naturalium
(Dr. rer. nat.)
im Fach Physik

eingereicht an der
Mathematisch-Naturwissenschaftlichen Fakultät
Humboldt-Universität zu Berlin

von
Dipl.-Phys. Judita Mamužić

Präsident der Humboldt-Universität zu Berlin:
Prof. Dr. Jan-Hendrik Olbertz

Dekan der Mathematisch-Naturwissenschaftlichen Fakultät:
Prof. Dr. Elmar Kulke

Gutachter:
1. PD Dr. Klaus Mönig
2. Prof. Dr. Thomas Lohse
3. Ass. Prof. Dr. Sascha Caron

Tag der mündlichen Prüfung: 28. 10. 2015.

For someone I miss the most,
my father Ivan Mamužić

Abstract

Supersymmetry (SUSY) is one of the best motivated extensions of the Standard Model, and its searches at the LHC represent an important result in the Physics Beyond the Standard Model. The subject of this thesis is the analysis of two SUSY scenarios using 20.3 fb^{-1} of ATLAS data at 8 TeV center of mass energy.

The main topic of the thesis is a study of the Non-Universal Higgs Masses model with gaugino mediation and $\tilde{\nu}_\tau$ NLSP (NUHMG). This is a R-parity conserving realistic SUSY model, where $\tilde{\nu}_\tau$ decays into ν_τ and $\tilde{G}$ LSP. The model is distinguished from other SUSY models by allowed $\tilde{l}_L$ decays, three-body decays of $\tilde{\tau}_1$, where the dominant decay is into a pair of fermions and missing transverse energy, and a mass spectrum where $\tilde{\chi}_1^0$ has visible decays. It is characterized by long decay chains with lots of soft leptons and jets. The produced missing transverse energy from neutrinos can cancel out with the missing transverse energy from the NLSP, which brings to relatively low missing transverse energy.

A study showed that NUHMG can be found using $\tilde{q}$ and $\tilde{g}$ production, using final states with zero leptons of transverse momenta higher than 10 GeV, multiple jets and missing transverse energy. This is the most inclusive selection, which in fact includes soft objects, but does not depend on the b-jet tagging or τ reconstruction. Therefore, an analysis using 2-6 jets and missing transverse energy has been set in place for the NUHMG model.

The NUHMG model viable parameter space for the 8 TeV data and 20.3 fb^{-1} of integrated luminosity has been determined using a simultaneous scan using multiple criteria. The selected parameter space points were selected to have the $\tilde{\nu}_\tau$ NLSP, that are not excluded by LEP, have Higgs mass close to 125 GeV, are not excluded by previous LHC searches, and have a viable cross-section for the analysis.

A dedicated optimization for the NUHMG model has been performed in three steps. First, the optimal sensitive variable and jet multiplicity has been determined, using a newly developed fast cut-flow optimization method. It relies on the Rectangular Cuts method with Genetic Algorithm in TMVA, where purely Monte Carlo input has been used for signal and background modeling. Second, the optimal variable combination and jet multiplicity have been further optimized using a setup which uses data in the control regions, and performs a likelihood fit to obtain Standard Model and potential SUSY signal estimates, accounting systematic uncertainties. Third, the obtained cut flow is further refined and integrated into a more general analysis with 2-6 jets and missing transverse energy as a signal region labeled 6jt+, within ATLAS inclusive searches for $\tilde{q}$ and $\tilde{g}$ with zero leptons.

A data analysis has been performed using the log likelihood fit, and a statistical analysis has been set up to interpret the data. For expected 4.9 ± 1.4 Standard Model events, 6 have been observed, which is within 1 sigma uncertainty of the expectation. As no significant excess of data has been seen, the 95% CL exclusion limits on the NUHMG model have been set, where $\tilde{q}$ and $\tilde{g}$ masses are excluded up to 1250 and 1400 GeV respectively. In addition, the 6jt+ signal region improves the exclusion limits by about 100 GeV for the $\tilde{g}$ in

the compact mass region, for the simplified model of gluino production, with one step decay via $\tilde{\chi}_1^{\pm}$. A search for the NUHMG using 1 lepton, multiple jets and missing transverse energy has shown to give compatible results.

Second SUSY model studied in this thesis is the Non-universal Higgs Masses model with $\tilde{\chi}_1^0$ LSP (NUHM). It is well motivated in the framework of Radiatively Driven Natural SUSY (RNS), where Higgs of mass around 125 GeV, $\tilde{q}$ and $\tilde{g}$ masses at the TeV scale are accommodated with low level of electroweak fine tuning.

A study of RNS NUHM model final states, mass spectrum and production cross-sections showed that the search for this model is viable using the direct gaugino production, using multiple leptons and missing transverse energy. A data analysis using a statistical combination of 2, 3 and 4 leptons has been performed. As no significant excess of data has been observed, 95% CL exclusion limits have been set on the RNS NUHM model. The statistical combination is driven by the analysis with 3 leptons, and it reaches $m_{1/2}$ up to 300 GeV, and extends up to the highest tested value of $\mu = 500$ GeV.

In addition to physics analyses, a program developed for online monitoring of the ATLAS trigger, called Trigger Presenter (TriP), is described in this thesis. It is aimed for a shifter and expert user in the control room. It receives the information from Level 1, Level 2 and Event Filter trigger rates and HLT computer farm status. Using various methods for reading out relevant information, and developed naming conventions, the information is received, calculated, and presented in a graphical user friendly interface. TriP was used in the ATLAS control room for trigger monitoring at the first LHC startup.

Zusammenfassung

Supersymmetrie (SUSY) ist eine der am besten motivierten Erweiterungen des Standardmodells, und die SUSY-Suchen am LHC sind ein wichtiger Beitrag zum Verständnis von neuer Physik. Das Thema dieser Doktorarbeit ist die Analyse von zwei SUSY-Szenarien unter Verwendung von 20.3 fb^{-1} an ATLAS-Daten, die bei einer Schwerpunktenergie ($\sqrt{s}$) von 8 TeV aufgezeichnet wurden.

Den Hauptteil der Arbeit stellt eine Untersuchung des "Non-Universal Higgs Masses model with gaugino mediation and $\tilde{\nu}_\tau$ NLSP" (NUHMG) dar. Es handelt sich um ein realistisches SUSY-Modell mit R-Paritätserhaltung, mit Zerfällen von $\tilde{\nu}_\tau$ in ν_τ und $\tilde{G}$ (leichtestes supersymmetrisches Teilchen, LSP). Dieses SUSY-Modell unterscheidet sich von anderen Modellen dadurch, dass $\tilde{l}_L$ Zerfälle erlaubt sind, durch Dreikörperzerfälle von $\tilde{\tau}_1$, vorwiegend in ein Fermionenpaar und das LSP, sowie durch ein Massenspektrum mit sichtbaren $\tilde{\chi}_1^0$ Zerfällen. Weiter wird es charakterisiert durch lange Zerfallsketten mit zahlreichen niederenergetischen Leptonen und Jets. Der Transversalimpuls von Neutrinos wird teilweise durch das LSP kompensiert, wodurch der fehlende Transversalimpuls insgesamt verhältnismäßig gering ausfällt.

Das NUHMG-Modell sollte sich anhand der erzeugten $\tilde{q}$ und $\tilde{g}$ nachweisen lassen, unter Verwendung von Endzuständen mit mehreren Jets und fehlendem Transversalimpuls, aber ohne Leptonen mit einem Transversalimpuls $p_T > 10$ GeV. Diese Kriterien sind sehr inklusiv, es werden Ereignisse mit niederenergetischen Objekten ausgewählt, und es wird kein Gebrauch von Algorithmen zur Erkennung von b-Jet oder zur Rekonstruktion von τ-Kandidaten gemacht. Eine entsprechende Analyse mit 2–6 Jets und fehlendem Transversalimpuls im Endzustand wurde aufgesetzt.

Der Teil des Parameterraums des NUHMG-Modells, welcher mit den von ATLAS bei $\sqrt{s} = 8$ TeV aufgezeichneten Daten erreichbar ist, wurde anhand einer systematischen Variation verschiedener Auswahlkriterien bestimmt. Die in Betracht gezogenen Punkte im Parameterraum mussten $\tilde{\nu}_\tau$ als NLSP haben, durften nicht bereits durch frühere Ergebnisse von LEP- oder LHC-Suchen ausgeschlossen sein, und mussten eine Higgs-Boson Masse nahe 125 GeV und einen ausreichenden Wirkungsquerschnitt aufweisen.

Eine gezielte Optimierung für den Nachweis des NUHMG-Modells wurde in drei Schritten vorgenommen: Zuerst wurden die Variablen mit der höchsten Sensitivität sowie eine geeignete Jet-Multiplizität ermittelt, wobei eine kürzlich entwickelte schnelle Optimierungsmethode zum Einsatz kam, welche auf einem genetischen Algorithmus basiert und mit einer Monte Carlo Methode simulierte pp-Kollisionsereignisse als Eingabe verwendete. Als zweites wurde die optimale Kombination von Variablen und Jet-Multiplizität durch die Definition von Kontrollregionen, in denen simulierte und mit dem ATLAS-Detektor aufgezeichneten Ereignisse verglichen werden, weiter verbessert. Hierbei kommt ein Likelihood-Fit zum Einsatz, mit dem die Normierung der Standardmodell-Beiträge angepasst wird und die Größe eines möglichen SUSY-Beitrags abgeschätzt wird, unter Berücksichtigung von systematischen Unsicherheiten. Drittens werden die erhaltenen Auswahlkriterien weiter verfeinert und als Signalregion "6jt+" in die inklusive Analyse (mit 2–6 Jets und fehlender Transversalimpuls im Endzustand) integriert.

Die ATLAS-Daten wurden mit dem optimierten Verfahren analysiert und anschließend statistisch ausgewertet. Es wurden 6 passende Ereignisse gezählt, gegenüber einer Erwartung von 4.9 ± 1.4 Standardmodell Ereignissen. Da also kein signifikanter Überschuss an Ereignissen beobachtet wurde, wurden experimentell ausgeschlossene Parameterbereiche des NUHMG-Modells bestimmt (bei einem Konfidenzniveau von 95%). Hierbei wurden $\tilde{q}$ und $\tilde{g}$ Massen unterhalb von 1250 GeV bzw. 1400 GeV ausgeschlossen. Zusätzlich verbessert die 6jt+ Signalregion die $\tilde{g}$ Ausschlussgrenzen um 100 GeV für vereinfachte Modelle mit Gluino-Erzeugung und Zerfällen via $\tilde{\chi}_1^{\pm}$ bei kleinen Massendifferenzen. Eine Suche nach dem NUHMG-Modell in Endzuständen mit 1 Lepton, mehreren Jets und fehlendem Transversalimpuls hat zu vergleichbaren Ergebnissen geführt.

Das zweite SUSY-Modell, das in dieser Doktorarbeit untersucht wird, ist das "Non-universal Higgs Masses model with $\tilde{\chi}_1^0$ LSP" (NUHM), welches innerhalb von "Radiatively Driven Natural SUSY" (RNS) angesiedelt ist, und das durch eine Higgs-Boson Masse nahe 125 GeV, $\tilde{q}$ und $\tilde{g}$ Massen im TeV-Bereich, sowie ein geringes Maß an Fine-Tuning gekennzeichnet ist.

Eine Untersuchung der vom RNS-NUHM Modell vorhergesagten Endzustände, des Massenspektrums und der Wirkungsquerschnitte zeigte, dass eine Suche nach diesem Modell unter der Annahme direkter Gaugino-Erzeugung machbar ist, unter Verwendung von Ereignissen mit mehreren Leptonen und fehlendem Transversalimpuls. Eine Datenanalyse mit einer statistischen Kombination von Ereignissen mit 2, 3 und 4 Leptonen wurde durchgeführt. Da kein signifikanter Überschuss von Ereignissen beobachtet wurde, wurden ausgeschlossene Parameterbereiche des RNS-NUHM Modells bestimmt. Der größte Beitrag kommt hierbei von der Analyse mit 3 Leptonen, und es werden Werte von $m_{1/2}$<300 GeV, und von μ<500 GeV ausgeschlossen.

Zusätzlich zu den genannten Analysen beschreibt diese Arbeit ein Programm, das für die Überwachung des ATLAS-Triggersystems entwickelt wurde, der sogenannte "Trigger Presenter" (TriP). Es ist für die Verwendung durch Schicht-Mitarbeiter und Trigger-Experten im ATLAS Kontrollraum gedacht. Es sammelt Informationen über Trigger-Raten von den verschiedenen Trigger-Unter systemen (Level 1, Level 2, Event Filter), sowie über den Status der Computeranlage des High Level Triggers. Die Information wird aus unterschiedlichen Quellen zusammengeführt und in einer grafischen Benutzeroberfläche einheitlich und übersichtlich dargestellt. TriP kam im ATLAS Kontrollraum zum Einsatz, beispielsweise in der wichtigen Phase der LHC Inbetriebnahme.

Contents

1. Introduction **1**

2. Physics in the Era of the Large Hadron Collider **5**
2.1. The Standard Model of Particle Physics 5
2.1.1. Gauge Invariance 7
2.1.2. Spontaneous Symmetry breaking 9
2.1.3. Electroweak Theory 9
2.1.4. The BEH Mechanism 11
2.1.5. Quantum Chromodynamics 14
2.1.6. The Standard Model Lagrangian 15
2.2. Standard Model and Higgs Measurements 16
2.3. Beyond the Standard Model 19

3. Supersymmetry **21**
3.1. Motivation for SUSY 21
3.2. Supersymmetric Lagrangian 26
3.2.1. Supersymmetry Algebra 26
3.2.2. Lagrangian for the Chiral Supermultiplets 28
3.2.3. Lagrangian for the Gauge Supermultiplets 30
3.2.4. Soft Supersymmetry Breaking 30
3.2.5. Supersymmetric Lagrangian 31
3.3. The Minimal Supersymmetric Standard Model 32
3.3.1. MSSM Particle Content 32
3.3.2. R-parity Conservation 33
3.3.3. MSSM Interactions 34
3.3.4. MSSM SUSY Models 34
3.4. Aspects of SUSY Searches in ATLAS 37
3.4.1. SUSY Search Strategies in ATLAS 38
3.4.2. Constrains on SUSY Searches 38

4. Non-Universal Higgs Masses Model and Radiatively Driven Natural SUSY **41**
4.1. Non-Universal Higgs Masses Model 41
4.2. Radiatively Driven Natural SUSY and NUHM 43

5. Gaugino Mediation Non-Universal Higgs Masses Model **47**
5.1. Gravitino Dark Matter and $\tilde{\nu}_\tau$ NLSP Motivation 47
5.2. Gaugino Mediation and NUHM with $\tilde{\nu}_\tau$ NLSP Model 49

6. ATLAS Detector at the LHC **53**
6.1. The Large Hadron Collider . . . 53
6.2. ATLAS Detector . . . 55
6.2.1. Coordinate system and Nomenclature . . . 55
6.2.2. Physics Requirements . . . 56
6.2.3. Detector Design . . . 58
6.3. Inner Detector . . . 61
6.4. Calorimetry . . . 62
6.5. Muon System . . . 62
6.6. Forward Detectors . . . 63
6.7. Trigger and Data Acquisition . . . 64

7. Reconstruction and Monte Carlo Event Generation **69**
7.1. Signal Mass Spectrum Generation . . . 70
7.2. Signal Decay Width and Branching Ratio Calculation . . . 71
7.3. Monte Carlo Event Generation . . . 72
7.3.1. Signal Event Generation . . . 72
7.3.2. Background Event Generation . . . 75
7.4. Monte Carlo Event Simulation . . . 76
7.5. Event Reconstruction . . . 78
7.5.1. Electron Reconstruction . . . 80
7.5.2. Muon Reconstruction . . . 81
7.5.3. Tau Reconstruction . . . 82
7.5.4. Jet Reconstruction . . . 83
7.5.5. b-jet Tagging . . . 84
7.5.6. Missing Transverse Energy . . . 85
7.6. NLO and NLL Cross-Section Calculation . . . 86

8. Methods of Statistical Analyses **89**
8.1. Multivariate Analyses and TMVA . . . 89
8.1.1. TMVA Implementation . . . 90
8.1.2. Rectangular Cut Optimization Method . . . 92
8.2. Likelihood-Based Tests of New Physics . . . 93
8.2.1. Formalism of a Search for New Physics Using a Statistical Test 94
8.2.2. Statistical Test Setup . . . 104
8.3. Likelihood-Based Combined Fit . . . 104
8.3.1. Combined Fit Tools and Formalism . . . 105

9. NUHMG Final States **109**
9.1. Typical Mass Spectrum and Dominant Decay Modes . . . 109
9.2. Final States at the LHC . . . 111

10. NUHMG Grid Properties **117**
10.1. LEP Limit and the Higgs Mass Constrain . . . 118

10.2. Mass Spectra for Grid Points . . . 118
10.3. Cross Section and Production Channel Analysis . . . 122

11. NUHMG Analysis Using Final States with Jets and Missing Transverse Momentum 127
11.1. Analysis Overview . . . 127
11.2. Data and Monte Carlo Samples . . . 129
11.2.1. Data Samples . . . 129
11.2.2. Monte Carlo Samples . . . 130
11.3. Event Reconstruction, Trigger and Event Cleaning . . . 132
11.3.1. Event Reconstruction . . . 132
11.3.2. Trigger Selection . . . 135
11.3.3. Event Cleaning . . . 136
11.4. Optimization for the NUHMG Model . . . 138
11.4.1. SUSY Signal Separation Variables . . . 139
11.4.2. NUHMG Strong Production Properties . . . 141
11.4.3. Fast Cut Flow Optimization Using TMVA . . . 145
11.4.4. Grid Optimization Using the Fit . . . 152
11.4.5. Addition of the 6jt+ Signal Region to the Analysis . . . 153
11.5. Event Selection . . . 158
11.5.1. Signal Regions Selection . . . 158
11.5.2. Control Regions Selection . . . 162
11.5.3. Validation Regions Selection . . . 164
11.6. Background Estimation . . . 166
11.6.1. QCD Multi-jet Background Estimation . . . 166
11.6.2. Electroweak Background Estimation . . . 170
11.7. Statistical Treatment and Systematic Uncertainties . . . 171
11.7.1. Statistical Treatment . . . 171
11.7.2. Systematic Uncertainties . . . 174
11.8. Results and Interpretation . . . 177
11.8.1. Background Fit Performance . . . 177
11.8.2. Validation . . . 181
11.8.3. Results . . . 182
11.8.4. Interpretation . . . 185
11.8.5. Comparison to Analysis with One Lepton, Jets and Missing Transverse Momentum . . . 189

12. Conclusion 195

13. Outlook 199

Appendix A. NUHM and Radiatively Driven Natural SUSY Analysis 201
A.1. NUHM Scans Compatibility with RNS . . . 201
A.2. NUHM Final States . . . 203

A.3. NUHM Grid Properties 207
A.4. NUHM 8 TeV Data Analysis 208

Appendix B. Online Monitoring of the Trigger in ATLAS with TriP **213**
B.1. Trigger Presenter Implementation 213
B.2. Graphical User Interface 220

1. Introduction

In the quest of high energy physics of finding the answers to the most fundamental questions in understanding the nature, large experiments need to be built to collect data for physics analyses. A number of advancements play an important role in this task. Firstly, the modern high energy physics has a very good understanding of fundamental particles and their interactions, described by the Standard Model of particle physics (SM) [1–9]. In order to confirm its validity, a discovery of the Higgs particle in July 2012 [10, 11] was of great importance. To understand if the newly found particle is indeed the predicted SM Higgs boson, a number of precision measurements are required. In addition, as there are signs of physics beyond the SM, a number of hypothetical models are constructed, and the search for their experimental confirmation is of great importance. Secondly, thanks to the great advancements in technology in recent history, the construction of the Large Hadron Collider (LHC) [12] was performed, which resulted in the input energy that has set a world record [13]. It is designed to operate at 14 TeV, currently reaching 8 TeV center of mass energy (c.m.e) in p-p collisions. The high integrated luminosity obtained by the ATLAS [14] and other LHC experiments [15–17], with high efficiency of data taking, while operating in radiation hard conditions, are wonderful technical achievements. Thirdly, the computing resources available at all levels of complexity, computing power and parallelism are a great asset in analyses performed at present. In addition, recent developments of Monte Carlo event generators [18] and techniques of statistical analyses play an important role in the data mining. All these ingredients are a necessity for the current physics searches.

There are two analyses described in this thesis, which use 20.3 fb^{-1} of ATLAS data collected at 8 TeV c.m.e p-p collisions. Their topic is in the physics beyond the SM, in the field of Supersymmetry (SUSY) [19–27]. The main topic of this thesis is the analysis of the Non-Universal Higgs Masses model with gaugino mediation and $\tilde{\nu}_\tau$ NLSP (NUHMG) [28]. Due to its distinguished event topology, a dedicated analysis was set in place, which in addition extends its field of searches in ATLAS. The second analysis explores the Non-Universal Higgs masses model [29] in the framework of Radiatively Driven Natural Supersymmetry [30]. It has a good motivation for LHC searches considering the recent Higgs discovery and no evidence of Supersymmetry up to the TeV scale at the LHC experiments. No signs of new physics have been found, and the analyses extend the exclusion reach in SUSY. Finally, in order to ensure correct data taking, a program for online trigger monitoring in ATLAS called Trigger Presenter (TriP) was developed, and its description is given here.

The thesis is organized in three parts, where the first gives the overall theoretical

introduction, the second gives details of the experimental setup, and finally, the third part gives a detailed explanation of the NUHMG model data analysis. The first appendix describes the NUHM data analysis which was done in addition, and the second appendix describes the more technical work on the program called TriP, done for the ATLAS detector operations. A more detailed overview of the thesis structure will be given here.

The chapters 2 - 5 describe the theoretical framework. A short introduction to the Standard Model of elementary particle physics is given in the chapter 2, with emphasis on the most recent measurements in the physics of the Standard Model and Higgs. The motivation for the LHC searches and the theoretical framework of Supersymmetry, as a theory beyond the Standard Model, is given in the chapter 3. Finally, for the two specific models studied in this thesis, the motivation and formalism are given in the chapters 4 and 5.

In the chapters 6 - 8 the experimental setup used in data taking and physics analyses is described. The ATLAS detector description is given in the chapter 6. Details about event reconstruction and Monte Carlo event simulation commonly used by the ATLAS experiment, and in these analyses, is given in the chapter 7. Finally, various methods for data mining and statistical interpretation are described in the chapter 8.

The chapters 9 - 11 describe the study of a NUHMG SUSY model using 20.3 fb^{-1} of ATLAS data collected at 8 TeV c.m.e. This work was performed in a couple of steps, and it resulted in joining this study to the more general search for $\tilde{q}$ and $\tilde{g}$, using final states with jets and missing transverse momentum and a lepton veto (0-lepton analysis) [31]. A short guideline for the 8 TeV data analysis will be given here.

First, a feasibility study of a NUHMG model for the 8 TeV LHC searches was performed. The SUSY mass spectrum, branching fractions and final states were explored to select the optimal search approach. This resulted in a motivation for a search with a lepton veto, multiple jets and missing transverse momentum. A detailed description of this work is given in the chapter 9.

Second, within this thesis the NUHMG SUSY parameter space grid was prepared. In order to ensure a study not already excluded by previous searches, the LEP limits [32], Higgs mass constraint [33, 34] and LHC $\tilde{q}$, $\tilde{g}$ and $\tilde{t}$ LHC limits [35] were considered in model generation. In addition, yields for the given energy and integrated luminosity were estimated. This resulted in the preparation of the NUHMG grid for further study. Details about the mass spectrum and cross-section analysis for the NUHMG grid are given in the section 10.

Third, the NUHMG model analysis was optimized. For this, a fast cut flow optimization method, using a framework for multivariate analyses TMVA [36], was developed. The analysis cut flow was refined using the standard setup of the 0-lepton analysis, with the background determination using dedicated regions for the standard model measurements, and statistical test using the CL_S technique [37], commonly used in the 0-lepton analysis. The optimal signal region was added to the

0-lepton analysis. As no significant excess of data was observed, the exclusion limits were set for the NUHMG model [31]. As a cross-check, the analysis of NUHMG model was performed using the search with one lepton, multiple jets and missing transverse momentum (one-lepton analysis) [38], by the one lepton analysis SUSY team. Details of the NUHMG analysis are given in the chapter 11. More details about the search with 0-leptons, multiple jets and missing transverse momentum can be found in [31]. The NUHMG model exclusion limits by the analysis with one lepton, multiple jets and missing transverse momentum can be seen in [38] for comparison. Finally, chapters 12 and 13 give a conclusion and outlook for all results described in the thesis.

As the Non-universal Higgs Masses model (NUHM) has a very good motivation for the LHC searches in the framework of Radiatively Driven Natural Supersymmetry, the feasibility study, NUHM grid generation, and analysis using the electroweak production and signatures with 2, 3 and 4 leptons for 20.3 fb^{-1} of 8 TeV ATLAS data is given in the appendix A.

In order to ensure good quality in ATLAS experiment data taking, the monitoring of different detector components and data taking systems are of great importance. A program called Trigger Presenter was prepared for the online monitoring of trigger, and it was used in ATLAS detector integration tests and data taking periods at the first LHC startup. The program implementation and short instructions for its usage are described in the appendix B.

2. Physics in the Era of the Large Hadron Collider

Current understanding of nature in elementary particle physics is summarized in the theoretical framework of the Standard Model (SM) [1–9]. It describes all known elementary particles and their interactions. It was well tested by the experiments in the past twenty years. LHC [12] has been designed to extend the tests on the SM, by confirming the existence of its last missing piece, the Higgs boson [10,11]. Therefore, measurements of the SM parameters and the Higgs physics are of great importance in understanding the nature and its modeling. As there is strong evidence of physics beyond the SM, LHC also has a goal to enable direct searches for new physics. In this chapter, the SM theoretical framework will be presented in the section 2.1. Experimental confirmations of the SM and Higgs physics, including the most recent results from the LHC measurements, will be shown in the section 2.2. Finally, motivation for physics beyond the SM, will be given in the section 2.3.

2.1. The Standard Model of Particle Physics

The Standard Model of particle physics is the theory which explains fundamental structure of matter and its interactions. It rests on the theoretical framework of effective field theories, which capture the basic experimental facts up to a certain scale. In this way, SM could be the theory functional up to the low-energy limit of some more fundamental physics. In this section, the SM particle content, the known particle physics interactions and the formalism of the SM, will be presented.

The theory of the SM is based on the relativistic quantum field theory, where the matter is modeled by the fermion fields, interactions are mediated by gauge bosons, and particles acquire mass via the Higgs mechanism [40–45]. The quantities obtained by the experiment are the elementary particle properties. In the table 2.1 a summary of SM particle content [39] is shown.

The matter particles are fermions with spin 1/2, and their respective antiparticles. They consist of quarks and leptons, and have three generations of particles which differ by their mass. Quarks interact via strong, electromagnetic and weak interaction, and carry quantum numbers of color, electric charge and weak isospin. Each generation has an up-type quark with electric charge of +2/3 (u,c,t) and an down-type quark with electric charge of -1/3 (d,s,b). Leptons interact via electromagnetic and weak interaction, but due to the fact that neutrinos are neutral, they interact only weakly. Each generation has an electron-type lepton (e,μ,τ) with electric charge

	Fermions S=$\frac{1}{2}$			**Gauge Bosons** S=1
Quarks	u m=$2.3^{+0.7}_{-0.5}$ MeV Q=2/3 e up	c m=1.275±0.025GeV Q=2/3 e charm	t m=173.21±0.51±0.71GeV Q=2/3 e top	γ m<1×10^{-18} eV Q< 1×10^{-35} e photon
	d m=$4.8^{+0.5}_{-0.3}$ MeV Q=-1/3 e down	s m=95±5 MeV Q=-1/3 e strange	b m=4.18±0.03 GeV Q=-1/3 e bottom	g m=0 Q=0 gluon
Leptons	ν_e m<2 eV Q=0 electron neutrino	ν_μ m<0.19 MeV Q=0 muon neutrino	ν_τ m<18.2 MeV Q=0 tau neutrino	Z^0 m=91.1876±0.0021GeV Q=0 Z boson
	e m=0.510 MeV Q=-1 e electron	μ m=105 MeV Q=-1 e muon	τ m=1776.82±0.16MeV Q=-1 e tau	$W^\pm$ m=80.385±0.015GeV Q=±1 e W boson

Higgs Boson S=0
H^0 m=125.7±0.4 GeV Q=0 Higgs

Table 2.1.: Standard Model particle content [39]. Fermions are matter particles which have a spin 1/2, and have corresponding antiparticles. They can be quarks, which interact in the strong, electromagnetic and weak interactions, and fermions, which interact in electromagnetic and weak interaction, where nearly massless neutrinos interact only weakly. Three generations of fermions differ in mass. Gauge bosons are interaction mediators, where electromagnetic interaction is mediated by γ, electroweak by $W^\pm$ and Z^0, and strong by g. Particles acquire mass via Higgs mechanism, and a quanta of the Higgs field is the Higgs particle. Uncertainties on e and μ mass are not shown in the table due to their high level of accuracy.

of -1, and neutrino-type lepton (ν_e,ν_μ,ν_τ) with no charge and very small mass. The matter particle interactions are mediated by the gauge bosons, which have a spin 1. The electromagnetic interaction is mediated by the photon γ, electroweak by the $W^\pm$ and Z^0 gauge bosons, and strong interaction by the gluon g.

The SM can be formulated in the quantum field theory via the Lagrangian formalism, where symmetries and the requirements on invariance of the Lagrangian under local gauge transformations need to be considered. The invariance under local transformation is obtained by including gauge fields into the Lagrangian, and consequently, the quanta of the gauge fields are the gauge bosons. The SM symmetry

group is given by:

$$SU(3)_C \otimes SU(2)_L \otimes U(1)_Y \tag{2.1}$$

where $SU(3)_C$ symmetry group describes the strong force mediated by eight gluons, and the $SU(2)_L \otimes U(1)_Y$ represents the electromagnetic and weak interaction, combined into the electroweak theory, mediated by $W^{\pm}$ and the Z^0 bosons and the photon γ. In total there are 12 types of gauge bosons in the SM. SM does not include gravitation, but on the scale of elementary particle interactions it is very weak and can be neglected.

The unification of electromagnetic and weak forces takes place via the Glashow Salam Weinberg mechanism. It represents a transformation of left-handed weak isospin doublets $SU(2)_L$, and hypercharge Y multiplets and singlets of $U(1)_Y$. When invariance of the Langrangian under these transformations is required, new massless vector fields need to be introduced ($W^{1,2,3}, B$). The observed bosons $W^{\pm}$, Z^0 and γ are their linear combinations. The spontaneous symmetry breaking performs a rotation by an angle θ_W of the W and B plane, the so called weak mixing angle or Weinberg angle, and produces Z^0 and γ gauge bosons. It also provides relations between W and Z boson masses, defined as $\cos\theta = \frac{m_W}{m_Z}$.

The gauge invariance would imply massless gauge bosons, which is in contradiction to the experimental measurements. Local gauge invariance in the SM would be broken by adding simple mass terms to the Lagrangian. Therefore, the mechanism of spontaneous symmetry breaking was introduced in order to explain particle masses. Particles of the SM acquire mass by the interaction with the scalar Higgs field, which results in a spontaneous electroweak symmetry breaking. As a consequence, a weakly coupling particle of spin zero is added to the theory, with a potential that is minimized at a non-zero value. The mechanism where particles acquire masses is called the Higgs mechanism, and the quantum of the Higgs field is a bosonic scalar Higgs particle (H^0).

In the next sections, the principles of gauge invariance and spontaneous symmetry breaking, will be shown. Also, the electroweak theory, together with the Higgs mechanism and quantum chromodynamics will be described. The following sections are based on the [46–48].

2.1.1. Gauge Invariance

When the **invariance under local gauge transformation** for the Langrangian density is required, gauge potential needs to be introduced, with couplings to elementary fermion matter field, which is completely determined by the symmetry principles, on a given scale.

The theory of electromagnetic interaction is introduced using the Dirac fermions. The invariance of the Lagrangian is required, where the space-time dependent transformation for fermions is given by:

$$\psi(x) \to e^{iq\alpha(x)}\psi(x) \tag{2.2}$$

where $\alpha(x)$ depends on coordinates in space-time. The invariance of the Lagrangian density under this transformation can be achieved using a covariant derivative D_μ. It requires introduction of the vector potential A_μ in the covariant derivative as:

$$D_\mu = \partial_\mu + iqA_\mu(x). \tag{2.3}$$

The Lagrangian then reads:

$$\mathcal{L} = i\overline{\psi}\gamma_\mu D^\mu\psi - m\overline{\psi}\psi - \frac{1}{4}F^{\mu\nu}F_{\mu\nu}. \tag{2.4}$$

where $F_{\mu\nu} = \partial_\mu A_\nu - \partial_\nu A_\mu$, and q_ψ is the charge of the field. Then it can be proved that in addition to the local phase transformation of the field ψ, and when the vector potential A_μ transforms inhomogeneously as:

$$A_\mu(x) \to A_\mu(x) - \partial_\mu\alpha(x) \tag{2.5}$$

the Lagrangian 2.4 will be invariant under a set of local gauge transformations. The phase transformations of the fermion 'matter' field forms a U(1) group, and the electrodynamics can be regarded as a gauge theory based on U(1) group. U(1) is a Abelian group, where the elements commute with one another. The photon field is required to be massless, as the mass term $\frac{1}{2}m_\gamma^2 A_\mu A^\mu$ would not be locally gauge invariant, while fermions have mass. Finally, the Lagrangian density of the Qunatum Electrodynamics (QED) is given by:

$$\begin{aligned}
\mathcal{L}_{QED} =& \overline{\psi}(i\gamma^\mu\partial_\mu - m)\psi && \left\{ \begin{array}{l} Fermion\ mass\ and \\ kinetic\ energy \end{array} \right. \\
& -q\overline{\psi}\gamma^\mu\psi A_\mu && \left\{ \begin{array}{l} \gamma\ kinetic \\ energy \end{array} \right. \\
& -\frac{1}{4}F^{\mu\nu}F_{\mu\nu}. && \left\{ \begin{array}{l} Interaction \end{array} \right.
\end{aligned} \tag{2.6}$$

The idea of matter field transformations can be futhrer generalized, by introducing more complicated non-Abelian transformations compared to U(1) group, as pointed out by Yang, Mills, and independently Shaw (and also Utiyama). In this approach there are several gauge fields in the representation of the gauge group. Matter and gauge fields $V_{a\mu}$ are 'minimally coupled' via transformation of the form:

$$\partial_\mu \to D_\mu = \partial_\mu + igt_a V_{a\mu} \tag{2.7}$$

where t_a is the matrix representation of the group generator, and g is the universal gauge coupling constant. For example, the generators of SU(2) group $t_a = \frac{1}{2}\sigma_a$, where σ_a, a=1,2,3, are Pauli matrices. Gauge potential mass terms are required to be zero, and the interaction of matter and gauge fields is determined by the local

gauge symmetry.

Note that the gauge field strength contains an additional term in comparison to the electromagnetic case, $F_{a\mu\nu} = \partial_\mu V_{a\nu} - \partial_\nu V_{a\mu} - g f_{abc} V_{b\mu} V_{c\nu}$, where the f_{abc} is the structure constant of the gauge group. This results in self interaction of the non-Abelian gauge fields, which for e.g. brings to a property of asymptotic freedom in QCD.

2.1.2. Spontaneous Symmetry breaking

In an example of a Hamiltonian invariance under symmetry transformation, it is not reflected as a symmetry of the solutions to the corresponding equations of motion. However, with a given solution to the equations of motion, other solutions with the same energy can be obtained using the symmetry transformation. If the solution is invariant under the symmetry transformation, new solutions cannot be generated in this way. In quantum field theory the symmetries of the ground state of the system are considered, where the excitations of the ground state are identified as particles. For the case when the ground state is not invariant under a symmetry, the ground state must be degenerate. If the symmetry transformation of the equations of motion leaves them invariant, it is labeled by a continuous parameter, and an infinity of ground states is found. Then the spectrum of excitations can be built by expressing the Hamiltonian with fields whose quanta correspond to excitations of one particular ground state. The original symmetry of the action is not present any more, and the underlying symmetry is hidden, and therefore named as **spontaneous symmetry breaking**.

Although the symmetry is not really broken, the observer in an experimental setup will find many excitations of the ground states. This feature gives the universality of gauge interactions even though the gauge symmetry is spontaneously broken. In building of Lagrangian density the mass terms of gauge bosons were explicitly required to be zero in order to accommodate for gauge invariance. However, gauge bosons may acquire mass via the Higgs mechanism using the spontaneous symmetry breaking.

2.1.3. Electroweak Theory

In order to explain the continuous energy spectrum of electron in the β decay, the neutrino was postulated by Pauli, and a theory of weak interactions was proposed by Fermi. The parity violating nature of weak interactions was first proposed by Lee and Yang and experimentally confirmed by Wu et.al. The Wu experiment showed that electrons emitted from the β decays of Cobalt 60 occur preferentially in the opposite direction of the nucleus spin. This means that the parity is not conserved in this process, since electron momentum transforms as a vector, and the spin like a axial vector. This phenomena is accounted for in the V-A extension of the Fermi theory, by introducing left and right chirality operators. However, both Fermi and

the V-A extension of the theory are valid only in the low energy regime, below the W boson mass, since the predicted cross sections rise quickly above this threshold.

Introducing intermediate vector bosons brings a solution to this problem. They are a consequence of the Lagrangian density invariance under a set of local gauge transformations. The weak interaction with parity violation can be accommodated in the $SU(2)_L$ group. The left-handed fermions are assembled in doublets of weak isospin, where for the first generation of leptons they are:

$$\psi_L = \begin{pmatrix} \psi_{1,L} \\ \psi_{2,L} \end{pmatrix} = \begin{pmatrix} \nu_L \\ e_L \end{pmatrix}. \tag{2.8}$$

The Lagrangian density of two free massless left-handed fermions is:

$$\mathcal{L}_L = \overline{\psi}_L (i\gamma^\mu \partial_\mu) \psi_L. \tag{2.9}$$

The invariance under local gauge transformation on the Lagrangian density is required to obtain mediators of the weak interaction, they are of the form:

$$\psi_L \rightarrow \psi' = e^{ig\alpha^a(x)T^a} \psi_L \tag{2.10}$$

where the $T^a = \frac{\sigma^a}{2}$ (a=1,2,3, and are σ^a Pauli matrices), are generators of $SU(2)_L$ group. The $\alpha(x)$ are arbitrary space and time dependent functions, and g is the coupling constant of the interaction. Next, to preserve invariance of the Lagrangian under $SU(2)_L$ transformations, a covariant derivative is of the form:

$$D_\mu = \partial_\mu igT^a W^a_\mu \tag{2.11}$$

where the W^a_μ are three new vector boson fields, which are required to transform as:

$$W^a_\mu \rightarrow W^a_\mu - \partial_\mu \alpha^a(x) - g\epsilon^{abc}\alpha^b(x) W^c_\mu \tag{2.12}$$

where the ϵ^{abc} is the Levi-Civita tensor. In order to accommodate kinetic energy, the gauge field tensor is defined:

$$W^a_{\mu\nu} = \partial_\mu W^a_\nu - \partial_\nu W^a_\mu - g\epsilon^{abc} W^b_\mu W^c_{nu}. \tag{2.13}$$

Despite the fact that $SU(2)_L$ describes well the weak interaction, it is not a complete theory. It does not describe well the observed masses of fermions and gauge bosons associated with vector fields, and it fails in describing the interactions mediated by the neutral Z boson. As a solution to this problem, electroweak theory is constructed using the combination of $SU(2)_L$ and $U(1)_Y$ symmetry group, where the Y is the so-called hypercharge. The transformations of the Langrangian under $U(1)_Y$ gauge transformations is the same as in the U(1) case of electromagnetic

interactions. The covariant derivative is given by:

$$D_\mu = \partial_\mu + \frac{1}{2} i g^{'} Y B_\mu \tag{2.14}$$

where the B_μ is the new vector field, and $g^{'}$ is the new coupling constant. The field strength tensor is given by:

$$B_{\mu\nu} = \partial_\mu B_\nu - \partial_\nu B_\mu. \tag{2.15}$$

Then the combined electroweak Lagrangian using the $SU(2)_L \otimes U(1)_Y$ groups with the combined covariant derivative:

$$D_\mu = \partial_\mu + i g T^a W_\mu^a + \frac{1}{2} i g^{'} Y B_\mu. \tag{2.16}$$

Then the combined electroweak Lagrangian density is given by:

$$\begin{aligned}
\mathcal{L}_{EW} = & -\frac{1}{4} W^{a\mu\nu} W^a_{\mu\nu} - \frac{1}{4} B^{\mu\nu} B_{\mu\nu} && \left\{ \begin{array}{l} Gauge\ field\ kinetic\ energy \\ and\ self-interaction \end{array} \right. \\
& + \overline{\psi}_L \gamma^\mu (i\partial_\mu - \frac{1}{2} g \sigma^a W_\mu^a - \frac{1}{2} g^{'} Y B_\mu) \psi_L && \left\{ \begin{array}{l} Left-chiral\ fermion\ kinetic \\ energy\ and\ interaction \end{array} \right. \\
& + \overline{\psi}_R \gamma^\mu (i\partial_\mu - \frac{1}{2} g^{'} Y B_\mu) \psi_R. && \left\{ \begin{array}{l} Right-chiral\ fermion\ kinetic \\ energy\ and\ interaction \end{array} \right.
\end{aligned} \tag{2.17}$$

The self-interaction of vector fields is a consequence of the non-Abelian nature of $SU(2)_L$ group, i.e. its generators do not commute. Note that $U(1)_Y$ symmetries affect both the left and right-chiral particles, while $SU(2)_L$ affects only the left ones. This Lagrangian accommodates well for the experimentally observed phenomena of charged and neutral currents of the electroweak interactions.

2.1.4. The BEH Mechanism

In the formalism described up to this point, SM describes well all physics phenomena except for the gauge bosons and fermion masses, as the mass terms were requested to be zero to accommodate for the gauge invariance. The particle masses in the SM are incorporated into the theory via the Brout, Englert and Higgs (BEH) mechanism, which introduces particle masses via spontaneous electroweak symmetry breaking.

In the Higgs mechanism a new complex scalar, the $SU(2)_L$ doublet, with the field of hypercharge Y=1, is postulated.

$$\phi = \begin{pmatrix} \phi^+ \\ \phi^0 \end{pmatrix} = \frac{1}{\sqrt{2}} \begin{pmatrix} \phi_1 + i\phi_2 \\ \phi_3 + i\phi_4 \end{pmatrix}. \tag{2.18}$$

Since the fields are complex, there are four degrees of freedom. The Lagrangian density of spin zero doublet is given by the Klein-Gordon equation:

$$\mathcal{L}_\phi = |D^\mu \phi|^2 - V(\phi) = (D^\mu \phi)^\dagger (D_\mu \phi) - V(\phi) \tag{2.19}$$

where the $D_\mu = \partial_\mu + igT^a W_\mu^a + \frac{1}{2} ig' Y B_\mu$ is the electroweak covariant derivative, and $V(\phi)$ is the new postulated potential, called the Higgs potential. The $V(\phi)$ is required to be invariant under local gauge transformations. This requires the potential 2.18 to be symmetric in all four components, which brings to the expression:

$$V(\phi) = -\mu^2 |\phi|^2 + \lambda |\phi|^4 \tag{2.20}$$

where μ^2 and λ are real constants. In the figure 2.1 the Higgs potential is shown. It has a distinctive form of a 'Mexican hat'. The potential has degenerate minima placed as a circle in the complex ϕ_1 vs ϕ_2 plane, with the radius of $v = \sqrt{\frac{\mu^2}{\lambda}}$, which is called the vacuum expectation value of the Higgs field.

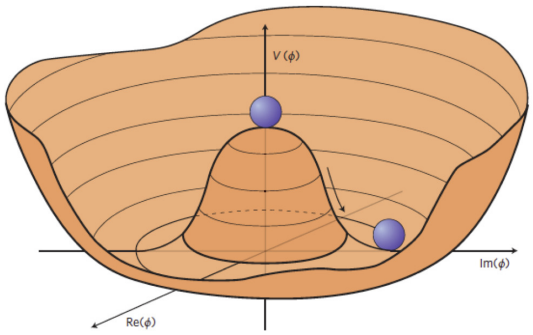

Figure 2.1.: The Higgs potential [49].

Further, the choice of a particular ground state breaks the symmetry spontaneously. The following ground states are chosen:

$$< \phi^+ >= 0, \quad < \phi^0 >= v. \tag{2.21}$$

Next, the expansion of fields around the ground state is made:

$$\phi(x) = \frac{1}{2} \begin{pmatrix} 0 + \eta_+(x) + i\xi_+(x) \\ v + \eta_0(x) + i\xi_0(x) \end{pmatrix}. \tag{2.22}$$

The $\eta_+(x), \xi_+(x), \xi_0(x)$ fields lead to massless Goldstone bosons. These terms can be absorbed, when the local gauge transformation is applied:

$$\phi \to \phi' = e^{ig\alpha^a(x)T^a} \phi \tag{2.23}$$

where $\alpha(x)$ is a arbitrary function. A consequence of the gauge transformation are three spin degrees of freedom for the vector bosons in the EW theory. The field is now given by:

$$\phi(x) = \frac{1}{2}\begin{pmatrix} 0 \\ v + \eta_0(x) \end{pmatrix}. \tag{2.24}$$

The $\eta_0(x)$ is associated with the field of the Higgs particle H. Consequently, the potential is now given by:

$$V(\phi) = -\frac{1}{2}(2\mu^2)H^2 + \lambda v H^3 + \frac{1}{4}\lambda H^4. \tag{2.25}$$

The first term in the equation is the Higgs mass $m_H = \sqrt{-2\mu^2}$, while the second and the third terms describe the Higgs field self-interactions with 3 and 4 particle vertexes.

The interaction of vector bosons in the EW theory with the Higgs boson can be determined using the covariant derivative on the Lagrangian density 2.19. This results in all terms including a photon field A^μ to be zero, since the photons are massless. Since ϕ^+=0, there is no mixing between $W^\pm$ and Z fields. The gauge boson masses are obtained to be:

$$m_W = \frac{1}{2}gv, \quad m_Z = \frac{1}{2}\sqrt{g^2 + g'^2}v. \tag{2.26}$$

From this the weak mixing angle can be determined as $\cos\theta_W = \frac{m_W}{m_Z}$. It can be derived that the $v = \frac{2M_Z}{g_Z}$, and from the experimental measurements of M_Z and g_Z one obtains a value of v=246 GeV, and also that the Higgs-vector boson couplings are proportional to the masses of the vector bosons.

The fermion masses cannot be explained in a same way as for gauge bosons. From the fact that fermion mass terms are not invariant under $SU(2)_L$ and $U(1)_Y$ gauge transformations, the so-called Yukawa interaction is obtained, and for the leptons is given as:

$$\mathcal{L}_Y = -\lambda_l(\overline{L}_L\phi^0 L_R + \overline{L}_R\phi^+ L_L) \tag{2.27}$$

for L_L left-handed lepton doublets and L_R right-handed lepton singlets. It is automatically invariant under $SU(2)_L$ because ϕ and L belong to the same doublet. Further, the electron mass is obtained to be $m_e = \lambda_e\frac{v}{\sqrt{2}}$, thus coupling to the Higgs field is proportional to the electron mass, while similar expressions are obtained for all leptons. The quark masses are obtained using the co-called Cabibbo-Kobayashi-Maskawa (CKM) matrix, where mass eigenstates are rotated with respect to the flavor eigenstates.

Finally, the Lagrangian density for the Higgs mechanism including the Yukawa

interaction is given as:

$$\begin{aligned}
\mathcal{L}_H =& |(i\partial_\mu - \frac{1}{2}ig\sigma^a W_\mu^a - \frac{1}{2}ig^{'}YB_\mu)\phi|^2 && \left\{ \begin{array}{l} H\ boson\ kinetic\ energy, \\ W^{\pm}/Z\ boson\ mass\ and \\ W^{\pm}/Z - H\ interaction \end{array} \right. \\
& +\mu^2|\psi|^2 - \lambda|\psi|^4 && \left\{ \begin{array}{l} H\ boson\ mass\ and \\ self - interaction \end{array} \right. \\
& +(M_1\overline{\psi}_L\phi\psi_R + M_2\overline{\psi}_L\phi^C\psi_R + h.c.). && \left\{ \begin{array}{l} Fermion\ Yukawa\ mass\ and \\ fermion - H\ interaction \end{array} \right.
\end{aligned} \tag{2.28}$$

2.1.5. Quantum Chromodynamics

The Quantum Chromodynamics(QCD) describes the strong interaction between the quarks and gluons. It is based on the $SU(3)_C$ symmetry group, where the resulting gauge bosons are gluons. Quarks are assigned a color charge C, which can take values of 'red', 'blue' and 'green', and gluons carry combinations of color-anticolor. Quarks are assembled in color triplets:

$$\psi = \begin{pmatrix} \psi_r \\ \psi_b \\ \psi_g \end{pmatrix}. \tag{2.29}$$

The Lagrangian density for free quarks is:

$$\mathcal{L} = \overline{\psi}(i\gamma^\mu\partial_\mu - m)\psi. \tag{2.30}$$

For the $SU(3)_C$ group, the local gauge invariance is required using a transformation:

$$\psi \rightarrow \psi^{'} = e^{ig_s\alpha^a(x)T^a}\psi \tag{2.31}$$

where the g_s is the strong coupling constant, $\alpha_s(x)$ are arbitrary functions of space and time, and T^a, a=1,...8, are generators of the non-Abelian symmetry group $SU(3)_C$.

In order to have invariant Lagrangian density under $SU(3)_C$ symmetry transformations, the covariant derivative is of the form:

$$D_\mu = \partial_\mu + ig_sT^aG_\mu^a \tag{2.32}$$

which contains eight new vector fields G_μ^a which correspond to massless gluons. Then the fields are required to transform as:

$$G_\mu^a \rightarrow G_\mu^a - \partial_\mu\alpha^a(x) - g_sf^{abc}\alpha^b(x)G_\mu^c \tag{2.33}$$

where the kinetic energy of the gluons is given by the field strength tensor $G_{\mu\nu}^a =$

$\partial_\mu G^a_\nu - \partial_\nu G^a_\mu - g_s f^{abc} G^b_\mu G^c_\nu$. This brings to the final Lagrangian density of QCD given by:

$$\begin{aligned}
\mathcal{L}_{QCD} =& \overline{\psi}(i\gamma^\mu \partial_\mu - m)\psi && \left\{ \begin{array}{l} q\ mass\ and \\ kinetic\ energy \end{array} \right. \\
& -\frac{1}{2} g_s \overline{\psi}(\gamma^\mu \lambda^a G^a_\mu)\psi && \left\{ \begin{array}{l} q-g\ field \\ interaction \end{array} \right. \\
& -\frac{1}{4} G^{a\mu\nu} G^a_{\mu\nu}. && \left\{ \begin{array}{l} Gauge\ field\ kinetic\ energy \\ and\ self-interaction \end{array} \right.
\end{aligned} \tag{2.34}$$

The self-interaction of the gluon fields is a consequence of the non-Abelian nature of the $SU(3)_C$ symmetry group. Confinement is the consequence of self-interaction, where colored particles combine into colorless hadrons, which have a total of zero colour charge.

2.1.6. The Standard Model Lagrangian

The SM has a symmetry of $SU(3)_C \otimes SU(2)L \otimes U(1)_Y$, where the $SU(2)_L \otimes U(1)_Y$ spontaneously breaks to $U(1)_{EM}$, while $SU(3)_C$ is considered to be unbroken. This results in a final SM Lagrangian density before the electroweak symmetry breaking given by:

$$\begin{aligned}
\mathcal{L}_{SM} =& -\frac{1}{4} B^{a\mu\nu} B^a_{\mu\nu} - \frac{1}{4} W^{a\mu\nu} W^a_{\mu\nu} - \frac{1}{4} G^{a\mu\nu} G^a_{\mu\nu} && \left\{ \begin{array}{l} Gauge\ field\ kinetic \\ energy\ and \\ self-interaction \end{array} \right. \\
& + \begin{array}{l} \overline{\psi}_L \gamma^\mu (i\partial_\mu - \frac{1}{2} g \sigma^a W^a_\mu - \frac{1}{2} g' Y B_\mu)\psi_L + \\ + \overline{\psi}_R \gamma^\mu (i\partial_\mu - \frac{1}{2} g' Y B_\mu)\psi_R \end{array} && \left\{ \begin{array}{l} Fermion\ kinetic \\ energy\ and \\ EW\ interaction \end{array} \right. \\
& + |(i\partial_\mu - \frac{1}{2} i g \sigma^a W^a_\mu - \frac{1}{2} i g' Y B_\mu)\phi|^2 && \left\{ \begin{array}{l} H\ kinetic\ energy, \\ W^\pm/Z\ mass\ and \\ W^\pm/Z - H\ interaction \end{array} \right. \\
& + \mu^2 |\psi|^2 - \lambda |\psi|^4 && \left\{ \begin{array}{l} H\ boson\ mass \\ and\ self-interaction \end{array} \right. \\
& + (M_1 \overline{\psi}_L \phi \psi_R + M_2 \overline{\psi}_L \phi^C \psi_R + h.c.) && \left\{ \begin{array}{l} Fermion\ Yukawa\ mass \\ and\ fermion - H \\ interaction \end{array} \right. \\
& + \frac{1}{2} g_s \overline{\psi}_q (\gamma^\mu \lambda^a G^a_\mu)\psi_q. && \left\{ \begin{array}{l} q-g\ field \\ interaction \end{array} \right.
\end{aligned} \tag{2.35}$$

2.2. Standard Model and Higgs Measurements

Throughout many years the SM predictions have been successfully experimentally confirmed [39]. In addition, SM predictions have passed stringent tests at the LHC using the Run 1 data. However, the highlight of LHC searches is certainly the Higgs-like particle discovery. In this section a selection of recent LHC analyses results in the physics of SM and Higgs will be presented.

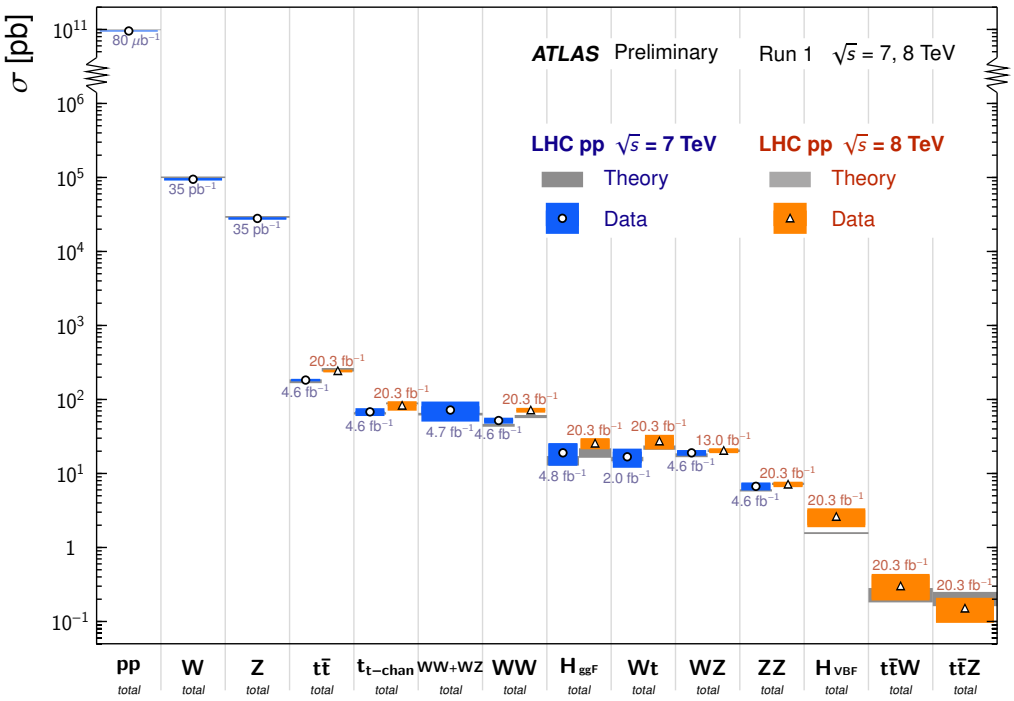

Figure 2.2.: Standard Model total production cross section measurements compared to corresponding theoretical expectations at NLO order or higher. The data set and integrated luminosity used in the measurement are indicated in the figure [50].

Standard Model Measurements

The theoretical predictions of SM process cross sections at the LHC have been successfully confirmed by the ATLAS and CMS experiments. Firstly, good agreement in the measurements of pure QCD jet production has been found over wide range of jet transverse momenta [51]. Secondly, excellent agreement has been obtained in the measurements of single and multiple $W^{\pm}$ and Z^0 production, single and pair top quark production, and also in association with vector bosons. In the figure 2.2

SM total cross sections production measurements for the ATLAS at 7 and 8 TeV are shown, and a good agreement of theoretical prediction and data is found. Thirdly, the observation of a $B_S \to \mu^+\mu^-$ process by the LHCb and CMS experiments [52] is in good agreement with the SM prediction. Namely, the Cabbibo Kobayashi Maskawa (CKM) description of flavor mixing and CP violations can be used to predict the branching ratio for this rare decay, which is sensitive to presence of new physics, but no significant deviations from the SM have been observed. These results give good confidence in the theoretical predictions and are a good confirmation of the SM theoretical framework.

Higgs Physics

The Higgs-like particle discovery has been reported in 2012 by the ATLAS and CMS experiments [53, 54]. Since then, this result has been confirmed with higher confidence by the analyses at these experiments, using more integrated luminosity. In the figure 2.3 the observed local p_0 as a function of m_H is shown for ATLAS and CMS. For the combined result using the $H \to \gamma\gamma$ and $H \to ZZ^* \to 4l$ processes significance of 7 and around 6 sigma is reached for these experiments respectively. The Higgs signal has been measured in a number of channels ($\gamma\gamma, ZZ^*, WW^*, b\bar{b}, \tau^+\tau^-$), and their signal strength is shown in the figure 2.4. The overall signal strength for both ATLAS and CMS is found to be around 1. Therefore the SM predictions for the Higgs boson across different channels and experiments are in agreement with data.

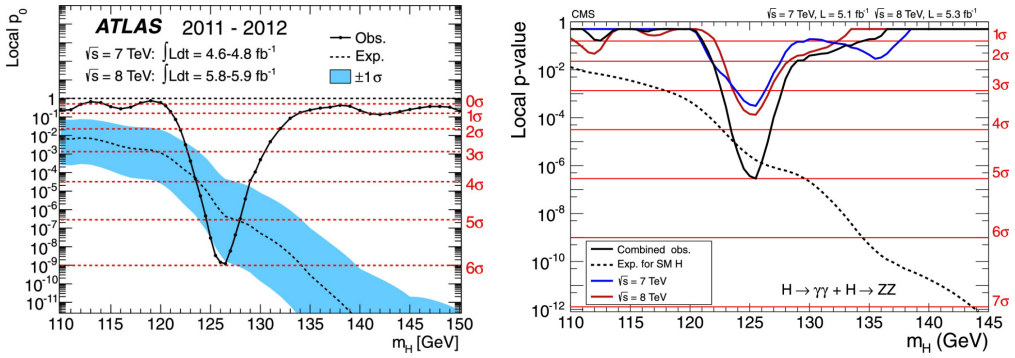

(a) (b)

Figure 2.3.: The observed local p_0 as a function of m_H for the ATLAS [10](a) and CMS [11](b) experiment using the combined $H \to \gamma\gamma$ and $H \to ZZ^* \to 4l$ processes. The dashed curves represent the median expected local p-value, and the solid lines are the experimental results. There is a 7σ and around 6σ signal-like peak for the ATLAS and CMS respectively. The c.m.e and integrated luminosity are indicated on the plots.

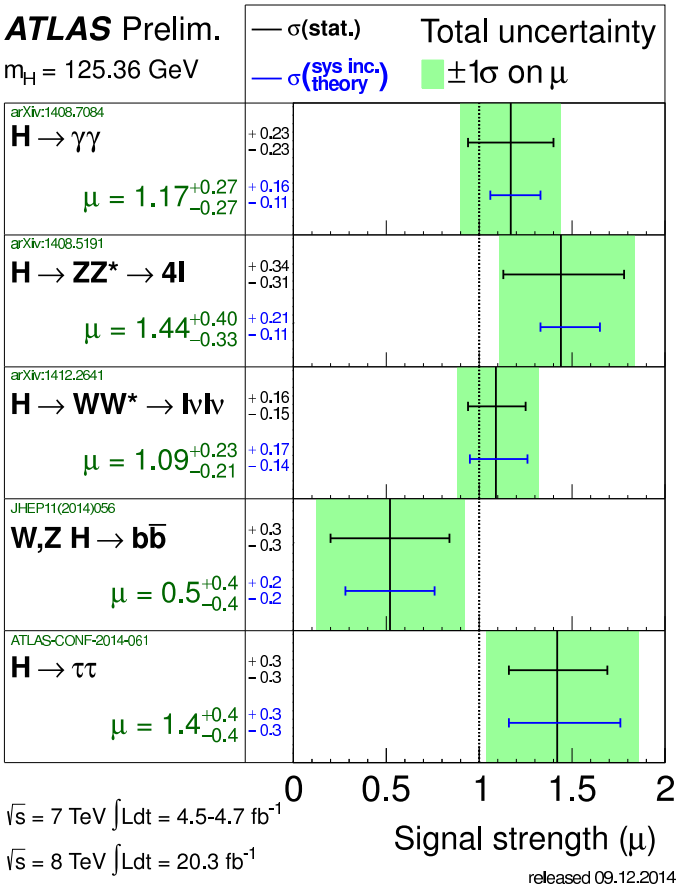

Figure 2.4.: Production strengths for a Higgs boson of mass $m_H = 125.36$ GeV, normalized to the SM expectations. Best fit values are shown with the black line, the total $\pm 1\sigma$ uncertainty is indicated in green [55].

	m_H [GeV] ATLAS [33]		m_H [GeV] CMS [34]	
$H \to \gamma\gamma$	$125.98 \pm 0.42 \pm 0.28$	125.98 ± 0.50	$124.70 \pm 0.31 \pm 0.15$	$124.70^{+0.35}_{-0.34}$
$H \to ZZ^* \to 4l$	$124.51 \pm 0.52 \pm 0.06$	124.51 ± 0.52	$125.6 \pm 0.4 \pm 0.2$	125.6 ± 0.4
$H \to \gamma\gamma$, $H \to ZZ^* \to 4l$	$125.36 \pm 0.37 \pm 0.18$	125.36 ± 0.41	$125.03^{+0.26\ +0.13}_{-0.27\ 0.15}$	125.03 ± 0.30
Δm_H	$1.47 \pm 0.67 \pm 0.18$		$-0.9 \pm 0.4 \pm 0.2^{+0.34}_{-0.35}$	
ATLAS, CMS [56]	$125.09 \pm 0.21 \pm 0.11$			

Table 2.2.: ATLAS and CMS Higgs mass measurements in the $H \to \gamma\gamma$ and $H \to ZZ^* \to 4l$ channels, and their combination. The measurements are presented with statistical and systematic uncertainty respectively.

The Higgs particle mass, is measured to be $125.09 \pm 0.21 \pm 0.11$ [56], using a sta-

tistical combination of ATLAS and CMS experiments. In the table 2.2 recent Higgs mass measurements are shown for ATLAS and CMS for the $H \to \gamma\gamma$ and $H \to ZZ^* \to 4l$ channels, and their combination. This value is in agreement with the relatively low Higgs mass predicted by the SM. In addition, Higgs spin and parity have been experimentally determined to be zero and dominantly CP-even with a high degree of confidence [57, 58].

An important aspect of Higgs physics analyses is the study of its couplings to fermions and gauge bosons. The ATLAS and CMS measurements are included in the global fit, and good agreement with SM predictions for the signal strength and coupling has been found [59]. The coupling measurements will play an important role in the Run 2 analyses.

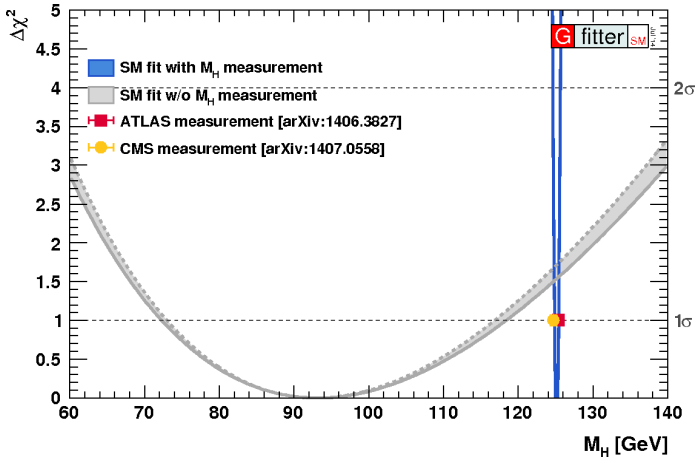

Figure 2.5.: Global SM fit to electroweak data comparison to the Higgs mass measurement [60]. The discrepancy between the fit obtained and the fit on the ATLAS and CMS data is consistent with $\Delta\chi^2$ $\sim$1.2σ level.

Finally, the global SM fit to electroweak precision data was obtained using the ATLAS and CMS measurements. In the figure 2.5 the comparison between the fit using precision data and no assumption of the Higgs mass is compared to the fit using the Higgs mass measurements. The electroweak fit obtained Higgs mass is $m_H = 94^{+25}_{-22}$ GeV, and the discrepancy between these values is $\sim$1.5σ, which shows good agreement [61]. Therefore, this result gives confidence in the SM as a theory.

2.3. Beyond the Standard Model

Despite the fact that good agreement of SM prediction compared to the data have been found in the SM and Higgs physics processes, a number of topics cannot be answered by the SM, or need to be interpreted using a more complex theory. A number of phenomena occurs in nature, that cannot be explained by the SM. This gives good motivation for physics beyond the SM (BSM).

It is assumed that in the Big Bang Nucleosynthesis equal amounts of matter and antimatter have been created. However, in the universe today mostly matter is observed. The SM does not explain well the evolution of such a system to present time, and additional theory is required to explain this fact. In the SM, neutrinos are required to have mass equal to 0. However, neutrino experiments have shown that neutrinos indeed have a mass. Adding extra terms to the SM to acquire mass for the neutrinos brings additional theoretical problems, which need to be well incorporated in the theory. The SM gives no explanation of the gravity, and it does not incorporate well the most successful theory of gravity, the general relativity. A possibility of finding a common theory for all known interactions should be considered. From the cosmological observations, only about 4.9% of the universe makes the known matter. The remaining 26.8% is considered to be dark matter, and 68.3% the dark energy [62]. A number of theories offer explanations to this phenomena, and a prominent one called Supersymmetry (SUSY), offers an explanation to the existence of dark matter, and it is the topic of this thesis. In the next chapter, more details about the SUSY motivation, theoretical framework, and searches strategy will be given. It should be noted that SUSY does not provide the explanation to the existence of dark energy. Dark energy is hypothesized to be 'filling' the space, and it is responsible for the acceleration and expansion of the universe. Numerous theories give possible explanations, where one of the approaches suggests that volume of space has some fundamental energy, where a cosmological constant Λ is introduced to quantify that. Some SUSY theories require the cosmological constant to be zero, which is in contradiction with the requirement of SUSY to be broken. SUSY is not able to offer a good explanation of the dark energy.

3. Supersymmetry

Supersymmetry (SUSY) [19–27] is one of the extensions of the SM, which offers solutions to the problems not explained by the SM. The SM describes well the fundamental particles and their interactions at energies from ∼eV up to a few 100 GeV, excluding the neutrino masses phenomena. The SM has been well tested at experiments up to the current energy reach. However, it does not explain phenomena such as the arbitrariness of gauge couplings, mixing angles, particle masses, the reasons for gauge theories, quantum numbers and generations, and does not add gravity into the theory. It is highly probable that new physics is present in the energy range from the current experimentally reachable TeV scales to the Planck scale of $\sim 10^{18}$ GeV, and SUSY gives a framework which incorporates this.

SUSY is postulated as a fundamental symmetry between fermions and bosons, and it introduces a new set of supersymmetric particles at the electroweak scale. It naturally offers solutions to a number of phenomena not incorporated into the SM, and makes one of the best motivated theories in physics BSM. In this chapter the motivation for SUSY will be given in the section 3.1, the formalism of SUSY in 3.2, minimal SUSY model with the particle content and phenomenology will be given in the section 3.3, and aspects of SUSY analyses in ATLAS will be shown in the section 3.4. This chapter is based on [63], and additional descriptions are taken from [46, 48, 64].

3.1. Motivation for SUSY

SUSY offers solutions to a number of phenomena, which cannot be explained in the SM. In this section, an overview of problems not covered by the SM, which are solved using SUSY, will be given as a motivation.

Hierarchy Problem and Naturalness

Supersymmetric field theories address the naturalness of a relatively light Higgs boson mass. Namely, the radiative corrections to the Higgs boson mass squared become extremely large when any particle couples to the Higgs directly or indirectly. In the figure 3.1 left, a one-loop quantum correction to the Δm_H^2 is shown for the fermionic loop, which is given by:

$$\Delta m_H^2 = -\frac{y_f^2}{8\pi^2}[2\Lambda^2 + 6m_f^2 \ln(\frac{\Lambda}{m_f}) + ...] \tag{3.1}$$

where Λ is the ultraviolet cutoff energy scale at which the SM remains valid. The Higgs mass diverges quadratically with Λ, and if it is assumed that the SM stays valid up to the Planck scale M_P, i.e. $\Lambda = M_P$, this correction is 10^{30} times bigger than the reasonable value of the $m_H^2 \sim 10^{20}$ GeV^2. Similarly, one-loop quantum correction to the Δm_H^2 via a scalar field S is presented in the figure 3.1 right, and is given by:

$$\Delta m_H^2 = \frac{\lambda_S}{16\pi^2}[\Lambda^2 - 2m_S^2 \ln(\frac{\Lambda}{m_S}) + ...] \tag{3.2}$$

where λ_S is the quadratic coupling to the Higgs boson.

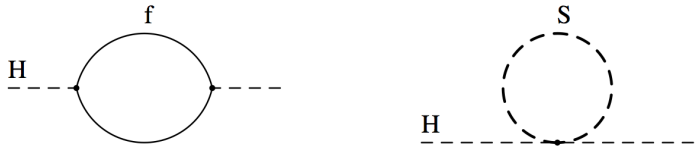

Figure 3.1.: One-loop quantum corrections to the Δm_H^2 due to the fermionic (left) and scalar boson (right) loop [46].

As the contributions of boson and fermion loops are of opposite sign, from the two expressions (3.1 and 3.2) it follows that divergent contributions with Λ^2 terms can be canceled out in the theory if for each fermionic loop there is a scalar loop with:

$$\lambda_s = 2y_f^2. \tag{3.3}$$

As a solution, SUSY imposes exactly this relationship 3.3, and in SUSY field theories, there are no quadratic divergences at one- and multi-loop levels. This allows for large mass differences in the mass scale hierarchy, called the 'hierarchy problem' [65–68], to be maintained in a natural way in SUSY with this solution [69–74]. Moreover, other logarithmic corrections to the couplings vanish in SUSY.

Gauge Couplings Unification

Grand Unified Theories aim to provide a unified description of electroweak and strong interactions [75]. This is done by embedding the gauge groups of SM $SU(3)_C \otimes SU(2)_L \otimes U(1)_Y$ into one universal symmetry group, where there will be one interaction with one coupling constant at the GUT scale. The couplings unification can be explored by taking the experimentally measured values of couplings, and extrapolating them to high energies, using the energy dependent renormalization formalism for gauge couplings. The couplings of each fundamental force in SM, when run by renormalization group equations of the SM to the high energy scale, never become equal at the same scale, see figure 3.2 (a). This implies that unification in a single point is not natural in SM, and it is ruled out by 7 standard deviations [75]. In order to obtain the unification of gauge couplings at the GUT scale, the running of gauge couplings to the GUT scale needs to be modified. This can be obtained by

introducing new physics between electroweak and Planck scale. For example, when SUSY particles are included in the renormalization group equations, and evolution of couplings is performed to the high energy scale, they appear to intersect at the energy scale of $\sim 10^{16}$ GeV. The best unification of gauge couplings is achieved for SUSY particle masses at the Planck scale. This gives a very good motivation for SUSY, as it favors unification of couplings at the high energy scale with high precision. Note that Grand Unification has been proposed [73, 75–82] using minimal SUSY, but it might not be the final solution to this problem.

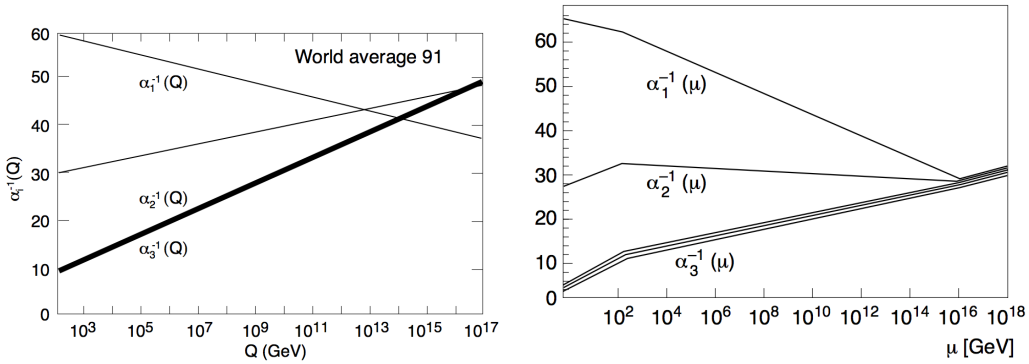

(a) SM (b) SUSY

Figure 3.2.: Gauge coupling strengths in SM do not evolve to a unified value (a), shown for the LEP measurements, but unify when SUSY is introduced (b) [46].

Cold Dark Matter Candidate

The observations show that galaxy rotation curves do not fall with the radial distance from the galactic center [39]. However, they can be explained by introducing a new type of weakly interacting matter, i.e. dark matter (DM). It is believed that DM originates from neutral relic from the early Universe, i.e. it should be neutral. In addition, to give explanation to the structure formation, DM should be non-relativistic at the time of structure formation, i.e. it should be cold. Therefore, the newly introduced particle needs to explain these effects, and accommodate for current estimate of cold dark matter (CDM) density from the astronomical measurements of cosmic microwave background, found to be $\Omega_{CDM}h^2 = 0.1198 \pm 0.0026$ for the Planck, WMAP and high resolution data from APC and SPT [83]. These particles can participate only in the weak and gravitational interaction, which makes their detection very hard. Due to the lack of electromagnetic interaction with normal matter, they are invisible through normal electromagnetic measurements, and due to large mass, they are not relativistic. The co-called, cold dark matter candidate needs to be a weakly interacting and massive particle (WIMP). Within the SM only

neutrinos can be considered as a DM candidate, but they are not massive, nor their abundance is large enough to reproduce the DM in the Universe.

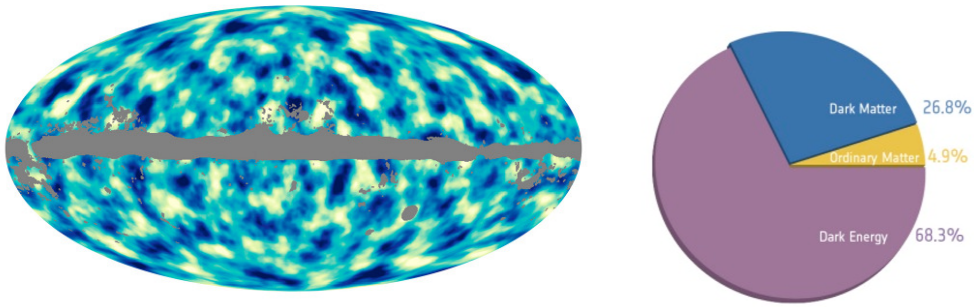

(a) (b)

Figure 3.3.: All-sky map of dark matter distribution in the universe (a) and the 'cosmic recipe' (b) obtained by the Planck measurements [84].

The lightest SUSY particle (LSP) could fit the properties of a WIMP. In many SUSY models, a newly defined property called R-parity is conserved. The lepton and baryon number conservation in SM has been tested with high precision, while in SUSY a violation of this symmetry can be present due to a number of renormalizable couplings in the theory. Therefore, these couplings need to be small in order to explain the data. The R-parity conservation forbids these couplings. As a consequence, the LSP is a stable particle, see more details in the section 3.3.2. Then in the evolution of particle content from the Big Bang Nucleosynthesis (BBN) up to the present time, the CDM density is calculated and compared to the measurement. Since relic from the BBN could consist of LSP, and could have the right amount of relic density to be the majority of the CDM, the LSP is a good CDM candidate. As an illustration, in the figure 3.3 the Planck measurement all-sky dark matter distribution, and the current 'cosmic recipe' which estimated 26.8% of dark matter in the universe, is shown.

SUSY is not the only BSM theory which offers the WIMP candidates. The Unified Extra Dimensions offer the lightest Kaluza-Klein particle (KLP), and Little Higgs models offer the Lightest T-odd particle (LTP). In addition, opposed to WIMP, there are other cold dark matter candidates, like massive compact halo objects (MACHO) and axions.

Instability of the Electroweak Vacuum

The effective electroweak potential in the SM resembles the Mexican hat, and the electroweak vacuum lies in the surrounding valley where v = 246 GeV. Beyond this valley the potential energy of the Higgs field rises, i.e. the brim of the hat rises. However, calculations show that when the renormalization by the top quark is performed, for the most up to date measured m_t and m_H, it overwhelms the

Higgs field itself, and the brim of the hat turns down at large Higgs field values. Consequently, the present electroweak vacuum is unstable, with a possibility of quantum tunneling through the brim of the hat [64].

According to current best SM calculations available, the Higgs field potential turns down at the Higgs scale Λ according to [85]:

$$log_{10}(\frac{\Lambda}{GeV}) = 11.3 + 1.0(\frac{m_H}{GeV} - 125.66) - 1.2(\frac{m_t}{GeV} - 173.10) + 0.4(\frac{\alpha_s(M_Z) - 0.1184}{0.0007}) \tag{3.4}$$

and when the world average values of m_H, m_t and α_s are used, the estimate is:

$$\Lambda = 10^{10.5 \pm 1.1} GeV. \tag{3.5}$$

In the figure 3.4 (a) quadratic Higgs self coupling λ is shown, where $\lambda < 0$ for a scale beyond the calculated Λ, i.e. the scale at which the brim of the hat turns down.

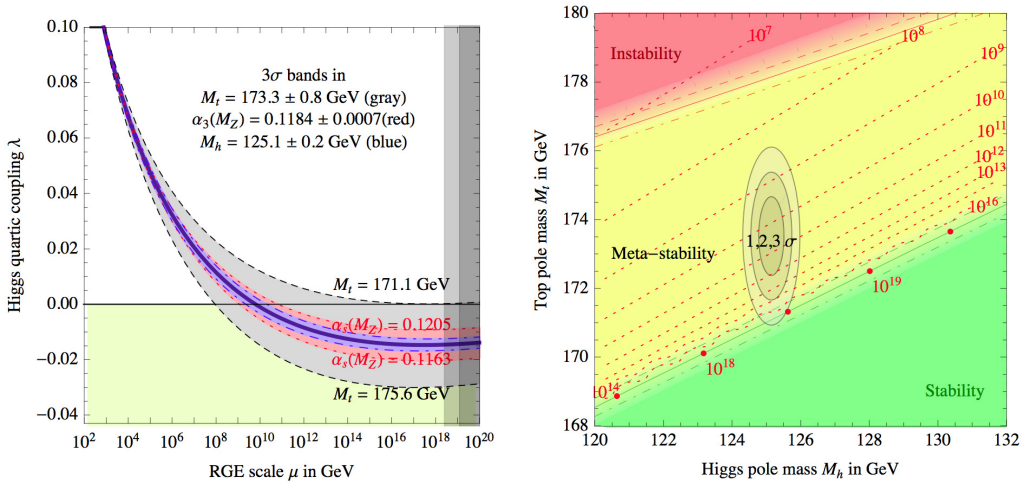

(a) (b)

Figure 3.4.: Quadratic Higgs self coupling λ (a) and electroweak vacuum stability (b). The $\lambda < 0$ for a values of quadratic Higgs self coupling higher than the cut-off scale. In the m_t vs m_H plane, for the world average masses and accuracy, the electroweak vacuum is in the meta stable region [85].

In the figure 3.4 (b) the regions of vacuum stability are shown in the m_t vs m_H plane, for the current top and Higgs mass measurements. It can be stable, meta-stable or instable, according to the Higgs scale Λ, where the stable would (probably) live longer than the age of the Universe. The red dashed iso-lines represent the Λ scale. It can be seen that with the current m_t and m_H we are in fact residing in the meta-stable region, but the uncertainty on the mass measurements is still relatively large. As the Λ calculation is most sensitive to the top mass calculation, a more precise measurement is required to make further distinction. For a higher

value of m_t further destabilization into meta-stable region would appear, where for a lower m_t the shift would be towards the stable region. In addition, improvement in implementations of m_t in Monte Carlo generators used by the experiments is needed.

Although SM resides in the meta-stable region, the lifetime of the universe is still very long. However, the SM might not be the final theory, and in various SUSY models, solutions to the problem of electroweak vacuum residing in the meta-stable region is given. Here the Λ is shifted towards the higher values, into the stable region, i.e. there is no brim of the hat. This gives an alternative solution, with even longer lifetime of the universe [64].

SUSY is a well motivated theory because it solves the hierarchy problem, it leads to gauge coupling unification and provides the dark matter candidate. Despite the fact that no experimental evidence of its existence has been seen so far, it is a framework that combines well most of known phenomena in HEP, and a search for its existence is of great importance.

However, SUSY has a few drawbacks. It does not provide a reason for the quark and lepton masses or mixing angles. Also, it does not give an explanation for the number of flavors. The CP violation is not explained by the SUSY, nor the barion asymmetry.

3.2. Supersymmetric Lagrangian

In order to accommodate for phenomena not included by the SM formalism, a new symmetry needs to be proposed. Bosons are mediators of interactions, and their statistics allows for coherent superposition, and formation of forces. Fermions are constitutes of matter, and their statistics has an additive character, and allows for formation of matter. Supersymmetry is a theory which introduces a new symmetry, between boson and fermion fields. However, generators of boson-fermion symmetry need to have new properties in comparison to the SM gauge symmetries represented by the $SU(3)_C \otimes SU(2)_L \otimes U(1)_Y$ groups, and details about the SUSY algebra need to be defined, so the SUSY Lagrangian density can be derived. A general formalism of SUSY will be given in this section.

3.2.1. Supersymmetry Algebra

A SUSY transformation turns a bosonic state into a fermionic state and reverse. The operator of this transformation Q must be an anticommuting spinor, given by:

$$\begin{aligned} Q|Boson\rangle &= |Fermion\rangle \\ Q|Fermion\rangle &= |Boson\rangle. \end{aligned} \tag{3.6}$$

Spinors are complex objects, so the hermitian conjugate of Q, $Q^\dagger$, is also a symmetry generator. Due to the fact that Q and $Q^\dagger$ are fermionic operators, they have to carry

spin angular momentum of $\frac{1}{2}$, and SUSY is a spacetime symmetry. The form of such a symmetry group is highly restricted, as shown by the theory of Haag, Lopuszanski and Sohnius [86], which is an extension of the Coleman and Mandula theorem [87]. The symmetry is called the supersymmetry, and it is a non-trivial extension of the Poincare symmetry. With a realistic approach in the theory, the fermions have chirality, i.e. left- and right-handed fermions transform differently under gauge transformations. Then the possibility of parity-violating interactions is allowed. This theorem implies that following algebra of commutation and anticommutation needs to be satisfied for the Q and $Q^\dagger$ operators (in the schematic form with the suppressed index notation):

$$\begin{aligned} \{Q, Q^\dagger\} &= P^\mu \\ \{Q, Q\} = \{Q^\dagger, Q^\dagger\} &= 0 \\ [P^\mu, Q] = [P^\mu, Q^\dagger] &= 0 \end{aligned} \tag{3.7}$$

where the P^μ is the four-momentum generator of spacetime translations. The P^μ transforms under Lorentz boost and rotations as spin-1 object, while Q and $Q^\dagger$ transform as spin-$\frac{1}{2}$ objects.

The supersymmetric algebra has the following consequences:

- The single-particle states of SUSY theory, where the bosonic and fermionic states have the opposite spin statistics, fall into representations of SUSY algebra, called the supermultiplets.
- Since the squared-mass operator commutes with both with Q and $Q^\dagger$ operators, and also spacetime and translation operators, the particles of the same supermultiplet must have the same eigenvalues of squared-mass operator, and the masses of superpartners must be equal.
- Since Q and $Q^\dagger$ SUSY generators commute with generators of gauge transformations, particle of the same supermultiplet must be in the same representation of the gauge group, and therefore have the same quantum numbers of charge, weak isospin and color.
- Each supermultiplet contains the same number of bosonic and fermionic degrees of freedom, i.e. $n_B = n_F$. This is a consequence of the fact that fermionic generators Q and $Q^\dagger$ map the bosonic sub-space B into fermionic sub-space F and vice versa, and the dimensionality of the two sub-spaces is preserved in the transformation. Then the transformation of $B \to F \to B$ also preserves the dimensionality, thus the number of bosonic and fermionic states must be equal.

From the given SUSY algebra consequences, a supermultiplets can consist of a:

- **Chiral supermultiplet**, which consists of one fermion with two spin degrees of freedom, i.e. $n_F = 2$, and two real scalar fields each with $n_B = 1$. By the

naming convention, to the SUSY scalar particle and extension 's' is added to the name, e.g. 'sfermion'.

- **Gauge supermultiplet**, which consists of massless spin - 1 vector bosons which has two helicity states, so the number of $n_B = 2$, and its superpartners, the spin-$\frac{1}{2}$ fermions with two helicity states, so the there are $n_F = 2$ superpartners. By the naming convention the SUSY particles get an extension 'ino' to their names, e.g. 'gaugino'.

The supermultiplets constellation and SUSY particle content can vary for different SUSY models. The particle content of minimal SUSY model will be examined in the section 3.3.

In the following sections, the SUSY Lagrangian density will be derived in order to get a general theory formulation which explains all particle masses and their interactions. First the Lagrangian of the chiral supermultiplet and its interactions in 3.2.2, and second, the gauge supermultiplet and its interactions in 3.2.3 will be derived. Then the soft SUSY breaking term will be added in 3.2.4, and the final SUSY Lagrangian density will be obtained in the section 3.2.5.

3.2.2. Lagrangian for the Chiral Supermultiplets

The starting point in the chiral supermultiplet Lagrangian density derivation is considered in the most simple SUSY model. This is a theory with only one chiral supermultiplet, the so-called massless non-interacting Wess-Zumino model [88]. It contains one left-handed two component Weil fermion ψ, and a complex scalar field ϕ superpartner. The Lagrangian density is then given by:

$$\begin{aligned} \mathcal{L}_{chiral,free} = \mathcal{L}_{scalar} + \mathcal{L}_{fermion} = \\ - \partial^\mu \phi^* \partial_\mu \phi + i\psi^\dagger \overline{\sigma}^\mu \partial_\mu \psi \end{aligned} \tag{3.8}$$

which contains two kinetic terms for the scalar and fermionic states.

The minimal SUSY transformations for the scalar fields are given by:

$$\begin{aligned} \delta\phi &= \epsilon\psi \\ \delta\phi^* &= \epsilon^\dagger \psi^\dagger \end{aligned} \tag{3.9}$$

where ϵ^α is an infinitesimal, anti-comuting, two-component Weyl fermion object, and it parametrizes the SUSY transformation. Then the scalar part of the Lagrangian transforms like:

$$\delta\,\mathcal{L}_{scalar} = -\epsilon\partial^\mu\psi\partial_\mu\phi^* + \epsilon^\dagger\partial^\mu\psi^\dagger\partial_\mu\phi. \tag{3.10}$$

The fermion part of the Lagrangian transforms as:

$$\delta\,\mathcal{L}_{fermion} = \epsilon\partial^\mu\psi\partial_\mu\phi^* + \epsilon^\dagger\partial^\mu\psi^\dagger\partial_\mu\phi - \partial_\mu(\epsilon\sigma^\nu\overline{\sigma}^\mu\psi\partial_\nu\phi^* + \epsilon\psi\partial^\mu\phi^* + \epsilon^\dagger\psi^\dagger\partial^\mu\phi). \tag{3.11}$$

The scalar and fermionic part transformations of 3.10 and 3.11 equations cancel up

to the total derivative, leaving the action invariant, and required by the Hamiltonian principle of action.

In order to have a SUSY algebra valid off-shell, the given formalism needs to be generalized by introducing an auxiliary field F, with the Lagrangian density:

$$\mathcal{L}_{auxiliary} = F^* F \tag{3.12}$$

where the kinematic term is equal to zero. Then the auxiliary fields transform as:

$$\begin{aligned} \delta F &= -i\epsilon^\dagger \overline{\sigma}^\mu \partial_\mu \psi \\ \delta F^* &= i\partial_\mu \psi^\dagger \overline{\sigma}^\mu \epsilon. \end{aligned} \tag{3.13}$$

The action needs to be invariant under transformations of:

$$\begin{aligned} \delta \psi_\alpha &= -i(\sigma^\mu \epsilon^\dagger)_\alpha \partial_\mu \phi + \epsilon_\alpha F \\ \delta \psi^\dagger_{\dot{\alpha}} &= i(\epsilon \sigma^\mu)_{\dot{\alpha}} \partial_\mu \phi^* + \epsilon^\dagger_{\dot{\alpha}} F^*. \end{aligned} \tag{3.14}$$

This brings to the Lagrangian density of the free chiral supermultiplet:

$$\mathcal{L}\, chiral, free = -\partial^\mu \phi^{*i} \partial_\mu \phi_i + i\psi^{\dagger i} \overline{\sigma}^\mu \partial_\mu \psi_i + F^{*i} F_i \tag{3.15}$$

where i is the index which runs over all flavor and gauge degrees of freedom.

Interactions of scalar and fermion fields within the same supermultiplet need to be considered. The interaction Lagrangian follows as:

$$\mathcal{L}_{chiral,int} = (-\frac{1}{2} W^{ij} \psi_i \psi_j + W^i F_i) + c.c. \tag{3.16}$$

where W^{ij} and W^i are the functions of scalar fields which participate in the interaction. With the requirement of invariance of the Lagrnangian under SUSY transformation, the the W superpotential is obtained as:

$$W = \frac{1}{2} M^{ij} \phi_i \phi_j + \frac{1}{6} y^{ijk} \phi_i \phi_j \phi_k \tag{3.17}$$

where M^{ij} is the SUSY fermion mass matrix and y^{ijk} is the Yukawa coupling of two fermion fields with one scalar.

Finally, the total Lagrangian density for the chiral suprmultiplet is given by:

$$\begin{aligned} \mathcal{L}_{chiral} = &-\partial^\mu \phi^{*i} \partial_\mu \phi_i - V(\phi, \phi^*) - i\psi^{\dagger i} \overline{\sigma}^\mu \partial_\mu \psi_i - \frac{1}{2} M^{ij} \psi_i \psi_j - \frac{1}{2} M^*_{ij} \psi^{\dagger i} \psi^{\dagger j} \\ &-\frac{1}{2} y^{ijk} \phi_i \psi_j \psi_k - \frac{1}{2} y^*_{ijk} \phi^{*i} \psi^{\dagger j} \psi^{\dagger k} \end{aligned} \tag{3.18}$$

where the $V(\phi, \phi^*)$ is the scalar potential. It can be shown that there are mass degenerate partner states for each supermultiplet, and that the scalar and fermionic coupling strengths cancel out as $\lambda_S = \lambda_f^2$ as postulated as a solution to the hierarchy

problem.

3.2.3. Lagrangian for the Gauge Supermultiplets

The gauge supermultiplet consists of massless gauge bosons A_μ^a and their gaugino SUSY partners λ_a:

$$\begin{pmatrix} A_\mu^a \\ \lambda_a \end{pmatrix} \tag{3.19}$$

where index a runs over representations of the group, e.g. a=1,...,8 for $SU(3)_C$. The SUSY transformations for the gauge supermultiplets are given by:

$$\begin{aligned} A_\mu^a \to A_\mu^a + \partial_\mu \Lambda^a + g f^{abc} A_\mu^b \Lambda^c \\ \lambda^a \to \lambda^a + g f^{abc} \lambda^b \Lambda^c \end{aligned} \tag{3.20}$$

where Λ is the infinitesimal gauge transformation parameter, g is the coupling strength of the interaction and f^{abc} is the structure constant. Then the Lagrangian density for the chiral supermultiplet is given by:

$$\mathcal{L}_{gauge} = -\frac{1}{4} F_{\mu\nu}^a F^{a\mu\nu} - i\lambda^{\dagger a} \overline{\sigma}^\mu D_\mu \lambda^a + \frac{1}{2} D^a D^a. \tag{3.21}$$

The first term describes the kinetic energy using the gauge filed tensor $F_{\mu\nu}^a = \partial_\mu A_\nu^a - \partial_\nu A_\mu^a + g f^{abc} A_\mu^b A_\nu^c$, for the respective gauge field components of the interaction A_μ. The second term is the kinetic energy of the gaugino fields, which contains interactions between gauge and gaugino fields and includes the covariant derivative $D_\mu \lambda^a = \partial_\mu \lambda^a + g f^{abc} A_\mu^b \lambda^c$. The third term is the auxiliary field D, which accounts for inequality of degrees of freedom within supermultiplets for the on- and off-shell case. This term vanishes for the on-shell case.

3.2.4. Soft Supersymmetry Breaking

Since no mass degenerate SUSY partners of SM particles have been experimentally found, if it exists, SUSY must be broken. The SUSY breaking must preserve the renormalizability of the theory, as well as cancellation of the quadratic divergences as a solution to the hierarchy problem. Therefore, a so-called 'soft-breaking' term is added to the SUSY Lagrangian density:

$$\mathcal{L}_{soft} = -(\frac{1}{2} M_a \lambda^a \lambda^a + \frac{1}{6} a^{ijk} \phi_i \phi_j \phi_k + \frac{1}{2} b^{ij} \phi_i \phi_j + c.c.) - (m^2)_j^i \phi^{j*} \phi_i \tag{3.22}$$

where the $(m^2)_j^i$ and b^{ij} are the squared mass terms, the a^{ijk} are the cubic scalar couplings, and M_a are the gaugino mass terms, given for each gauge group. This expression has only scalar and gaugino terms, thus the symmetry is broken by adding mass to the associated particles. Examples of SUSY breaking will be given in the section 3.3.4.

3.2.5. Supersymmetric Lagrangian

From the chiral and gauge supermultiplets and the soft SUSY breaking Lagrangian density terms, the total SUSY Lagrangian density can be obtained. Firstly, in order to preserve gauge invariance, the derivatives of the scalar and fermion fields should be replaced by their covariant derivatives as:

$$\begin{aligned} \partial_\mu \psi \to D_\mu \psi &= \partial_\mu \psi + igA^a_\mu T^a \psi \\ \partial_\mu \phi \to D_\mu \phi &= \partial_\mu \phi + igA^a_\mu T^a \phi \end{aligned} \tag{3.23}$$

where the T^a is the generator of the gauge groups. This expression describes the couplings between gauge bosons, and scalar and fermionic fields of the chiral supermultiplet.

The possible renormalizable couplings of gaugino λ^a and auxiliary D fields can contribute with the following term:

$$-\sqrt{2}g(\phi^* T^a \psi)\lambda^a - \sqrt{2}g\lambda^{\dagger a}(\psi^\dagger T^a \phi) + g(\psi^* T^a \phi)D^a. \tag{3.24}$$

The D-term in the 3.24 and 3.21 combine into the equation of motion:

$$D^a = g(\phi^* T^a \phi). \tag{3.25}$$

Since this expression contains only scalar fields, it is often written with the scalar potential as:

$$V(\phi, \phi^*) = W_i^* W^i + \frac{1}{2}g^2(\phi^* T \phi)^2. \tag{3.26}$$

The resulting total Lagrangian density for Supersymmetry is then given by:

$$\begin{aligned} \mathcal{L}_{SUSY} = & -D^\mu \phi^* D_\mu \phi - i\psi^\dagger \overline{\sigma}^\mu D_\mu \psi && \left\{ \begin{array}{l} scalars\ and\ fermions \end{array} \right. \\ & -\frac{1}{2}(W^{ij}\psi_i\psi_j + W^{ij*}\psi^{i\dagger}\psi^{j\dagger}) && \left\{ \begin{array}{l} fermion\ mass\ and \\ Yukawa\ coupling \end{array} \right. \\ & -W^i W_i^* - \frac{1}{2}g^2(\phi^* T \phi) && \left\{ \begin{array}{l} scalar\ potential \end{array} \right. \\ & -\frac{1}{4}F^a_{\mu\nu}F^{a\mu\nu} - i\lambda^{\dagger a}\overline{\sigma}^\mu D_\mu \lambda^a && \left\{ \begin{array}{l} gauge\ bosons \\ and\ gauginos \end{array} \right. \\ & -\sqrt{2}g(\phi^* T^a \psi)\lambda^a - \sqrt{2}g\lambda^{\dagger a}(\psi^\dagger T^a \phi) && \left\{ \begin{array}{l} additional\ couplings \end{array} \right. \\ & + \mathcal{L}_{soft}\,. && \left\{ \begin{array}{l} soft\ breaking \end{array} \right. \end{aligned} \tag{3.27}$$

3.3. The Minimal Supersymmetric Standard Model

In most of the current experimental SUSY searches, the minimal extension of the SM is considered, the Minimal Supersymmetric Standard Model (MSSM) [69, 89–92]. It contains the minimal number of couplings and fields. In this section the MSSM particle content, and its features will be presented.

3.3.1. MSSM Particle Content

The MSSM field consists of chiral supermultiplets, which consist of SM quarks and leptons, and their scalar SUSY partners 'squarks' and 'sleptons', and gauge supermultiplets, which consist of SM gauge bosons and their SUSY partners 'gauginos'.

	Name		**Scalars** ϕ $J=0$	**Fermions** ψ $J=\frac{1}{2}$
Chiral	Squarks, Quarks (3 generations)	Q_1	$(\tilde{u}_L, \tilde{d}_L)$	(u_L, d_L)
		$\bar{U}_1$	$\bar{u}_R^*$	$\bar{u}_R^\dagger$
		$\bar{D}_1$	$\bar{d}_R^*$	$\bar{d}_R^\dagger$
	Sleptons, Leptons (3 generations)	L_1	$(\tilde{\nu}_e, \tilde{e}_L)$	(ν_e, e_L)
		$\bar{E}_1$	$\tilde{e}_R^*$	$\tilde{e}_R^\dagger$
	Higgs, Higgsino	H_u	(H_u^+, H_u^0)	$(\tilde{H}_u^+, \tilde{H}_u^0)$
		H_d	(H_d^0, H_d^-)	$(\tilde{H}_d^0, \tilde{H}_d^-)$

	Name	**Bosons** A^μ $J=1$	**Fermions** λ $J=\frac{1}{2}$
Gauge	Gluon, Gluino	g	$\tilde{g}$
	W-Bosons, Winos	$W^\pm, W^0$	$\tilde{W}^\pm, \tilde{W}^0$
	B-Boson, Bino	B^0	$\tilde{B}^0$

Table 3.1.: MSSM particle content, given for chiral and gauge supermultiplets. The Q_i and L_i represent the supermultiplets containing $SU(2)_L$ doublets, and $\bar{U}_i, \bar{D}_i$ and $\bar{E}_i$ are the corresponding conjugate right-handed singlets [63]. The mass eigenstates are obtained by mixing.

In the table 3.1 particle content for chiral and gauge supermultiplets is presented. The chiral supermultiplets have SM fermions with two chiral states, which transform differently under gauge symmetry, and each has its scalar superpartner. All chiral left-handed fermions are defined as Weil-spinors, so the conjugation is applied to the right-handed fields.

The Higgs chiral supermultiplets are accommodated into the Higgs and Higgsino sector. However, in MSSM one Higgs-doublet would not be sufficient to have cancellations for gauge anomalies, and the two Higgs-doublets are introduced. They are

also required to give mass to all fermions via electroweak symmetry breaking. The Higgs-doublets are of the form:

$$\begin{pmatrix} H_u^+ \\ H_u^0 \end{pmatrix} \quad , \quad \begin{pmatrix} H_d^0 \\ H_d^- \end{pmatrix}. \tag{3.28}$$

There are 4 complex and 8 real degrees of freedom in the Higgs doublets. Three phases are absorbed by the Goldstone bosons, like in the SM, and there are 5 physical Higgs eigenstates:

- h, the light neutral scalar Higgs
- H, the heavy neutral scalar Higgs
- A, the neutral CP-odd pseudoscalar Higgs
- $H^{\pm}$, two charged scalar Higgs particles.

The gauge supermultiplets contain mediators of SM interactions and their superpartners. They are 8 gluons and gluinos for $SU(3)_C$ symmetry, and $W^{\pm}, W^0, B^0$ and their superpartners for $SU(2)_L \otimes U(1)_Y$ symmetry. Via electroweak symmetry breaking the mass eigenstates are obtained via mixing, where the new mass eigenstates are formed from the electroweak gauginos and Higgsinos of the same charge, since the mixing partners have the same quantum numbers. The neutral 'Neutralinos' $\tilde{\chi}^0_{1,2,3,4}$ are formed from $\tilde{W}^0, \tilde{B}^0, \tilde{H}^0_u$ and $\tilde{H}^0_d$ mixing, and 'Charginos' $\tilde{\chi}^{\pm}_{1,2}$ are formed from $\tilde{W}^{\pm}, \tilde{H}^+_u$ and $\tilde{H}^-_d$ mixing.

For the case when gravity is included in the theory, called the Supergravity, an additional supermultiplet is introduced, which contains the spin-2 Graviton and its spin-$\frac{3}{2}$ superpartner 'Gravitino'.

3.3.2. R-parity Conservation

In MSSM an new quantum number, called R-parity, is introduced. In SM the baryon and lepton numbers are conserved. In SUSY there are interaction terms that could lead to violation of this symmetry. For this reason, in MSSM a conservation or R-parity is required, where R is defined as:

$$R = (-1)^{3(B-L)+2S} \tag{3.29}$$

where B and L are barion and lepton numbers, and S is the spin of particles participating in the process. All SM fields carry R-parity of +1, while all superfields carry parity of -1, and R-parity is a multiplicative quantum number.

Consequently, when the R-party is conserved, from SM particles the SUSY particles are produced in pairs. For e.g. two SM particles have $R_{total} = 1^2$, and they can produce two SUSY particles because $R_{total} = (-1)^2$. Also, the lightest SUSY particle (LSP) is stable due to R-parity conservation, because LSP with R=-1 cannot decay into SM particles, and due to its lowest mass, it cannot decay into SUSY

particles, thus it is stable. However, some SUSY models allow R-parity violation, up to the compatibility with the measured proton lifetime.

3.3.3. MSSM Interactions

In MSSM the generic superpotential is of the form:

$$W_{MSSM} = y_u \bar{U} Q H_u - y_d \bar{D} Q H_d - y_e \bar{E} L H_d + \mu H_u H_d \tag{3.30}$$

given for chiral and gauge superfields of supermultiplets, where indices for quark and lepton generations are omitted. The 3×3 matrices y_u, y_d and y_e are Yukawa couplings they determine the CKM mixing angles and masses after electroweak breaking. The μ is the SUSY Higgs mass parameter.

From the generic superpotential, the Yukawa interactions can be derived, i.e. the couplings of fermions, Higgs and Higgsino fields, while from the kinetic term in the SUSY Lagrangian the couplings of SM gauge bosons to SUSY particles are determined.

3.3.4. MSSM SUSY Models

Although MSSM represents the minimal extension of the SM, due to the soft symmetry breaking, in the SUSY Lagrangian density there are 105 new parameters compared to the SM, which include masses, phases and mixing angles of the particles. Therefore, in the $\mathcal{L}_{SUSY}$ there are too many free parameters, and the experimental search in such a setup is practically not possible. There are two points which help to overcome this problem. First, introducing certain symmetry breaking assumptions and providing minimal models in those frameworks. Second, focusing on the sparticle masses, decay products and event kinematics using certain simplifications in the SUSY model. This motivates a construction of two types of models for analyses, the realistic and simplified models.

Realistic SUSY Models

In most of the SUSY models, a spontaneous symmetry breaking occurs using a so-called 'hidden sector'. In order to preserve the gauge invariance in SUSY, the MSSM fields, the so-called 'visible sector', must have zero vacuum expectation value. The spontaneous SUSY breaking is then communicated to the observable MSSM sector via hypothetical flavour-blind messenger fields. However, the mediation mechanism is highly dependent on the model assumptions.

In addition, in the considered model generation, additional assumptions on the sparticle masses can be added. Namely, the number of SUSY parameters can be significantly reduced if a few parameters are selected at the high Planck scale, and the SUSY particle masses at the electroweak scale are obtained by the renormalization group equations, which depend on the model assumptions including the spontaneous

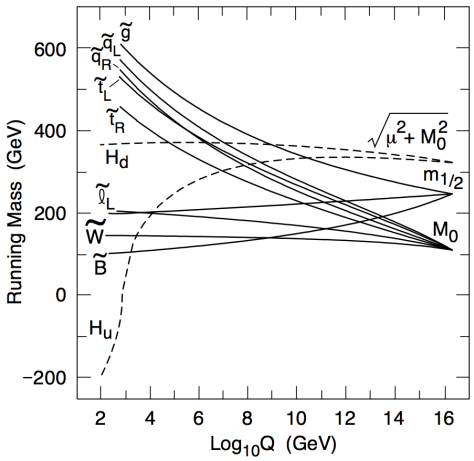

Figure 3.5.: Running of renormalization group equations, an example of mSUGRA /CMSSM model. Parameters m_0 and $m_{1/2}$ are given at the high GUT scale, and the SUSY particle masses are obtained at the electroweak scale [46].

symmetry breaking model. This reduces the total number of free parameters in the model to a few.

For example, the running of renormalization group equations from the high mass scale to the electroweak scale, can be examined for the Minimal Supergravity (mSUGRA) model. This model makes a connection between SUSY and General Relativity, which are unified into one theory called Supergravity. This theory is non-renormalizable, thus not a candidate for Theory of Everything. The SUSY is put to be the local symmetry, and at the same time it represents an effective theory for phenomena below the Planck scale ($10^{16} GeV$), and a mechanism for SUSY breaking. Being a local gauge theory, new gauge fields need to be introduced, carried by graviton (spin 2) and its superpartner gravitino (spin $\frac{3}{2}$). The model implies soft breaking terms, which reduces the number of model parameters to 5, see more details below. In the figure 3.5 the selected model parameters m_0 and $m_{1/2}$ at the high mass scale are run down to the electroweak scale.

The most common SUSY models, based on their respective supersymmetry braking, are [93]:

- **Constrained MSSM** (CMSSM) [94–99]. Since gravity couples universally to the energy, gravitational interaction is the obvious choice for mediating of supersymmetry breaking. In addition, in this model gaugino masses unify to common value of $m_{1/2}$ at the GUT scale, and SUSY breaking masses of all sfermions and Higgs doublets unify to value of m_0 at the GUT scale. The model in addition has a common trilinear supersymmetry breaking parameter A_0 at the GUT scale. The ratio of Higgs vacuum expectation values $\tan\beta$ and the sign of the Higgs mixing parameter sign(μ), both are defined at the electroweak scale.

- **Minimal Supergravity Model** (mSUGRA) [94–99]. The CMSSM can be restricted even more, by assumption of a relation between trilinear (A_0), bilinear (B_0) supersymmetry breaking parameters and universal scalar masses m_0 ($A_0 = B_0 + m_0$). The model parameters are universal scalar mass m_0, universal gaugino mass $m_{1/2}$, universal trilinear couplings A_0, ratio of vacuum expectation of two Higgs doublets $\tan\beta$, and sign of the Higgs mixing parameter $\text{sing}(\mu)$.

- **Non-Universal Higgs Masses** (NUHM) [29]. To allow for more free parameters, NUHM is a less strict version of CMSSM, where $m_{H_u} \neq m_{H_d} \neq m_0$ at the high mass scale. The analysis of this model is done in this thesis, where details about the model are given in the chapter 4 and the analysis description in the appendix A.

- **Anomaly Mediated Supersymmetry Breaking** (AMSB) [100,101]. This is a special case of gravity mediated SUSY breaking, with no direct tree-level couplings between the sectors and SUSY particle masses are generated with higher order loop corrections.

- **Gauge Mediated Supersymmetry Breaking** (GMSB) [102–107]. The SM gauge interactions act as 'messenger fields' that couple directly to the hidden sector, and produce the effect of SUSY breaking to the SUSY partners.

- **Gaugino Mediated Supersymmetry Breaking** [108] is a model based on extra dimensions. The chiral supermultiplets reside on one brane, while the SUSY breaking sector is confined to a different brane. Gravity and gauge superfields directly couple to fields on both branes, so gauginos acquire mass. Scalars acquire mass dominantly from the interaction with gauginos, which results in suppressed scalar supersymmetry breaking masses. A special case of Non-Universal Higgs Masses model with gaugino mediation is the main topic of this thesis. The model description is given in the chapter 5 and the physics analysis is described in the chapters 9, 10 and 11.

- **Phenomenological MSSM** (pMSSM) [109]. This model has 19 free parameters, where the supersymmetry breaking mechanism and running of renormalization used in previous models, is replaced by a higher number of parameters at the electroweak scale. The parameters are chosen to satisfy all existing experimental and theoretical constrains, as described in the section 3.4.2. In this way the SUSY particle mass spectrum at the electroweak scale can be explored directly, without an assumption on the supersymmetry breaking. In this way, analyses which focus on the final states can be examined by generating large amounts of parameter space points.

In addition, models Beyond the MSSM are considered:

- **MSSM with R-Parity Violation** (RPV-CMSSM) [110]. The CMSSM can be generated with R-parity violation. R-parity, which was introduced to

guarantee for the proton stability, is replaced by different symmetry (barion-triality or lepton-parity), which guarantees proton stability but allows either lepton number, or barion number violation. The LSP is not stable, but can be long lived and can decay inside the detector.

- **Next-to-MSSM** (NMSSM) [111]. NMSSM is the minimal extension of the MSSM with the scale invariant superpotential. The superpotential μ-term is replaced by the coupling to the gauge singlet superfield S. This implies more Higgs states (3 neutral CP-even and 2 neutral CP-odd states) and more neutralinos (5 neutralinos). However, due to its complexity, there is no Run 1 exclusion of this model, and analyses are being prepared for the Run 2 data.

These models differ in their phenomenological characteristics, and often require dedicated analyses in experimental searches.

Simplified SUSY Models

In order to have a systematic approach in the experimental searches for SUSY, the so-called Simplified Models [112] are used. They are designed to involve only a few particles and interactions, and they can be described by a small number of parameters which are related to collider physics observables, e.g. particle masses, production cross-sections and branching fractions. Although they are to an extent model dependent, the limits obtained by them are based on the signal topology, therefore more general. The physics analysis can be optimized and presented as a function of a few selected parameters of a simplified model.

3.4. Aspects of SUSY Searches in ATLAS

A distinguished characteristics of physics events which involve SUSY are the long cascade decay chains. Namely, in R-parity conserving models, the higher SUSY particles decay into lower ones and a SM one. The SM leptons and jets from the quarks, together with the missing energy from the stable LSP represent a typical signature of SUSY. The R-parity violating models have slightly different topology, but long decay chains are their characteristics as well.

In ATLAS an approach of SUSY searches by the final state is used. Therefore, the searches are more general than the initial assumptions of the model used for the optimization and analysis. The SUSY search result obtained by the experiment, with the detailed description of the model, background determination, analysis technique and final statistical interpretation can be also re-used for the analysis in the theoretical approach with different model assumptions for a given final state. For the SUSY models which have a good physics motivation, however, dedicated analyses are designed. In this section a brief description of organization in ATLAS SUSY searches will be given. Also, the constrains on the SUSY parameter space, that needs to be incorporated in the analyses strategy, is also added.

3.4.1. SUSY Search Strategies in ATLAS

SUSY searches aim to have a full coverage of parameter space which is viable for a given c.m.e. Therefore, the analyses need to be designed such that the regions not covered by any search is minimized. The aim so to explore highly diverse SUSY models, with their distinguished phenomenology. For this, various realistic SUSY models and Simplified Models are explored. In ATLAS all search approaches are grouped according to the dominant production channels:

- **Strong Production SUSY Searches of Squarks and Gluinos** includes a number of simplified models which have a dominant $\tilde{q}$ and $\tilde{g}$ production. The highest number of SUSY models predicts this production to be dominant, see figure 3.6. Their final state can involve multiple leptons, jets and missing energy.
- **Third Generation SUSY Searches** have a good motivation by the requirement of low level of fine tuning in the SUSY model. The $\tilde{t}_1$is favored to be below 1 TeV [113]. Therefore, these searches have a high physics motivation. Their final states can include t, b or c quark.
- **Electroweak SUSY Searches** despite the fact that electroweak production is not expected to be dominant, these searches have high motivation because the $\tilde{q}$ and $\tilde{g}$ are excluded up to $\sim$ 1.7 TeV [35], and if SUSY is realized in nature and reachable at the LHC, it can be via the gaugino production. Their characteristic signature involves multiple leptons.
- **R-Parity Violation and Long-Lived SUSY Model Searches** are studied in order to explore topologies if the assumption of R-parity conservation is not valid, or if the SUSY particles live long enough to leave a visible trace in the detector.

3.4.2. Constrains on SUSY Searches

The measurements of certain parameters in the SM can exclude some SUSY models. For this reason the following constrains need to be considered:

- $B_S \rightarrow \mu\mu$ is a flavor changing neutral current, and it can occur at one-loop level with a suppressed branching ratio of 10^{-9}. In SUSY the branching ratio of this process is enhanced due to additional flavor violating processes at one-loop level due to the SUSY Higgs sector.The recent measurements by LHCb and CMS put an upper limit on this branching ratio, and consequently strong constrains on SUSY. It affects more the large $\tan\beta$ regions where this effect is stronger.

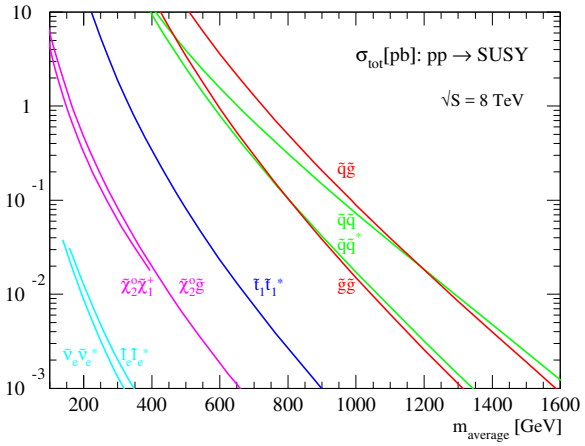

Figure 3.6.: Average production cross-sections for different production channels at 8 TeV, obtained by the Prospino 2.1 [114].

- $b \to s\gamma$ is a flavor changing process which in SM involves loops with W bosons and up-type quarks. In SUSY additional loops with SUSY particles are allowed. The measurements of the branching ratio for this process put strong constrains on a number of SUSY models.

- Cold Dark Matter density measurements puts bounds on some SUSY models. It is assumed that in the BBN WIMP-s were created in the early universe. They stayed in the thermal equilibrium until temperatures dropped below the mass of the WIMP, and their production was suppressed. The increasing distance between particles reduced the annihilation rates up to the current relic cold dark matter density Ω at the current temperatures. Precise measurements of the relic density have been measured by the WMAP experiment [83], and they put bounds on SUSY models if the WIMP is the LSP. From the constructed SUSY model, the relic density produced by the LSP can be estimated, and models which are not in agreement with the relic density measurement are excluded.

- Higgs mass puts a strong constrain on large amount of SUSY models. The newly discovered Higgs particle mass needs to be generated by the renormalization group equations in the SUSY models, however, for large amount of SUSY models the lightest Higgs h is not compatible with the measured Higgs mass.

- LEP and LHC previous measurements need to be included in SUSY searches. The LEP bounds on sleptons and lower gauginos put bounds on SUSY models. Also, the previous LHC measurements put strong bounds on the $\tilde{q}$, $\tilde{g}$, $\tilde{t}$ e.t.c. masses. These limits need to be considered as well [35].

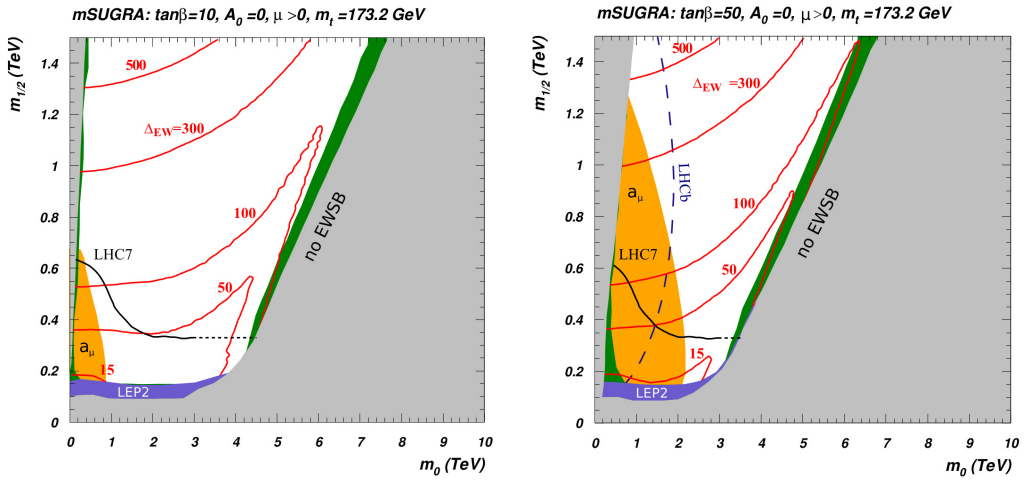

(a) (b)

Figure 3.7.: Experimental and theoretical constrains for mSUGRA/CMSSM model using $\tan\beta = 10$ (a) and $\tan\beta = 50$ (b) [115]. Green shaded area represents WMAP cosmological constrains [116], blue shaded area is the LEP2 chargino limit [117], dashed blue line is the LHCb $B_S \to \mu^+\mu^-$ limit [118], orange shaded area is favored by g-2 anomaly measurements [119], black solid line are exclusion limits from direct LHC measurements [120, 121], and red line represents the amount of fine tuning [115].

- Muon anomalous magnetic moment. The magnetic moment of the muon is given by $\mu = \frac{eg}{2mc}\mathbf{S}$, for a spin operator S and giromagnetic factor g. The muon anomaly defined as $a_\mu = (g-2)/2$ is a low energy observable, which has been measured by the Muon g-2 Collaboration, and it was found to have a 3 sigma deviation from the SM expectation [122]. This anomaly can be explained in SUSY by additional neutralino-smuon and chargino-sneutrino loops. The g-2 anomaly explored using MSSM, favors positive values of Higgs mixing parameter μ, and high values of $\tan\beta$.

In the figure 3.7 a comparison of constrains for SUSY models are given for the mSUGRA/CMSSM model. WMAP cosmological measurements exclude the area along the diagonal for very high m_0 and $m_{1/2}$ masses. LHC measurements have stronger limits than LEP2 measurements by a large amount. $B_S \to \mu\mu$ measurements exclude SUSY for very low m_0 values, but extend to very high values of $m_{1/2}$. The favored g-2 anomaly region is better excluded by LHC measurements for low $\tan\beta$.

4. Non-Universal Higgs Masses Model and Radiatively Driven Natural SUSY

The Non-Universal Higgs Masses (NUHM) [29] is a model with two extra free parameters at the high mass scale compared to CMSSM [94–99]. (A special case of NUHM with gaugino mediation and $\tilde{\nu}_\tau$ NLSP [28] will be described in the next section 5.) In the framework of Radiatively-Driven Natural SUSY (RNS) [30], regions with low level of electroweak fine-tuning need to be achieved for SUSY mass spectrum with h mass ~ 125.5 GeV and $\tilde{q}$ and $\tilde{g}$ masses at the TeV scale. This can be accommodated in the NUHM model. As the electroweak fine tuning depends on the SUSY particle masses at the electroweak scale, the NUHM can be considered as an effective theory which contains a more constrained theory, with the same phenomenology and the same level of electroweak fine-tuning. This makes the RNS NUHM analysis more general. The details of NUHM model and RNS motivation will be described in this chapter, while the RNS NUHM 8 TeV analysis will be given in the appendix A A.

4.1. Non-Universal Higgs Masses Model

The MSSM can be explored in a Non-Universal Higgs Masses model, where the soft supersymmetry-breaking masses of the Higgs multiplets, $m_{H_1}(M_X)$ and $m_{H_2}(M_X)$, are allowed to be non-universal, given at the high mass scale M_X, usually chosen to be the GUT. In comparison to the constrained MSSM (CMSSM), where these terms are set to be equal to the soft SUSY-breaking masses m_0 of the $\tilde{q}$ and $\tilde{l}$, in NUHM they are independent $m_{H_1}(M_X) \neq m_{H_2}(M_X) \neq m_0$. Consequently, in CMSSM the Higgs mixing parameter μ and pseudoscalar Higgs mass m_A are calculated, while in NUHM they are two extra free parameters. The NUHM model description in this section will be given as in the model proposal in [29].

The free parameters in NUHM are the soft SUSY-breaking scalar mass m_0 for $\tilde{q}$ and $\tilde{l}$, the soft-SUSY breaking gaugino mass $m_{1/2}$, trilinear SUSY-breaking parameter A_0, the ratio of Higgs vacuum expectation values $\tan\beta$, the Higgs superpotential coupling μ and the pseudoscalar Higgs boson mass m_A. From the electroweak symmetry breaking conditions, the connections between parameters at the high mass scale M_X, and low M_Z scale can be made, and the last two parameters can be expressed in terms of Higgs masses at the high mass scale m_{H_1} and m_{H_2}. In CMSSM due to electroweak symmetry-breaking vacuum conditions which are normally used, the value of μ is fixed up to the sign ambiguity and m_A is fixed in terms of other pa-

rameters $(m_0, m_{1/2}, A_0, \tan\beta)$, which in effect has less free parameters than NUHM.

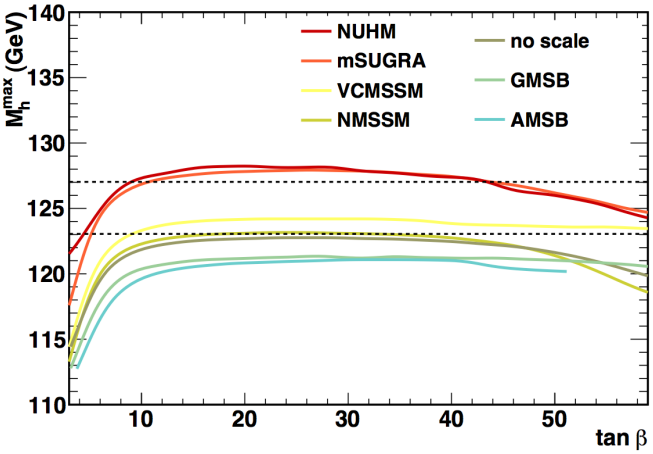

Figure 4.1.: Maximal h mass vs $\tan\beta$ for various SUSY models. Random scan for SUSY parameters was performed, and the m_h was measured. The m_h^{max} is defined as the value for which 99% of scan points have m_h smaller than it [123].

As the RGE in NUHM have extra terms in comparison to CMSSM, the resulting SUSY particle spectrum can differ significantly from the CMSSM case. In CMSSM the LSP is usually a $\tilde{\chi}_1^0$. In the NUHM parameter space there can be found regions with the following LSPs: $\tilde{\chi}_1^0$, $\tilde{\tau}_1$, $\tilde{e}_R$, $\tilde{\mu}_R$, $\tilde{e}_L$, $\tilde{\mu}_L$, $\tilde{\nu}_{e,\mu}$, $\tilde{\nu}_\tau$, $\tilde{t}$ or $\tilde{b}$. However, the weakly interacting neutral DM candidate is favored [29], which can be $\tilde{\chi}_1^0$ and $\tilde{\nu}$. The $\tilde{\nu}$ LSP is excluded by the LEP direct measurements if the majority of the CDM is the LSP [124]. Therefore, the $\tilde{\chi}_1^0$ LSP and specific case for $\tilde{\nu}_\tau$ NLSP, see chapter 5, are considered here. The major topic of the thesis is the analysis of the $\tilde{\nu}_\tau$ NLSP incarnation of NUHM model with gaugino mediation, given in 11, and the NUHM with $\tilde{\chi}_1^0$ LSP analysis is given in the appendix A.

A note should be given concerning the NUHM model notation in literature [93]. There are two levels of complexity studied (all parameters given at the M_X scale, except for $\tan\beta$, sign(μ), m_A and μ which are at the m_Z scale):

- NUHM1 :
$$m_{1/2}, m_0, m_H, A_0, \tan\beta, \text{sign}(\mu) \tag{4.1}$$
where $m_H = m_{H_1} = m_{H_2}$ and it can be traded for m_A and μ free parameters.

- NUHM2 :
$$m_{1/2}, m_0, m_{H_1}, m_{H_2}, A_0, \tan\beta, \text{sign}(\mu) \tag{4.2}$$
where $m_{H_1} \neq m_{H_2}$ and they can be traded for m_A and μ as free parameters.

In this thesis the NUHM2 model complexity is considered.

The Higgs-like particle discovery with the mass of ∼125.5 GeV [125] puts strong constraints on large amount of SUSY models. In the figure 4.1 the viability of highest h mass for different SUSY models is given, shown as a function of $\tan\beta$. The SUSY parameters were varied for different SUSY models, and the maximal m_h vs $\tan\beta$ was determined for each SUSY scenario. The m_h^{max} is defined as the mass point at which 99% of the scan points have the m_h below it. The m_h for NUHM reaches up to 128.5±1.0 GeV for the region of $10 < \tan\beta < 40$, see more details in [123]. This gives a very good motivation for studies of NUHM model as it is in agreement with the Higss mass measurement.

4.2. Radiatively Driven Natural SUSY and NUHM

Radiatively-driven Natural SUSY allows Z and Higgs masses around ∼ 100 GeV while $\tilde{q}$ and $\tilde{g}$ masses are maintained beyond the TeV range. When no large cancellations at the electroweak scale are required for $m_Z = 91.2$ GeV and $m_h \sim 125$ GeV, the sparticle spectrum has light higgsinos 100 - 300 GeV, gauginos 300 - 1200 GeV, $\tilde{g}$ with 1 - 4 TeV, $\tilde{t}$ and $\tilde{b}$ 1 - 4 TeV, and remaining SUSY Higgses of 5 - 30 TeV. In RNS high degree of electroweak naturaleness can be achieved, and it can be studied using the NUHM model, therefore analysis in this framework has good motivation in LHC searches. The RNS with NUHM will be given in this section following the proposal in [30], while the 8 TeV analysis will be given in the appendix A A.

In the light of recent results of SUSY searches at the LHC [35], the observed limits on the $\tilde{q}$ and $\tilde{g}$ are reaching order of TeV, and the rather large value of $m_h \sim 125$ GeV. This requires high mixing of top squarks with masses typically beyond TeV. Then the weak-scale SUSY is questioned if it can naturally accommodate these phenomena, together with the values of the SM particle masses of $W^{\pm}$, Z and h ∼ 100 GeV. In particular, in the expression of the Z-mass obtained from the minimization of the one loop MSSM Higgs potential, these limits require large cancellations of terms in:

$$\frac{M_Z^2}{2} = \frac{m_{H_2}^2 + \sum_d^d - (m_{H_1}^2 + \sum_u^u)\tan^2\beta}{\tan^2\beta - 1} - \mu^2 \tag{4.3}$$

for all terms at the electroweak scale (M_Z), where the $\sum_d^d$ and $\sum_u^u$ terms contain 1-loop corrections to the Higgs field potential [30]. When no large cancellation of terms is required for the $M_Z^2/2$, each term in equation 4.3 should be of the same order.

Then the electroweak fine tuning parameter can be defined as:

$$\Delta_{EW} = max_i \frac{|C_i|}{M_Z^2/2} \tag{4.4}$$

where C_i represents each term in equation 4.3. In the Δ_{EW} expression they are compared to $M_Z^2/2$. The Δ_{EW} depends only on the weak scale terms, and does not contain any information about the high scale origin of SUSY masses or couplings,

which are contained in the usual fine-tuning measures, see more details in [30]. Therefore, the Δ_{EW} quantifies the minimal fine tuning that must be present, which is determined by the SUSY mass spectrum at the electroweak scale, independently of the high-scale mechanism that generates it. Then a SUSY model with high Δ_{EW} is fine-tuned, while with low Δ_{EW} it has a possibility to have low fine-tuning.

In order to achieve low Δ_{EW}, as mentioned above, all terms in 4.3 need to be of the same order as $M_Z^2/2$. This can be achieved with the following conditions [30]:

- $100 < |\mu| < 300$ GeV for $\Delta_{EW} < 30$
- $m_{H_1}(M_X) \sim$ (1.3 - 2) m_0, which leads to $m_{H_1}(M_Z) \sim$ -$M_Z^2/2$
- large $\tilde{t}$ mixing from $A_0 \sim \pm 1.6 m_0$, which reduce $\tilde{t}$ radiative corrections and increases m_h to $\sim$ 125 GeV.

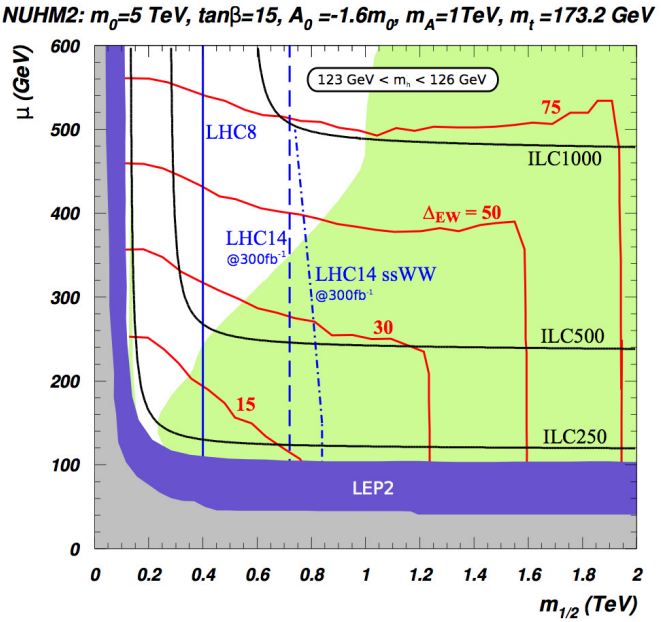

Figure 4.2.: Radiatively-driven natural SUSY using NUHM model for $m_0 = 5$ TeV, $\tan\beta = 15$, A_0 = -1.6m_0, $m_A = 1$ TeV. The red line shows the Δ_{EW}, the solid blue is the 8 TeV LHC reach, in dashed and dot-dashed is the 14 TeV LHC reach, the black solid line shows the ILC reach. The blue and gray shaded area are LEP2 and LEP1 exclusion limits for gauginos, and light gray area has $\Omega^{std}_{\tilde{\chi}^0_1} h^2 < 0.12$ [30].

In mSUGRA/CMSSM the lowest achieved $\Delta_{EW} \sim 200$, which makes this model fine-tuned. However, in NUHM $\Delta_{EW} \sim$ 7 - 10 can be reached using these conditions. Then the NUHM model can be considered as an effective theory which contains

a more constrained theory with fewer parameters. Then the constrained theory phenomenology would be the same as for NUHM, as Δ_{EW} is determined by the SUSY mass spectrum at the electroweak scale.

Detailed scans for NUHM with low Δ_{EW} (EWFT) have been performed in [30]. Low level of EWFT of 3 - 15 % for $123 < m_h < 127$ GeV can be achieved for the following NUHM parameters. $m_0 \sim 1$ - 7 TeV, $m_{1/2} \sim 0.3$ - 1.5 TeV, $A_0 \sim \pm$ (1 - 2)m_0, $\tan\beta \sim 5$ - 50, $\mu \sim 100$ - 300 GeV and m_A in wide range of values. This framework is named the **Radiatively Driven Natural SUSY (RNS)** because the $m^2_{H_1}(M_Z) \sim M_Z$ has been generated radiatively while running from the GUT scale.

The RNS typical phenomenology has Higgsino-like gauginos $\tilde{\chi}^0_1$, $\tilde{\chi}^\pm_1 \sim 100$ - 300 GeV with mass gap $\tilde{\chi}^0_1$- $\tilde{\chi}^0_2 \sim 10$ - 30 GeV, $m_{\tilde{t}_1} \sim 1$ - 2 TeV, $m_{\tilde{t}_2}, m_{\tilde{b}} \sim 2$ - 4 TeV, $m_{\tilde{g}} \sim$ 1 - 5 TeV and $m_{\tilde{q}}, m_{\tilde{l}} \sim 5$ - 10 TeV. Therefore, RNS retains light Higgsinos, $\tilde{t}$ and $\tilde{b}$are considerably heavier than previous natural SUSY estimates, and $\tilde{g}$ can be very heavy ~ 5 TeV. Due to the large $\tilde{q}$ and $\tilde{g}$ masses, the dominant production processes are gaugino production, which gives strong motivation for electroweak searches using 2,3 or 4 leptons in the final state.

In this thesis the NUHM parameter space proposed in [30] is studied using $m_0 =$ 5 TeV, $\tan\beta = 15$, $A_0 =$ -1.6m_0, $m_A = 1$ TeV in the $m_{1/2}$ vs μ plane. In the figure 4.2 the NUHM model parameter space is shown. For $100 < \mu < 300$ GeV low level of EWFT is achieved. At the same time, 8 TeV searches can have a reach up to about $m_{1/2} \sim 400$ GeV, as shown in the study [30]. Therefore, in this thesis a region of NUHM parameter space up to $m_{1/2} \sim 500$ GeV and $\mu \sim 500$ GeV will be considered in the 8 TeV analysis, using 2, 3 and 4 lepton final states in the electroweak SUSY searches. This analysis is presented in the appendix A A.

5. Gaugino Mediation Non-Universal Higgs Masses Model

In this section the Non-universal Higgs masses model with gaugino mediation and $\tilde{\nu}_\tau$ NLSP (NUHMG) will be presented. This is a R-parity conserving and a gravitino dark matter model, with $\tilde{G}$ mass in the GeV range. The phenomenological features of this model are low mass splitting for gauginos and sleptons, which produces signatures with lots of soft leptons, jets and missing energy. It is distinguished from MSSM models like mSUGRA by having allowed decays of $\tilde{\chi}_1^0$ into $\tilde{\tau}$, or $\tilde{e}$ or $\tilde{\mu}$ in some parameter space. This chapter is based on the model description given in [28], and will cover theoretical motivation for gravitino dark matter and $\tilde{\nu}_\tau$ NLSP in section 5.1 and gaugino mediation NUHM in the section 5.2.

5.1. Gravitino Dark Matter and $\tilde{\nu}_\tau$ NLSP Motivation

In SUSY models with R-parity conservation, if the gravitino $\tilde{G}$ is in the GeV range, it can be long lived or stable, and therefore be the LSP [126]. Therefore, $\tilde{G}$ represents a good Cold Dark Matter (CDM) candidate. In this section the motivation for $\tilde{G}$ CDM will be explained. Additionally, $\tilde{\nu}_\tau$ LSP has heavy constraints from the Big Bang Nucleosynthesis (BBN). Consequently, the motivation for $\tilde{\nu}_\tau$ NLSP, with its decay into $\tilde{G}$ and ν_τ will be given.

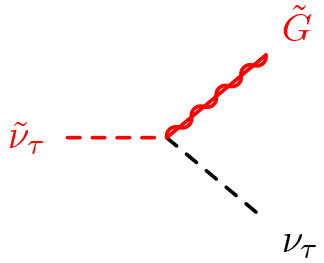

Figure 5.1.: Fyenman diagram for a $\tilde{\nu}_\tau$ NLSP decay into $\tilde{G}$ LSP and ν_τ.

Gravitinos are produced thermally and non-thermally. In the thermal production, gravitinos are produced via thermal scatterings at high temperatures, even if they are not in thermal equilibrium, giving the energy density of:

$$\Omega_{3/2}^{th} h^2 \simeq 0.27 \left(\frac{T_R}{10^{10} GeV}\right) \left(\frac{100 GeV}{m_{3/2}}\right) \left(\frac{m_{\tilde{g}}}{1 TeV}\right)^2 \tag{5.1}$$

where the $m_{\tilde{g}}$ is the gluino mass at the EW scale, T_R is the maximal reheating temperature, obtained for heaviest allowed $\tilde{G}$ mass for the given $m_{\tilde{g}}$ [127, 128].

In the non-thermal production, gravitinos are produced via NLSP decays, given by:

$$\Omega_{3/2}^{non-th}h^2 = \frac{m_{3/2}}{m_{NLSP}}\Omega_{NLSP}^{th}h^2 \tag{5.2}$$

where the $\Omega_{NLSP}^{th}h^2$ is the relic density of NLSP from thermal freeze-out without its decay [129].

Therefore, the total energy density when $\tilde{G}$ is the LSP has to be equal or smaller than the cosmological observation of the CDM density:

$$\Omega_{3/2}h^2 = \Omega_{3/2}^{th}h^2 + \Omega_{3/2}^{non-th}h^2. \tag{5.3}$$

So the total energy density of $\tilde{G}$ LSP if it makes up the whole CDM, should be equal or smaller than the measured non-baryonic CDM density:

$$\Omega_{3/2}h^2 \leq 0.1198 \pm 0.0026 \tag{5.4}$$

given for the combined measurement of Planck, WMAP and high resolution data from APC and SPT [83]. It was found that the right CDM energy density, if the $\tilde{G}$ makes the whole CDM, can be obtained for the SUSY mass spectrum in the GeV-TeV range [130, 131].

NLSP decays into $\tilde{G}$ can alter the primordial abundances of elements, because the NLSP decays release electromagnetic and hadronic energy [130, 131]. Therefore, due to the BBN, the nature, lifetime and freeze-out abundance of the NLSP is constrained. In addition, if NLSP is charged, the bound states can effect the nuclear reactions and the BBN predictions need to be modified [132–134].

In order to have a NLSP compatible with the BBN predictions, its lifetime needs to be shorter than 10^3s [28]. In effect, the SUSY mass spectrum is very heavy or its abundance has no strong suppression in comparison to the thermal freeze-out prediction [135,136], e.g. the contribution from the late entropy production is small. For the model of minimal setting of simple freeze-out and masses of $\tilde{G}$ and NLSP in the GeV range, the $\tilde{\chi}_1^0$ [137] and $\tilde{\tau}$ [138] NLSP are incompatible with the BBN predictions. In addition, $\tilde{t}$ NLSP is viable for some regions of the SUSY parameter space [139]. However, a $\tilde{\nu}_\tau$ NLSP is neutral and decays into $\tilde{G}$ and ν_τ, which have no electromagnetic or hadronic activity, so they will not modify the abundance of the CDM. BBN bounds from neutrino interactions and sub-dominant decays into quarks are much weaker than the interactions of $\tilde{\chi}_1^0$ or $\tilde{l}$ NLSP [140,141]. Therefore, in this model the $\tilde{\nu}_\tau$ NLSP decaying into $\tilde{G}$ LSP and ν_τ will be considered, see figure 5.1.

5.2. Gaugino Mediation and NUHM with $\tilde{\nu}_\tau$ NLSP Model

In the models with non-universal Higgs masses, previously described in the section 4.1, where $|m^2_{H_1} - m^2_{H_2}| > 0$, the SUSY mass spectrum can have sparticle masses in different order than in models with universal scalar (m_0) and gaugino ($m_{1/2}$) masses at the high scale. In CMSSM $m_{\tilde{\ell}_R} < m_{\tilde{\ell}_L}$ and $m_{\tilde{\ell}_R} < m_{\tilde{\nu}}$, while this order can be reversed in NUHM.

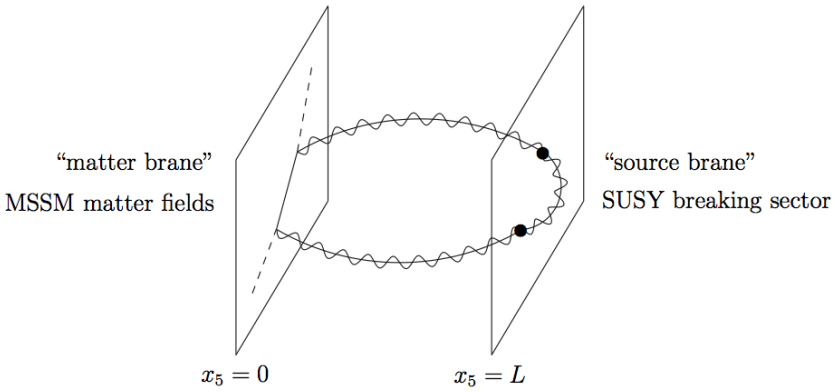

Figure 5.2.: SUSY breaking for gaugino mediation. In the bulk, SUSY breaking couples directly to gauginos, while coupling between matter fields and SUSY breaking sector is forbidden due to their location in the extra dimensions [142].

The SUSY model studied in this thesis has non-universal boundary conditions with gaugino mediation. Here the SUSY breaking is realized on a four-dimensional brane within a higher dimensional theory [108, 142]. Due to different locations of fields, SUSY breaking will occur with different strength, see figure 5.2. Firstly, SUSY breaking sector is located on one of the four-dimensional branes. Gauge and Higgs super-fields, located in the bulk, directly couple to the chiral super-field S, which realizes SUSY breaking. Therefore, gaugino and Higgs fields acquire soft SUSY breaking masses at the tree level. Secondly, squarks and sleptons are confined on some other branes, so they have no direct coupling to the chiral super-field S, which yields no-scale boundary conditions for their masses [143, 144]. Thge following boundary conditions at the compactification scale M_C, assuming $M_C = M_{GUT}$ are given for this model, as shown is studies [28, 108]:

- Gaugino masses: $M_1 = M_2 = M_3 = m_{1/2}$
- Squark and slepton masses: $m_0 = 0$

- A term: $A_0 = 0$
- Higgs masses: $\mu, m_{H^2_{1,2}} \neq 0$.

Therefore, the free parameters of the model are:

$$m_{1/2}, m^2_{H_1}, m^2_{H_2}, \tan\beta \text{ and } \text{sign}(\mu). \tag{5.5}$$

The SUSY mass spectrum is determined from the given boundary conditions and the renormalization group equations. The NUHMG model for $\tilde{G}$ LSP and $\tilde{\nu}_\tau$ NLSP favors lower $\tan\beta$ values ($10 \leq \tan\beta \leq 25$), $m^2_{H_2} \leq 0.5 TeV^2$ and large values of $m^2_{H_1} \simeq 2 - 3TeV^2$ [28].

The NUHMG model with free $m^2_{H_1}$ and $m_{1/2}$ parameters is investigated for $\tan\beta = 10$, $m_0 = 0$, $m^2_{H_2} = 0$, $A_0 = 0$, $|\mu| = 1$ in [28]. The region with realized $\tilde{\nu}_\tau$ NLSP is considered, shown in orange in the figure 5.3. For fixed $m_{1/2}$ and increasing $m^2_{H_1}$ the $m_{\tilde{\nu}_\tau}$, $m_{\tilde{\tau}_1}$, $m_{\tilde{l}}$ ($\tilde{l} = (\tilde{e}\ ,\tilde{\mu}\ )$) decrease, while $\tilde{\chi}^0_1$ is unchanged. This brings to distinction of three regions, labeled A, B and C, which differ in the mass order as $m_{\tilde{\tau}_1} > m_{\tilde{\chi}^0_1} > m_{\tilde{\nu}_\tau}$, $m_{\tilde{\chi}^0_1} > m_{\tilde{\tau}_1} > m_{\tilde{\nu}_\tau}$ and $m_{\tilde{\chi}^0_1} > m_{\tilde{l}} > m_{\tilde{\tau}_1} > m_{\tilde{\nu}_\tau}$ respectively. In addition the mass difference for $m_{\tilde{\tau}_1} - m_{\tilde{\nu}_\tau}$ is always very low, and obtains values 0 - 12 GeV. The $\tilde{q}$ and $\tilde{g}$ masses run as $m_{1/2}$.

In the A and B regions $m_{\tilde{\chi}^0_2} > m_{\tilde{l}_L} > m_{\tilde{\chi}^0_1}$ and there can be a cascade $\tilde{\chi}^0_2 \to \tilde{l} \to \tilde{\chi}^0_1$, but in the region C $m_{\tilde{\chi}^0_1} > m_{\tilde{l}_L}$ and the decay chain is shorter with the possibility of only $\tilde{\chi}^0_{1,2} \to \tilde{l}$ cascade, where slepton decays directly to $\tilde{\nu}_\tau$.

A distinctive feature of the NUHMG model is that $m_{\tilde{l}_L} > m_{\tilde{l}_R}$ and $\tilde{l}_L$ are produced in the cascade, to the contrast of the Constrained Minimal Supersymmetry/Minimal Supergravity (CMSSM/mSUGRA) model where $m_{\tilde{l}_R} > m_{\tilde{l}_L}$ and only the $\tilde{l}_R$ appears in the cascades [28]. This brings to a higher number of allowed decays and consequently a possible longer decay chains. The decay chain can be examined further through decays of $\tilde{\chi}^0_1$ and $\tilde{\tau}_1$ which depend on the A, B or C regions mass order.

For the case of NUHMG studied in this thesis, where $m_{H_2} = 0$, $\tilde{\chi}^0_1$ is manly a bino, and its mostly produced via the decay of $\tilde{q}_R \to q\tilde{\chi}^0_1$. If $m_{\tilde{\tau}_1} + m_\tau > m_{\tilde{\chi}^0_1} > m_{\tilde{\nu}_\tau}$, which can be realized in the region A, the cascade will be invisible after the $\tilde{\chi}^0_1$ and the signature will look like the $\tilde{\chi}^0_1$ LSP case. However, in the regions B and C the mass order is $m_{\tilde{\chi}^0_1} > m_{\tilde{\tau}_1} + m_\tau > m_{\tilde{\nu}_\tau}$ and $\tilde{\chi}^0_1$ can have decays into $\tilde{\tau}_1$. In more detail, $\tilde{\chi}^0_1$ can decay into $\tilde{\nu}_l$, $\tilde{l}$ or $\tilde{\tau}_1$:

- Region A, where $m_{\tilde{\tau}_1} > m_{\tilde{\chi}^0_1} > m_{\tilde{\nu}_\tau}$, there are decays of $\tilde{\chi}^0_1 \to \nu\tilde{\nu}_\tau$.
- Region B, where $m_{\tilde{\chi}^0_1} > m_{\tilde{\tau}_1} > m_{\tilde{\nu}_\tau}$, there are both, decays of $\tilde{\chi}^0_1 \to \nu\tilde{\nu}_\tau$ and $\tilde{\chi}^0_1 \to \tau\tilde{\tau}_1$.
- Region C, where $\tilde{l}$ is lighter than the $\tilde{\tau}_1$ and $m_{\tilde{\chi}^0_1} > m_{\tilde{l}} > m_{\tilde{\tau}_1} > m_{\tilde{\nu}_\tau}$, there are three types of decays $\tilde{\chi}^0_1 \to \nu\tilde{\nu}_\tau$, $\tilde{\chi}^0_1 \to \tau\tilde{\tau}_1$ and $\tilde{\chi}^0_1 \to l\tilde{l}$.

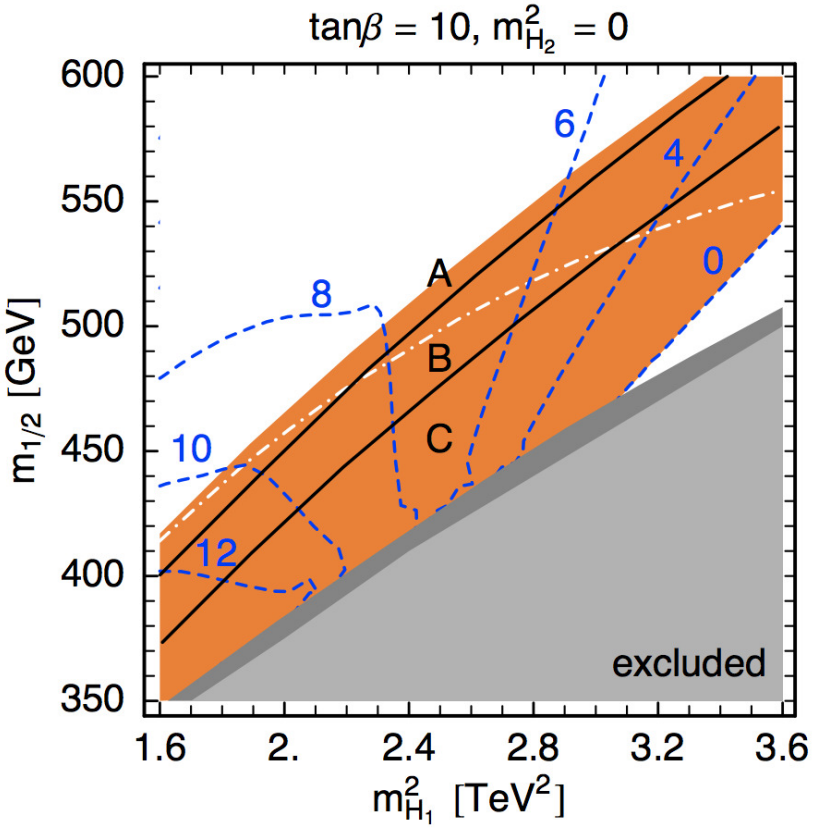

Figure 5.3.: NUHMG model for $\tan\beta = 10$, $m_0 = 0$, $m^2_{H_2} = 0$, $A_0 = 0$ and $|\mu| = 1$ has three regions which differ in sparticle mass order as A ($m_{\tilde{\tau}_1} > m_{\tilde{\chi}^0_1} > m_{\tilde{\nu}_\tau}$), B ($m_{\tilde{\chi}^0_1} > m_{\tilde{\tau}_1} > m_{\tilde{\nu}_\tau}$) and C ($m_{\tilde{\chi}^0_1} > m_{\tilde{l}} > m_{\tilde{\tau}_1} > m_{\tilde{\nu}_\tau}$). Orange area has a satisfied $\tilde{\nu}_\tau$ NLSP, light gray is where $\tilde{\tau}_1$ NLSP is not viable, while dark gray has a $\tilde{\tau}_1$ NLSP excluded by LEP limit. Left white area has a $\tilde{\tau}_1$ satisfied NLSP, while right white area is where $\tilde{\chi}^0_1$ is the LSP/NLSP, which are not considered in this model. Dashed blue equidistant lines represent the mass difference for $m_{\tilde{\tau}_1} - m_{\tilde{\nu}_\tau}$ in GeV. Region below white dash-dotted line satisfies BBN bounds for any $\tilde{G}$ mass [28].

An interesting feature appearing in NUHMG model is the $\tilde{\tau}_1$ decay. In the region A there is a possibility of $m_{\tilde{\tau}_1} > m_{\tilde{\chi}^0_1} + m_\tau$ and a decay of $\tilde{\tau}_1 \to \tau\tilde{\chi}^0_1$ is dominant, while due to small mass splittings ($m_{\tilde{\tau}_1} - m_{\tilde{\nu}_\tau} < 12$ GeV, see figure 5.3) decays of $\tilde{\tau}_1 \to W\tilde{\nu}_\tau$ or $\tilde{\tau}_1 \to H\tilde{\nu}_\tau$ are kinematically forbidden. In the case of $m_{\tilde{\tau}_1} < m_{\tilde{\chi}^0_1} + m_\tau$, which can appear in all three A, B and C regions, the $\tilde{\tau}_1$ has only 3-body decays leading to a signature of soft ff' with missing energy. A dominant contribution is realized with the W exchange, shown in figure 5.4. The $\tilde{\tau}_1$ lifetime for $m_{\tilde{\tau}_1} + m_{\tilde{\nu}_\tau} \sim$ 5-10 GeV is in the order of 10^{-16} - 10^{-18} s, while a displaced vertex is obtained

only for a quasi-degenerate case of $\tilde{\nu}_\tau$ and $\tilde{\tau}_1$ [28]. The $\tilde{\nu}_\tau$ NLSP decay into $\tilde{G}$ is invisible regardless of $\tilde{\nu}_\tau$ lifetime.

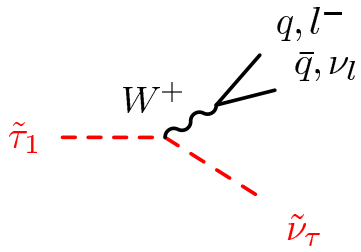

Figure 5.4.: Feynman diagram for a dominant three-body decay of $\tilde{\tau}_1$ into $\tilde{\nu}_\tau$ with the W exchange [28].

In summary, the Non-universal Higgs masses model with gaugino mediation and $\tilde{\nu}_\tau$ NLSP is a phenomenological model which is not covered by searches based on CMSSM model. It is R-parity conserving with $\tilde{G}$ DM. The model has non-universal boundary conditions with gaugino mediation, and has mass spectrum with allowed decays of $\tilde{\chi}_1^0$. Due to its distinguished mass spectrum and kinematics, it represents an interesting model to be studied at the LHC. The free parameters of the model are $m_{1/2}$, $m^2_{H_1}$, $m^2_{H_2}$, $\tan\beta$ and sign(μ). The grid is investigated in the $m^2_{H_1}$ vs $m_{1/2}$ plane for fixed $m^2_{H_2}$=0, m_0=0, $\tan\beta = 10$. The main topic of this thesis is the analysis of the NUHMG model. The study of final states interesting for SUSY searches at the LHC is given in the chapter 9. The analysis of the viable parameter space for searches at 8 TeV, taking into account recent measurements in the filed of SUSY and Higgs physics is given in the chapter 10. The optimization and data analysis of the model is described in detail in the chapter 11.

6. ATLAS Detector at the LHC

The Large Hadron Collider was designed to give answers to the most fundamental questions, to experimentally confirm or disprove the presence of the SM Higgs boson, and give insights into the physics BSM. It is aimed for p-p, Pb-Pb and p-Pb collisons. LHC has been operational at 7 and 8 TeV. Four detectors are placed at four interaction points, the ATLAS, CMS, LHCb and ALICE. The physics analysis described in this thesis has been using the ATLAS data with 20.3 fb−1 of p-p collision data, with the peak luminosity of $7{\times}10^{33} cm^2 s^{-1}$. However, the LHC design energy is 14 TeV, with instantaneous luminosity of 10^{34} $cm^{-2}s^{-1}$, so all detector components have been developed to accommodate for those conditions.

In this chapter the LHC design will be explained in the section 6.1, and the ATLAS detector, with its physics motivation and requirements in the section 6.2. An overview of all ATLAS detector components will be given for inner detector in 6.3, calorimeters in 6.4, muon detectors in 6.5, and finally the trigger and data acquisition system in the section 6.7.

6.1. The Large Hadron Collider

The Large Hadron Collider is a circular accelerator, which accelerates hadrons in a 26.7 km circumference ring, using superconducting magnet technology. It is situated from 45 to 170 m below the surface. The hadrons are pre-accelerated, and then injected into the LHC ring to obtain the high design energies. The acceleration is performed in the two ring system of superconducting magnets, and the detectors are placed at the interaction points. The LHC is designed to have high operational energy, and high instantaneous and integrated luminosity [12].

To achieve high energy, hadrons are accelerated in the LHC accelerator complex, shown in the figure 6.1. The protons are first accelerated in the Linear Collider 2 (LINAC) up to 50 MeV. Then they are inserted into the Proton Synchrotron Booster (PS Booster) and their energy is ramped up to 1.4 GeV. Next, the protons are injected into the Proton Synchrotron (PS) and accelerated up to 25 GeV. Then they are injected into Super Proton Synchrotron (SPS) and accelerated up to 450 GeV. These beams are then injected into the LHC where their energy is ramped up to the energy of 4 TeV, as in this thesis, or 7 TeV as in the design of the LHC. There are four interaction points at the LHC, where the ATLAS [14], LHCb [16], CMS [15] and ALICE [17] experiments are placed.

LHC ring consists of magnets, which are designed to steer two hadron beams in opposite directions. The LHC consists of superconducting magnets based on

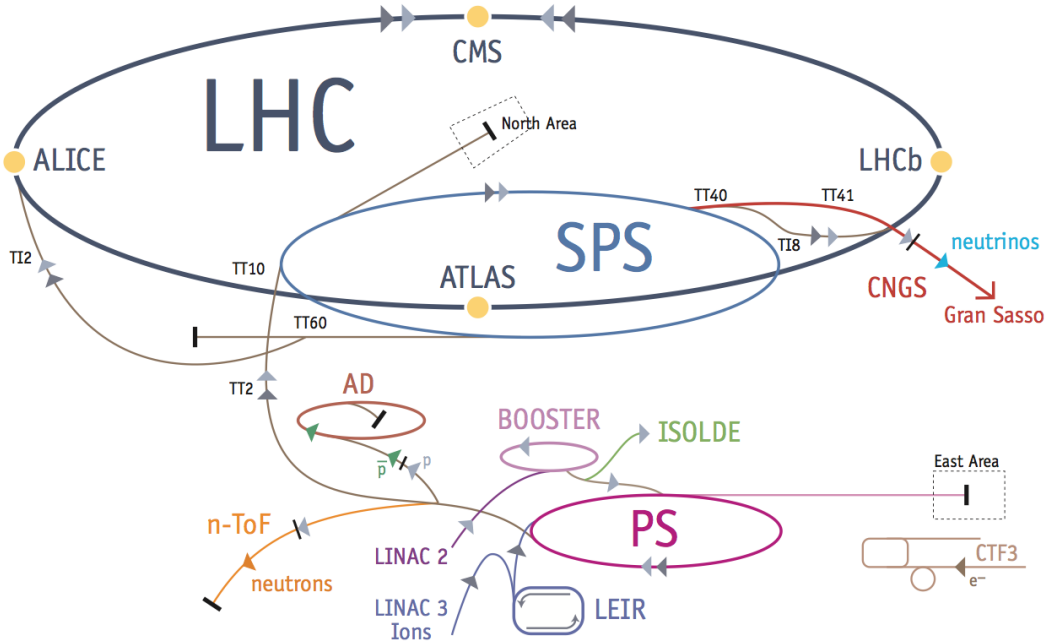

Figure 6.1.: Large Hadron Collider accelerator complex [145]. The protons are accelerated in steps via Linac2 (50 MeV), PS Booster (1.4 GeV), PS (25 GeV), SPS (450 GeV) and LHC (4 TeV in this thesis, 7 TeV design).

the NbTi Rutherford cables, and they are cooled to temperatures below 2 K using superfluid Helium. Firstly, there are 1232 Main Dipoles (MB), which steer the beams in a circular path around the LHC ring, they are 14.3 m long, and achieve magnetic fields of 8 T. Secondly, there are ∼400 Main Quadrupoles (MQ) which focalize the beams, they are 3.1 m in length and achieve magnetic field of 233 T/m. Thirdly, there are ∼6400 more complex magnets, which are used for field error compensation, adjustment of the beam orbit and tuning of the beam parameters. They are 0.15 - 1.5 m long, and operate at 0.1 - 3 T [146].

The LHC machine luminosity depends on the beam parameters, and for a Gaussian beam distribution, it is given by:

$$L = \frac{N_b^2 n_b f_{rev} \gamma_r}{4\pi \epsilon_n \beta^*} F \tag{6.1}$$

where the N_b is the number of particles per bunch, n_b number of bunches per beam, f_{rev} is the revolution frequency, γ_r is the relativistic gamma factor, ϵ_n is the normalized beam emittance, β^* is the beta function at the collision point, and F the geometric luminosity reduction factor which is a consequence of crossing angle at the interaction point. Therefore, in order to achieve high luminosity required by the experiments, the hadron beams have very high intensity.

6.2. ATLAS Detector

The ATLAS detector has been designed to be a multi-purpose detector, namely, to collect data for all types of physics questions that can be answered at the LHC energies and luminosity. This section will start with general definitions for the ATLAS detector in 6.2.1. Major points of physics motivation and consequently the detector design will be explained in the subsections 6.2.2 and 6.2.3.

6.2.1. Coordinate system and Nomenclature

To ensure consistency of all analyses, a common coordinate system and nomenclature for the ATLAS detector and particles emerging from p-p collisions have been defined [14]:

- z-axis is defined by the beam direction, and the x-y plane is transverse to the beam direction.
- Positive x-axis is defined to be pointing from the detector interaction point towards the LHC ring center.
- Positive y-axis is defined to point upwards.
- Side-A of the detector is defined to be the side with the positive z direction.
- Side-C of the detector is defined to be the side with the negative z direction.
- Azimuthal angle ϕ is measured around the beam axis.
- Polar angle θ is measured from the beam axis.
- Rapidity is defined as $y = \frac{1}{2} \ln \frac{E+p_z}{E-p_z}$, where E is the particle energy and p_z is the longitudinal particle momenta.
- Pseudorapidity is defined as $\eta \equiv -\ln \tan(\frac{\theta}{2})$.
- p_T is the transverse momentum.
- E_T is the transverse energy.
- E_T^{miss} is the missing transverse energy, defined in the x-y plane.
- $\Delta R = \sqrt{\Delta\eta^2 + \Delta\phi^2}$ is the distance in the pseudorapidity - azimuthal angle space.

6.2.2. Physics Requirements

With the knowledge of the typical expected decays of interesting events, it is possible to estimate the required dimensions of the detector parts and materials to be used for detection of different outgoing particles and their properties. Namely, the aim is to make sure that the majority of typical events that bring answers to the relevant physics questions, are collected for further analysis. Therefore, the detector design has to meet very specific demands. Here a short overview of relevant topics in physics of the LHC and ways for their detection, with specific requirements for the ATLAS detector design will be given.

In the ATLAS detector design, a number of physics topics were considered:

- **Standard Model physics**. For physics at the LHC, understanding of Standard Model background is of high importance. First, the production cross sections measurements of SM processes are made, since they are important for gaining confidence in the detector performance and the SM backgrounds estimation. With more accumulated data, precise measurements on a number of properties give confirmations of SM predictions, or can give hints towards the BSM physics. The deviations can occur in the invariant mass distributions, shape discrepancies in kinematic distributions, or as an excess in the counting experiments. To be able to claim the discovery if deviations take place, one has to understand the backgrounds with high confidence, in order to exclude misinterpretations.

- **Higgs physics**. Standard Model Higgs boson decay channels have been used as major benchmarks for the construction of the ATLAS detector. ATLAS detector was built in a way to enable detection of any possible Higgs incarnation at the LHC. Therefore, the low mass Higgs ($m_H < 2m_Z = 180GeV$) would be characterized by a narrow width in order of few MeV, therefore it would be determined by the detector resolution. Since the dominant decay of Higgs into hadrons is hard to distinguish from the QCD background, there are other interesting decays, like the decay of Higgs into two photons, or associated production of Higgs in the processes like $t\bar{t}H$, WH and ZH, where the event selection is performed using the top decay, or one lepton from W or Z, and also the Higgs decays into $b\bar{b}$, which relies on the efficient b-tagging. For the Higgs in the mass range 130-600 GeV, dominant is the $H \to ZZ^{(*)}$ decay, where the decays of Z bosons produce a pair of oppositely charged leptons. This is considered to be the cleanest channel for the Higgs detection. The Higgs in the mass range higher than 600 GeV has decays of WW and ZZ into jets or they involve neutrinos, but also the detection can be performed using forward jets from the WW or ZZ fusion. The possibility of Supersymmetric Higgs bosons can be investigated using τ leptons and b tagging.

- **New interactions**. As a possibility of existing new interactions, W' and Z' should be investigated, using high resolution lepton measurements and charge calculation in the high p_T range of 1 TeV. Further, by using the high p_T

jets reconstruction, the benchmark process of quark compositeness can be investigated, where the deviation in the jet cross-section from the QCD expectation should occur. Signs of new physics can be also investigated using flavor changing neutral currents, lepton flavor violation and by measuring triple and quadratic gauge couplings in corresponding decays with photons and leptons.

- **Supersymmetry**. If nature is realized through Supersymmetry, the typical decay for a model with conserved R-parity has cascade decays with characteristic jets of high transverse momenta and possible leptons, and it ends with the decay into the lightest supersymmetrical particle (LSP). As the LSP is weakly interacting, it passes the detector without any interaction, thus produces only a signal of missing transverse energy.

- **Extra Dimensions**. The models which propose existence of extra dimensions with the energy scale of quantum gravity in the TeV region, have emissions of gravitons escaping into extra dimensions, leaving a typical signature of missing transverse energy. Also, the emission of Kaluza-Klein excitations can take place, leaving detectable Z-like resonances, which are characterized by a typical mass separation of ∼TeV. Additionally, interesting signatures can have anomalous high-mass di-jet production, and finally there is the scenario of mini black hole production, where they decay democratically to all particles of the Standard Model (SM), therefore having a signature with high multiplicity and high energy and transverse momentum particles.

- **Rare events**. Due to the fact that interesting physics processes have a very low cross section, LHC has been designed to provide high luminosity in p-p collisions of 10^9 inelastic events/s. However, each interesting event will on average be accompanied by additional 23 inelastic events per bunch crossing. In addition, QCD background characterized by high jet production is a dominant process. Therefore, selection of interesting events should be performed using additional parameters. For this, variables like missing transverse energy or secondary vertices play an important role, since they improve the particle identification and event selection significantly.

Having in mind the characteristics of these benchmark physics processes, and the conditions of high luminosity p-p collisions, a list of general requirements has been set up [14]:

- Radiation-hard electronics and sensors are required, because of high c.m.e. and instantaneous luminosity of LHC p-p collisions. Also, due to the high particle fluxes, high detector granularity is required to perform reliable object reconstruction and to resolve overlap of hard interaction.

- Large acceptance in pseudorapidity and azimuthal angle to efficiently cover the almost full phase-space of the detector.

- Good inner detector momentum resolution and reconstruction efficiency for charged particles. Vertex detectors are close to the interaction region, and they need to resolve secondary vertices, which are important in τ-lepton and b-jet tagging.
- Very good electromagnetic calorimetry for electron and photon identification and full-coverage hadronic calorimetry for jet and missing transverse momentum measurements, because they are essential for many interesting physics analyses.
- Good muon momentum resolution and identification efficiency for a wide range of transverse momenta, with additional high accuracy in muon charge measurement.
- Highly efficient triggering system for high and low transverse momentum objects with very good background rejection.

Detector component	**Required resolution**	η **coverage** Measurements	Trigger
Tracking	$\sigma_{p_T}/p_T = 0.05\% P_T \oplus 1\%$	± 2.5	
EM calorimetry	$\sigma_E/E = 10\%/\sqrt{E} \oplus 0.7\%$	± 3.2	± 2.5
Hadronic calorimetry			
barrel and end-cap	$\sigma_E/E = 50\%/\sqrt{E} \oplus 3\%$	± 3.2	± 3.2
forward	$\sigma_E/E = 100\%/\sqrt{E} \oplus 10\%$	$3.1 < \lvert\eta\rvert < 4.9$	$3.1 < \lvert\eta\rvert < 4.9$
Muon spectrometer	$\sigma_{p_T}/p_T = 10\%, p_T = 1TeV$	± 2.7	± 2.4

Table 6.1.: Performance goals for the ATLAS detector [14]. High requirement on the resolution and η coverage for the reconstruction of tracks, electrons, photons, jets and muons. The units for E and p_T are in GeV.

More precise specification of requirements for the detector resolution and coverage are summarized in the table 6.1. There is a very high resolution request for the reconstruction of high number of charged particle tracks, but due to their slow reconstruction, they are not used for the trigger. The detection of photons and electrons is performed using the Electromagnetic Calorimetry, with high η coverage and high resolution, which is requested according to the deposited energy of the objects. Similarly, jets need be reconstructed with Hadronic Calorimetry with good η coverage and good resolution relative to the jets energy. The muons are to be detected with good resolution and high η coverage in the Muon Spectrometer.

6.2.3. Detector Design

With the aim to be the multi purpose detector, ATLAS has a hermetic 4π construction. For the good coverage in all directions, a design of barrel with end-caps has

been put in place. To ensure detection of different kinds of particles, the layered structure has been introduced. For the distinction of charged particles, the tracking system has been put inside the superconducting solenoid magnet. Toroidal superconducting magnet has been deployed to bend the trajectory of muons, to ensure their path is in the detector volume. The detector has a length of 44 m and a diameter of 25 m.

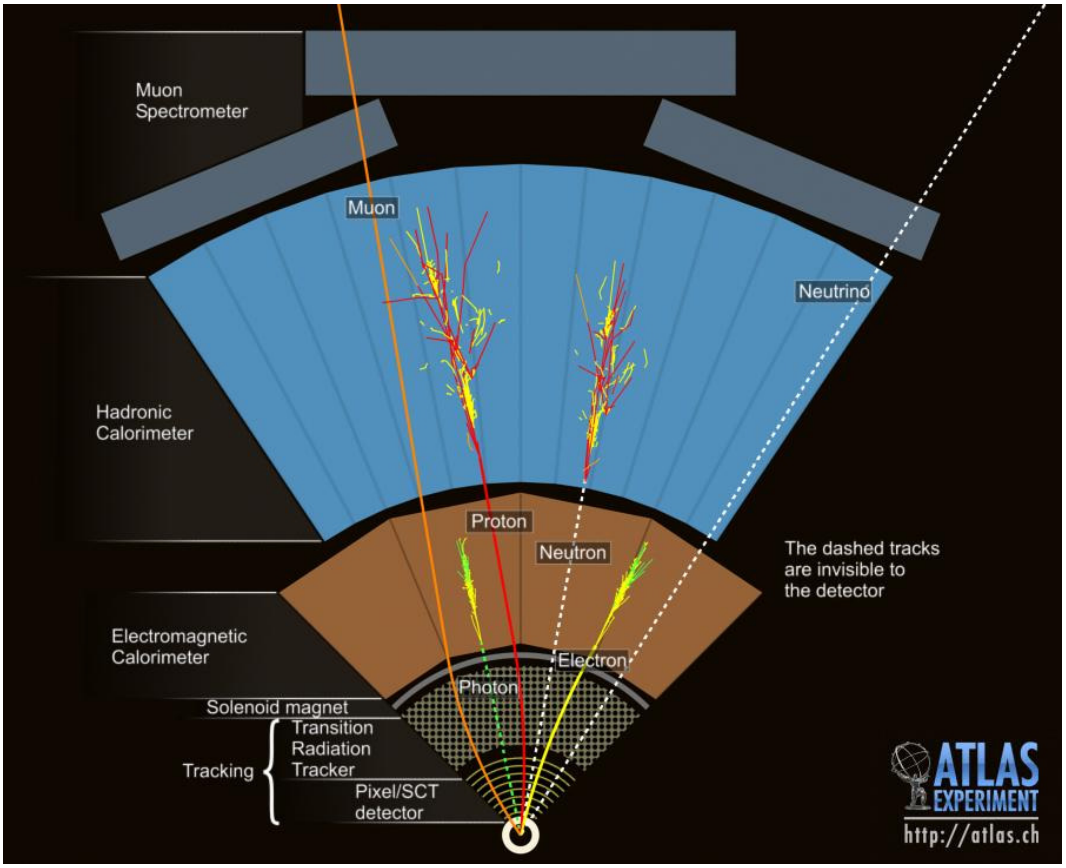

Figure 6.2.: Passage of particles through the ATLAS detector. Charged particles like electron, muon and proton leave a track in the inner detector. The electron and photon leave a shower in the Electromagnetic Calorimeter, while proton and neutron leave a hadronic shower in the hadronic calorimeter, muon is detected by the muon spectrometer, and neutrino is reconstructed as missing energy in the transverse plane [147].

Due to different characteristics of detectable particles, like charge and energy loss in interaction with the detector material, they can be detected using reconstructed tracks and energy deposition, shown on the figure 6.2. Also, particles which don't interact with any detector material, can be reconstructed as the missing energy.

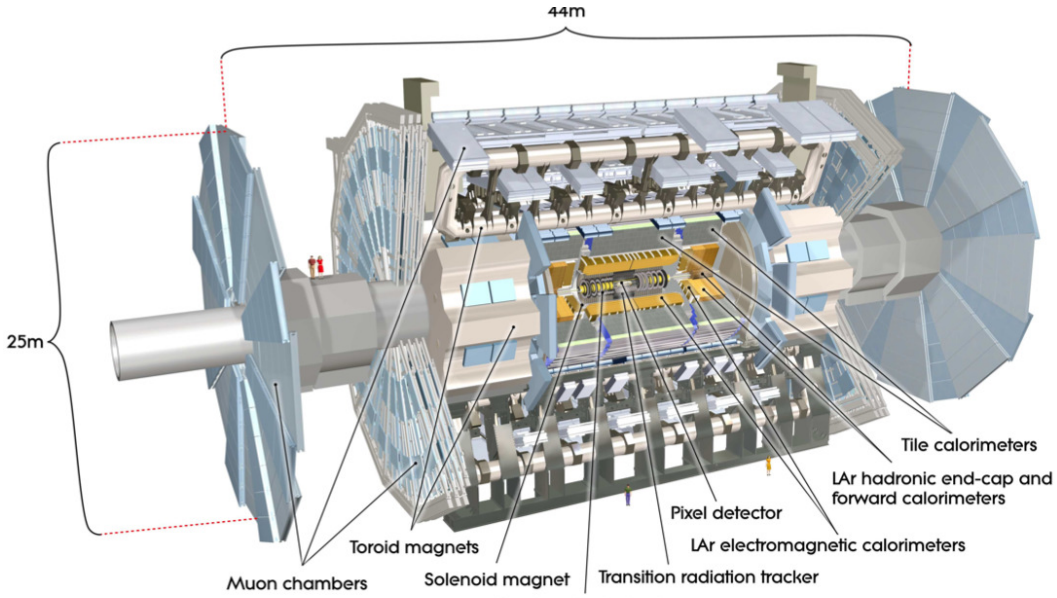

Figure 6.3.: Schematic view of the ATLAS detector. Inner detector consists of Pixel, Semiconductor Tracker and Transition Radiation Tracker, and it is placed inside the solenoid magnet. Liquid Argon and Tile calorimeters are outside of the solenoid magnet. Toroid magnet is placed around the calorimeters. Muon spectrometers are placed within and outside of the toroid magnet [14].

Electron will leave a track in the inner detector, and produce a shower in the electromagnetic calorimeter. Photon, will similarly, leave a shower in the electromagnetic calorimeter, but having no charge, it will not be detected in the tracker. However, proton, being a charged particle, will leave a track and have most of the energy deposition in the hadronic detector. Neutron, being neutral, will interact in the hadronic calorimeter but will leave no track. Charged particles in the transition radiation tracker induce transition radiation photons, which produce a ionization cascade with an energy proportional to the mass of the initial particle (E/m). This property is used to distinguish electrons from pions, kaons e.t.c. Muon will be passing the whole volume of the detector leaving tracks. Finally, neutrino, being neutral and weakly interacting, will leave the detector without any interaction. However, with the precise calculation of the total deposited energy in all directions, its energy can be reconstructed in the transverse plane.

The design and size of the detector is driven by the requirements for the magnet system. The inner detector is surrounded by the thin superconducting solenoid, which produces axial magnetic field of 2 T. Its outer diameter is 2.56 m, and it has a length of 5.8 m. In addition, there is a system of large superconducting toroidal magnets. The barrel region consists of eight toroid coils arranged in azimuthal symmetry

outside of the calorimeter, producing a toroidal magnetic filed of approximately 0.5 T. Its outer diameter is 20.1 m and the length is 25.3 m. The system also includes A and C side end-caps consisting out of eight coils each, producing a toroidal magnetic field of approximately 1 T. They have an outer diameter of 10.7 m and length of 2.5 m each [14]. With the selected design of the magnets, the sizes of other detector parts are determined. Their layered structure is presented in the figure 6.3. More details about the detector components will be presented in the following sections.

While p-p bunch crossing, for the design luminosity of $10^{34} cm^{-2} s^{-1}$, occur at the rate of 40 MHz, due to the technical limitations, the event data recording can be performed at 200 Hz. Therefore, event reduction needs to be in order of 10^6. For this, the trigger system has been set up, which selects events interesting for physics analysis from the background dominated by the soft QCD. In ATLAS, the trigger system consists of three levels. Level 1 is hardware based and reduces the rate down to about 75 kHz, it performs a very fast decision based on the reduced detector information. Level 2 and Event Filter are the remaining two software based trigger levels that reduce the rate down to 100 kHz and 200 Hz respectively. The Level 2 uses the selection from Level 1 to look into interesting regions of the detector and perform selection using more detailed detector information, while event filter uses Level 2 decision and performs the final selection using the full detector full granularity information from the interesting regions. The selected data is being recorded to the permanent storage and is being distributed for the physics analyses. Details about the trigger and data acquisition will be given in section 6.7.

6.3. Inner Detector

The inner detector is shown in the figure 6.4. The tracking system is placed inside the magnetic field of the solenoid. It consists of high-resolution semiconductor detectors placed at smaller radii covering $|\eta| < 2.5$, arranged in the barrel region in concentric cylinders around the beam axis and on end-cap holders perpendicular to them 6.4. The pixel detector has the highest granularity and is closest to the beam line. Around it are the layers of the silicon strip detector (SCT). The semiconductor detectors in the barrel region are surrounded by layers of transition radiation tracker (TRT) straw tubes, which provide only the $R - \phi$ information, and not the z position of the hit. The TRT barrel region is covered up to $|\eta| < 2$, and the end-cap regions have panels with radial placement of TRT tubes. This combination of very high precision tracking at small radii in the Pixel and SCT detectors, and very good momentum resolution obtained from high number of hits in the layers of transition radiation tubes, gives a good cross check for momentum measurement and track reconstruction. Inner tracker is primarily used for electron identification and vertex reconstruction, but it is essential for impact parameter measurements, secondary vertex reconstruction and vertex measurements for b-tagging and τ-lepton identification.

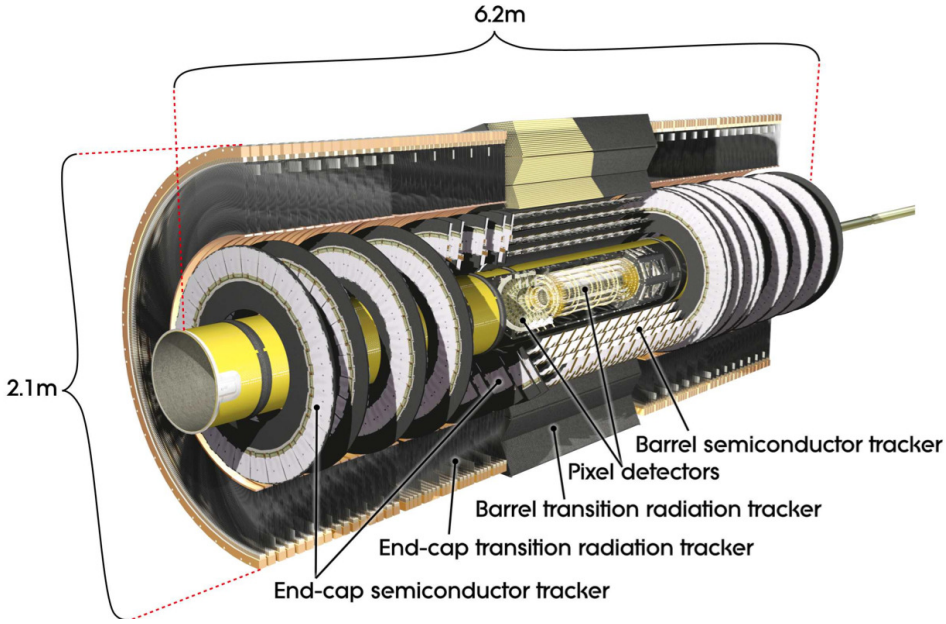

Figure 6.4.: Inner detector components have a design of barrel and end-caps placed inside the solenoid magnet. Closest to the beam-line are the Pixel and Silicon micro-strip tracker (SCT), surrounded by the Transition radiation tracker (TRT) [14].

6.4. Calorimetry

The system for calorimetry is shown in the figure 6.5. It consists of electromagnetic liquid Argon (LAr) sampling calorimeter covering $|\eta| < 3.2$ and hadronic tile scintillator calorimeter in the barrel region covering $|\eta| < 1.7$, with the end-caps made in LAr technology, covering the remaining $1.5 < |\eta| < 3.2$ range. To improve the pseudorapidity coverage the LAr forward calorimeters have been put in place up to the $|\eta| < 4.9$ region. The depth of the calorimeters has been calculated in such a way that they have a good coverage for electromagnetic and hadronic showers, but also need to be absorbent enough to prevent punch through of these objects to the muon detector. The barrel and end-cap region of the electromagnetic LAr detector with its fine granularity is used together with the tracking system for precision electron and photon measurements. The outer smaller granularity of the hadronic detector is well suited for jet reconstruction and measurements of E_T^{miss}.

6.5. Muon System

The muon system is shown in the figure 6.6. It is built around the calorimeter as a large volume of light structure within the air-core toroid system. The layered detector structure provides very good resolution, with the barrel and end-cap pseudorapidity coverage of $|\eta| < 2.7$. The magnet configuration of barrel part with large

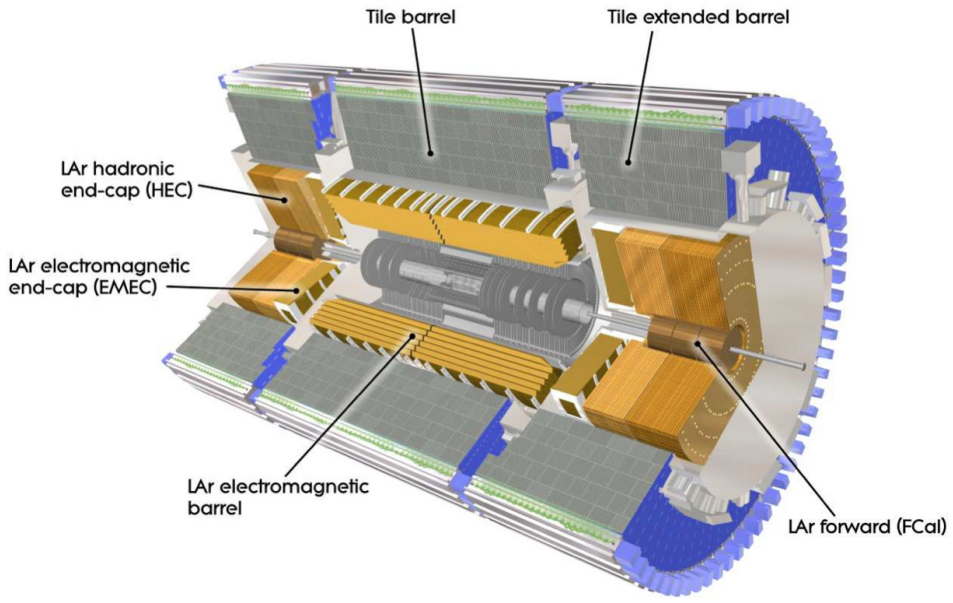

Figure 6.5.: Calorimetry at the ATLAS experiment is placed outside the solenoid magnet. It consists of electromagnetic and hadronic Liquid Argon (LAr), and Tile calorimeters in the barrel and end-cap regions [14].

toroid magnets, smaller toroids at end-caps and the transition region between these two, provide a magnetic field which is mostly orthogonal to the muon trajectory. The expected high particle flux lead to a design which has high granularity, fast readout capability, radiation hardness and good aging properties. The system consists of two types of chambers. Namely, for precision measurements the Monitored Drift Tubes (MDT) and Cathode Strip Chambers (CSC) at high pseudorapidities are put in place, and for the fast trigger system there are Resistive Plate Chambers (RPC) in barrel and Thin Gap Chambers (TGC) in the end-cap region, which are essential for bunch-crossing identification, defining p_T thresholds and measurements of the muon coordinate in the direction orthogonal to the precision tracking measurement. The outer size of the muon chambers determines the final size of the ATLAS detector.

6.6. Forward Detectors

In addition to these detector parts, there are dedicated forward detectors built for precise luminosity measurements. At ±17 m from ATLAS interaction point (IP) is Luminosity measurement using Cerenkov Integrating Detector (LUCID) which detects inelastic p-p scattering in the forward region and measures the on-line relative luminosity for ATLAS. At ± 140 m from the IP is the Zero Degree Calorimeter (ZDC) is designed to measure the centrality of p-p collisions. It is constructed from

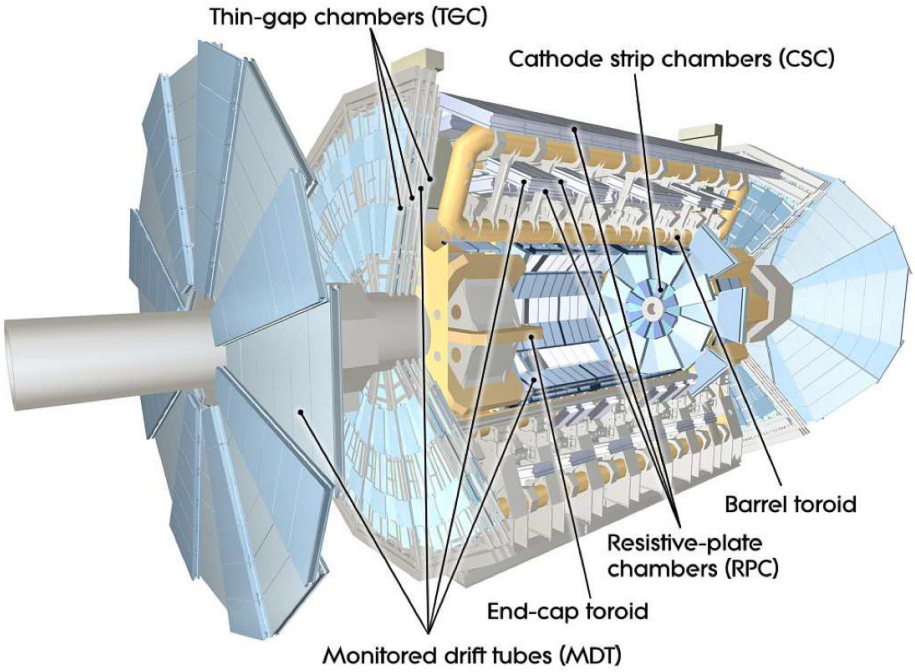

Figure 6.6.: Muon Detector system at the ATLAS experiment consists of Monitored Drift Tubes (MDT) and Cathode Strip Chambers (CSC) for precision measurements, and Resistive Plate Chambers (RPC) and Thin Gap Chambers (TGC) for fast triggering [14].

quartz rods and tungsten plates, and is able to detect neutral particles at very high pseudorapidities of $|\eta| < 8.2$. At ± 240 m from IP is the Absolute Luminosity For ATLAS (ALFA), which approaches as close as 1 mm to the beam and is constructed of scintillating fiber trackers inside Roman pots for absolute luminosity measurement.

6.7. Trigger and Data Acquisition

The ATLAS experiment is designed to extract data for the physics analyses from LHC p-p collisions at the design energy of 14 TeV and instantaneous luminosity reaching $10^{34}\text{cm}^2\text{s}^{-1}$. At nominal operation, the bunches contain 10^{11} protons, and collisions occur at 40 MHz, which results in about 20 p-p interactions per bunch crossing [148]. Only a small fraction of these events are used for physics analyses. The Trigger and Data Acquisition (TDAQ) System of ATLAS has the aim to select manageable rates of physics events for the mass storage, where the potentially interesting physics events are kept for the analyses. As the recording rate reaches a few hundreds of Hz, the trigger system needs to have a high reduction power. In ATLAS, a design using the so-called Regions of Interest (RoI) is used, with the three level trigger system. In this section details of the the ATLAS trigger system, data

acquisition and its monitoring will be presented. More details about the program called Trigger Presenter (TriP) designed for the online monitoring of the ATLAS trigger is shown in the appendix B.

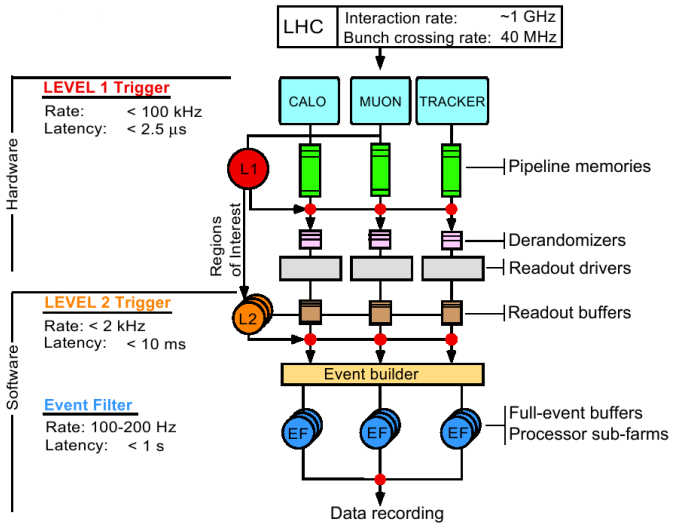

Figure 6.7.: Three level trigger system at the ATLAS experiment. The input bunch crossing rate of ∼40 MHz is reduced to < 75 kHz by the hardware based Level 1 trigger, where regions of interest (RoI) are built with latency of 2.5 μs using the reduced detector information from calorimeters and muon detectors. The software based Level 2 and Event Filter triggers reduce the event rate in two steps, to a few kHz by the Level 2 with latency of 10 ms by adding the tracking information in the RoI, and finally to a few hundreds of Hz by the event filter with latency of less than 1s using the full detector information in the RoI [149].

The ATLAS three level trigger system is schematically shown in the figure 6.7. The mechanism of early rejection is used to minimize the total decision time and maximize the interesting physics event rate within the manageable output recording rate.

The Level 1 of the trigger system reduces the rate from 40 MHz to about 75 kHz. It is hardware based and uses custom electronics, mainly ASIC and FPGA technology [150]. It performs the early event selection based on the high p_T objects, using the configurable threshold selection. These are high p_T muons, electrons, photons, jets, hadronically decaying τ leptons, large missing and total transverse energy. For this purpose the data collected by the fast muon detector components and reduced readout of calorimeter systems is used. The decision latency of Level 1 is 2.5 μs, and in this period data is collected in the pipeline memories. For accepted events, the geometrical locations of the objects in η and ϕ of the detector, called the Regions of Interest (RoI), are sent to the Level 2, and the data is moved to the Read-out

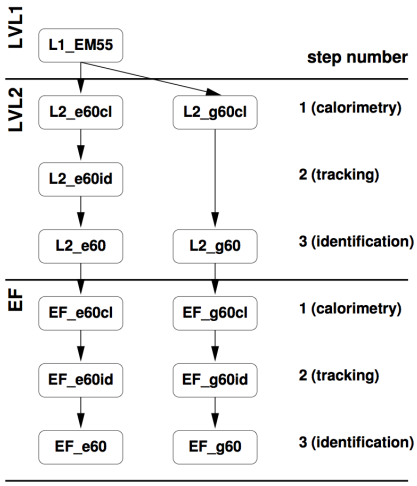

Figure 6.8.: Trigger chains of the ATLAS High-Level Trigger steering algorithm. The trigger decision is performed in a step-wise, seeded and consecutive way. The boxes represent algorithm tests which start from Level 1 decision. Multiple algorithms are run at Level 2 using the information in the RoI. Similar procedure is performed at the Event Filter using the full detector information. [150].

Buffers (ROB) [151].

The Level 2 and Event Filter, together called High-Level Trigger (HLT), are software based triggers running on commodity computing and network technology. Level 2 reduces the event rate from $\sim$ 75 kHz to a few kHz, with latency of $\sim$ 10 ms. Level 2 algorithms are optimized for high speed. They use the data retrieved from ROB but only in the RoI identified by the Level 1 decision. The Level 2 trigger decision is proceeded by the Event Filter triggers. They reduce the rate from a few kHz to a few hundreds of Hz. They make use of a higher latency of 1 s, and perform more complex algorithms. The Event Filter refines the Level 2 decision, using the full detector information from the ROB, and it benefits from a more detailed calibration and alignment than at Level 2.

In order to minimize the computing time, the HLT is designed to perform an early event rejection. A number of sub-trigger decisions, called 'trigger chains', are used from a Level 1 passed decision with the RoI, called 'trigger item'. Two types of HLT algorithms are used. First are the Feature Extraction (FEX) algorithms, which perform time consuming operations of data unpacking and calculation of physics quantities for the physics objects (e.g. electron, muon). Second are the hypothesis (Hypo) algorithms which perform quick selection cuts based on the previously calculated features (e.g. energy, isolation). The trigger chain selection is performed in steps, where each trigger decision algorithm is called a 'trigger element'. The decision is performed from a 'seed' coming from the previous level of decision, and proceeded by the next consecutive trigger element. Trigger elements that fail the

algorithm test are not processed further. At the end of each level a prescale factor can be applied for each trigger chain in order to reduce the output rate. In the figure 6.8 an example of trigger chains for an electron and photon with p_T of at least 60 GeV is shown. In this example two trigger chains, for an electron and a photon, are run with consecutive steps requirements on calorimetry, tracking and object identification.

In order to prepare relevant trigger selection for the data taking, the so called 'trigger menu' is prepared. It contains all the trigger chains that are run for given data taking conditions. The offline trigger simulation uses the same algorithms as online HLT. The trigger selection cuts are optimized in order to provide optimal selection to accommodate event rates into limitations at each trigger level.

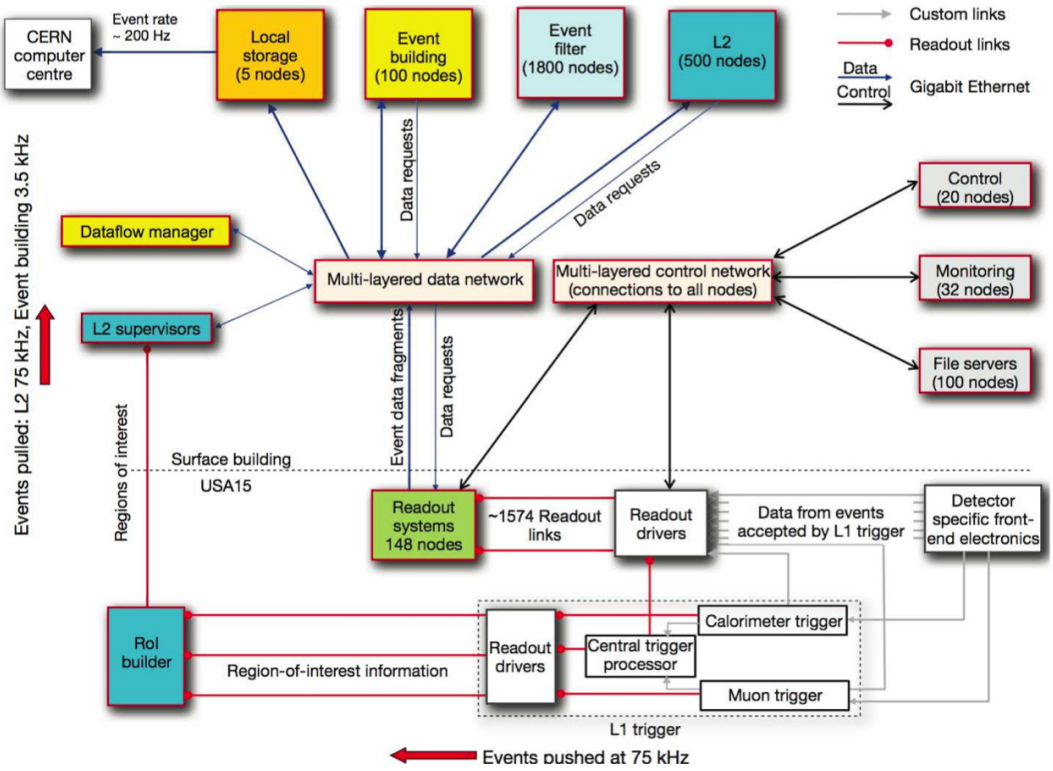

Figure 6.9.: Trigger and data acquisition system at the ATLAS experiment [14].

The Level 1 and HLT are accommodated in the Data Acquisition (DAQ) system, see figure 6.9. The detector information is read out into Read out Drivers, and Level 1 decision is performed by the Central Trigger Processor using the trigger decisions from the calorimeter and muon triggers. Level 1 decision and RoI information are pushed to the RoI builder. Level 2 supervisor pulls the Level 1 information together with the detector data, and sends the jobs for algorithm processing to the Level 2 processing units at the HLT farm. The Level 2 result is further distributed by the

Data Flow Manager of the Event Filter into a Event Filter processing task at the HLT farm. The Event Filter decision is attached to the full detector information produced by the Event Builder and sent to the local and permanent data storage. The whole system can be configured, controlled and monitored from the control network [14].

In order to ensure stable data taking, a number of data quality monitoring tools is used in ATLAS. The trigger rate and PC farm status information is published to the Information Service (IS) system and Online Histogramming Service (OH). Frequently used quality cross-checks for selected values are performed in the Data Quality Framework (DQM) where tailored algorithms are run for subscribed information in order to obtain a flag of OK, WARNING or ERROR [152].

The trigger online monitoring plays an important role, and a number of points need to be considered. In the first place, the Level 1, Level 2 and Event Filter summary rates need to be in the right range. Also, the rates of individual trigger items and chains need to be monitored, as the history of their evolution can provide information for their understanding. Second, as the HLT runs on commodity PC farms, the performance of all PCs needs to be monitored. To allow for monitoring of these details a program called Trigger Presenter was designed, and more details can be found in the appendix B.

7. Reconstruction and Monte Carlo Event Generation

In physics beyond the standard model (BSM), the prospects of discovery need to be investigated for a variety of approaches, from changing model assumptions to adjustments in physics analysis. A good starting point is to have a simulation of the events that would occur for a given analysis. In experimental high energy physics, a common approach is to use Monte Carlo (MC) event generators, which according to the implemented physics model and additional tuning to the data, produce events based on the current knowledge about physics processes. Moreover, they enable implementing hypothetical physics models and investigation of their discovery. In this chapter, the complete process of event generation is described, from the chosen BSM signal mass spectrum production and new particles branching ratios calculation, through events generation with their kinematic topology and probability, to the simulation of the detector response for particles passing through different layers of detector material, and to the final event reconstruction algorithms overview. In this way a representation of new physics processes is obtained, so the physics analysis and trigger selection can be optimized.

MC analysis in BSM physics needs to start with the mass spectrum generation of the investigated model, described in section 7.1. For the selected set of parameters, the software calculates the masses of all model particles at the electroweak scale. For example in SUSY, the input parameters can be a few constrained model parameters at the GUT scale, which are extrapolated to the electroweak scale according to the renormalization group equations (RGE) using the appropriate software. This mass spectrum makes the starting point for a given model investigation.

To have a completely defined SUSY point for a given model and input parameters, the next step is to run a decay width and branching ratio calculator, described in section 7.2. From the previously calculated mass spectrum, it determines the decay widths and branching ratios for the SM and MSSM Higgs boson, and all SUSY particles. This output is then ready to be used for further event generation.

Monte Carlo (MC) event generators produce representations of high energy physics events. They simulate the outgoing particles according to analytic physics equations and a variety of QCD models, and generate numbers of events using MC techniques. The output are sets of outgoing particles produced in interactions between two incoming particles (i.e. p-p collisions for LHC) which are used for analysis of model properties. In the section 7.3 a more detailed description of Pythia MC generator, used in the signal generation, and a comparison of MC generations in the background event generation, will be given.

To have a realistic representation of the physics event in the detector, it is necessary to have a simulation and digitization of particles passage through complex detector geometry, and estimate their tracks and hits in detector material, as described in section 7.4. This includes electromagnetic and hadronic processes for various particles in different energy range (from eV to TeV) passing through different materials. The software takes the generated event particles as a original information, and then for a given detector construction, with all the materials and dimensions, simulates the detection hits, and possible tracks left in the detector. After this, in digitization process the calculation of the voltages and timing of detector components is performed. In this way, the simulation of the full detector response of all event particles is obtained.

The final step in the event generation is the event reconstruction, where the same software is used for MC and data events, described in section 7.5. From the raw data, i.e. voltages, timing, energy deposition in detector components, reconstruction of events is performed. This includes various algorithms for different physics objects reconstruction, like electrons, muons, photons, jets, taus, heavy quarks, etc. From the MC generated events, different physics scenarios can be investigated and optimization of object definition can be performed. From the data reconstruction, the physics analysis can be performed.

In order to have a right amount of events of different productions of signal and background, i.e. to be able to perform weighting of MC samples in the physics analysis, it is required to obtain a good higher order cross-section calculation for different physics processes. Although event generators are constructed to have good event description, they are not well developed in the cross-section calculations. Therefore, NLO and NLL cross-section calculations are done with dedicated programs for analytic cross-section calculation, see section 7.6.

MC analysis, on the one side, plays a crucial role in preparing physics analyses, and on the other, gives confidence in understanding physics processes seen in the data. Being able to produce large amounts of events similar to the events recorded by the detector, one can perform generation of different contributions of events, from the well known SM ones, to the hypothetical of BSM physics. Despite the fact that MC generators use a large number of models and built in assumptions, these tools undoubtedly make an important apparatus for physics analyses and understanding of data. In ATLAS a number of MC generators, and tools for simulation, digitization and reconstruction are embedded in a common framework called Athena [153], which is commonly used throughout the experiment, with user and group defined specifications.

7.1. Signal Mass Spectrum Generation

The starting point for the SUSY model analysis is the calculation of the sparticle masses at the electro weak scale (EW). The model investigated in this thesis belongs to the group of R-parity conserving MSSM models and has non-universal

Higgs masses ($m_{H_1} \neq m_{H_2}$). Therefore, the natural choice for the mass spectrum generator in this thesis is SOFTSUSY 3.1.2 [154] which calculates the sparticle mass spectrum and supports MSSM and its extensions. Since MSSM models are constructed to reduce the number of free parameters in the SUSY breaking sector, the dimensionality of the problem is significantly smaller, and it is therefore possible to perform various parameter scans.

SOFTSUSY is a mass spectrum generator for MSSM models, which calculates the Higgs and sparticle masses. It uses SM constraints, i.e. the fermion masses obtained from low energy measurements, gauge couplings and EW gauge boson masses. The soft SUSY breaking parameters provided by the user and the specified SUSY breaking model are being used. It calculates renormalization group equations for SUSY parameters (Higgses and sparticle masses with the usage of SUSY radiative corrections, and couplings) with the requirement of consistency of resulting MSSM parameters with the Higgs potential, which leads to observed EW boson masses. Through an iterative procedure, it calculates the superpotential μ which agrees well with input constrains, and finally calculates all the Higgses and sparticle masses and their mixings. The details of this algorithm will be given in the following paragraphs, as described in [154].

The program is a C++ code, where the input can be given via command line or in the SUSY Les Houches accord [155]. In this thesis, the input files have been prepared to contain the "nonUniversal" model specification. In order to obtain the final Les Houches file of each SUSY point, the next step is to get the decay widths and branching ratios of the sparticles, which will be explained in the next section.

7.2. Signal Decay Width and Branching Ratio Calculation

In order to achieve high accuracy in decay width and branching ratio calculation, a good theoretical model can be obtained with the package called SUSY-HIT (SUspect-SdecaY-Hdecay-InTerface [156]). It represents an interface between the SuSpect sparticle mass generator, HDECAY [157] MSSM Higgs bosons and SDECAY [158] sparticles decay width and branching ratio calculators. The program also provides a possibility of using an input Les Houches file for the sparticle and MSSM Higgs mass spectrum. It has been chosen for this analysis since it calculates the 3-body decay at the tree level, typical for the NUHMG model investigated in this thesis.

The HDECAY program, interfaced through SUSY-HIT, calculates the SM and MSSM neutral and charged Higgses decay widths and branching ratios with most up to date theoretical models. Namely, it supports 2-body and multi-body decays, and in MSSM the cascade and SUSY decays. It includes higher order QCD corrections for decays into quarks, as well as double off-shell decays of CP-even MSSM Higgs bosons into massive gauge bosons, and 3-body decays with heavy off-shell t, off-shell gauge boson and heavy neutral Higgs decays with one off-shell Higgs boson. In MSSM calculation it includes NLO radiative corrections and all kinematically

allowed decays into SUSY particles.

The SDECAY program, via SUSY-HIT, calculates the sparticle decay widths and branching ratios in MSSM. It supports 2-body decays for sfermions, SUSY QCD corrections for colored sparticles, the top MSSM decays, and most importantly for this analysis, the 3-body decays of gauginos, gluino, stops and sbottoms, as described in [156].

SUSY-HIT is a FORTRAN program, which can be used with the SUSY and Higgs mass spectrum obtained with SOFTSUSY in the Les Houches format. The program adds to the Les Houches format mass spectrum the calculated decay widths and branching ratios. In the next section, the MC event generation will be described in more detail.

7.3. Monte Carlo Event Generation

The major purpose of using MC event generators in the physics analysis is to obtain good prediction of the final state in the collision events. They also play an important role in the analyses for the detector and trigger design. For example, the physics analyses need to be optimized with the prediction of signal and background, and trigger can be optimized to successfully reduce background and keep the signal. MC generators are used to design the detector components and to evaluate required corrections to the accumulated data.

Particles produced in one collision and recorded by the detector are considered to belong to one event. Quantum mechanics predicts production of particles with certain probability, but averages of various parameter distributions can be used to reproduce these probabilities. In this way, Monte Carlo event generators use pseudo random numbers to reproduce the quantum mechanical probabilities of event outcomes. They generate complete particle content for each event, and estimate the total cross-section for a selected production.

In this section a detailed description of the Pythia [159] MC generator will be given, which was used in the SUSY signal event generation since it has an implementation which can handle 3-body decays which occur in the NUHMG model studied in this thesis. Background event generation was performed using various MC generators, and some of their characteristics will be compared at the end of this section.

7.3.1. Signal Event Generation

In order to produce an event in a MC generator, the physics event can be modeled in somewhat independent stages. The building of an event in the generator can be done in sequential steps, where in each step more complexity is added to the event. Each event ends with hundreds of outgoing particles with around ten degrees of freedom, e.g. mass, momentum, production vertex, lifetime. The aim of MC generators is to have a good description of relevant parameter distributions, and the size of their

fluctuations. In this section the MC event generation with Pythia MC generator, which was used in signal event generation, will be described as in [159, 160].

A p-p collision can be represented in couple of stages, see figure 7.1. Two hadrons on a collision course first produce a hard process (e.g. $u\bar{d} \to W^+$ in SM or $gg \to \tilde{g}\tilde{g}$ in BSM). Some events produce relatively short-lived particles like t, $W^{\pm}$ or Z^0, so together with their decay products are considered as part of the same process, because their correlations are propagated from the production to the decay stages (e.g. spin correlation). This event topology can be obtained by the matrix element calculation. Since bremsstrahlung occurs with the accelerated color or EM charge of the incoming partons, emissions called Initial State Radiation (ISR) on the two incoming partons are formed. Also, emissions from the outgoing particles occur, called Finite State Radiation (FSR). Additionally, more partons from the incoming hadrons might produce an interaction within the same collision. They are called Multiparton Interactions (MPI) and produce their ISR and FSR as well. Beam remnants, the partons which do not undergo an interaction, take away much of the input energy and continue to travel in the original direction. Also, they carry the color taken away by the colliding partons.

With the produced particles propagation, the confinement becomes strong, so the structure and evolution of the formed field needs to be modeled, since this QCD problem is too complicated to be calculated from the first principles. It is assumed that for each color there is a separate confinement field between color and its anti-color (where gluon is considered a sum of color and anti-color, and all colors are distinguishable from each other). These fields can break with the production of a quark-antiquark pair, and by combining can produce a primary hadron, in the process called hadronization. The produced hadrons can be unstable and decay further while some are long-lived and are visible in the detector. At this stage MC generators result can be passed further to the detector simulation programs to obtain a good description of a detected event.

The cross-section for the selected final state is calculated by integrating over relevant phase-space regions which are associated with the hard process, and summed up over subsequent steps (eg. parton showers, hadronization) using probabilities for transition from the hard process to the final state:

$$\sigma_{final\ state} = \sigma_{hard\ process}\ P_{tot,hard\ process \to final\ state}\ . \tag{7.1}$$

Thanks to the modular structure of the physics event calculation, different programs can be used for different parts of the calculation. Also, SUSY model specifications can be calculated by dedicated programs, and passed on to the MC generator with the usage of the Les Houches Accord [155]. However, multi purpose generators are used to calculate the bulk of the event, and specific calculations are included by the usage of external packages. Namely, the hard sub-process matrix element calculation for the SM particles is done by the generator, while for the BSM model (eg. SUSY) particle spectrum, decay widths and branching ratios have been calculated with the external package. These are combined and used further for the process

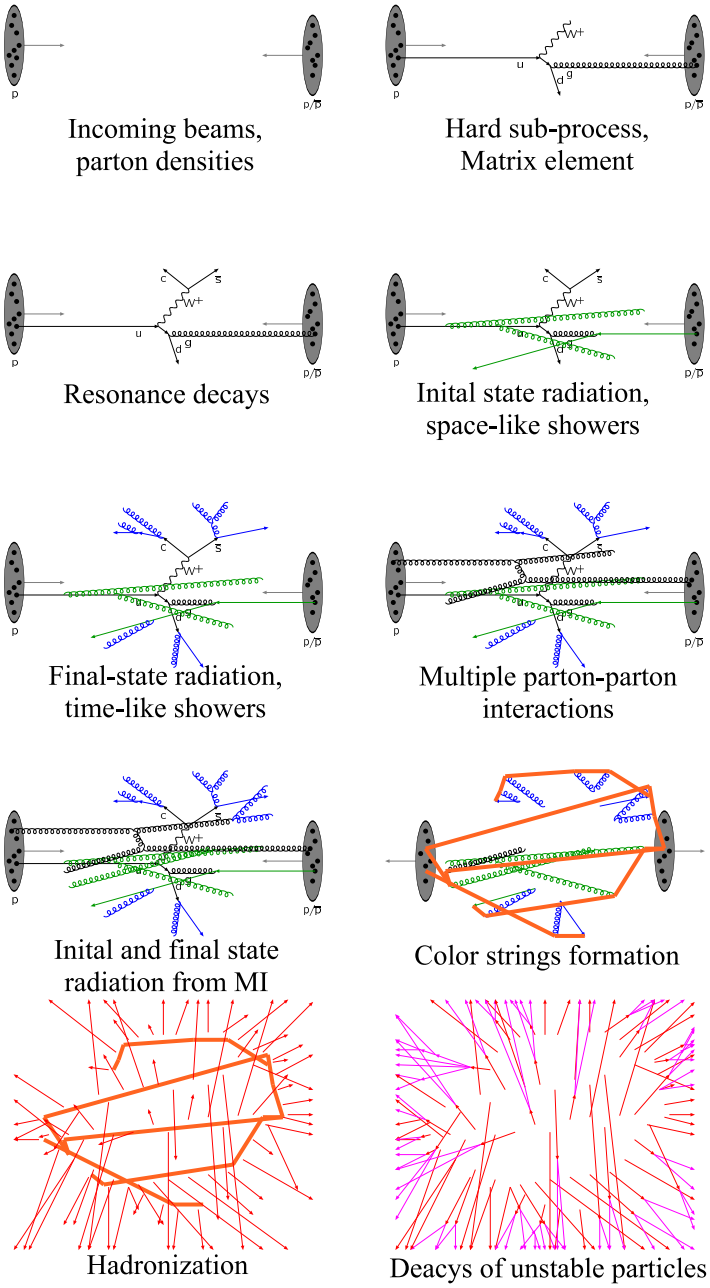

Figure 7.1.: PYTHIA, the multi purpose event generator, performs calculation through consecutive steps, [161, 162]. First the incoming p-p beams properties are determined using parton densities. Next, the hard sub-process is calculated using matrix elements, and the initial and final state radiation are added. Then the multiple parton-parton interactions with their initial and final state radiation are calculated. Finally, the color strings are formed, the hadronisation and the decays of unstable particles are calculated.

selection and resonance decays. Next, the parton showers, MPI and beam remnants calculations can be calculated using the external libraries for different PDF sets, like LHAPDF (Les Houches Accord Parton Density Functions library [163]. The hadronization and final decays of unstable particles can be refined by using external programs. In this thesis, the general purpose generator PYTHIA [159] is used with external packages for τ decays TAUOLA [164] and photon QED radiative corrections PHOTOS [165].

7.3.2. Background Event Generation

There is a number of MC generators that can be used for the background event generation. In practice for each SM contribution, the MC-data agreement is checked for a dedicated selection, usually targeting one dominant SM process. The MC generators used in this thesis include the following:

- SHERPA [166] is distinguished from other MC generators by performing automated merging of leading-order matrix elements (ME) for multijet production together with parton showers (PS). It provides two independent matrix element generators for the case of large final state multiplicity for a number of models. It treats infrared divergent structures in NLO QCD corrections, and it treats matching of parton showers with NLO matrix elements in an automated way. In this thesis it is used for bulk MC production of W+jets, Z+jets and γ+jets processes, with up to 4 extra partons in the final state, as it is a multi-parton ME+PS generator which includes hadronization.

- ALPGEN [167] is a new event generator dedicated for multiparton hard processes in hadronic collisions. It performs at LO for QCD and EW interactions, calculates the exact matrix elements for a large set of parton-level processes for Tevatron and LHC. Events at parton-level have the full information on the color, flavor structure, which allows for evolution of partons to the fully hadronized states. In this thesis it is used for W+jets, Z+jets and γ+jets processes for the systematic uncertainty determination related to theoretical uncertainties, in the event generation with up to 5 partons. It can be used for multi-parton bulk event production, with an interface to multi purpose generators like Pythia, HERWIG++ for PS and fragmentation.

- POWHEG-BOX [168] is a Positive Weight Hardest Emission Generator, which performs NLO accuracy calculation with parton shower event generation, following the POWHEG method. It is used in MC generation with extra event complexity. In addition, it contains a library of previously included processes, which enables faster event generation. All modern shower MC programs that support Les Houches accord [169] have an interface to it. In this thesis it is used for $t\bar{t}$ event generation with an interface to Pythia MC generator for parton showering. It is also used as a secondary MC event generator for systematic uncertainty determination for processes of W+jets, Z+jets and γ+jets.

- HERWIG++ [170] has an implementation which includes parton shower modeling including coherence effects, detailed model of underlying event, several processes at NLO accuracy, number of BSM models simulations including spin correlations and detailed hadron and tau decays. It is well suitable for signal event generation in the analysis with 2-6 jets and missing transverse energy, but the NUHMG model event generation was performed using Pythia as it supports the typical 3-body decay at the end of the decay chain.

- MC@NLO [171] is based on HERWIG and HERWIG++ MC generators, where it combines the MC event generation at NLO accuracy in rates for QCD processes. It allows the NLO QCD matrix elements consistently into a parton shower framework. It is suitable for MC generation of events with extra complexity. Processes include hard production of single vector and Higgs bosons, vector boson pairs, heavy quark pairs, single top in association with W or Higgs in type I or II 2HDM models, pairs of leptons, and Higgs in association with W or Z. It includes spin correlations, except for the ZZ process. In this thesis it is used for single t s-channel production, interfaced to HERWIG++ MC generator for PS modeling. It is also used as a secondary MC event generation for $t\bar{t}$ processes for the systematic uncertainty determination related to theoretical uncertainties.

- MADGRAPH5 [172] has a fully staged simulation chain implementation for multi-jet production and merging. It has interfaces to automatic computation of loop amplitudes, combination of real corrections, and automatic interface via the MC@NLO method to HERWIG++ and Pythia parton showering and hadronization. It is able to generate multi-leg events at the NLO accuracy for any process in various models, and typically it is interfaced to PS MC generators like Pythia. In this thesis it is used for $t\bar{t}$ with electroweak boson and jets event generation, interfaced to Pythia for PS.

7.4. Monte Carlo Event Simulation

In order to get a realistic description of the event in the detector, the event simulation and digitization is performed. In ATLAS the GEANT4 [173] simulation toolkit is used for events generated by the dedicated event generator, and a faster parametrized event simulation using the ATLFAST-II [174] simulation. A detailed implementation of all detector components and material budget is included in the Athena framework.

GEANT4 is a toolkit which simulates the passage of particles through matter, where simulation of charged particle tracks in the inner detector and muon spectrometer, and particle showers for e.g. electrons and jets in the calorimeter system are simulated. It includes a wide range of functionality for detector geometry description, tracking, physics models and hits in the detector. It has been designed to enable complex detector geometry consideration. Physics processes include wide

range of electromagnetic and hadronic processes, and cover energy range up to TeV range.

In the Athena implementation of the ATLAS detector using GEANT4, the following aspects were considered for simulation. The detectors geometry, materials, particle interactions with the detector components inside the electromagnetic fields, tracking of particles through the detector material, response of detector components, digitization and hit management, generation of event and track data, and storage of event information.

The event simulation is performed in stages, where GEANT4 classes are used:

- **Event** represents the main unit of the simulation, which is used to store information for processing down the simulation chain. In data taking, an event is a unit which contains the collision products, starting from the primary vertex to the full detector response of particles passing through the detector. In simulation it contains the primary vertexes and primary particles as input, and as a result after full simulation process, it contains generated hits and digitization, and trajectories of simulated particles.

- **Geometry and Representations** are used to describe the geometrical structure of the detector, for the passage of particles through it. In the experimental setup, detectors are designed to enable particle detection using their properties and interaction with the detector components. Sophisticated analyses are set in place to determine the optimal size and materials while designing the detector, but also large number of events of particles passing through the detector need to be generated in order to optimize physics analyses. The geometry is represented via logical volumes of simple shape, which can be arranged in repetitive patterns, with larger structures holding smaller within. The more complicated detector volumes are represented via smaller simple volumes connected via bounding surfaces, the boundary representations.

- **Tracking of GEANT4** is a simulation implementation which takes each particle and 'transports' it step by step to the next position. The passage of particles through the detector volume can be modeled in stages. The physics processes associated with the particle propose the next step. There are three types of physics processes implemented. First, for a particle at rest (e.g decay at rest), second, energy loss or secondary particle production that happen continuously (e.g. Cherenkov radiation), and third, the final step (e.g. secondary particle production by decay or interaction).

- **Physics** processes in GEANT4 include **electromagnetic** and **hadronic** processes. The physics process which occur in a collision and in interaction of outgoing particles with the detector components can be modeled in stages. The particle decay step length is calculated from the mean lifetime of a particle. Electromagnetic interactions of electrons, positrons, photons and hadron interactions can be implemented for soft and hard objects independently.

They can include ionization, bremsstrahlung, multiple scattering, Compton and Rayleigh scattering, photo-electric effect, pair conversion, annihilation, synchrotron and transition radiation, scintillation, refraction, reflection, absorption, Cherenkov effect e.t.c. The energy loss for soft and hard muons is calculated separately. Hadronic decay final state generation is implemented using a so called 'Russian doll' approach. A higher sub-level has specifications for the ancestor level in the hadronic shower simulation, where various shower modelings are used.

- **Particles and materials** are used to describe the particle-matter interactions. The interaction of outgoing particles with the detector components is modeled in a sophisticated manner, where different particle properties determine their interaction with the material and dimensions of the detector components. Particles are defined by their properties, where leptons, bosons, mesons, baryons, etc. are considered, with properties like particle mass, charge, etc., list of processes to which they are sensitive to, and cut ranges for different information. The materials of the detector define its properties, where elements, isotopes, or their mixtures are considered, while physical properties for materials are described in a generic way. Characteristics like radiation, interaction length, excitation energy loss, coefficients in the Bethe-Bloch formula, shell correction factors etc. are implemented for elements and isotopes, and their combinations can be derived in a specific GEANT4 implementation.

The details of each detector component and the interactions for all particles are, therefore, implemented for the ATLAS detector design. Then large number of MC events can be simulated in order to get a realistic detector response used in physics analyses. As a last step before reconstruction, the digitization is performed. Full detector response is transferred into a signal, which would be produced by the detector components and read out by the reconstruction software.

Since the computation time of event simulation using GEANT4 represents the most demanding step in the event simulation, in ATLAS it is often replaced by the ATLFAST-II [174] event simulation. Here the particle showers in the calorimeters are used in a parametrized implementation, which reduces the long computation time. The obtained distributions using the ATLFAST-II are compared to the GEANT4 simulation, and when good agreement is achieved, full simulation using GEANT4 can be replaced by the ATLFAST-II fast simulation.

7.5. Event Reconstruction

The reconstruction of objects like electrons, muons, taus, jets, b-jets and missing energy is performed for MC and data using the same software. The objects are reconstructed using sophisticated algorithms. In the figure 7.2 the electron, muon and $E_{\mathrm{T}}^{\mathrm{miss}}$ reconstruction efficiency and the jet energy scale uncertainty using the 8 TeV 2012 data is shown. It can be seen that high reconstruction efficiency is

achieved for all objects and that the fractional jet energy scale uncertainty is at the percent level. This shows a very good performance of both, the MC event generation and data reconstruction, and gives good confidence in the MC predictions and the ATLAS detector performance. Details for object reconstruction used in this thesis will be given in this section. More details about vertex reconstruction and overlap removal procedures used in ATLAS can be found in [175].

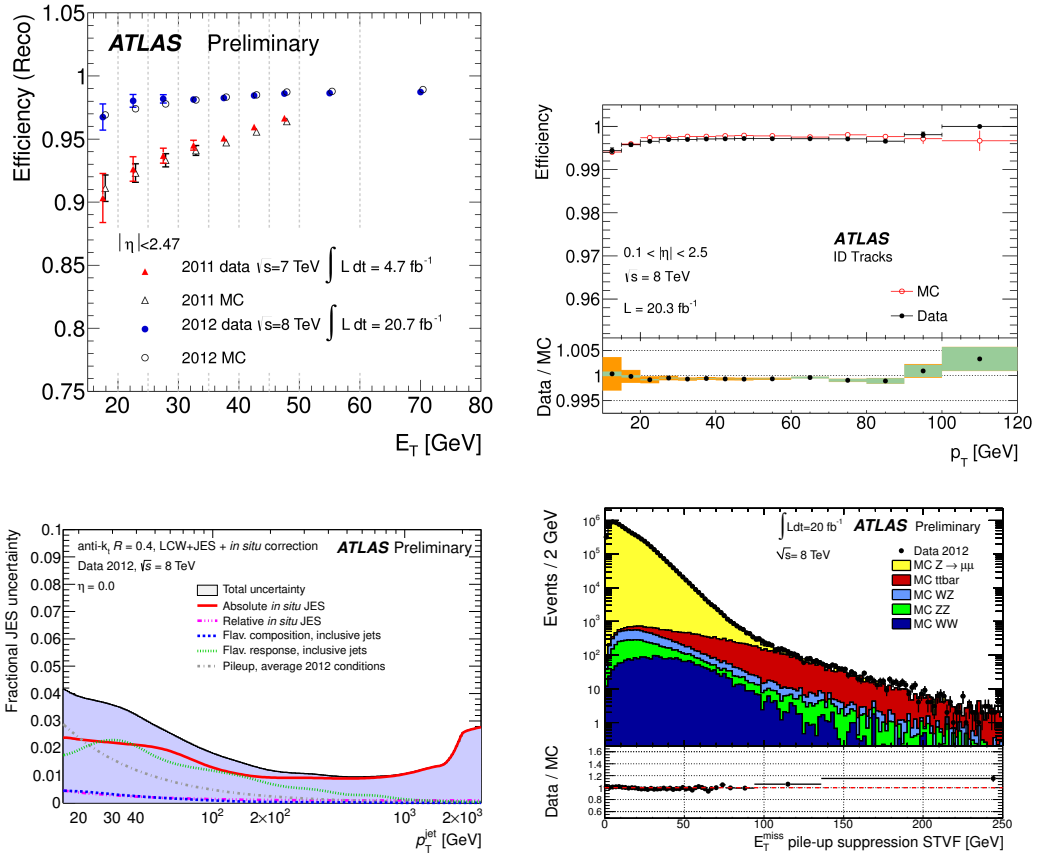

Figure 7.2.: Electron (a) [176], muon (b) [177] i $E_{\mathrm{T}}^{\mathrm{miss}}$ (c) [178] reconstruction efficiency, and jet energy scale uncertainty (d) [178] for 8 TeV 2012 ATLAS data. The muon reconstruction efficiency shown for inner detector muons. $E_{\mathrm{T}}^{\mathrm{miss}}$ shown for after pile-up suppression. Fractional jet energy scale as a function of anti-kt jets p_T with R=0.4 calibrated using LCW+JES calibration scheme, for average pile-up conditions.

In increased instantaneous luminosity conditions, there is a higher number of inelastic pp interactions per bunch crossing, i.e. there is pile-up. The mean number

of inelastic interactions per bunch crossing $\langle\mu\rangle$ is given by:

$$\langle\mu\rangle = \frac{L \times \sigma_{inel}}{N_{bunch} \times f_{LHC}} \tag{7.2}$$

where L is the instantaneous luminosity, σ_{inel} is the total inelastic pp cross-section, and $N_{bunch} \times f_{LHC}$ is the average frequency of bunch crossing in the LHC [179]. Therefore, for higher instantaneous luminosity, the $\langle\mu\rangle$ increases. The pile-up is present in events in two ways. First, in the triggered event additional interactions are present in the same bunch crossing, i.e. in-time-pile-up. Second, multiple interactions are present in the neighboring bunch crossings, i.e. out-of-time-pile-up. This brings to distortion of signals in electromagnetic and hadronic calorimeters, and corrections for this effect need to be set in place, in particular in the electron and jet reconstruction.

7.5.1. Electron Reconstruction

Electron reconstruction in the range $|\eta|<2.47$ of the ATLAS detector will be considered here [176]. It takes clusters of energy deposited in the EM calorimeter and associates them to the reconstructed tracks of charged particles in the inner detector (ID) in the following way:

- **Seed clusters** are reconstructed from the calorimeter towers of a size 0.025×0.025 in η and ϕ placed longitudinally in the detector. Then the so-called sliding algorithm, of a window size 3×5 calorimeter towers, scans over the calorimeter volume and identifies the so-called seed clusters with a minimum transverse energy of 2.5 GeV.

- **Electron track candidate** is reconstructed in the ID using the standard ATLAS track reconstruction algorithms [180]. The tracks are extrapolated to the middle layer of EM calorimeter, and matched to the seed clusters. For tracks additional requirements are placed on the angular distance between the extrapolated track and EM cluster to have $|\Delta\eta|< 0.05$, and $\Delta\phi< 0.1$ in the bending direction of the track, to account for bremsstrahlung loss, and $\Delta\phi<0.05$ in the opposite direction. The tracks with hits in the silicon detector and smallest value of $\Delta R = \sqrt{\Delta\eta^2 + \Delta\phi^2}$ are preferred.

- **Electron candidate** is reconstructed by forming the electromagnetic cluster from the track-matched seed using the 3×7 and 5×5 blocks of longitudinal calorimeter towers in barrel and end-cap respectively. The electron energy is calculated from the energy deposits in the cluster cells, with corrections for the energy loss upstream of the calorimeter and for lateral and longitudinal leakage. The electron direction is determined from the η and ϕ directions of the reconstructed ID track at the vertex position.

- **Electron identification** is performed by placing additional criteria to increase the fraction of true signal electrons and reject background from photon conversions, pion decays and hadronic jets faking an electron. There are several selection criteria used for the electron, labeled with 'loose', 'medium' or 'tight'. They include cuts on electron identification variables which describe the hadronic leakage, track quality, track-cluster matching and number of hits in detector layers. In order to account for pile-up, which occurs in high instantaneous luminosity conditions, additional tighter selection criteria are applied, which are labeled with '++'. In pile-up conditions, due to higher overall energy deposition in the event, shower shapes get distorted. The selection criteria are adjusted, where looser selection is performed on the pile-up sensitive variables, and tighter cuts are applied on the other variables, such that the reconstruction efficiency is constant for changing number of primary vertices.

In this thesis the electron reconstruction was used for the lepton selection or a lepton veto. In a similar way to electron reconstruction, the photons are reconstructed using the seed clusters in the EM calorimeter, which have no associated tracks.

7.5.2. Muon Reconstruction

Detector information from the muon spectrometer (MS) and inner detector (ID) is used for the muon reconstruction. MS enables large eta coverage up to $|\eta|$=2.7. The ID provides independent measurement of the muon track in the region close to the interaction point (IP). There are four different types of muon identification [177]:

- Stand-Alone (SA) muons. The muon track is reconstructed only form the MS information, they are mostly used to extend the acceptance of the ID in the region $2.5 < |\eta| < 2.7$. At least two track segments in different layers of MS are sufficient to obtain the muon track. The parameters of the muon track at the interaction point are obtained by extrapolating the muon track to the point of closest approach to the beam line, while energy loss of the muon in the calorimeters is taken into account.

- Combined (CB) muons. The muon track is reconstructed for MS and ID track segments independently, and a combined track is constructed for a successful combinations. This type of muon identification has the highest muon purity.

- Segment-tagged (ST) muons. The ID muon track is extrapolated to MS and accepted if there is at least one hit in the MDT or CSC detector. It is used to increase the acceptance of the tracks in the MS.

- Calorimeter-tagged (CaloTag) muons. A track in ID is identified as a muon if its particle energy deposition in the calorimeter can be associated with a minim ionizing particle. They are optimized for $|\eta| < 0.1$ and $25 \leq p_T \leq 100$ GeV.

In order to combine muon tracks from MS and ID the implementations of MUONBOY, STACO and MuTag algorithms [181] were developed. The MUONBOY uses stand-alone muons from the RPC and TGC η and ϕ regions, and local track segments are reconstructed. Next, the track segments are combined to form track candidates, and a global track fit is applied through the full MS to determine the track parameters. Then the track is extrapolated to the beam line, and additional corrections to the energy loss in the calorimeters are added. The STACO algorithm performs a statistical combination of tracks measured separately in MS and ID. It has a good momentum resolution and enables muon rejections from secondary interactions. The MuTag taggs ID tracks not used by the STACO algorithm for a requirement of a track segment match in the MS. It recovers muons with low p_T which can be detected only by the ID inner layers. In this thesis the STACO muons were used for the lepton selection or a lepton veto.

7.5.3. Tau Reconstruction

Tau lepton, due to its high mass, is the only lepton that can have decays into both, leptons ($\mathrm{Br}(\tau \to e\nu_e\nu_\tau) = 17.8\%$, $\mathrm{Br}(\tau \to \mu\nu_\nu\nu_\tau) = 17.4\%$) and hadrons (64.8 %, predominantely into one or three $\pi^{\pm}$, a ν and posibly additional π^0, and with 2.9% into kaons) [182, 183]. Due to its short lifetime, the proper decay length is very short, and decay is inside the beam pipe. Therefore, they can be identified only using their decay products. The hadronically decaying τ_{had} lepton reconstruction considers two classes of decays with respect to a number of charged decay products which leave tracks in the detector, i.e. 'prongs'. These are 1-prong decays (49.5%) and 3-prong decays (15.2 %), where percentage is given relative to all τ decays. The leptonically decaying τ leptons are very hard to deistinguish from prompt e or μ. Therefore, τ identiffication is perfomred using its hadronic decays.

The hadronically decaying τ has a very similar signature to jets from a q or g, but they can be distinguished using their 1 and 3-prong signature, relatively narrow clustering of tracks and energy deposited in the calorimeters. Additionally, the 1-prong τ decay can be mis-identified as e or μ, and they are distinguished using various methods for their separation from QCD jets. Additional refinement to the τ identification is done to account for the conditions of high pile-up.

In this thesis a p_T-correlated track counting algorithm has been used for τ identification. It uses inner detector information for track reconstruction, where additionally charge of tracks and their collimation are considered, and calorimeter information on energy depositions of visible τ decay products. τ leptons have narrow showers in the electromagnetic calorimeter, and for 1-prong decay they contain one or a few π^0, which bring large yields in the calorimeter. The algorithm requires a narrow calorimeter cluster to match the track(s).

The reconstruction and identification of the visible decay products of a τ lepton, i.e. τ_{had_vis}, is performed in a few steps. First, each jet is considered as τ_{had_vis} candidate, and their kinematic properties are calculated. Second, tracks which satisfy selection criteria are associated to clusters, and the kinematic properties of tracks

associated to jets are calculated. Third, the calculated variables are combined into a multivariate discriminant which is used to reject QCD jets and electrons. In the analysis, τ_{had_vis} candidates are selected using the output discriminant for a required background rejection and signal efficiency.

7.5.4. Jet Reconstruction

In MC event generation, definitions of parton level and particle level jets were used, while in the reconstruction, which is used on the data and simulated and digitized MC, the detector level jets are used. Parton level jets at the end of the shower are the final state particles from the hard scattering process that develop into jets. The particle level jets consist of stable particles after the fragmentation and hadronization. The detector level jets are calculated using the energy deposition in the detector of stable particles.

The jet reconstruction can be performed in two ways [184,185], using calorimeter towers or topological calorimeter clusters, i.e. topoclusters. **Calorimeter towers** represent regions in η and ϕ where the energy deposition in calorimeter cells is summed up in radial direction. **Topoclusters** are formed around the seed calorimeter cell that has a large excess of energy compared to the expected level of noise. The neighboring cells with energy higher than the expected level of noise, using a lower threshold, are grouped with the seed cell. The resulting topojet represents a three dimensional object which consists of calorimeter cells. In this thesis topocluster jets reconstructed with Anit-k_T algorithm are used.

The **Anti-k_T** jet reconstruction algorithm [186] is based on topoclusters, and performs sequential clustering, i.e. it adds clusters in an iterative way. The algorithm uses distances between topoclusters in the event and merges the closest ones. The distance between two topoclusters i and j, and a topocluster i and beam B, are defined as:

$$\begin{aligned} d_{ij} =& min(k_{ti}^{2p}, k_{tj}^{2p}) \frac{\Delta_{ij}^2}{R^2} \\ d_{iB} =& k_{ti}^{2p} \end{aligned} \tag{7.3}$$

where the k_{ti} and k_{tj} are the transverse momenta of objects. The $\Delta_{ij}^2 = \Delta y_{ij}^2 + \Delta\phi_{ij}^2$ is the radial distance between two objects with rapidity and azimuthal angle differences Δy_{ij}^2 and $\Delta\phi_{ij}$. The R is the user defined radius parameter of the algorithm, and for the Anti-k_T algorithm p = -1. The algorithm performs in an iterative way. First a list of topocluster distances d_{ij} is prepared, and the topoclusters with a smallest distances are merged. The list is remade, and the merging is repeated until $d_{iB} = k_{ti}^{2p}$ is the smallest distance. The merged object is called a jet, and removed from the list. The Anti-k_T algorithm is infrared and collinear safe, i.e. the result is unaffected by emission of soft particles and splitting of a jet into two close by jets respectively.

Initially the energy of reconstructed jets is measured using the electromagnetic scale, i.e. the default energy scale of calorimeters calibration. However, the jet en-

ergy needs to be corrected using a p_T and η dependent calibration scheme, called the EM+JES scheme, for the lower energy response in the hadronic calorimeters. This calibration is obtained using the comparison of MC simulated truth jets with reconstructed jets. The corrections for pile-up interactions and primary vertex position are included as well [187].

Jet reconstruction is in particular sensitive to the effect of pile-up, and the pile-up correction for jets in ATLAS is performed using the so-called jet area method [179]. Namely, particles associated with a jet are placed in a large area of the detector, and pile-up interactions can overlap with the jet. For a larger jet area, the effect of pile-up is stronger. In addition, the pile-up contributes to a larger jet multiplicity in the event. Therefore, corrections are estimated using the jet-by-jet sensitivity to the pile-up and event-by-event pile-up activity.

7.5.5. b-jet Tagging

Tagging of b-jets represents a powerful tool for separation of e.g. $t\bar{t}$ background from other SM processes, because $BR(t \to Wb) \sim 1$ and one b-jet is expected from each t quark decay. The b-jets originate from b-quarks, and they can be distinguished from the light and c-jets, using the b-jet topology where a secondary vertex is present inside the b-jet. It originates from the b-hadron decay, produced in the process of fragmentation, which has a decay length 0.5 mm before the decay. The c-jet in a similar way contains a c-hadron. In order to distinguish a b-jet from a c-jet, a shorter mean lifetime of the c-hadron and the p_T spectra of the decay products are used, where heavier b-hadrons produce decay products with higher p_T. In addition, some b-tagging algorithms make use of further decay of the b-hadron due to electroweak interactions, which brings to a transition of the b-quark into a c-quark, which has a weak decay, producing a tertiary vertex.

A number of algorithms for b-jet tagging have been developed in ATLAS [188, 189].

- IP3D is a impact parameter based algorithm. It makes use of the secondary vertex topology, where the likelihood ratio algorithm computes the compatibility of a given jet with a b-jet and a light jet hypothesis, using the transverse and longitudinal impact parameters of the tracks associated with the jet.

- SV1 is a secondary vertex based algorithm. It makes use of the reconstructed decay products of the b-hadron and possible c-hadron from a tertiary vertex, a so called inclusive vertex. It looks for pairs of tracks associated to a jet, with a distinguished vertex sufficiently far from the primary vertex. Tracks from all good vertices are combined into one inclusive vertex, then the tracks are removed in an iterative procedure until the best χ^2 test is achieved for a inclusive vertex. Then the properties of the inclusive vertex, like decay length, invariant mass of the tracks associated to the inclusive vertex, and the tracks energy and topology, are used to compute the b-tagging weights using the likelihood ratio technique.

- JetFitter is a tertiary vertex based algorithm. It exploits the topology of the secondary and tertiary vertex of a b-jet. The Kalman filter is used to reconstruct the flight of the b-hadron and following c-hadron from the primary vertex. With the reconstructed primary and secondary vertex, their properties are further used to obtain the b-jet weights, where likelihood ratio technique is used to distinguish b, c and light jets.

- MV1 is a multi-variate based algorithm. It combines outputs of simpler algorithms, and obtains b-jet weights using multivariate techniques. First the IP3D and JetFitter outputs are used to obtain a discriminator using Artificial Neural Networks (ANN) in a JetFitterCombNN algorithm. Then MV1 uses tagging weights for b-jets of the IP3D, SV1 and JetFitterCombNN algorithms, and obtains a stronger discriminating performance compared to individual algorithms.

MV1 tagger is used for b-tagging in this thesis.

7.5.6. Missing Transverse Energy

The $E_{\mathrm{T}}^{\mathrm{miss}}$ reconstruction [190] [178] is based on using energy deposition in calorimeters and reconstructed muons. The calculation uses reconstructed and calibrated physics objects. The **calorimeter** energy deposit can be calculated in two ways. First is the cell-based way, where the energy deposits of individual calorimeter cells are summed up. Second is an object-based way, where the energy deposits of calorimeter cells associated with the physics objects using their calibration, are summed up. The second approach is used in this thesis. The **muon** energy deposit is calculated using the muon reconstruction as explained in the subsection 7.5.2. In addition, deposits not associated with any reconstructed and identified object are included in the calculation.

The $E_{\mathrm{T}}^{\mathrm{miss}}$ is calculated as a negative sum of calibrated reconstructed objects x and y projections as:

$$E_{x(y)}^{miss} = E_{x(y)}^{miss,e} + E_{x(y)}^{miss,\gamma} + E_{x(y)}^{miss,\tau} + E_{x(y)}^{miss,jets} + E_{x(y)}^{miss,SoftTerm} + E_{x(y)}^{miss,\mu} \quad (7.4)$$

where the summed up objects are reconstructed in a specified order as: electrons, photons, hadronically decaying τ, jets, energy not associated with any object, i.e. soft term, and finally muons. The soft term is calculated using only the energy deposits from topoclusters. To avoid double counting of energy deposits if the combined muon is used, the parametrized muon energy loss in the calorimeters is subtracted from the $E_{\mathrm{T}}^{\mathrm{miss}}$ calculation.

Each term based on calorimeter information is calculated using x and y projections

for each cell energy deposition as:

$$E_x^{miss,term} = -\sum_{i=1}^{N_{cell}^{term}} E_i \sin\theta_i \cos\phi_i$$
$$E_y^{miss,term} = -\sum_{i=1}^{N_{cell}^{term}} E_i \sin\theta_i \sin\phi_i \tag{7.5}$$

where i runs over all cells associated with specified objects in $|\eta| < 4.5$, E_i is the cell energy, θ_i is the polar and ϕ_i azimuthal angle of a given cell. The remaining muon term is calculated from muon momentum of tracks reconstructed in $\eta < 2.7$ as:

$$E_{x(y)}^{miss,\mu} = -\sum_{muons} p_{p(y)}^{\mu}. \tag{7.6}$$

Then the final $E_{\mathrm{T}}^{\mathrm{miss}}$ is calculated as:

$$E_{\mathrm{T}}^{\mathrm{miss}} = \sqrt{(E_x^{miss})^2 + (E_y^{miss})^2} \tag{7.7}$$

for missing energy in the x and y direction.

7.6. NLO and NLL Cross-Section Calculation

MC events need to be produced in the amount which occurs the experimental data, therefore a good cross-section calculation is needed in the analysis. MC events for a given physics process are generated in a size that is reasonable to obtain technically, so weighting of the generated samples according to the channel cross-section has to be introduced in order to have their right amounts. For a SUSY model cross-section calculation, one has to use a dedicated NLO cross-section calculator. In this thesis, the PROSPINO 2.1 cross-section calculator (PROduction of Supersymmetric Particles In Next-to-leading Order QCD) [114, 191] has been used. The most recent version has the processes of $\tilde{\chi}^0/\tilde{\chi}^{\pm}$ and $\tilde{l}$ [192], $\tilde{\chi}^0/\tilde{\chi}^{\pm}$ and $\tilde{g}$ [193], $\tilde{\chi}^0/\tilde{\chi}^{\pm}$ and $\tilde{q}$ /$\tilde{g}$ [194], $\tilde{q}$ and $\tilde{g}$ [195], and pairs of $\tilde{t}$ /$\tilde{b}$ [196] production channels cross-section calculation included. The sparticle masses are read from the input Les Houches file, parton densities can be linked to the program for a user provided collider choice.

The program calculates the differential cross-sections in transverse momenta and pseudorapidity of the outgoing particles for a selected production channel, and its LO and NLO cross-section. Also, it provides the K-factor ($K = \sigma_{NLO}/\sigma_{LO}$) and uncertainties for different production channels. In this thesis the R-parity conserving models are considered, therefore, SUSY particles are produced in pairs. The double-differential cross-section calculated at NLO for outgoing SUSY initial state particles

$\tilde{a}, \tilde{b}$ in the process $pp \rightarrow \tilde{a}, \tilde{b}$) is given as [197]:

$$\sigma_{\tilde{a},\tilde{b}} = \sum_{i,j=\tilde{a},\tilde{b}} \int \mathrm{d}x_1 \mathrm{d}x_2 f_i(x_1, \mu_F) f_j(x_2, \mu_F) \hat{\sigma}_{i,j}(x_1, x_2, \mu_F, \mu_R) \tag{7.8}$$

where $ij = \tilde{g}\tilde{g}, \tilde{q}\tilde{q}, \tilde{g}\tilde{q}, \tilde{t}\tilde{t}, \tilde{b}\tilde{b}, \tilde{l}\tilde{l}, \tilde{\chi}^0\tilde{\chi}^0, \tilde{\chi}^\pm\tilde{\chi}^\pm, \tilde{\chi}^0\tilde{\chi}^\pm$ processes, $x_{i/j}$ are the partonic momentum fraction for the partons i/j, $f_{i/j}$ are the parton density functions for the partons i/j, $\hat{\sigma}_{i,j}$ is the partonic cross-section, and μ_F and μ_R are factorization and renormalization scales respectively. NLO cross-sections have been obtained by summing up of over all production channels for each signal parameter space point. Theoretical systematic uncertainty estimation for PDF and α_S variations have been obtained with CTEQ6.6, according to recommendations in [197].

The $\tilde{q}$ and $\tilde{g}$ hadronic production cross-section can also be calculated with NLO supersymmetric QCD corrections and the resummation of soft gluon emission and Next-to-Leading-Logarithmic (NLL) accuracy. For this the NLL-FAST [195, 198–202] program is used. Using the pre-computed cross-sections and their uncertainties, for a requested sparticle masses and processes, the program performs interpolation to obtain the NLO+NLL accuracy cross-sections. Therefore, this program has a limitation, where cross-sections can be obtained only for present implementations. These include $\tilde{g}$ pair, $\tilde{q}$ pair, $\tilde{q}\,\bar{\tilde{q}}$, $\tilde{q}\,\tilde{g}$, $\tilde{t}$ pair and $\tilde{b}$ pair production for clearly defined ranges. Theoretical systematic uncertainty estimation for PDF and α_S variations are obtained with CTEQ6.6, according to recommendations in [197].

In this thesis the signal cross-sections have been calculated at NLO+NLL accuracy using the NLL-FAST for the signal sparticle masses and processes where available. All other cross-sections have been calculated at NLO accuracy using PROSPINO, according to recommendations in [197].

8. Methods of Statistical Analyses

The HEP experiments are characterized by large amounts of collected data. The data is collected by the detector, the pre-selection is performed using the trigger, and the potentially interesting data is fully reconstructed for the data analysis. In order to perform optimal signal selection from the large background, and to provide good understanding of the significance for a potential new physics yield or lack of it, tools of statistical analyses are used, and their description will be given in this section. The methods often used for optimization of the signal separation using multivariate techniques will be described in the section 8.1. The statistical interpretation of yields after the selection using the background or signal hypothesis will be described in the section 8.2. In order to perform background modeling, various statistical fits are used, and in the section 8.3 details of the combined fit used for the background determination in this thesis will be described.

8.1. Multivariate Analyses and TMVA

In the searches for new physics at the LHC, very often, yields of the BSM physics processes are much smaller than the ones originating from the SM background processes. The differences in kinematic distributions of BSM and SM events are used to extract the signal. Typically, high number of kinematic variable distributions need to be used at the same time. In order to select variables which perform a better signal separation, and to find the optimal selection criteria, multivariate classification methods based on the machine learning are used. In HEP the toolkit for multivariate data analysis TMVA is used [36]. In this section the implementation and usage of TMVA methods in section 8.1.1 will be described. In addition, description of the Rectangular Cuts method used in this thesis will be given in the section 8.1.2.

A number of multivariate classification methods are used in HEP, and many of them are implemented in the C++ ROOT-based analysis framework, called TMVA [36]. These include Projective Likelihood Estimation (PDE), Artificial Neural Networks
(ANN), Support Vector Machine (SVM), Boosted Decision Trees (BDT), Rectangular Cuts etc., and more details about these methods can be found in [36]. All of TMVA methods belong to the family of 'supervised learning' algorithms, see more details in [203]. In this approach, a fraction of the data events are used for 'training', where the signal and background yields are known. Then the signal separation is optimized using multiple variable distributions, and a optimal cut on the resulting function is obtained. The classification is performed on the remaining fraction of the

sample, i.e. 'application' is performed. In practice, all methods need specific tuning for a given MC or data samples and their chosen distributions, in order to obtain optimal classification capabilities, and for this various methods of 'evaluation' for method performance are used.

In HEP there is a number of examples of physics analyses with multivariate techniques. They are used when better separation is obtained compared to simple algorithms or cut and count selection. For the b-tagging in ATLAS a MV1 algorithm [204] is used. It combines the jet tagging weights information taken from a number of relatively simple b-tagging algorithms, using the ANN multivariate method. It uses the information on the impact parameter, secondary vertex, the topology of weak decays of b and c quarks inside the jet, where the Kalman filter is used to reconstruct the primary vertex to the secondary vertex, and additional variables like jet transverse momenta and $|\eta|$. In SUSY searches, a number of analyses are based on multivariate techniques. They use discriminating variables which exploit geometric and kinematic features of SUSY decays, which typically have lots of jets, high transverse momentum, large missing transverse momentum and spherical distribution of outgoing particles. Often the ANN and BDT multivariate methods are used to obtain better signal separation. However, in this thesis, a multivariate technique has been used in an indirect way. Multiple variables were used with a multivariate technique in order to obtain a optimal cut and count analysis.

8.1.1. TMVA Implementation

The machine learning techniques use multiple variable distributions, typically, to construct a sensitive variable on which a cut is applied to make a optimal signal selection. In the analysis, a cut on the newly constructed variable is used. For this reason, the TMVA implementation consists of two classes, the Factory and the Reader, and specific user implementation scripts for training and application of classification are used, see figure 8.1. The tasks of preparation of MC or data samples, defining variables and MVA methods to be used, training of the MVA methods, testing and evaluation of their performance on the fraction of the input samples is done in the Factory. The obtained optimal results of multiple MVA methods can next be used in the Reader, and obtained classification method can be used on the other fraction of the data. The advantage of this implementation is that multiple MVA algorithms can be used at the same time on the same sample, and the results of their optimization can be evaluated and compared.

In order to ensure that optimization using multivariate techniques is not dependent on the chosen MC/data sample, the sample that is used for the optimization, needs to be different from the sample that is used in the separation. Typically, the MC and/or data sample is divided into two or three sub samples. In a simpler approach, the training and evaluation is performed on the fist half of the samples, and application of the classification is done on the second. In a more strict approach, sample is divided into three parts, where first is used for training, second is used for evaluation, and the third is used for classification. In this thesis TMVA is used with

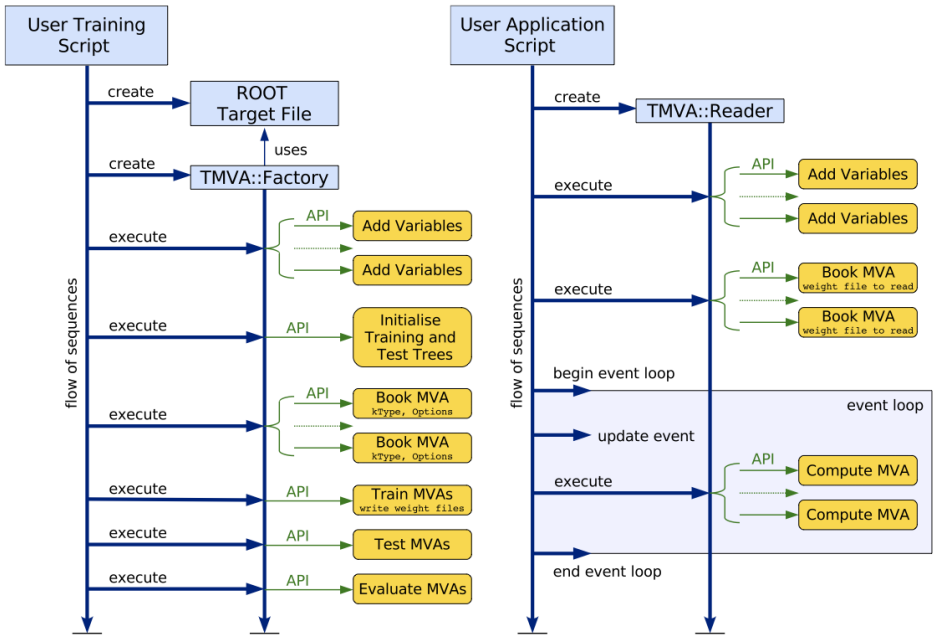

Figure 8.1.: TMVA Factory and Reader class implementation. The user provides a script with specifications for the MVA method and discriminating variables for the training sample. The event weighing, samples distribution preparation is performed. The specified MVA methods are trained, and the result is tested and evaluated by Factory for all specified MVA methods simultaneously. The user also provides a script for the Reader, including used variables and MVA methods, and the event classification is performed for all specified MVA methods simultaneously [36].

MC samples for SUSY signal and SM background, where the training and evaluation is performed on one half of the sample, and classification is performed on the other.

The performance of multivariate techniques can be enhanced by incorporating previous physics knowledge into their usage. For this reason, first the variable distributions of MC/data samples need to be prepared. This is done in the Factory using the event weighting. A number of pre-analyses are performed on the training samples to provide more information for the optimization. For the selected (weighted) kinematic variable distributions the linear correlations are calculated, where strongly correlated variables are not expected to bring improvement in the selection, so some of them can be removed from the analysis. Also, variables can be linearly transformed, projected upon their principal components, or transformed into a normalized Gaussian shape, in order to obtain better results in classification. For some MVA methods, the ranking by the strength of kinematic variable for the signal separation is done, and less sensitive variables can be removed from the analysis.

The performance of used MVA methods is evaluated by comparing their signal

efficiency and background rejection, and the quality of the training. TMVA provides a number of scripts for visualization of these results, in order to select the optimal method and its specifications.

After the MVA method has been optimized and its performance evaluated and compared to other MVA methods, the application on can be performed on the testing sample, where the classification is done by the Reader. The same conditions as specified in the Factory are used, and the results of the MC or data classification can be used for further statistical hypothesis testing in the physics analysis.

8.1.2. Rectangular Cut Optimization Method

In supervised learning techniques, typically, the output discriminating variable is constructed, which is in the function of the input variables for the signal and background samples. Highly complex and powerful algorithms have been developed for the classification. In this thesis the Rectangular Cut Optimization method is used, and its detailed description will be given in this section.

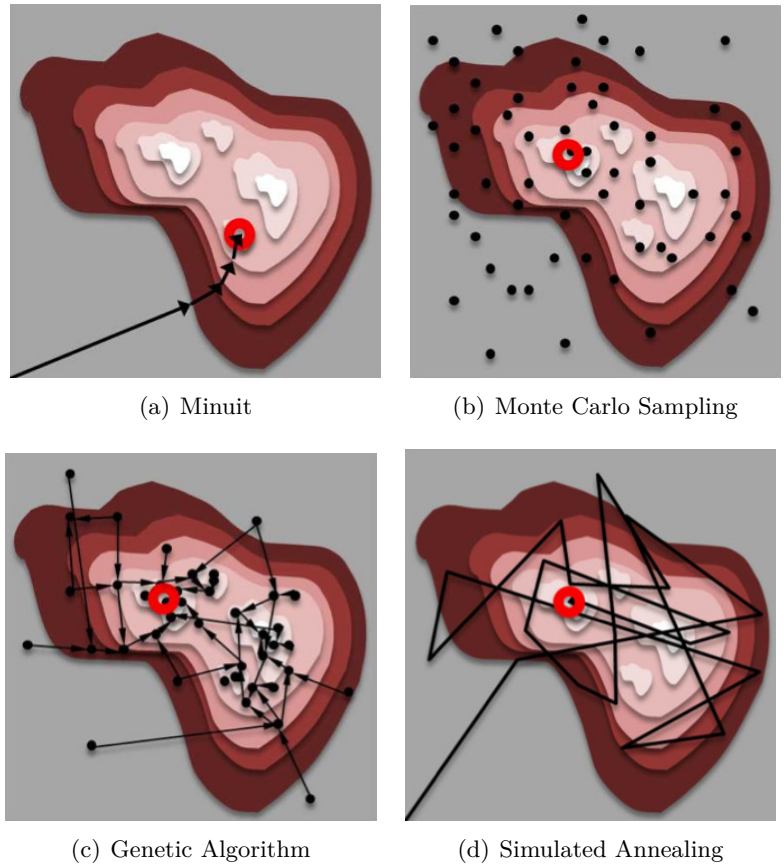

(a) Minuit (b) Monte Carlo Sampling

(c) Genetic Algorithm (d) Simulated Annealing

Figure 8.2.: Minimization algorithms schematic representation [205].

Rectangular cuts optimization method represents the simplest and most commonly used method in signal separation optimization for the cut based physics analyses. This method does not use variable combinations in the optimization as MVA methods, so technically is is not regarded as a MVA technique. However, the result is obtained by using multiple variable distributions for the signal and background samples. The scan on signal efficiency is performed, with maximizing the background rejection. The optimization criteria used is the maximum in significance, defined in TMVA as:

$$Z_A = \frac{\varepsilon_s N_S}{\sqrt{\varepsilon_S N_S + \varepsilon_B N_B}} \tag{8.1}$$

where ε_S,ε_B are the signal and background efficiencies, and N_S, N_B are the signal and background event yields before applying the cuts. The cut ensemble leading to maximum significance is obtained for each working point at the signal efficiency curve. The cut optimization is performed using the multivariate parameter fitters. In this thesis the Genetic Algorithm is used.

In TMVA for the rectangular cut optimization method the Minuit, Monte Carlo Sampling, Genetic Algorithm and Simulated Annealing fitters are available. In the figure 8.2 schematic comparison for reaching a global minimum is presented for these fitters [205]. Minuit has shown to give worse results in finding the global minimum, therefore its usage in Rectangular Cuts optimization is not recommended. Monte Carlo Sampling takes random samples for fitting parameters. It is performing well in finding the global minimum, but at the same time it is highly inefficient. Simulated annealing performs minimization by 'freezing' the states far from minimum, while moving towards states of lower values. It is good in finding the global minimum, but its performance is slower than for the Genetic Algorithm, see more details in [36].

The Genetic algorithm is a minimization algorithm which finds approximate solutions in optimization or finding a minimum. An initial random selection of points in the multidimensional parameter space is chosen. The minimization criteria is evaluated. The worst performing points are discarded, and new points are selected for the next round of evaluation. New points are produced in a random way choosing parameter values between the parameter values of the points successfully passing the minimization criteria. The user defines the number of points at each step of evaluation and the number of evaluation steps. Genetic Algorithm is known to be the one of the best minimization algorithms in finding the global minimum and in the speed of its performance. Therefore, it was chosen as the minimization algorithm for the Rectangular Cuts Optimization used in this thesis.

8.2. Likelihood-Based Tests of New Physics

In particle physics search experiments, results are presented using statistical interpretation, and there are two approaches that can be considered. First is the interpretation of experimental results using Bayesian credible intervals, where prior probability distributions are included in the result. In this way, certain subjectivity

is included into a measurement, e.g. by assuming that some parameters from previous measurements are true. Second is the interpretation using frequentist confidence intervals, which is done purely using statistics, and a hypothesis is tested for data given with theory. In the search for new physics, it is favored that the experimental results are summarized with the frequentist approach. Although these two methods converge for large statistics which is dominated by the signal, frequentist approach needs to be interpreted with care for the case when statistics is small, and signal is small compared to the background.

In order to quantify the statistical significance of a possible observed excess (or lack) of data, the p-value or its equivalent in Gaussian standard deviations, is often used. However, frequentist statistics interpretation may bring to false statements about the signal if the size of background is not considered. For example, for two experiments with the same efficiency and observations, the experiment with larger expected background can quote stronger limits on the physical constant. This can bring to a situation where experiment with largest expected background has better exclusion limit for lower signal rates, than the experiment with higher signal rates, see more details in [206]. In ATLAS the frequentist CL_S technique is used for interpretation of search results, which incorporates the size of the background into the statistical interpretation. In order to show the sensitivity of an experiment to a given analysis, the expected significance is estimated for a number of signal hypothesis.

In this section the formalism of a statistical search will be explained, and definitions of p-value, CL_s and expected significance Z_0 will be given in the section 8.2.1. Recommendations for frequentist limits in ATLAS will be presented in the section 8.2.2. Further details about fits typically used for the background determination in BSM are given in the section 8.3. Detailed description of statistical test and background fit implementation used in this thesis is given in the section 11.7.

8.2.1. Formalism of a Search for New Physics Using a Statistical Test

The frequentist statistical test in the search for new physics phenomena, considers two cases. First is the test for the **discovery** of new physics signal. It tests the null hypothesis H_0 that includes all known processes, i.e. background only hypothesis, against the alternative hypothesis H_1, which includes background plus hypothetical new physics signal processes. Second is the case of **setting limits** if no new physics has been found, where the null hypothesis H_0 now includes signal plus background processes, and the alternative hypothesis H_1 is the background-only hypothesis. Then the agreement of data with the considered hypothesis H is quantified by computing the p-value, which is defined as the probability under assumption of true H, of finding data of equal or greater incompatibility with the prediction of H. The measure of incompatibility can be computed from the number of events found in selected regions of certain distributions, or the corresponding likelihood ratio for signal and background. Then the considered hypothesis is excluded if its p-value is below a certain threshold. It should be noted that in scientific context, the discov-

ery of a new phenomena should not be based only on the statistical rejection of a background only hypothesis. In addition, the plausibility of a new signal hypothesis and a degree of how well it describes the data should be taken into account as well [207].

In HEP the p-value is also expressed in equivalent of significance Z, where for a Gaussian distribution of a variable, for a Z standard deviations above its mean, the upper-tail has a probability equal to p (here the one-sided definition is used where for Z = 0 it is p = 0.5). This can be expressed using the quantile Φ^{-1} of the standard Gaussian, i.e. inverse of a cumulative distribution:

$$Z = \Phi^{-1}(1 - p). \tag{8.2}$$

In the case of a discovery for a signal like the presence of a Higgs boson processes, the background only hypothesis is rejected for significance of at least Z = 5, which corresponds to p = 2.87×10^{-7}. For exclusion of a signal hypothesis, the threshold of p = 0.05 is used, i.e. 95% confidence level, which corresponds to Z = 1.64.

In addition, in HEP it is useful to quantify the sensitivity of an experiment, by computing the **expected significance** for a number of signal hypotheses, which would be computed for the background-only H_0 hypothesis expectation, under the signal process assumption H_1.

Profile Likelihood Ratio Test

A common procedure in HEP for testing a hypothesis is based on a frequentest significance test approach, using a **profile likelihood ratio** test. Here the input parameters are the counts of the processes. In addition, the **nuisance parameters** coming from the uncertainties on the modeling of the signal and background are included as input. In the following the profile likelihood ratio test formalism will be shown using an experiment where kinematic variables are measured for each event. The measured kinematic distributions will be presented using binned histograms, where an unbinned formalism can be derived as an extension to the binned approach.

For each event in the signal sample the measured variable x can be presented in a histogram of counts in N bins $\mathbf{n} = (n_1, ..., n_N)$, where the expectation value for counts in i-th bin n_i using the signal and background can be written as:

$$E[n_i] = \mu s_i + b_i \tag{8.3}$$

where μ is the **strength parameter** of the signal process. The $\mu = 0$ represents a background only hypothesis, and $\mu = 1$ is the nominal signal hypothesis. The mean number of entries in the i-th bin for signal and background are:

$$s_i = s_{tot} \int_{bini} f_s(x, \theta_s) dx \tag{8.4}$$

$$b_i = b_{tot} \int_{bini} f_b(x, \theta_b) dx \tag{8.5}$$

where $f_s(x, \theta_s)$ and $f_b(x, \theta_b)$ are the probability density functions of the variable x for signal and background. θ_s and θ_b represent sets of parameters that characterize the shapes of pdfs, $s_{tot} = N_S \varepsilon_S$ and $b_{tot} = N_B \varepsilon_B$ are the total mean number of signal and background events for their respective event yields N_S, N_B and efficiencies ε_S, ε_B. The integrals represent the probabilities of finding a signal or background event in the i-th bin. In the following all nuisance parameters will be denoted by $\theta = (\theta_s, \theta_b, b_{tot})$, as they are all adjustable, however s_{tot} is fixed to a value predicted by a considered signal model [207].

In order to further constrain nuisance parameters, additional measurements are set in place in control samples, which are designed to be populated mainly by background events. Then the measured kinematic variable can be presented in a histogram with counts in M number of bins $\mathbf{m} = (m_1, ..., m_M)$. The expectation value of counts in i-th bin m_i is:

$$E[m_i] = u_i(\theta) \tag{8.6}$$

where u_i are quantities which depend on nuisance parameters and can be calculated. For example this is used to obtain the normalization parameters for the background to obtain b_{tot} in the signal region, or even obtain signal and background shape parameters [207].

The **likelihood function** L can be presented as a product of Poisson probabilities for all bins as:

$$L(\mu, \theta) = \prod_{j=1}^{N} \frac{(\mu s_j + b_j)^{n_j}}{n_j!} e^{-(\mu s_j + b_j)} \prod_{k=1}^{M} \frac{u_k^{m_k}}{m_k!} e^{-u_k}. \tag{8.7}$$

Further, the **profile likelihood ratio** $\lambda(\mu)$ is used to test the hypothesized value of μ:

$$\lambda(\mu) = \frac{L(\mu, \hat{\hat{\theta}})}{L(\hat{\mu}, \hat{\theta})} \tag{8.8}$$

where $\hat{\hat{\theta}}$ is the value of θ that maximizes the likelihood L for specified μ, i.e. it is the conditional maximum-likelihood (ML) estimator of θ which is in a function of μ, while $\hat{\mu}$ and $\hat{\theta}$ are unconditional maximum-likelihood estimators [207].

It should be noted that in SUSY and Higgs searches, the presence of the signal is expected to manifest as an excess in the data, and consequently the contribution of the signal to the mean number of events is assumed to be non-negative. This implies that all physical estimators for μ must be non-negative. However, it is useful to define $\hat{\mu}$ effective estimator as the value of μ that maximizes the likelihood, including the case $\hat{\mu} < 0$, with a condition that the Poisson mean values stay non-negative $\mu s_i + b_i > 0$. This will allow to model the $\hat{\mu}$ estimator by the Gaussian distribution, which will be used in further test statistics distribution modeling. For

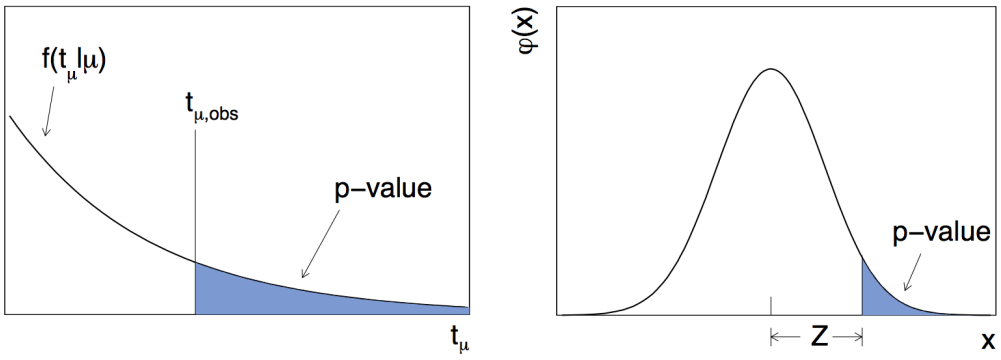

(a) (b)

Figure 8.3.: Test statistics t_μ distribution and p-value (a) and significance Z relation to p-value for the Gaussian distribution $\varphi(x) = (1/\sqrt{2\pi})e^{-x^2/2}$ (b) [207].

this reason, $\hat{\mu}$ will be allowed to take negative values in the following.

Test Statistics t_μ and p-value

From the definition of $\lambda(\mu)$ given in equation 8.8, for good agreement of data and hypothetical value of μ it will be around 1, which brings to $\lambda(\mu) \leq 1$. Due to the request of $\mu s_i + b_i > 0$, it will be $\lambda(\mu) \geq 0$, which brings to $0 \leq \lambda(\mu) \leq 1$. A statistical test for a hypothesized value of μ needs to be performed. This is done by introducing the test statistics t_μ, which is a measure of discrepancy between data and hypothesis, and is defined as:

$$t_\mu = -2 \ln \lambda(\mu) \tag{8.9}$$

where higher values of t_μ correspond to higher disagreement of data and hypothetical μ. In order to quantify the level of disagreement between the data and hypothetical μ, the p-value is computed as:

$$p_\mu = \int_{t_{\mu,obs}}^{\infty} f(t_\mu|\mu) dt_\mu \tag{8.10}$$

where $t_{\mu,obs}$ is the observed statistic in the data, and $f(t_\mu|\mu)$ is the pdf of t_μ under a given assumption of signal strength μ. The relation between the p-value and the observed statistic $t_{\mu,obs}$, and significance Z and p-value are shown in the figure 8.3.

The test statistics t_μ can take low p-values in two cases, distinguished by the relation of estimated signal strength $\hat{\mu}$ and hypothesized value of μ, as $\hat{\mu} > \mu$ and $\hat{\mu} < \mu$. The hypothesized μ values are rejected because their p-values are below a certain threshold α, but they can lie on both sides of not rejected hypothesized μ values. Therefore, two-sided confidence intervals can be obtained for hypothesized value of μ.

Test Statistics $\tilde{t}_\mu$ for $\mu \geq 0$

As explained above, in SUSY and Higgs searches the presence of new signal is expected only to increase the mean event rate on top of expected background. For presence of signal, the hypothesized signal strength is always $\mu \geq 0$. However, $\hat{\mu}$ was allowed to take negative values in order to increase maximum likelihood. This brings to a situation where hypothesized signal strength is $\mu \geq 0$, but estimated signal strength can take values of $\hat{\mu}$ <0. For this case, the best agreement of data and hypothesized value μ occurs for μ=0. Then the profile likelihood and test statistics need to be re-defined as:

$$\tilde{\lambda}(\mu) = \begin{cases} \frac{L(\mu,\hat{\hat{\theta}}(\mu))}{L(\hat{\mu},\hat{\theta})} & \hat{\mu} \geq 0, \\ \frac{L(\mu,\hat{\hat{\theta}}(\mu))}{L(0,\hat{\hat{\theta}}(0))} & \hat{\mu} < 0. \end{cases} \tag{8.11}$$

where $\hat{\hat{\theta}}(0)$ and $\hat{\hat{\theta}}(\mu)$ are conditional maximized likelihood estimators of θ for strength parameter 0 and μ respectively. Consequently, the corresponding test statistic is:

$$\tilde{t}_\mu = -2\ln\tilde{\lambda}(\mu) = \begin{cases} -2\ln\frac{L(\mu,\hat{\hat{\theta}}(\mu))}{L(\hat{\mu},\hat{\theta})} & \hat{\mu} \geq 0, \\ -2\ln\frac{L(\mu,\hat{\hat{\theta}}(\mu))}{L(0,\hat{\hat{\theta}}(0))} & \hat{\mu} < 0. \end{cases} \tag{8.12}$$

The p-value is determined in an unchanged way as in p-value definition 8.10. The $\hat{t_\mu}$ statistics can be determined using approximated statistics distribution, as explained in detail in reference [207]. The μ values excluded by given data set can be above or below $\hat{\mu}$, in a same way as in t_μ case, and they can form two-sided confidence intervals for μ.

Test Statistics q_0 for Discovery of a Positive Signal

An important statistics test $\tilde{t}_\mu$ is a test for the discovery, which is obtained for the case of rejecting the $\mu = 0$ hypothesis. This is done by using the test statistics $\tilde{t}_\mu$ as in equation 8.12 using $\mu = 0$, which is then labeled q_0, where $q_0 = \tilde{t_0}$ and:

$$q_0 = \begin{cases} -2\ln\lambda(0) & \hat{\mu} \geq 0, \\ 0 & \hat{\mu} < 0. \end{cases} \tag{8.13}$$

Consequently the p-value is computed as:

$$p_0 = \int_{q_0,obs}^{\infty} f(q_0|0)dq_0 \tag{8.14}$$

where $f(q_0|0)$ is the pdf of the q_0 statistic under assumption of background-only hypothesis (μ=0). Additional approximations of this pdf is explained in detail in [207]. For higher q_0, which occurs for higher $\hat{\mu}$ when event yields are higher than

the expected background, there is higher incompatibility of data with the $\mu = 0$ hypothesis, i.e. the case of discovery.

In physics searches where signal could contain an upward or downward fluctuations in data, like in neutrino experiments, t_0 statistics is used like in equation 8.12. In searches where the signal is expected to be an upward fluctuation in the data, like in Higgs and SUSY searches, the q_0 statistics is used. For the case of disagreement of data with the background-only hypothesis, here only the $\hat{\mu} > 0$ cases are considered. If the value of $\hat{\mu}$ is much below 0, this would rather point to certain disagreement in the background modeling or unaccounted systematic uncertainties, and not to the presence of the signal.

Test Statistics q_μ for Upper Limits

In addition to the discovery test, it is important to establish upper limits on the signal strength parameter μ, i.e. μ values which are not compatible with the data need to be rejected. Here the relation between expected signal strength $\hat{\mu}$ and hypothesized signal strength μ are considered. As mentioned above, in the rejected region where p-value is below threshold α, $\hat{\mu}$ can take values of $\hat{\mu} > \mu$ and $\hat{\mu} < \mu$. However, the statistics test with expected signal strength higher than the hypothesized signal strength, $\hat{\mu} > \mu$, does not have a stronger test on μ than with the obtained data. Therefore, this statistics is not included in the test for rejecting a μ hypothesis, and q_μ is set to 0 in this region. Then the test statistics for upper limits q_μ is defined as:

$$q_\mu = \begin{cases} -2\ln\lambda(\mu) & \hat{\mu} \leq \mu, \\ 0 & \hat{\mu} > \mu \end{cases} \tag{8.15}$$

where $\lambda(\mu)$ is defined as in equation 8.8 in the $\hat{\mu} \leq \mu$ case. In a same way as in t_μ case, for higher q_μ values, there is is greater disagreement of data with the μ hypothesis.

Consequently, the p-value is:

$$p_\mu = \int_{q_\mu,obs}^{\infty} f(q_\mu|\mu)dq_\mu \tag{8.16}$$

where $f(q_\mu|\mu)$ is the pdf of q_μ assuming a hypothesis μ. Additional approximations of q_μ statistics are explained in reference [207].

Further, the q_μ statistics can be considered for $\hat{\mu} \geq 0$ case, which is applicable in SUSY and Higgs searches. The $\tilde{\lambda}(\mu)$ definition is used instead of $\lambda(\mu)$ as in equation 8.11. Then the test statistics for upper limits for the case of signal upward fluctuation is:

$$\tilde{q_\mu} = \begin{cases} -2\ln\frac{L(\mu,\hat{\hat{\theta}}(\mu))}{L(0,\hat{\hat{\theta}}(0))} & \hat{\mu} < 0, \\ -2\ln\frac{L(\mu,\hat{\hat{\theta}}(\mu))}{L(\hat{\mu},\hat{\theta})} & 0 \leq \hat{\mu} \leq \mu, \\ 0 & \hat{\mu} > \mu. \end{cases} \tag{8.17}$$

However, it has been shown that statistical tests based on q_μ and $\tilde{q_\mu}$ have negligible differences and lead to same results [207], so using q_μ calculation is much simpler.

Distributions and Approximation of Test Statistics

In order to obtain p-values for the discovery test and upper limit, test statistics probability density functions need to be determined. The test statistic can be generated using Monte Carlo by calculating the logarithmic log likelihood ratio for smeared nuisance parameters θ. The p-value for the case of discovery and finding an upper limit, is calculated using the equations 8.14 and 8.16 respectively. For the case of the test for **discovery**, the $\mu = 0$, q_0 is defined as in equation 8.13 and the pdf $f(q_0|0)$ needs to be determined. For the case of finding a **upper limit** for the non zero μ value, the test statistics is given by q_μ as in equation 8.15 or $\hat{q}_\mu$ given by 8.17. However, the computing time for generating the test statistics can be shortened by using approximations. As the p-value is calculated from the given test statistics, for the case of approximation it is essential to have a good model, that describes the Monte Carlo generated test statistics well.

The approximations of the test statistics and p-value calculations rely on three theorems, of Wilks, Wald and Asimov:

- Wald theorem [208] states that for the case of one parameter of interest, the test statistics distribution $\hat{\mu}$ can be approximated by a Gaussian distribution with mean μ' and standard deviation σ. The σ can be determined from the covariance matrix of all nuisance parameter estimators $\hat{\theta}$.

- Wilk's theorem [209] suggests that if $\hat{\mu}$ can be approximated by the Gaussian distribution, the test statistics follows a non-central χ^2 distribution with one degree of freedom, where non-centrality parameter is given by $\Lambda = \frac{(\mu-\mu')^2}{\sigma^2}$. For the special case of $\mu' = \mu$ it will be $\Lambda = 0$, and test statistics is given by χ^2 distribution with one degree of freedom. (The Wald and Wilk's theorem can be generalized for a case of more parameters of interest, if they can be identified with a subset of parameters θ.)

- The toy Monte Carlo samples can be generated using the so-called Asimov data set [207], which relies on the Wald and Wilk's theorems. In the asymptotic regime, p-value can be obtained from a formula.

In practice, these approximations become exact in the large statistics sample, and fairly accurate for small sample sizes, while for very small sample sizes, Monte Carlo distributions need to be used instead.

In order to obtain the CL_S and p-value for the discovery and upper limit, the test statistics given in equations 8.13 and 8.15, q_0 and q_μ, are typically generated using toy MC. For a large sample, the test statistics can be approximated by the χ^2 distribution with one degree of freedom. The test statistics for the discovery case

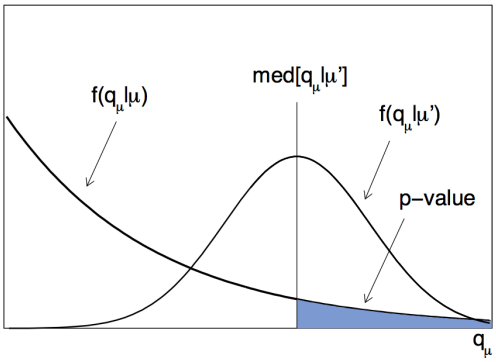

Figure 8.4.: Sensitivity of an experiment. The median q_μ statistics assuming strength parameter μ' relation to p-value in the pdf for q_μ assuming strength parameter μ [207].

then reads:

$$q_0 = \begin{cases} \frac{\hat{\mu}^2}{\sigma^2} & \hat{\mu} \geq 0, \\ 0 & \hat{\mu} < 0. \end{cases} \tag{8.18}$$

where μ has a Gaussian distribution, with the mean μ' and standard deviation σ. The p-value is given by:

$$p_0 = 1 - \Phi(\sqrt{q_0}) \tag{8.19}$$

where Φ is the cumulative distribution of the Gaussian with mean of 0, and variance of 1. Similarly, for the upper limit case, the test statistics reads:

$$q_\mu = \begin{cases} \frac{(\mu-\hat{\mu})^2}{\sigma^2} & \hat{\mu} < \mu, \\ 0 & \hat{\mu} > \mu. \end{cases} \tag{8.20}$$

The p-value for the upper limit case using the approximation is given by:

$$p_\mu = 1 - \Phi(\sqrt{q_\mu}). \tag{8.21}$$

Experimental Sensitivity with Significance Approximation Z_0

In the evaluation of the experiment sensitivity, it is more interesting to obtain the significance for different μ values, than just using one data set. In particular, for the case of discovery it is interesting to know the median of test statistics where the background-only hypothesis is rejected, for a nominal signal model ($\mu = 1$). For the case of setting exclusion upper limits, the experimental sensitivity is described by median significance for the $\mu = 0$ hypothesis with which the $\mu \neq 0$ hypothesis is rejected (at most interest is the $\mu = 1$ case).

The sensitivity of an experiment can be shown in the following way. For a test statistic q_μ for assumed strength parameter μ and median μ', the pdf can be presented as in figure 8.4. The distribution $f(q_\mu|\mu')$ is shifted to higher values of q_μ, which corresponds to lower p-values. The experimental sensitivity can be char-

acterized by giving the p-value of the test statistic q_μ which corresponds to the median of q_μ under an assumption of μ'. To determine experimental sensitivity of the experiment, Asimov data set approximations are used, and asymptotic formula for the significance estimation can be derived. For the counting experiment, if we consider the background to be known, and the signal hypothesis (μ=1), the median significance reads:

$$Z_0 = \sqrt{2((s+b)\ln(1+\frac{s}{b}) - s)} \tag{8.22}$$

where by logarithmic expansion, significance can be approximated with:

$$Z_0 \approx \frac{s}{\sqrt{b}}. \tag{8.23}$$

However, in this thesis, in the experimental significance estimation, an asymptotic formula which includes the effect of background uncertainty is used:

$$Z_0 \approx \frac{s}{\sqrt{b+\sigma_b^2}} \tag{8.24}$$

where σ_b is the background uncertainty, as justified in [210].

The CL_s Method for Setting Exclusion Limits

In the new physics searches there are two tests that are interesting for consideration. One is to confirm the presence of new phenomena, and the other is to perform exclusion of certain theories in the case of no discovery. In addition, it should be tested if given experimental data agrees with a certain theory, so the experiment needs to be sensitive to the parameters of the theory, because confidence intervals for the experiment with no sensitivity are uninformative. In ATLAS new physics searches, in the exclusion limits setting procedure the CL_S techniques is recommended [37,211]. It is well motivated due to its robustness against the possibilities of misinterpretations for the cases of low signal or large background counts. It is designed to obtain greater values than the standard confidence level, taken by convention to be 95%, for the cases where the experiment sensitivity to the new physics search is very low. It also allows comparison to previous experiments at Tevatron and LEP, and other LHC experiments like CMS. In previous experiments, a CL_s definition was used where the parameters determined by previous measurements were assumed to be correct. However, a good enough comparison to current definition of CL_s is viable. The CL_s technique motivation and definition will be shown in this section. For the non-search oriented statistical tests it is not recommended to use the CL_s technique, e.g. determination of boundaries on parameters, where more details about these recommendations in ATLAS can be found in [211].

In the figure 8.5(a) the test statistics q pdf distributions for the case of signal strength $\mu = 1$ (s+b hypothesis) and $\mu = 0$ (b only hypothesis), and the observed statistics q_{obs} are shown for the case of good experimental sensitivity, where the two

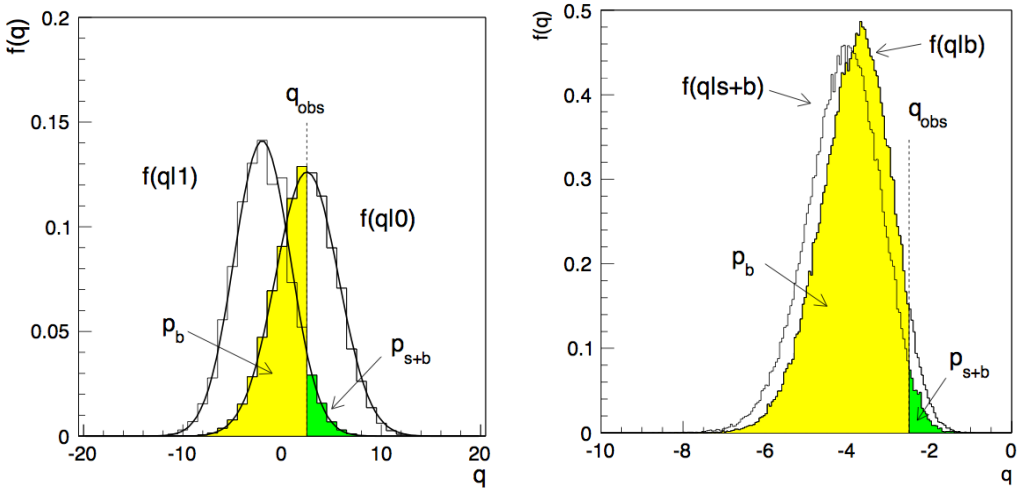

(a) (b)

Figure 8.5.: Test statistics q distribution under s + b and b only hypothesis for good (a) and poor sensitivity (b) [37]. (Note that test statistics here are represented by Gaussian distributions, while in practice they satisfy the chi-square distribution.)

distributions are well separated. The probability of excluding a s+b hypothesis is given by:

$$p_{s+b} = P(q \geq q_{obs}|s+b) = \int_{q_{obs}}^{\infty} f(q|s+b)dq. \tag{8.25}$$

The probability of not excluding the background-only hypothesis is given by:

$$p_b = P(q \leq q_{obs}|b) = \int_{-\infty}^{q_{obs}} f(q|b)dq. \tag{8.26}$$

The signal model can be regarded as excluded at confidence level CL = 95% when the probability p_{s+b} is not passing the α thereshold:

$$CL_{s+b} \equiv p_{s+b} < \alpha \tag{8.27}$$

where 1 - α = 95%, so α = 0.05. A confidence interval at 95% confidence level is constructed for the not excluded rates or cross-section. The upper limit (on the rate or cross-section) is the largest value of rate or cross-section not excluded. All values of rate or cross-section are excluded within the interval from 0 to the upper limit rate or cross-section value, with at least 95% confidence.

However, in the case where the experiment has very low or no sensitivity, so there number of signal events is much lower than the number of background events, the pdf distributions of test statistics q for s+b and b-only hypothesis are almost overlapping, like in the figure 8.5(b). In this case, using just the equation 8.27

would result in excluding with 95% confidence level any signal hypothesis to which the experiment has no sensitivity. For this, a penalty (increase) factor of 1/(1 - p_b) has been introduced to the p_{s+b} probability, and the CL_s for determining the 95% confidence level exclusion is defined as:

$$CL_s \equiv \frac{p_{s+b}}{1 - p_b} < \alpha. \tag{8.28}$$

For the case of good experimental sensitivity, when the test statistics distributions for the s+b and b-only hypothesis are well separated, the 1 - p_b is close to 1, and the penalty is very small, so the CL_s exclusion does not differ much from the p_{s+b}. For the case of low experimental sensitivity, the 1 - p_b becomes small, and the p_{s+b} is penalized (increased). Similarly, the upper limit using the CL_s method is weaker than by using the p_{s+b}. In this way the exclusion of signal models for low experimental sensitivity is prevented. Therefore, the excluded models by $CL_s < \alpha$ are a subset of $p_{s+b} < \alpha$ number of excluded models, and therefore, this procedure is considered conservative.

When CL_s method is used for setting upper limits on the cross-section, parameter μ is defined as the ratio of the measured and model theory predicted cross-section. For a large sample, the test statistics can be calculated using the Asimov data sets, while for small samples Monte Carlo tests statistics needs to be generated.

8.2.2. Statistical Test Setup

The usual procedure in the ATLAS new physics searches for the statistical tests is summarized in this section, following the prescription in [37, 211, 212]. To quantify the possible excess in the test of the discovery, the p-value is calculated, and in order to perform exclusion, the CL_s value needs to be computed. In SUSY searches, the scans in parameter space of a considered model are investigated, where the statistical procedure is repeated for each point in the parameter space grid. One should note that these tests need to be performed both for the observed and the expected case. They are for discovery/exclusion purpose only, and not for the measurement of parameter values.

8.3. Likelihood-Based Combined Fit

In a typical SUSY analysis there are three types of data or MC selection regions, which are used to determine the background by using the fit. First are the signal regions (SR) which are signal-enriched and have negligible contribution to the background determination parameters. Second are the control regions (CR), which are background-enriched regions with negligible signal contamination. They are used in the fit to estimate background population in the SR. Third are the validation regions (VR), which are designed not to be included in the SR, yet similar to it, which are used to validate the background extrapolation from CR to the SR. In order to

ensure statistical independence, the SR and CR selections need to be designed such that they have no overlap, i.e. the SR and CR selections need to be orthogonal. Then their parameter distributions can be modeled by separate probability density functions (pdf) which can be combined into a simultaneous fit.

All backgrounds from CR and SR and their systematic uncertainties are included in a combined fit based on the profile likelihood method. The likelihood function is built from binned pdf-s in all regions of the fit. The fit performs adjustment of pdf-s using MC in all CR to data and determines the optimal parameters, which include relative contributions of the background samples and the nuisance parameters which are used to model the statistical and systematic uncertainties. The formalism of the pdf parametrization and profile likelihood method in the combined fit will be discussed in the section 8.3.1. Short technical explanations of tools and the combined fit used in this analysis, are provided in the section 11.7.

8.3.1. Combined Fit Tools and Formalism

The simultaneous fit is required to have flexible treatment of counts in the selection regions and also different systematic uncertainties of each sample. This can be achieved by using the parametrized probability density functions. They are required to include multiple signal and background samples, possibility for unconstrained scaling for normalization of samples, ability to parametrize normalization, ability to parametrize the shapes of samples due to systematic effects, include bin-by-bin statistical uncertainty, and ability to combine multiple channels of disjoint event selections and correlate parameters across them.

In ATLAS SUSY searches the simultaneous fit is performed using the HistFitter [213] package. This is a wrapper around the HistFactory [214] tool which builds parametrized probability density functions using the ROOT [215] histograms and RooFit [216] tool used for the fit, and RooStats [217] used for the statistical interpretation. Note that the hypothesis testing and limit setting are typically done at the same time as the combined fit, in order to share pdf distributions, obtained optimal results of the fit and final signal and background counts with their associated uncertainties. In the following, the parametrized probability density function formalism as implemented in HistFactory will be presented.

The starting point of the statistical interpretation is the construction of the likelihood function, previously given by equation 8.7. It consists of two terms, where the first term represents the product of Poisson probabilities for all bins of a selected variable distribution, and second is the product of all Poisson probabilities of the control samples, used to constrain the nuisance parameters. In the HistFactory notation, the probability model $\mathcal{P}$ is used, and it represents the likelihood function if the data is considered to be fixed. The implementation can consider a more general case, where multiple channels, i.e. selections, for SR and and CRs can be used, and multiple samples can be used in the selection, e.g. multiple background samples.

The probability model $\mathcal{P}$ in the HistFactory notation, can be written as a product of Poisson distributions for each bin in a histogram of some parameter

distribution for each channel (see details below):

$$\mathcal{P}(n_{cb}, a_p|\phi_p, \theta_p, \gamma_b) = \prod_c \prod_b Pois(n_{cb}|\nu_{cb}) \cdot G(L_0|\lambda, \Delta_L) \cdot \prod_p f_p(a_p|\theta_p). \tag{8.29}$$

The expected mean number of events for a channel in a bin, depending on a sample, previously defined as 8.4 and 8.5 for the signal and background respectively, in the HistFactory notation is given by:

$$\nu_{cb}(\phi_p, \theta_p, \gamma_b) = \lambda_{cs}\gamma_{cb}\phi_{cs}\eta_{cs}(\theta)\sigma_{csb}(\theta) \tag{8.30}$$

where the probability density function is given by:

$$f_c(x_e|\phi_p, \theta_p, \gamma_b) = \frac{\nu_{cb_e}}{\nu_c}, \tag{8.31}$$

where $\nu_c = \sum_b \nu_{cb}$, b_e is the bin number, and x_e its content for the variable distribution. In the probability model the following notation is used:

- c - channel index in the fit, which labels event selection region (consists of a SR with sets of CR and VR)
- b - bin index in the fit, which labels the bin of parameter distributions in a given channel
- p - parameter index in the fit, which labels the parameter distribution, runs over constrained parameters which may be channel or bin dependent
- s - sample index in the fit, which labels the sample
- n_{cb} - number of events in the bin for a given channel
- a_p - auxiliary measurement for a parameter to constrain the nuisance parameters θ_p
- ϕ_p - the unconstrained normalization parameters
- θ_p - the nuisance parameters with external constrains, associated to systematics
- γ_{cb} - bin-by-bin constrained uncertainties (statistical error, shape systematics)
- $\prod_p f_p(a_p|\theta_p)$ - constant term describing auxiliary measurements a_p to constrain nuisance parameters θ_p
- $Pois(n_{cb}|\nu_{cb})$ - Poisson probability of observing n_{cb} for expected ν_{cb} events for a given channel and bin
- $G(L_0|\lambda, \Delta_L)$ - Gaussian penalty term for nominal luminosity L_0 and luminosity uncertainty Δ_L

- ν_{cb} - mean number of events in a bin for a given channel
- λ_{cs} - luminosity parameter for a given channel and sample. It can take values of nominal luminosity L_0, or it can be a common parameter for all samples of a given channel
- γ_{cb} - bin-by-bin scale factor used for statistical uncertainties, shape systematics and data driven shape extrapolations. It is unchanged for samples for a given bin and channel. For statistical error Poissonian distribution is assumed.
- $\phi_{cs} = \prod_p \phi_p$ - normalization factor, product of unconstrained normalization factors for a given sample and channel (e.g. signal cross-section or branching ratio)
- $\eta_{cs}(\theta)$ - parametrized normalization uncertainties for a given sample and channel (typically around 1)
- $\sigma_{csb}(\theta)$ - parametrized histogram for a given sample and channel, where parametrization is done as a linear interpolation between the upward and downward scaled histogram by the input given uncertainty. It is fully correlated across bins of the histogram.

The probability model implementation in the HistFactory, i.e. likelihood function for fixed data, is further used by multiple programs. The HistFitter performs the steering in order to obtain the background normalization and statistical interpretation. Here the RooFit program is used to obtain the optimal normalization factors for background samples, by performing the maximum likelihood fit, i.e. taking the logarithm of the likelihood, where information from CRs is used. The statistical interpretation is performed using the log likelihood ratio and test statistics, to obtain the p-value and CLs values, as explained in the previous section 8.2.1, using the RooStats package. Here the test statistics can be obtained both for toy MC and Asimov data set. Details about the SR, CRs, systematic uncertainties and statistical treatment used in this thesis is given in the section 11.7.

9. NUHMG Final States

In this chapter the NUHMG model, described in the chapter 5, search strategy at the LHC is explored. This is a R-parity conserving model and has $\tilde{\nu}_\tau$ as the NLSP. It is characterized by allowed decays of $\tilde{\chi}_1^0$ and low mass splittings for gauginos and sleptons, and therefore has a signature with lots of soft leptons, together with jets and missing energy, due to long cascade decay chains. This chapter will give details about the NUHMG model typical mass spectrum and dominant decay modes in the section 9.1 and final states at the LHC will be described in the section 9.2.

9.1. Typical Mass Spectrum and Dominant Decay Modes

In this section the NUHMG model mass spectrum and dominant decay modes are investigated. The final states expected at 8 TeV LHC collisions are shown in the next section 9.2. However, more details about the NUHMG grid parameters and its preparation are shown in the chapter 10.

The SUSY and Higgs mass spectrum and mixing angles have been computed using SOFTSUSY 3.3.4 [154], while the SUSY and Higgs particle decays have been calculated using SUSY-HIT [156] as an interface to decay calculators SDECAY 1.3 [158] and HDECAY 3.302 [157] respectively. The assumption of $\tilde{G}$ LSP is used, and parameter space with $\tilde{\nu}_\tau$ NLSP is chosen. SM input parameters are $m_t = 173.2$ GeV, $m_b(m_b) = 4.2$ GeV and $\alpha_S^{SMMS} = 0.1184$. This SUSY parameter space region has a $\tilde{G}$ mass $m_{3/2} > 10$ GeV [28]. The high mass compactification scale is set to be $M_X = M_{GUT} = 1.987{\times}10^{16}$ GeV.

As previously shown in the figure 5.3, the NUHMG model parameter space has three regions which differ in the sparticle mass order as:

- A: $m_{\tilde{\tau}_1} > m_{\tilde{\chi}_1^0} > m_{\tilde{\nu}_\tau}$
- B: $m_{\tilde{\chi}_1^0} > m_{\tilde{\tau}_1} > m_{\tilde{\nu}_\tau}$
- C: $m_{\tilde{\chi}_1^0} > m_{\tilde{l}} > m_{\tilde{\tau}_1} > m_{\tilde{\nu}_\tau}$.

The mass spectrum and dominant decays for one typical point in the C region is given in the table 9.1. The dominant productions are direct production of $\tilde{q}$ and $\tilde{g}$, or the production of $\tilde{l}$ and gauginos, i.e. strong and electro-weak production respectively. Strong production has decays of $\tilde{q}$ and $\tilde{g}$ into $\tilde{\chi}_1^0$ and $\tilde{\chi}_1^\pm/\tilde{\chi}_2^\pm$, while in electro-weak production $\tilde{l}$ and higher gauginos typically decay into lower gauginos. A detailed analysis of final states at the LHC will be given in the next section 9.2.

Mass spectrum of three points for the same $m_{1/2}$, which results in same $\tilde{q}$ and $\tilde{g}$ masses, are presented in the figure 9.1. In this model $\tilde{g}$ is always heavier than the

	Mass (GeV)	Decay Modes
$\tilde{g}$	1047	$\tilde{q}_{\rm L}q(10\%)$, $\tilde{q}_{\rm R}q(33\%)$, $\tilde{t}_1t(37\%)$, $\tilde{b}_{1,2}b(20\%)$
$\tilde{q}_{\rm L}$	972	$\tilde{\chi}_1^{\pm}q(\ 65\%)$, $\tilde{\chi}_2^0q(\ 32\%)$, $\tilde{\chi}_{1,3,4}^0q(\ 2\%)$
$\tilde{q}_{\rm R}$	910	$\tilde{\chi}_1^0q(99\%)$
$\tilde{\chi}_4^0$	732	$\tilde{t}_1t(66\%)$, $\tilde{\chi}_1^{\pm}W(18\%)$, $\tilde{\chi}_2^0h(8\%)$
$\tilde{\chi}_2^{\pm}$	733	$\tilde{t}_1b(58\%)$, $\tilde{\chi}_2^0W(12\%)$, $\tilde{\chi}_1^{\pm}Z(11\%)$, $\tilde{\chi}_1^{\pm}h(11\%)$
$\tilde{\chi}_3^0$	725	$\tilde{\chi}_1^{\pm}W(55\%)$, $\tilde{\chi}_2^0Z(24\%)$, $\tilde{\chi}_1^0Z(8\%)$
$\tilde{t}_1$	544	$\tilde{\chi}_1^{\pm}b(74\%)$, $\tilde{\chi}_1^0t(15\%)$, $\tilde{\chi}_2^0t(11\%)$
$\tilde{\ell}_{\rm R}$	415	$\tilde{\chi}_1^0l(99\%)$
$\tilde{\chi}_1^{\pm}$	350	$\tilde{\nu}_ll(33\%)$, $\tilde{\ell}_{\rm L}\nu_l(28\%)$, $\tilde{\nu}_\tau\ \tau(20\%)$, $\tilde{\tau}_1\nu_\tau(18\%)$
$\tilde{\chi}_2^0$	349	$\tilde{\nu}_l\nu_l(32\%)$, $\tilde{\ell}_{\rm L}l(30\%)$, $\tilde{\nu}_\tau\ \nu_\tau(19\%)$, $\tilde{\tau}_1\tau(19\%)$
$\tilde{\chi}_1^0$	183	$\tilde{\nu}_l\nu_l(28\%)$, $\tilde{\ell}_{\rm L}l(11\%)$, $\tilde{\nu}_\tau\ \nu_\tau(37\%)$, $\tilde{\tau}_1\tau(24\%)$
$\tilde{\ell}_{\rm L}$	146	$\tilde{\nu}_\tau\ \tau\nu_l(100\%)$
$\tilde{\nu}_l$	124	$\tilde{\nu}_\tau\ \nu_l\nu_\tau(91\%)$, $\tilde{\nu}_\tau\ l\tau(9\%)$
$\tilde{\tau}_1$	92	$\tilde{\nu}_\tau\ l\nu_l(30\%)$, $\tilde{\nu}_\tau\ qq'(70\%)$
$\tilde{\nu}_\tau$	63	$\tilde{G}\ \nu_\tau(100\%)$ NLSP

Table 9.1.: NUHMG point $m_{H_1}^2 = 2.8$ TeV^2, $m_{1/2} = 450$ GeV (C region) mass spectrum and branching ratios. Higher chargino and neutralino decays are relevant only for the direct gaugino production. $\tilde{q}$ and $\tilde{l}$ masses are given for the average of the first two generations, as they are almost degenerate. ($\tan\beta = 10$, $m_0 = 0$, $m_{H_2}^2 = 0$, $A_0 < 0$, sign(μ) > 0, l = (e,μ), q = (u,d,c,s), $\tilde{l} = (\tilde{e}\ ,\tilde{\mu}\ )$, $\tilde{q} = (\tilde{u},\tilde{d},\tilde{c},\tilde{s})$.)

$\tilde{q}$. Higher gauginos are of the same order of mass as light $\tilde{q}$, while lower gauginos have masses of the same order as $\tilde{l}$ and $\tilde{\nu}$ and make a compact mass spectrum. The regions A, B and C differ with the mass order of $\tilde{\chi}_1^0$, $\tilde{\tau}_1$, $\tilde{l}$ and $\tilde{\nu}$.

A note should be made concerning the A region ($m_{\tilde{\ell}_{\rm L}} > m_{\tilde{\tau}} > m_{\tilde{\chi}_1^0} > m_{\tilde{\nu}_\tau}$) which shifts towards the upper diagonal. With $A_0 < 0$ used in this analysis in the m_h maximization, all gaugino masses shift towards higher values compared to the $A_0 = 0$ case. This partially distorts the $\tilde{\ell}_{\rm L}$, $\tilde{\tau}_1$ and $\tilde{\chi}_1^0$ mass order, and consequently the placement of A, B and C regions, leading to dominant C, narrow B and vanishing A region.

A comment concerning the Higgs mass is in order. As a gaugino mediation model, the m_h in fact does not satisfy the Higgs mass constraint of $121 < m_h < 127$ GeV for all points. Studies of the Gauge Mediated Symmetry Model (GMSB) have shown that the Higgs mass constraint can be achieved for $\tilde{t}$ masses in the TeV range, where the slepton masses are related to squark masses. However, modifications to the minimal GMSB can allow for the Higgs mass within the constraint without changing the sparticle masses [219–221]. In a similar way as in GMSB, the NUHMG model can be extended to accommodate for the Higgs mass constraint, while all sparticle masses stay unchanged, and the targeted final state and its kinematics

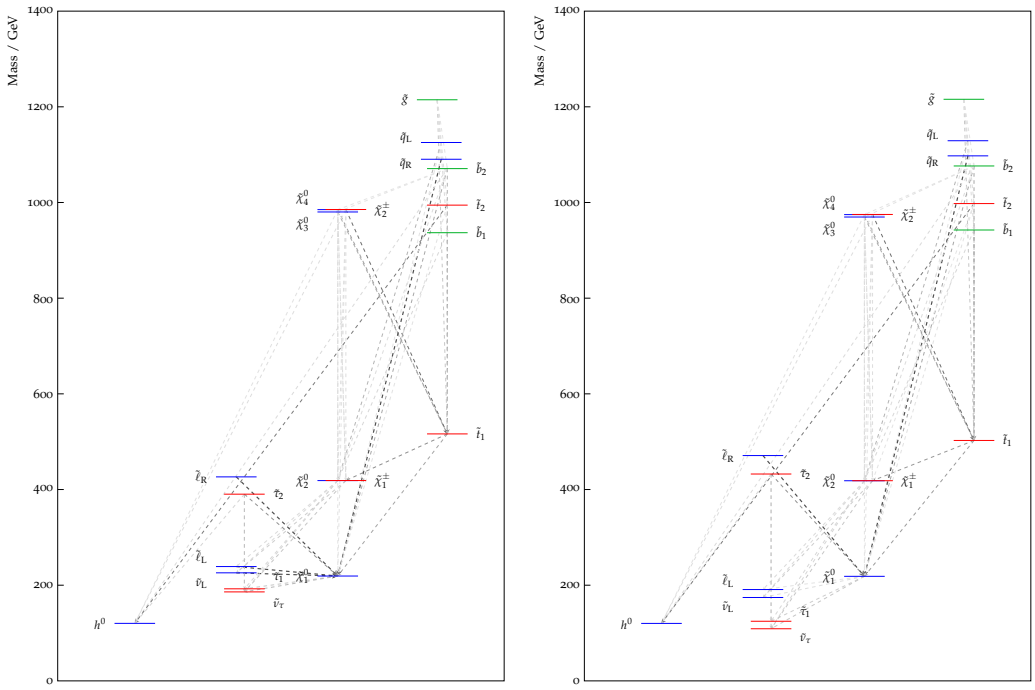

(a) $m^2_{H_1} = 2.8$ TeV^2, $m_{1/2} = 530$ GeV. (b) $m^2_{H_1} = 3.6$ TeV^2, $m_{1/2} = 530$ GeV.

Figure 9.1.: NUHMG points mass spectrum and branching ratio lines. Mass order for $\tilde{\chi}^0_1$, $\tilde{e}$ and $\tilde{\tau}$ differs for increasing $m^2_{H_1}$, where $\tilde{\ell}_{\mathrm{L}}$ and $\tilde{\tau}_1$ masses shift in comparison to $\tilde{\chi}^0_1$. Region A ($m_{\tilde{\ell}_{\mathrm{L}}} > m_{\tilde{\tau}} > m_{\tilde{\chi}^0_1} > m_{\tilde{\nu}_\tau}$) is not presented as it is very close to the diagonal, while regions B ($m_{\tilde{\ell}_{\mathrm{L}}} > m_{\tilde{\chi}^0_1} > m_{\tilde{\tau}} > m_{\tilde{\nu}_\tau}$) and C ($m_{\tilde{\chi}^0_1} > m_{\tilde{\ell}_{\mathrm{L}}} > m_{\tilde{\tau}} > m_{\tilde{\nu}_\tau}$) are present in a) and b) figures respectively. Thickness of the gray lines is scaled to the value of the branching ratio. ($\tan\beta = 10$, $m_0 = 0$, $m^2_{H_2} = 0$, $A_0 < 0$, sign(μ) > 0,$\tilde{l}$ = ($\tilde{e}$,$\tilde{\mu}$), $\tilde{q}$ = ($\tilde{u}$,$\tilde{d}$,$\tilde{c}$,$\tilde{s}$).) Sparticle mass spectrum plots are obtained using the PySLHA [218].

stay unaffected by this extension.

9.2. Final States at the LHC

In the following section the cascade decays of the NUHMG model will be examined. First the production cross-section will be considered. Next, the possible decays for A, B and C NUHMG model parameter space regions will be examined for different parts of the decay chain. Finally, the targeted final states will be justified.

In the considered m_{H_1} vs $m_{1/2}$ parameter space the $\tilde{q}$ and $\tilde{g}$ masses are in the TeV range, which results in large cross-sections at the LHC, in the range of 10-100 fb for the strong production. In the figure 9.2 production cross-section for the $\tilde{q}$ and $\tilde{g}$ production is shown. As mentioned in the previous section, in this model $\tilde{g}$

is always heavier than the $\tilde{q}$ due to $m_0 = 0$, which is set by the model construction. This results in large direct $\tilde{q}$ pair production cross-section. The $\tilde{t}_1$is lighter than the $\tilde{q}$ by a small amount, which results in similar and slightly larger cross section. As the higher gaugino masses are of the same order as light squarks, the electro-weak production has large cross-sections as well, where higher gauginos decay into lower ones. In this thesis an emphasis on the $\tilde{q}$ and $\tilde{g}$ production including the third generation, $\tilde{q}$ -gaugino, $\tilde{g}$ -gaugino production will be given, shown as total in the figure 9.2. See more details about the NUHMG cross-section in the section 10.3.

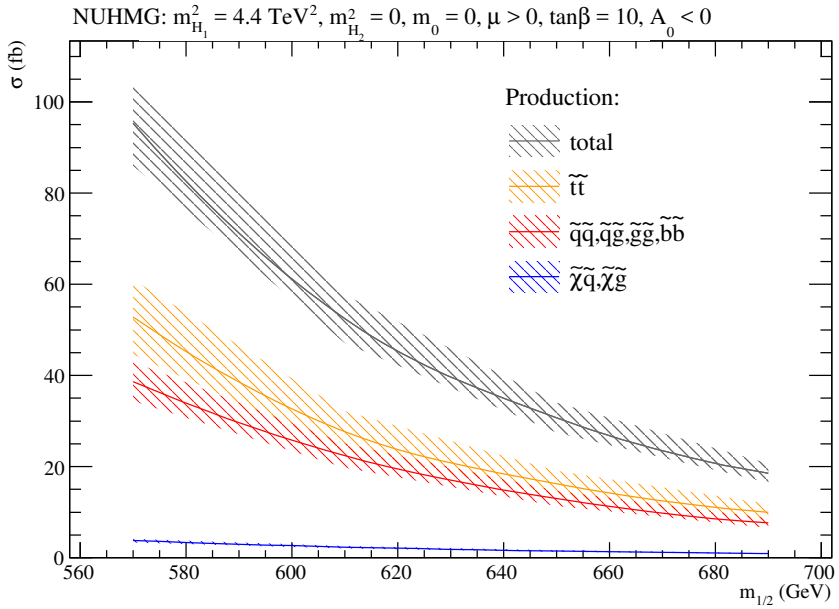

Figure 9.2.: NUHMG model cross-section for the strong production processes, with included $\tilde{q}$ -gaugino and $\tilde{g}$ -gaugino production. For all squark generations anti-squark production is included, and $\tilde{\chi}$ denotes all $\tilde{\chi}^0$ and $\tilde{\chi}^{\pm}$ generations. Total includes the processes of $\tilde{t}\tilde{t}, \tilde{q}\tilde{q}, \tilde{q}\tilde{g}, \tilde{g}\tilde{g}, \tilde{b}\tilde{b}, \tilde{\chi}\tilde{q}, \tilde{\chi}\tilde{g}$ production.

The features of the NUHMG model and typical decays have been explained in the section 5.2. The beginning of the decay chain of $\tilde{g}$ and $\tilde{q}$ production has dominant decays into lower gauginos with a quark, see table 9.1. The model is characterized with a possibility of forming longer decay chains, and a typical signature with lots of leptons and jets. Due to its typical mass spectrum, where $\tilde{\chi}_1^0$ is not the LSP, there are allowed decays of $\tilde{\chi}_1^0$. Due to $m_{\tilde{l}_L} > m_{\tilde{l}_R}$ and allowed decays of $\tilde{l}_L$, it can be produced in the cascade. Also, $\tilde{\tau}_1$ has a three-body decay, which produces a pair of fermions and missing transverse energy. Since the mass spectrum is compact, the visible decay products tend to be soft. The $\tilde{\nu}_\tau$ NLSP produced at the end of the chain, decays into $\tilde{G}$ and ν_τ, leaving a signature with missing transverse energy.

Strong production with light jets	Direct $\tilde{q}$ production 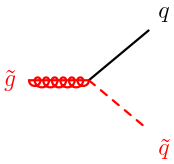	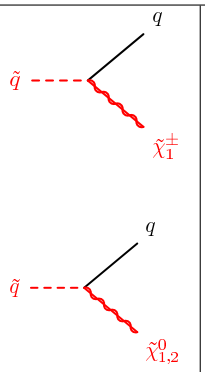	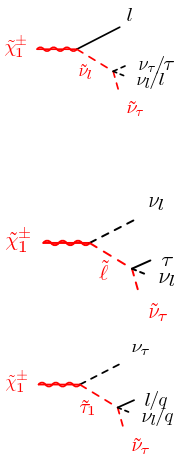	2-4 q 0-4 (q) 0-4 (l) 0-2 (τ) $E_{\mathrm{T}}^{\mathrm{miss}}$
Strong production with third generation	Direct $\tilde{t}_1$ production 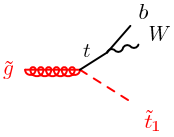	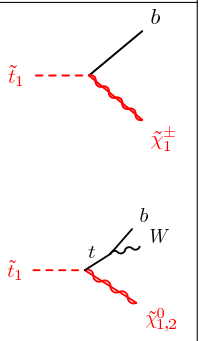	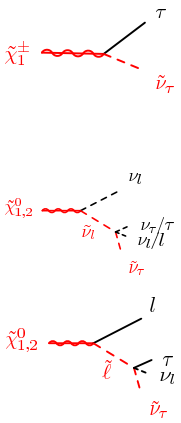	2-4 b 0-4 W 0-4 (q) 0-4 (l) 0-2 (τ) $E_{\mathrm{T}}^{\mathrm{miss}}$
Gaugino production with W,Z and h	Direct gaugino production	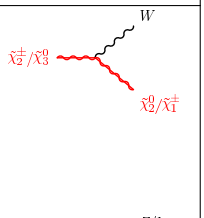	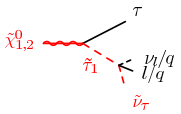	2 W 0-4 (q) 0-4 (l) 0-2 (τ) $E_{\mathrm{T}}^{\mathrm{miss}}$
		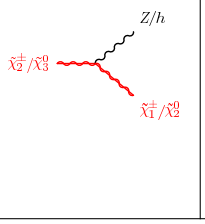	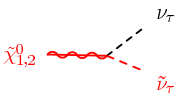	2 Z/h 0-4 (q) 0-4 (l) 0-2 (τ) $E_{\mathrm{T}}^{\mathrm{miss}}$

Table 9.2.: NUHMG decay chains (from left to right) and final states for a point in the region C. Strong production has 2-4 light jets and $E_{\mathrm{T}}^{\mathrm{miss}}$, and similarly strong production with third generation has 2-4 b-jets, 0-4 W and $E_{\mathrm{T}}^{\mathrm{miss}}$. The gaugino production has 2 W, 2 Z or 2 h and $E_{\mathrm{T}}^{\mathrm{miss}}$. All final states in addition can have more soft l,τ or jets. l = (e,μ), q = (u,d,c,s), $\tilde{l}$ = ($\tilde{e}$,$\tilde{\mu}$).

In the long decay chains the produced missing transverse energy from neutrinos can cancel out with the missing transverse energy of the NLSP, bringing to a signature with low missing transverse energy. Although this model offers possible signatures with lots of soft leptons and taus at the end of the decay chain, a more robust search, which will not depend on the small lepton or tau p_T, using a signature with more jets and missing energy, is investigated in the table 9.2. The cascade decays and final states for each production channel characteristics are:

- Strong production with light jets, can have decay chains starting with a $\tilde{g}$ or $\tilde{q}$, which decay into $\tilde{\chi}_1^0$ or $\tilde{\chi}_1^\pm$ with jets. Further $\tilde{\chi}_1^0$ or $\tilde{\chi}_1^\pm$ have decays into $\tilde{\nu}_\tau$. If there is an intermediate $\tilde{l}$ or $\tilde{\tau}_1$ the signature will have a l or τ of moderate p_t. Further decay of $\tilde{l}$, $\tilde{\tau}_1$ or $\tilde{\nu}_\tau$ will give only soft fermions and missing energy. Due to the fact that the decay chain is long and the mass spectrum is compact, the $\tilde{\nu}_\tau$ and ν are produced in different directions. This brings to a relatively low missing energy in the final state due to the vectorial cancellation of missing transverse momenta of $\tilde{\nu}_\tau$ and ν. Therefore, the final state will have 2-4 jets and relatively low missing transverse momenta, with possible additional jets, leptons and taus. In addition, this search is viable due to the large $\tilde{q}$ and $\tilde{g}$ production cross-section.

- Strong production with third generation, in a similar way, has a final state with 2-4 b-jets and 0-4 W, which can decay hadronically or leptonically, missing transverse momenta and possible additional jets, leptons and taus. Also, the cross-section for the $\tilde{t}$ pair production is large, which makes this search viable.

- Gaugino production can have final states with 2W or 2Z/h and missing energy, with possible additional jets, leptons and taus. Although the production cross-section is relatively large, this search is more difficult since the decay products are soft.

- Direct slepton production can be difficult for analysis because $\tilde{\ell}_\mathrm{R}$ decays into $\tilde{\chi}_1^0$ and $\tilde{\ell}_\mathrm{L}$ decays into $\tilde{\nu}_\tau$, leaving signatures with soft leptons or tau. Since the decay chain is very short and boosted, the decay products are back to back, thus the missing transverse momenta is very low.

This brings to the final conclusion that NUHMG can be found using final states with multiple jets and low missing energy using the strong production. This is the most inclusive selection which does not depend on the b-jet tagging nor τ reconstruction. Also, it does not depend on the low p_T of possible l or τ, but with a lepton veto of 10 GeV it in fact includes states with soft objects. However, the search using multiple jets, l and missing transverse momenta should give complementary results. The Feynman diagrams of targeted final states using multiple jets, missing transverse momenta and a lepton veto are shown in the figure 9.3. These are $\tilde{g}$ pair production with up to 8 jets and low $E_\mathrm{T}^\mathrm{miss}$, $\tilde{q}$ pair production with up to 6 jets and $E_\mathrm{T}^\mathrm{miss}$, and $\tilde{t}_1$ pair production with 2 b-jets, up to 4 light jets and $E_\mathrm{T}^\mathrm{miss}$.

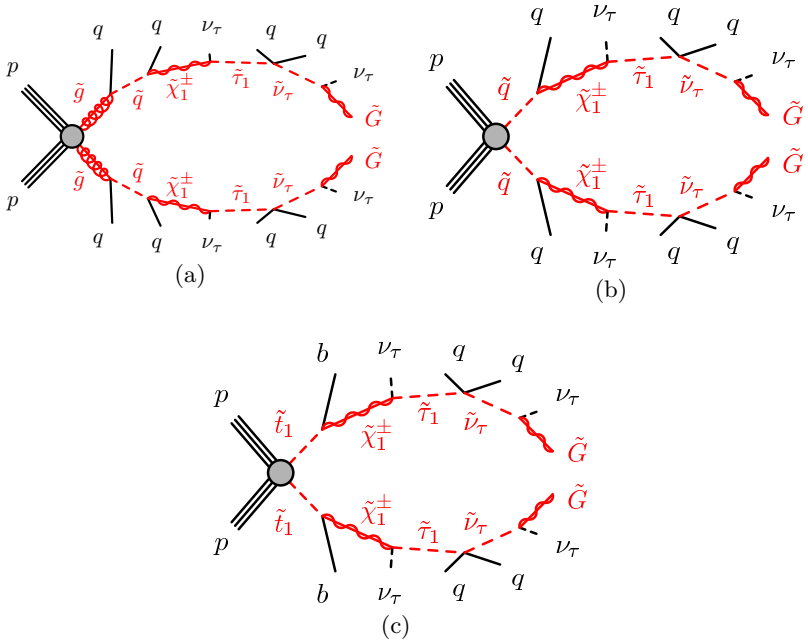

Figure 9.3.: Targeted NUHMG final states with multiple jets and $E_{\mathrm{T}}^{\mathrm{miss}}$. $\tilde{g}$ pair production with up to 8 jets and $E_{\mathrm{T}}^{\mathrm{miss}}$ (a), $\tilde{q}$ pair production with up to 6 jets and $E_{\mathrm{T}}^{\mathrm{miss}}$ (b), and $\tilde{t}_1$ pair production with 2 b-jets, up to 4 light jets and $E_{\mathrm{T}}^{\mathrm{miss}}$ (c). Same final state using a lepton veto can be used when soft τ or l is present. If no b-tag is applied, $\tilde{t}_1$ pair production with multiple jets can be found as well. l = (e,μ), q = (u,d,c,s).

A note should be made concerning the slepton and gaugino production, which is not negligible for NUHMG model. Final states with 2W, 2Z or 2h with missing energy could provide interesting searches, but since these events are mostly back-to-back with short decay chains, large fraction remains with very low canceled out $E_{\mathrm{T}}^{\mathrm{miss}}$. This brings to the conclusion that a search with the slepton and gaugino production could be used in the NUHMG searches. However, in this thesis an approach of a search with strong production has been selected due to its larger effective cross-section and more inclusive and robust approach, using the analysis of 2-6 jets, missing transverse momentum and a lepton veto, see full description of the analysis in the chapter 11. In addition, a complementary search for strong production with 1 l with 2-6 jets and missing transverse momentum was performed, and the results are given in the section 11.8.5 for comparison.

10. NUHMG Grid Properties

In order to perform the data analysis of a SUSY model, a grid of SUSY parameter points needs to be selected such that the search is viable for given experimental conditions, while it satisfies selected constrains and is not already excluded by previous experiments. The details of the NUHMG grid preparation are shown in this chapter. The NUHMG model is therefore investigated in the $m^2_{H_1}$ vs $m_{1/2}$ plane for fixed $m_0 = 0$, $m^2_{H_2} = 0$, $\text{sign}(\mu) > 0$, $\tan\beta = 10$, see table 10.1. The interesting parameter space region is selected with the requirement of $\tilde{\nu}_\tau$ NLSP, and $\tilde{\tau}_1$, $\tilde{\chi}^0_1$ and $\tilde{\chi}^\pm_1$ masses higher than the LEP limit [39]. An additional scan has been performed to obtain the lightest SUSY Higgs mass h closest to the Higgs mass constrain of $m_h = 125.5$ GeV [222]. This resulted in an estimate for the viable NUHMG model region of $2.0 \leq m^2_{H_1} \leq 7.2$ TeV^2 and $450 \leq m_{1/2} \leq 890$ GeV.

A note should be made concerning the LEP limit on the $\tilde{\nu}_\tau$ mass. All the LEP limits on $\tilde{\nu}_\tau$ have been done using the $\tilde{\chi}^0_1$ LSP case [39], while $\tilde{\nu}_\tau$ LSP is excluded [124], therefore, there are no limits made for the $\tilde{\nu}_\tau$ NLSP case, and no mass constrain on the $\tilde{\nu}_\tau$ was considered in this analysis.

Fixed parameters	$m_0 = 0$ $m^2_{H_2} = 0$ $\text{sign}(\mu) > 0$ $\tan\beta = 10$
NLSP and LEP limit checks	$\tilde{\nu}_\tau$ NLSP $\tilde{\tau}_1 >$ 81.9 GeV $\tilde{\chi}^0_1 >$ 46 GeV $\tilde{\chi}^\pm_1 >$ 94 GeV
Higgs mass constrain	$A_0 < 0$, varied to obtain h mass closest to 125.5 GeV, step 10 GeV
Grid parameters	$2.0 \leq m^2_{H_1} \leq 7.2$ TeV^2, step 0.4 TeV^2 $450 \leq m_{1/2} \leq 890$ GeV, step 40 GeV

Table 10.1.: NUHMG grid parameters. Grid is prepared in $m^2_{H_1}$ vs $m_{1/2}$ parameter space for given fixed parameters. $\tilde{\nu}_\tau$ NLSP and LEP limit [39] checks performed, together with the Higgs mass constrain [222].

To summarize, NUHMG model parameter space points have been examined in three aspects at the same time. Firstly, the scan on parameters, with the LEP limit constrain and a scan to obtain the best h mass is performed, described in the section

10.1. Secondly, the sparticle mass spectrum has been explored to determine regions which are not covered by other LHC searches, and more details will be shown in the section 10.2. Thirdly, the points cross-sections have been calculated and details about the production channel dependency on the c.m.e. are given in the section 10.3 in order to define regions with yields viable for 8 TeV LHC conditions. The scan has been performed on a wider range, but the plots in this thesis represent the final parameters selection.

10.1. LEP Limit and the Higgs Mass Constrain

In the NUHMG grid preparation, the SUSY parameter space points with the right $\tilde{\nu}_\tau$ NLSP and points not excluded by the LEP measurements, should be considered. The grid scan has been performed using the same setup for mass spectrum, mixing and branching ratios generation as described in the section 9.1, using the scan details previously shown in the table 10.1. First, for the given fixed parameters a point for a scan on $m^2_{H_1}$ and $m_{1/2}$ parameters is generated using $A_0 = 0$. Next, the check for the $\tilde{\nu}_\tau$ NLSP and LEP limits on $\tilde{\chi}^0_1$, $\tilde{\chi}^\pm_1$ and $\tilde{\tau}_1$ is added. For a point satisfying these criteria a scan into negative values of A_0 is performed, using a step of 10 GeV, where the point with m_h closest to 125.5 GeV is kept. The cross-check for the $\tilde{\nu}_\tau$ NLSP and LEP limits is repeated on the obtained points.

In more detail, the viable $\tilde{\nu}_\tau$ NLSP and LEP limit constrain for points using $A_0 = 0$ are shown in red in the figure 10.1(a), i.e. before the scan for the Higgs mass constrain. The resulting points, shown as circled, are distributed somewhat diagonally in the $m^2_{H_1}$ vs $m_{1/2}$ plane in the range $2.0 \leq m^2_{H_1} \leq 7.2$ TeV^2 and $450 \leq m_{1/2} \leq 890$ GeV. Next the Higgs mass constrain scan is run by testing the Higss mass of each attempt. The resulting Higgs mass closest to 125.5 GeV is shown in the figure 10.1(b) and the used A_0 value is shown at 10.1(c). For the point with best Higgs mass obtained the LEP limits on $\tilde{\chi}^0_1$, $\tilde{\chi}^\pm_1$and $\tilde{\tau}$ are checked one more time, shown in figures 10.1(d), 10.1(e) and 10.1(f) respectively. All points satisfy the LEP limits.

10.2. Mass Spectra for Grid Points

In the NUHMG grid preparation, points which are not already excluded by other LHC measurements need to be investigated. In the first place its $\tilde{g}$ and $\tilde{q}$ masses need to be in the TeV range in order to be comparable to the LHC measurements for strong production and compact mass spectrum [35]. The naturalness criteria favour stop mass $m_{\tilde{t}_1}$ around 700 GeV [113], therefore the NUHMG points need to have $\tilde{t}_1$ masses of this order.

The $\tilde{g}$ and $\tilde{q}$ mass are shown in figures 10.2(a) and 10.2(b) respectively. They take values in the range $1045 < m_{\tilde{g}} < 1962$ GeV and $965 < m_{\tilde{q}} < 1805$ GeV, and they depend on $m_{1/2}$ but not on $m^2_{H_1}$. They are in the somewhat lower range for the LHC

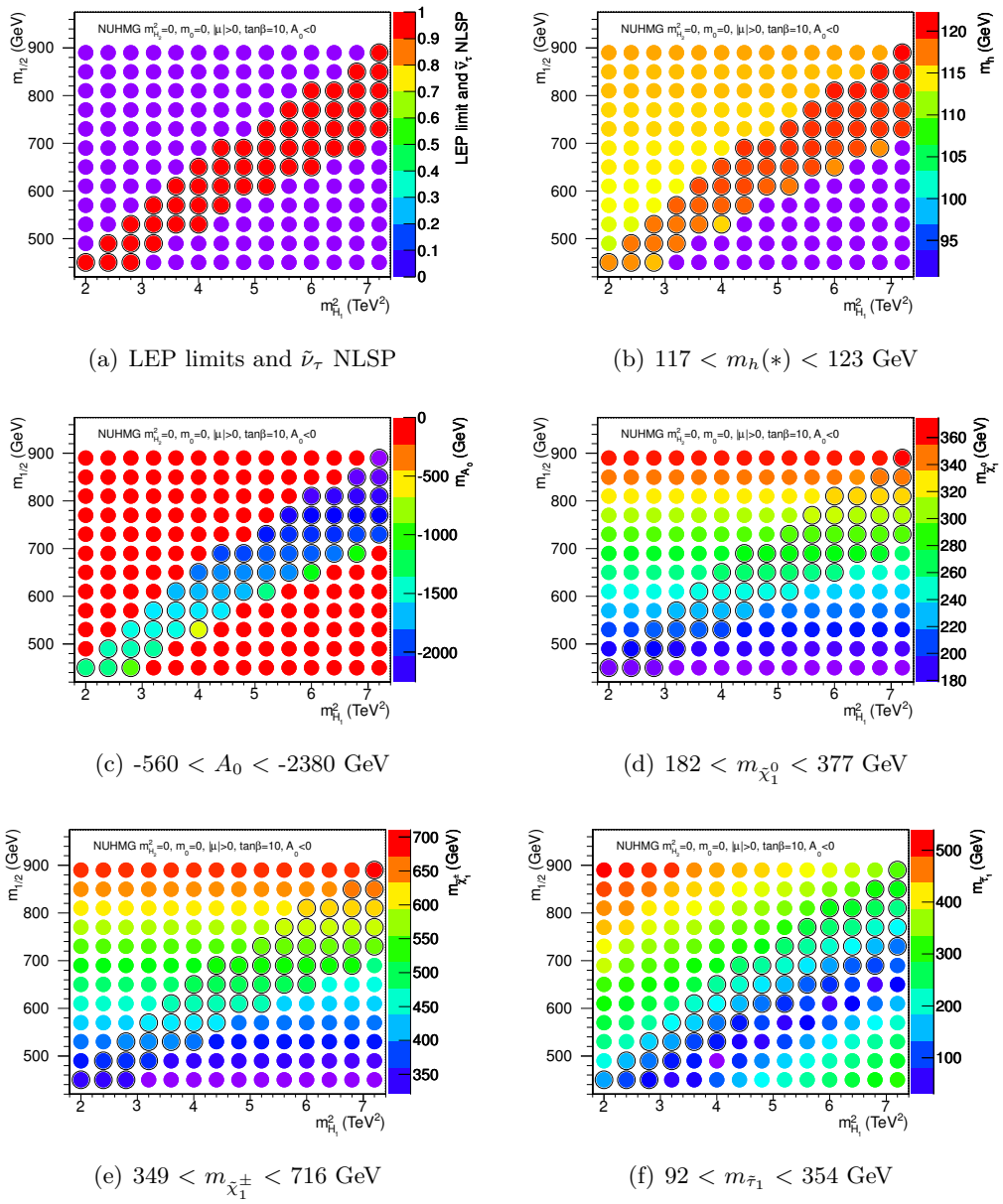

(a) LEP limits and $\tilde{\nu}_\tau$ NLSP

(b) $117 < m_h(*) < 123$ GeV

(c) -560 $< A_0 <$ -2380 GeV

(d) $182 < m_{\tilde{\chi}_1^0} < 377$ GeV

(e) $349 < m_{\tilde{\chi}_1^\pm} < 716$ GeV

(f) $92 < m_{\tilde{\tau}_1} < 354$ GeV

Figure 10.1.: NUHMG grid scan using $\tilde{\nu}_\tau$ NLSP selection and LEP limits constrain with the scan on the Higgs mass constrain. First the satisfying points for $A_0 = 0$, are selected for the grid, shown in red at a). Next, the scan into negative values of A_0 was performed and the point with highest m_h was selected. The best obtained Higgs mass is shown at b) and the corresponding value of A_0 is shown at c). All grid points, shown as circled, satisfy the LEP limits for $\tilde{\chi}_1^0$, $\tilde{\chi}_1^\pm$and $\tilde{\tau}_1$mass for both $A_0 = 0$ and after the $A_0 < 0$ scan, shown at d), e) and f) respectively for the $A_0 < 0$ case. (*) The m_h represents the obtained h mass for each point in the grid, maximized to be close to the experimental Higgs mass measurement $\sim$ 125.5 GeV.

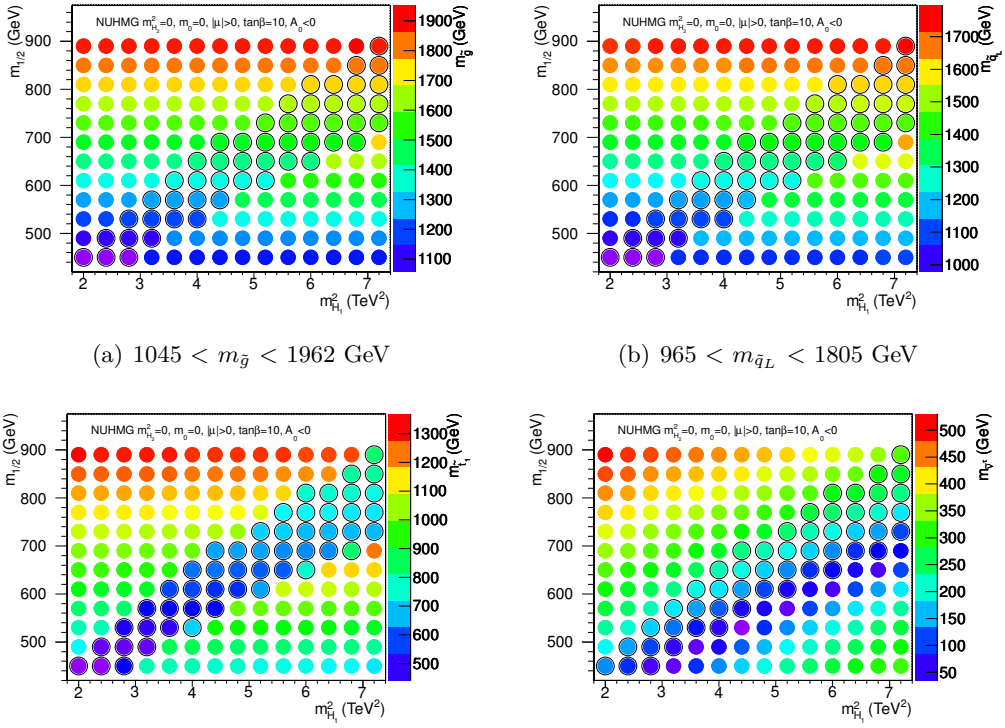

(a) $1045 < m_{\tilde{g}} < 1962$ GeV

(b) $965 < m_{\tilde{q}_L} < 1805$ GeV

(c) $417 < m_{\tilde{t}_1} < 885$ GeV

(d) $63 < m_{\tilde{\nu}_\tau} < 351$ GeV

Figure 10.2.: NUHMG grid check for $\tilde{g}$, $\tilde{q}$ and $\tilde{t}_1$masses. For all points $\tilde{q}$, $\tilde{g}$ and $\tilde{t}_1$ masses run with $m_{1/2}$ parameter. $\tilde{q}$ and $\tilde{g}$ masses are in the 1-2 TeV range, shown at a) and b), and $\tilde{t}_1$ has masses below 1 TeV, shown at c). $\tilde{\nu}_\tau$ mass shown at d).

measurements, but since the NUHMG model explores compact mass spectrum, these are not excluded yet, and therefore represent an interesting region for the analysis. In the plot 10.2(c) the $\tilde{t}_1$ mass takes values in the range $417 < m_{\tilde{t}} < 885$ GeV, due to the very low production cross-section for direct $\tilde{t}$ production these points are not yet excluded by LHC measurements and have the right masses for the naturalness criteria. The $\tilde{\nu}_\tau$ mass is shown in the figure 10.2(d), but there is no exclusion done for the $\tilde{\nu}_\tau$ NLSP case, so there is no constrain made for its mass.

The mass spectrum of individual points has been already investigated in the section 9.1 and the mass spectrum for two points in the B and C regions has been shown in the figure 9.1. In the figure 10.3(a) the NUHMG grid mass spectrum for the fixed $m_{1/2} = 530$ GeV is shown. For a constant $m_{1/2}$ the $\tilde{q}$ and $\tilde{g}$ masses are constant as well, and $\tilde{g}$ is always heavier than the $\tilde{q}$. Spectrum of gauginos and $\tilde{l}$ is more compact for lower $m^2_{H_1}$, but the $\tilde{g}$, $\tilde{q}$ and $\tilde{t}_1$ mass difference is almost unchanged. Also, these points have a larger strong production cross-section. The crossing of the $\tilde{\chi}^0_1$ and $\tilde{\ell}_{\mathrm{L}}$ line around $m^2_{H_1} = 3.15$ TeV^2 shows the transition between

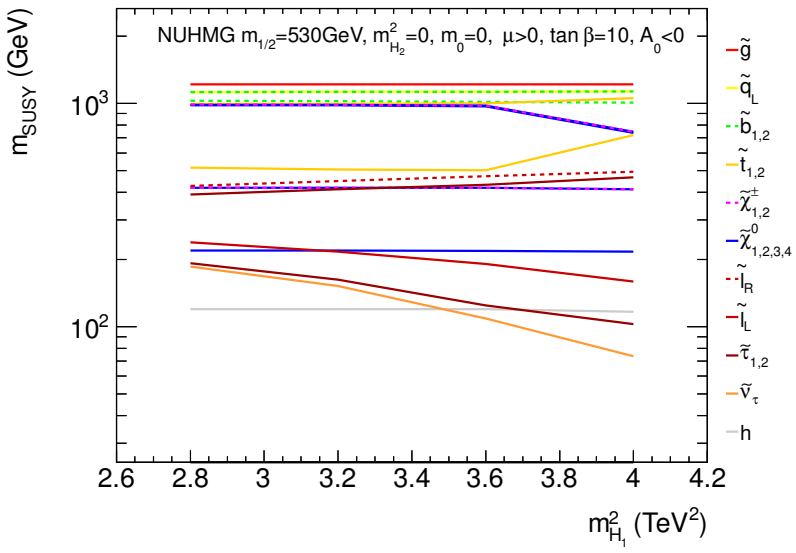

(a) $m_{1/2} = 530$ GeV

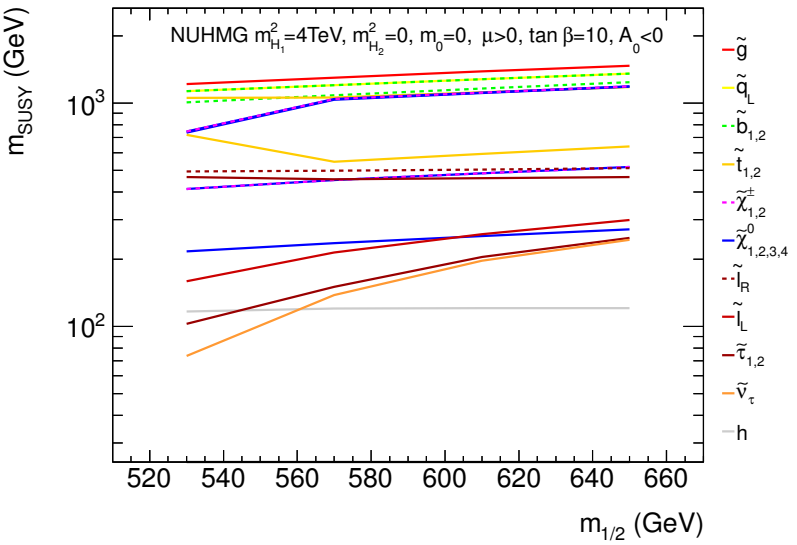

(b) $m^2_{H_1} = 4$ TeV^2

Figure 10.3.: NUHMG model sparticle masses for $m_{H_1^2}$ and fixed $m_{1/2} = 530$ GeV (a) and for $m_{1/2}$ and fixed $m^2_{H_1} = 4$ TeV^2 (b).

the B and C regions. In the figure 10.3(b) the mass spectrum is shown for fixed $m^2_{H_1}$ = 4 TeV. Here the $\tilde{q}$ and $\tilde{g}$ masses increase for higher $m_{1/2}$ but their mass differences are preserved, and the mass spectrum of gauginos and $\tilde{l}$ is more compact for high $m_{1/2}$ values. The transition from C to B region is around $m_{1/2} = 600$ GeV. This

brings to the conclusion that jets production will not vary to a large extent, while l and τ p_T and missing transverse momenta will differ for different points in the grid.

10.3. Cross Section and Production Channel Analysis

The NUHMG grid needs to be investigated in the parameter space range which has high enough cross-section at 8 TeV LHC p-p collsions. For this reason the total and the strong production cross-section is investigated. Firstly, the dependency of the production is investigated with respect to different c.m.e., and secondly the NUHMG grid cross-section at 8 TeV is shown for all points for different productions.

An interesting feature of the NUHMG model is the strong production cross-section dependency on the c.m.e. Namely, in this model the slepton and gaugino production have a high branching fraction which also depends on the c.m.e. In the figure 10.4 the LO cross-section 10.4(a) and branching fraction 10.4(b) for all productions are shown for one point of Minimal Supergravity Model, mSUGRA (left), and NUHMG (right) model. The total cross-section is of the same order for both models, but strong production cross section for NUHMG is smaller than for mSUGRA. Namely, the branching fraction into strong production takes values from 40% for 8 TeV to 60% at 13 TeV for NUHMG, in contrast to mSUGRA which has 70% strong production at 8 TeV and 80% at 13 TeV. This shows that NUHMG model search strategy needs to be tailored for specific c.m.e.

The grid range needs to be selected to include viable points for 8 TeV searches. In the figure 10.5 the leading order (LO) cross-section obtained with PYTHIA 6.4.26 [159] for processes of $\tilde{q}\,\tilde{q}$, $\tilde{g}\,\tilde{g}$ and $\tilde{q}\,\tilde{g}$ production at 8 TeV is shown for total 10.5(a) and strong 10.5(b) production. The total production cross-section is in the range 2.5 pb - 10 fb, while strong production is around 1 - 300 fb. The branching fraction for the strong production is shown at 10.5(c), where strong production takes only 30-40 % of the total production for most of the points. Previous searches with 2-6 jets and mising transverse energy had the signal efficiency in the range below 1 % to more than 20 % [223]. The estimate of expected signal events was performed for assumed 3.5 % efficiency and 21 fb^{-1}, and is shown at 10.5(d).

With the aim to perform the strong production analysis, the estimate for the number of events for assumed signal efficiency and integrated luminosity is interesting up to 1 expected event, in order to be able to present exclusion limits including the systematic uncertainty. Therefore, the upper grid parameters range has been selected to have at least 1 expected signal event for assumed 3.5% signal efficiency and 21 fb^{-1}. The grid granularity has been chosen to fit the technically allocated budget of 1 million events. The resulting NUHMG grid was generated with 50 points and 20000 events per point.

The cross section used for the analysis of the NUHMG model has been calcualted at next-to-leading order (NLO) in the strong coupling constant, with added next-to-leading-log (NLL) accuarcy for the resummation of soft fluon emision, following the prescription from [224]. This allows for high reduction of theoretical uncertainties

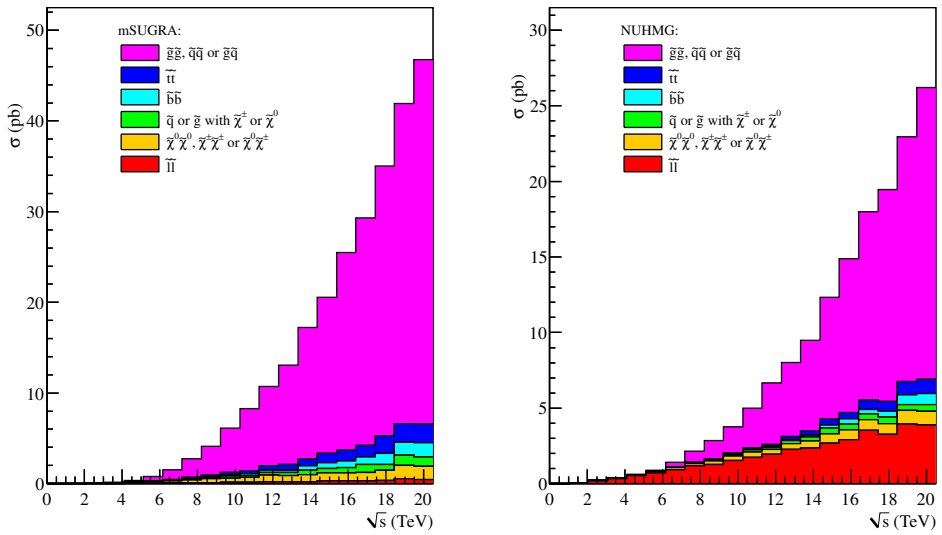

(a)

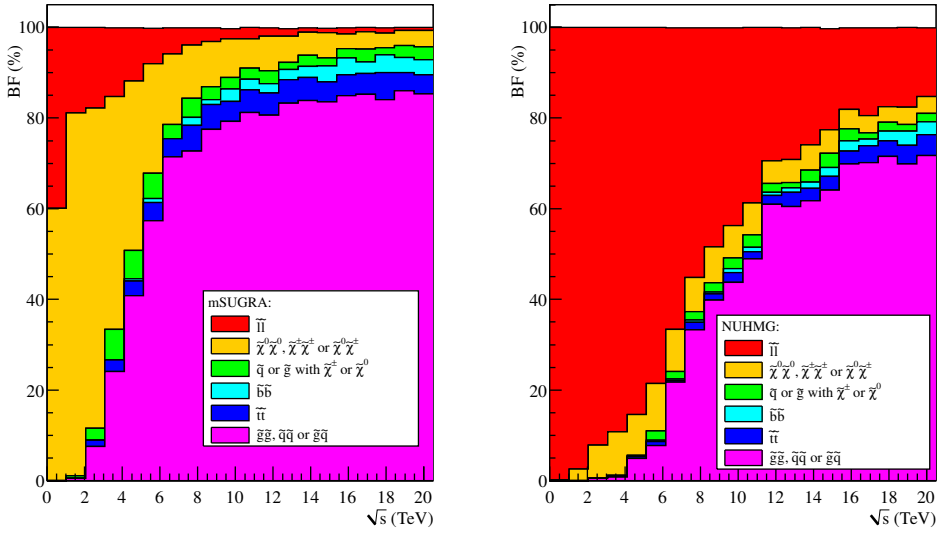

(b)

Figure 10.4.: NUHMG (left) and mSUGRA (right) typical points cross section (a) and branching fractions (b) at LO obtained with PYTHIA 6.4.22 [159] at different c.m.e. Given for the mSUGRA point (SU3) with $\tan\beta$=6, sign(μ)>0, m_0=100 GeV, $m_{1/2}$=300 GeV, A_0=-300 GeV, and NUHMG point with $\tan\beta$=10, sign(μ)>0, m_0=0, $m_{1/2}$=350 GeV, m_{H_2}=0, m_{H_1}=1.5 TeV, A_0=0 parameters.

due to unknown higher perturbative orders. Namely, for the strong production the interpolation tool NLL-fast [198] is used to obtain NLL+NLO cross-sections. As some parameter space regions are not covered with this method, the remaining parameter space cross-sections are calculated at NLO using PROSPINO 2.1 [191]. To obtain the systematic uncertainty on the cross section calculation, the 68% confidence level up and down variations for CTEQ6.6 [225], including uncertainty on the α_S, and MSTW2008 [226] PDF sets, together with the variations on the renormalization and facotrization scales by a factor of two, were varied according to prescription given in [224]. The nominal strong production NLL+NLO cross-section is shown in the figure 10.6 for all points of the NUHMG grid, where it takes values in the range 2 - 520 fb.

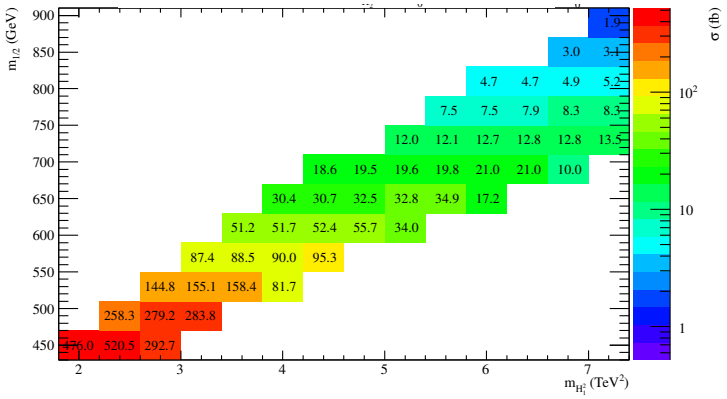

Figure 10.6.: NUHMG grid strong production cross-section at NLL+NLO obtained following the prescription from [224] using NLL-fast [198] and PROSPINO 2.1 [191] used in the analysis. It includes production processes of $\tilde{q}\ \tilde{q}$,$\tilde{g}\ \tilde{g}$,$\tilde{q}\ \tilde{g}$,$\tilde{b}\tilde{b}$,$\tilde{t}\ \tilde{t}$, $\tilde{\chi}\tilde{g}$ and $\tilde{\chi}\tilde{q}$. $\tilde{\chi}$ denotes all generations of $\tilde{\chi}^0$ and $\tilde{\chi}^{\pm}$. All cross-sections include both squark and anti-squark production.

In summary, an interesting feature of the NUHMG model is its high dependency of the strong production with the c.m.e in LHC conditions, therefore analysis needs to be tailored to a certain c.m.e. The NUHMG grid has been generated using constrains from the LEP measurements on the $\tilde{\chi}_1^0$, $\tilde{\chi}_1^{\pm}$ and $\tilde{\tau}_1$ masses. A scan into negative values of A_0 has been used to obtain m_h closest to 125.5 GeV. The resulting points are not excluded by previous measurements at the LHC, in particular measurements for the strong and third generation production, i.e. the $\tilde{q}$, $\tilde{g}$ and $\tilde{t}_1$ masses are in the right range. With the aim to perform strong production analysis the total and strong production cross-section at LO has been used for estimates. For NUHMG the strong production takes only 30-40 % of the total production, and cross-sections are in the pb-fb range at 8 TeV for $2.0 \leq m^2_{H_1} \leq 7.2$ TeV^2 and $450 \leq m_{1/2} \leq 890$ GeV. The cross-section used in the data analysis is calculated at NLL+NLO order for 50 NUHMG grid points.

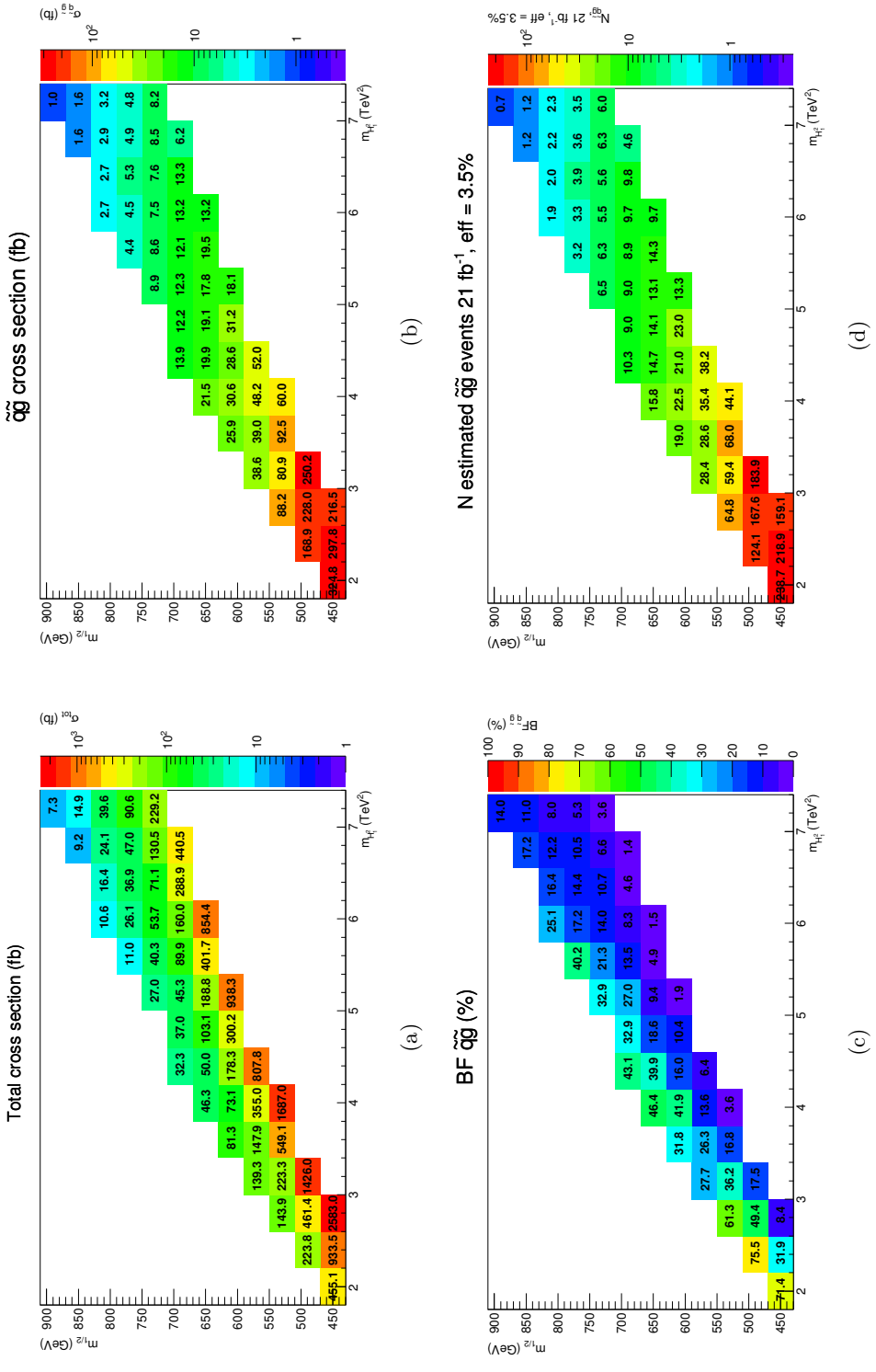

Figure 10.5.: NUHMG grid cross section at LO obtained with PYTHIA 6.4.26 [159] used for the estimate of yields in the 8 TeV search. Total cross section (a), $\tilde{q}\,\tilde{q}$, $\tilde{q}\,\tilde{g}$, $\tilde{g}\,\tilde{g}$, $\tilde{t}\tilde{t}$ and $\tilde{b}\tilde{b}$ production cross section (b), branching fraction of the $\tilde{q}\,\tilde{g}$ (all generations) production (c) and estimated number of $\tilde{q}\,\tilde{g}$ (all generations) signal events for 21 fb^{-1} and assumed signal efficiency of 3.5 % (d) are shown. All cross-sections include both squark and anti-squark production.

11. NUHMG Analysis Using Final States with Jets and Missing Transverse Momentum

NUHMG model analysis has been performed with a search for a $\tilde{q}$ and $\tilde{g}$ using final states with a lepton veto, multiple jets and missing transverse momentum with the 20.3 fb^{-1} of 8 TeV p-p collision ATLAS data. A dedicated signal region has been optimized for this model and added to the search with 0 leptons. A short analysis overview is shown in the section 11.1. The details of commonly used data and MC samples in section 11.2, event reconstruction, trigger and event cleaning in 11.3 are presented. The NUHMG grid cut flow optimization procedure in 11.4 and event selection including the new signal region in 11.5 are described. The standard model background determination in 11.6 and statistical treatment with systematic uncertainty considered in the analysis in 11.7 are described. The results, their interpretation and comparison are presented in the section 11.8.

11.1. Analysis Overview

The analysis using final states with jets and missing transverse momentum is dedicated to decays of heavy SUSY particles which produce long cascade decays with short-lived SUSY particles and visible jets, with the invisible LSP at the end of the decay chain showing up as missing energy in the detector. A good discriminant of the SUSY signal from the SM background are the variables which consider missing transverse momentum and transverse momentum of jets.

The 0-lepton search is targeting decays of $\tilde{q}$ and $\tilde{g}$ into an invisible $\tilde{\chi}_1^0$ with a possible intermediate $\tilde{\chi}_1^\pm$ in the decay chain. For this purpose, the so called 'simplified models' have been used. In addition, the performance is cross-checked using physical models like mSUGRA. In this scope, NUHMG model analysis has been added to the search with 0 leptons due to the similar final state when soft leptons are not passing the criteria of the lepton veto. The NUHMG model final states have been discussed in the section 9.2 and the targeted final states are shown in the figure 9.3. Due to the specific mass spectrum and specific kinematics of the NUHMG decays, a dedicated analysis has been set and added to the search.

The 0-lepton analysis consists of 15 signal regions (SR), with channels of inclusive jet multiplicities for 2-6 jets and additional cuts. The low jet multiplicity channels target direct decays of $\tilde{q}\,\tilde{q}$ production into the $\tilde{\chi}_1^0$ LSP, and the higher jet multiplicity is dedicated to longer decay chains in one-step decays of $\tilde{g}\,\tilde{g}$ production via $\tilde{\chi}_1^\pm$ into

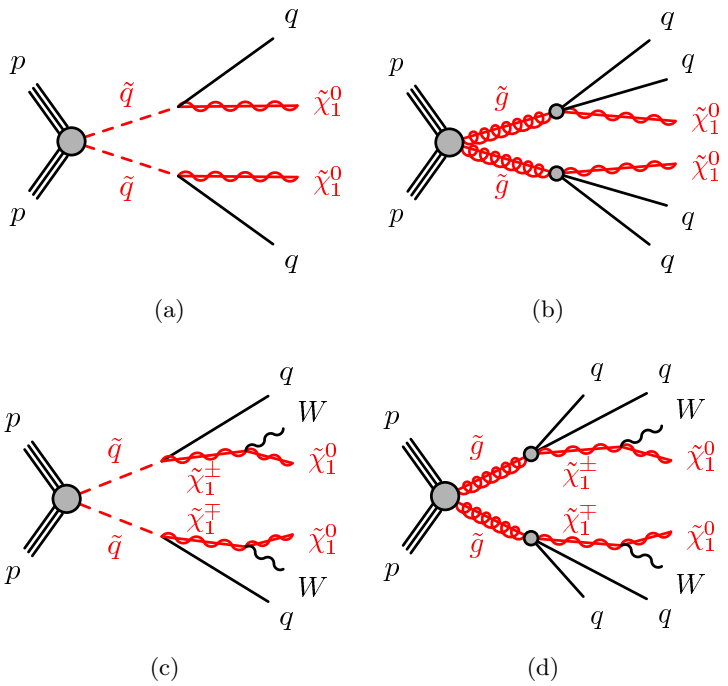

Figure 11.1.: Targeted final states in the search with no leptons, jets and missing transverse momenta. Feynman diagrams of direct decays of $\tilde{q}\,\tilde{q}$ (a) and $\tilde{g}\,\tilde{g}$ (b), and one step decays via $\tilde{\chi}_1^{\pm}$ for $\tilde{q}\,\tilde{q}$ (b) and $\tilde{g}\,\tilde{g}$ (c) are shown.

$\tilde{\chi}_1^0$ LSP, see figure 11.1. The NUHMG targeted final states have been shown in the figure 9.3, and a dedicated analysis uses the 6-jet selection.

Each SR has associated control regions (CR) which are used to estimate the SM content in the SR. They are placed close to SR region edges in order to reduce the uncertainties related to extrapolation from low p_T scale to the hard one. They are:

- $W(\rightarrow l\nu)$ with jets CR uses a b-veto and a selection with one lepton.
- $t\bar{t}$ and single t background uses a CR with a b-tag and the one lepton selection.
- Multi-jet background uses CR which has tightened and reversed cuts depending on the SR cut specifications.
- $Z(\rightarrow \nu\nu)$ with jets uses CR with the isolated photon selection, but in addition normalization of the SR estimate is performed using the $Z \rightarrow ll$ with jets events using a dedicated CR.
- Diboson with jets background estimate in the SR is performed using MC.

Validation regions are used as a cross check of the SR counts estimates, and are placed close to the SR cuts.

The first estimate of each background content in the SR is calculated using the so-called transfer factors (TF). They are determined from the ratio of expected number of MC events in the SR and CR. See more details in the section 11.7.1, where the TF is given by the equation 11.15 and estimated number of events in the SR calculated as in equation 11.16. The total uncertainty in the SR has contributions from the CR statistic uncertainty and the residual uncertainty from the extrapolation using the TF. In effect, the total uncertainty on the SR is significantly reduced due to the ratio of MC estimates in the TF. This motivates a looser CR definitions, to allow lower statistical uncertainty, without significantly increasing the uncertainty on the TF [213].

Next, the simultaneous likelihood fit using the counts in each CR of each SM processes is performed to have agreement of the observed and expected events for each CR. In this way normalization on the counts in SR for each background process is performed. In this procedure CR contamination by different SM processes and/or SUSY signal events are taken into account. The final total background estimate consists of central value for each process TF and its associated uncertainties.

The result of the likelihood fit for each SR is a set of normalized background estimates and uncertainties with a p-value calculated for each SR. First, a search for the excess of the SUSY signal is performed, with an assumption that SUSY has no contribution to the yields in the CRs, but contributes to the SR only, i.e. TF for the signal are not included in the fit. Second, if no excess is observed, fit using a MC estimate of the signal in the SR is performed, i.e. TF for the signal are included in the fit. Limits are set for examined SUSY parameter space, where theoretical and experimental uncertainties for the signal and background are included in the fit.

11.2. Data and Monte Carlo Samples

The data and MC samples commonly used in the analysis with jets and missing transverse momentum are described in this section, and further details can be found at [227].

11.2.1. Data Samples

The data sample used in this analysis was collected in 2012 with LHC p-p collisions at 8 TeV. The raw recorded data had 20.7 fb^{-1}, and after applying the beam, detector and data-quality requirements, it resulted in 20.3 fb^{-1}, see figure 11.2(a). The mean number of p-p interactions per bunch crossing was was 20.7, with a maximal value around 40 interactions per bunch crossing, see figure 11.2(b). The peak instantaneous luminosity per LHC fill had the typical value of $7\times10^{33}cm^2s^{-1}$, see figure 11.2(c) for the year 2012.

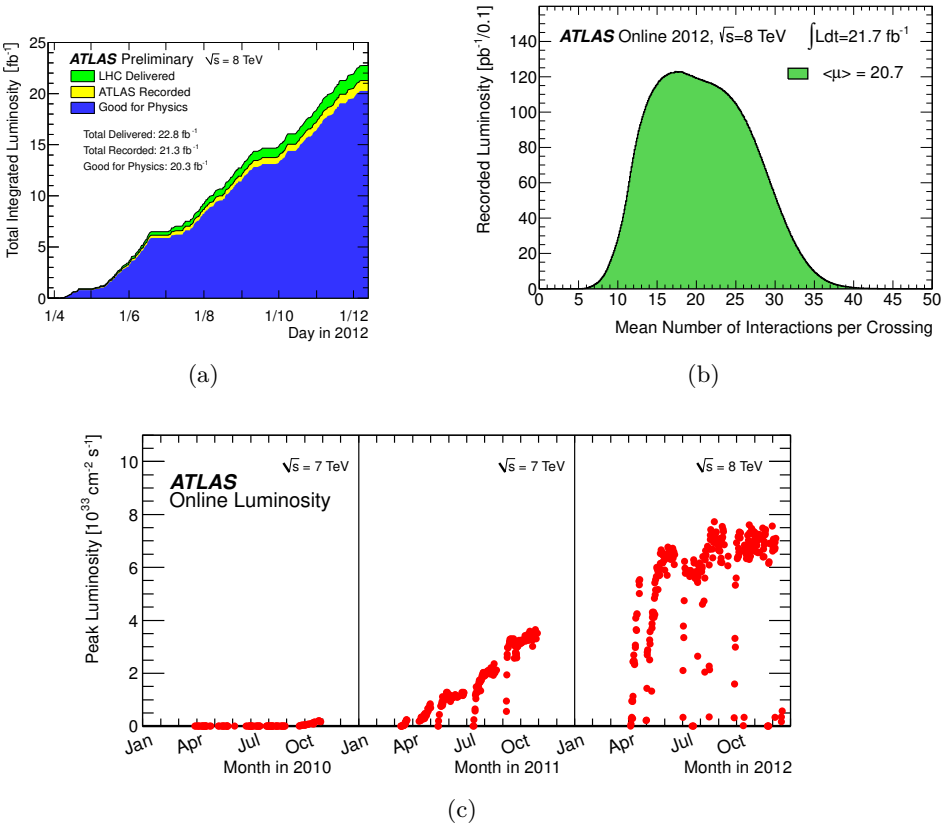

Figure 11.2.: Details of the data sample at 8 TeV p-p collisions used in the analysis. The collected integrated luminosity in 2012 was 20.3 fb^{-1} (a), mean number of p-p interactions per bunch crossing was 20.7 (b), and average the peak instantaneous luminosity per LHC fill in 2012 was 7×10^{33}cm^{2}s^{-1} (c) [228].

11.2.2. Monte Carlo Samples

Monte Carlo (MC) simulation samples are used to develop and optimize selections, determine SM background normalization factors from the data/MC ratio, and to access the SUSY signal sensitivity for the models. The considered backgrounds are those that can mimic the signal, with jets and missing transverse momentum in the event. These are W with jets, Z with jets, γ with jets, $t\bar{t}$ and single t events, and diboson MC samples. The table 11.1 shows the MC generators used for each background. In addition, the order of α_s cross-section calculation, tunes for the underlying event and parton distribution functions (PDF) sets used for each sample are shown. QCD multi-jet MC generated samples are used only for the data versus MC comparison and no corresponding uncertainty is evaluated [227], as this background is estimated using a data driven technique described in the section 11.5.2. The multi-jet MC events are generated using PYTHIA8 [229] using the

CT10 NLO PDF sets and the ATLAS tune AUET2B, see table 11.1.

Process	Generator + frag./had.	Cross-section order in α_s	Tune	PDF set
W+jets	SHERPA-1.4.0 [166]	NNLO [230]	SHERPA default	CT10 [231]
W+jets (•)	ALPGEN-2.14 [167] + HERWIG-6.520 [170, 234]	NNLO [230]	AUET2B [232]	CTEQ6L1 [233]
Z/γ^*+jets	SHERPA-1.4.0	NNLO [230]	SHERPA default	CT10
Z/γ^*+jets (•)	ALPGEN-2.14 + HERWIG-6.520	NNLO [230]	AUET2B	CTEQ6L1
γ+jets	SHERPA-1.4.0	LO	SHERPA default	CT10
γ+jets (•)	ALPGEN-2.14 + HERWIG-6.520	LO	AUET2B	CTEQ6L1
$t\bar{t}$	POWHEG-BOX-1.0 [235–237] + PYTHIA-6.426 [159]	NNLO+NNLL [238, 239]	PERUGIA2011C [240, 241]	CT10
$t\bar{t}$ (•)	MC@NLO-4.03 [171, 242] + HERWIG-6.520	NNLO+NNLL [238, 239]	AUET2B	CT10
Single top				
t-channel	ACERMC-38 [243] + PYTHIA-6.426	NNLO+NNLL [244]	AUET2B	CTEQ6L1
s-channel, Wt	MC@NLO-4.03 + HERWIG-6.520	NNLO+NNLL [245, 246]	AUET2B	CT10
$t\bar{t}$+EW boson	MADGRAPH-5.0 [172] + PYTHIA-6.426	NLO [247–249]	AUET2B	CTEQ6L1
Dibosons WW, WZ, ZZ, $W\gamma$ and $Z\gamma$	SHERPA-1.4.0	NLO [250, 251]	SHERPA default	CT10

Table 11.1.: Details of the SM background MC simulation samples used in the analysis [31]. The MC generator, order of α_s of cross-section calculation, tune used for the underlying event and PDF sets are shown. Samples marked with (•) are used for the systematic uncertainty evaluation. For the γ+jets process the LO cross-section is taken directly form the MC generator. Where it is leading order (LO), next-to-leading order (NLO), next-to-next-to-leading order (NNLO), next-to-next-to-leading logarithm (NNLL).

The dominant background processes of W/Z + jets and $t\bar{t}$ use the nominal MC for the background estimate. The Z+jets background estimate, in addition, uses the γ + jets MC samples in the data-driven normalization procedure in order to estimate the systematic uncertainty, where more details about this technique are provided in the section 11.5.2. The $t\bar{t}$ nominal MC events sample has been reweighed in bins of p_T to match the top quark pair differential cross-section observed in ATLAS data [252, 253]. No such procedure has been applied to the alternative MC sample for $t\bar{t}$, used for the theoretical uncertainty determination, because this MC reproduces better its p_T distribution. However, this MC generator is not used for the nominal sample as it does not reproduce well the high jet-multiplicity events.

The NUHMG MC signal sample was generated using the same setup as described in the section 9.1. The SUSY and Higgs mass spectrum and mixing angles are

computed with SOFTSUSY 3.3.4 [154], while the SUSY and Higgs particle decays are calculated using SUSY-HIT [156] as an interface to decay calculators SDECAY 1.3 [158] and HDECAY 3.302 [157] respectively. The event generation was performed using PYTHIA-6.426 [159] using PDF set CTEQ6L1. Signal cross-section calculation is already described in the section 10.3 using the NLO+NLL order calculation from the prescription [224] using NLL-fast [198] and PROSPINO 2.1 [191] calculators. Namely, the signal cross-section is calculated at NLO order in the α_S, including the resummation of the soft gluon emission at the NLL accuracy [195, 199–202]. The nominal cross-section and its uncertainty are determined from the variations in different PDF sets, factorization and renormalization scales.

All MC samples are generated using the standard ATLAS wide parameters, as defined in [232, 254, 255]. The SM background samples are generated using the full ATLAS detector simulation [174] which uses GEANT4 [256]. Only the W/Z/γ + jets with $p_T < 280$ GeV and nominal $t\bar{t}$ samples are generated using the fast simulation which uses parametrisation of the ATLAS detector for EM and hadronic calorimeters and GEANT4 for the remaining detector components. The same fast simulation setup is used for the SUSY signal simulation, where fast simulation was validated against full GEANT4 simulation for several SUSY signal points.

In the step of digitization each event is overlaid with additional minimum bias events, which are generated using the PYTHIA8, AM2 tune and LO PDF set of MSTW2008LO. To obtain the same pile-up conditions as in data, each MC event is re-weighted to the distribution of the mean number of interactions observed in data.

11.3. Event Reconstruction, Trigger and Event Cleaning

The event reconstruction, trigger selection and event cleaning commonly used in the analysis with jets and missing transverse momentum are described in this section, and further details can be found at [227].

11.3.1. Event Reconstruction

In the event reconstruction the following object definitions have been commonly used in the analysis with jets and missing transverse energy. The signal region selection requires jets, missing transverse energy and a veto on the electrons and muons. The photons are used for the Z + jets background normalization and b-jet tagging for the W/Z/γ* + jets and $t\bar{t}$ control region definitions, while τ definition is used only for dedicated τ validation regions. In addition, the main sources of uncertainty are presented for each object definition and the overlap removal procedures used in the analysis are explained.

Jet candidates are reconstructed using the anti-k_T algorithm [186, 257] with a radius distance parameter $R = 0.4$, which is suitable for a SUSY analysis with large jet multiplicity. This algorithm takes as input the energies of clusters [184, 185] of calorimeter cells seeded by clusters with energy high above the measured noise. The

jet momenta are constructed by summing up on all cell clusters four-momenta and using a zero mass.

The jets are corrected for pile-up effect, using the method described in [258]. The effect of pile-up occurs due to high instantaneous luminosity of p-p interactions, where multiple interactions occur in the same bunch crossing, and additional interactions can be detected in the callorimeters due to interactions in the neighbouring bunch crossings. Since particles associated with a jet can be detected in wide area of the detector, reconstruction and calibration of jets is sensitive to the pile-up. Jets which occupy large detector area are more affected by the pile-up interactions. Therefore, each jet needs to be corrected for the pile-up on the event by event basis. First the event-by-event pile-up activity and jet sensitivity to the pile-up are estimated. Next, the effect of pile-up on the jet is subtracted, by applying a correction on four momenta of each jet in the event for the pile-up fluctuation, based on jet area and event pile-up activity [179].

The jet calibration scheme classifies topological jet clusters as electromagnetic or hadronic using the local cluster weighting (LCW) jet calibration method [185, 259], where two jet type corrections are determined from MC and data, and applied on each jet accordingly. In this way the jet energy resolution (JER) is improved by different weighting of electromagnetic and hadronic showers. On top of this, the 'jet energy scale' (JES) corrections are applied, related to the calorimeter response to the true jet energy [185, 260]. Only jet candidates with $p_T > 20$ GeV in $|\eta| < 4.5$ after all corrections are considered in the analysis. There are two types of uncertainties for jets, which are related to JER and JES scale.

The b and c quark jets are identified using the 'MV1' b-tagging algorithm at the 70% efficiency and a light quark rejection factor of 140, which was determined with simulated $t\bar{t}$ events [261]. The b-tagged jet candidates with $p_T > 40$ GeV and $|\eta| > 2.5$ are considered in the analysis.

Lepton candidates have two levels of definitions in the analysis with jets and missing transverse momentum, since they are rejected in the signal region, but are used in the control region selection. 'Baseline' lepton definition is designed to maximize W + jets and $t\bar{t}$ background rejection with the lepton veto in the signal region selection. The 'high-purity' definition leptons are used in the control region estimates for the W + jets and $t\bar{t}$ backgrounds and they have additional requirements on the leptons for higher purity.

Electron candidates for baseline selection are required to have $p_T > 10$ GeV and $|\eta| > 2.47$, and to satisfy 'medium' electron shower shape and track selection criteria as described in Ref. [262], with a modification which reduces the impact of pile-up and is suitable for 2012 tighter trigger selection criteria. High-purity electrons must have $p_T > 25$ GeV, 'tight' modified selection criteria, the primary vertex transverse impact parameter must be $|d_0^{PV}| < 1$ mm and the longitudinal $z_0^{PV} < 2$ mm.

Muon candidates for the baseline selection need to have hits in the muon spectrometer and in the inner detector, as described in the [263]. They need to have $p_T > 10$ GeV and $|\eta| < 2.4$. High purity muon candidates in addition need to have p_T

$>$ 25 GeV and $|\eta| < 2.4$,, tracks must be isolated, and the primary vertex transverse impact parameter $d_0^{PV} < 0.2$ mm and longitudinal $|z_\mu - z_0^{PV}| < 1$ mm requirements are added to reject the cosmic events.

Resolving overlapping objects needs to be performed in case when objects passing the selection criteria are overlapping, in order to select just one object for the analysis [264]. The selection uses a geometric variable $\Delta R = \sqrt{\Delta\Phi^2 + \Delta\eta^2}$ between each two considered objects, and criteria are applied in the following order for jets in $|\eta| < 2.8$. First, since most of the electrons are reconstructed by the jet algorithm, if an electron and a jet are in $\Delta R < 0.2$, the object is interpreted as an electron, and the jet is discarded. Same is applied for a overlapping photon with a jet. Second, in order to separate prompt muons from the muons originating from a hadron decay within a jet, the reconstructed muons which are not isolated are rejected. If a muon and a jet are in $\Delta R < 0.4$, the selected object is the jet, while the muon is discarded. Third, is the case when a hadron jet looses a fraction of its energy to the electron, then if any remaining electron in $0.2 \leq \Delta R < 0.4$ is overlapping with a jet, the jet is kept and the lepton is discarded.

Missing transverse momentum $E_{\mathrm{T}}^{\mathrm{miss}}$ is calculated by performing the vector sum of the momenta in a transverse plane for each reconstructed object, and by balancing this sum to obtain zero momentum. Namely, clusters are associated to objects like electron, photon, jet or a muon. Remaining clusters not classified in any of these objects are grouped under a 'soft term'. Then the $E_{\mathrm{T}}^{\mathrm{miss}}$ is calculated from a negative sum of calibrated cluster energies inside the objects in x and y direction as:

$$E_{\mathrm{T}}^{\mathrm{miss}}{}_{x,y}^{RefFinal} = E_{\mathrm{T}}^{\mathrm{miss}}{}_{x,y}^{RefEle} + E_{\mathrm{T}}^{\mathrm{miss}}{}_{x,y}^{RefGamma} + E_{\mathrm{T}}^{\mathrm{miss}}{}_{x,y}^{RefJet} + E_{\mathrm{T}}^{\mathrm{miss}}{}_{x,y}^{Muons} + E_{\mathrm{T}}^{\mathrm{miss}}{}_{x,y}^{SoftT}$$

where $E_{\mathrm{T}}^{\mathrm{miss}}{}_{x,y}^{RefEle}$ is the contribution from the electrons, $E_{\mathrm{T}}^{\mathrm{miss}}{}_{x,y}^{RefGamma}$ from photons, $E_{\mathrm{T}}^{\mathrm{miss}}{}_{x,y}^{Muons}$ from muons and $E_{\mathrm{T}}^{\mathrm{miss}}{}_{x,y}^{SoftT}$ which is calculated from locally calibrated clusters which are not included in the reconstructed objects. This definition does not include a contribution using the τ object definition, but its contribution is included via terms of $E_{\mathrm{T}}^{\mathrm{miss}}{}_{x,y}^{RefJet}$ or $E_{\mathrm{T}}^{\mathrm{miss}}{}_{x,y}^{SoftT}$ [178, 190]. The uncertainties arising from each object are propagated to the $E_{\mathrm{T}}^{\mathrm{miss}}$ uncertainty using the uncertainties on the scale and resolution.

Photon object definition is used only in the Z + jet background estimation, and not in the signal region selection. Photons are required to have $p_T > 130$ GeV and $|\eta| < 1.37$ or $1.52 < |\eta| < 2.47$, satisfy photon shower shape and electron rejection criteria, and isolation [265]. The resolving of jets and photons is done with the removal of jets in the $\Delta R < 0.2$ of a photon candidate.

Tau object definition is not used in any step of the selection, but only in the tau related validation regions. The tau objects need to be reconstructed with p_T-correlated track counting algorithm as described in Ref. [182]. For hadronically decaying τ the purity of the validation in the background events is in the range of 65% - 90 %.

11.3.2. Trigger Selection

The triggers commonly used in the analysis were chosen to allow for full efficiency in the signal region and to have high statistics in the control regions for the data driven estimates. In the table 11.2 all trigger chains used in the analysis are presented, using ATLAS trigger naming scheme. The trigger for the analysis SR requires events with a jet of $p_T > 80$ GeV before any jet correction and uncorrected missing transverse energy of at least 100 GeV. The triggers which are used for the selection in the control and validation regions require an isolated electron with $p_T > 24$ GeV, muon with $p_T > 24$ GeV or a photon with $p_T > 120$ GeV. For multi-jet background determination single jet triggers were used, where average of pre-scales over full data taking sample are given in the table. In the QCD background estimation procedure, average over data taking periods is used [227]. Details about SR, CR and VR selections will be given in the section 11.5.

Region	Trigger Chain	L2 Chain	L1 Seed	Prescale
SR	EF_j80_a4tchad_xe100_tclcw_veryloose	L2_j75_c4cchad_xe55	L1_J50_XE40	1
CRY	EF_g120_loose	L2_g120_loose	L1_EM30	1
VRZ	EF_mu24i_tight	L2_mu24i_tight	L1_MU15	1
CRW	EF_e24vhi_medium1	L2_e24vhi_medium1	L1_EM18VH	1
CRT	EF_e60_medium1	L2_e60_medium1	L1_EM30	1
QCD	EF_j55_a4tchad	L2_j50_c4cchad	L1_J15	28919
	EF_j80_a4tchad	L2_j65_c4cchad	L1_J30	5511
	EF_j110_a4tchad	L2_j105_c4cchad	L1_J50	1282
	EF_j145_a4tchad	L2_j140_c4cchad	L1_J75	341
	EF_j180_a4tchad	L2_j165_c4cchad	L1_J75	195
	EF_j220_a4tchad	L2_j165_c4cchad	L1_J75	48
	EF_j280_a4tchad	L2_j165_c4cchad	L1_J75	9
	EF_j360_a4tchad	L2_j165_c4cchad	L1_J75	1
	EF_j460_a4tchad	L2_j165_c4cchad	L1_J75	1

Table 11.2.: Triggers used in the analysis. Trigger dedicated to SR uses 1 jet and $E_{\mathrm{T}}^{\mathrm{miss}}$, CRY uses a trigger with a photon, and VRZ, CRW, CRT use selections with a lepton or muon. The CRQ uses triggers with at least one jet, and the average trigger prescale over the full data sample is shown. However, the QCD estimation procedure uses average prescale for each trigger per data taking period [227].

Trigger efficiencies were estimated using a so called bootstrapping method [266], where a looser trigger is used with applying tighter selections to choose the optimal trigger for the given analysis requirements. In the figure 11.3 efficiency curves for the trigger $EF\_j80\_a4tchad\_xe100\_tclcw\_veryloose$ used for the SR selection, are shown by using the looser trigger $EF_xe50_a4tchad$ for bootsrapping. Trigger reaches full efficiency for jet $p_T > 130$ GeV (a), and for $E_{\mathrm{T}}^{\mathrm{miss}} > 160$ GeV (b), using the LCW jet calibration. The trigger efficiency over different data taking periods is unchanged, shown in (c). Therefore, in this analysis, for the SR selection trigger $EF\_j80\_a4tchad\_xe100\_tclcw\_veryloose$, and cuts on the first jet $p_T > 130$ GeV and $E_{\mathrm{T}}^{\mathrm{miss}} > 160$ GeV are chosen for signal selection to allow for high trigger efficiency [227].

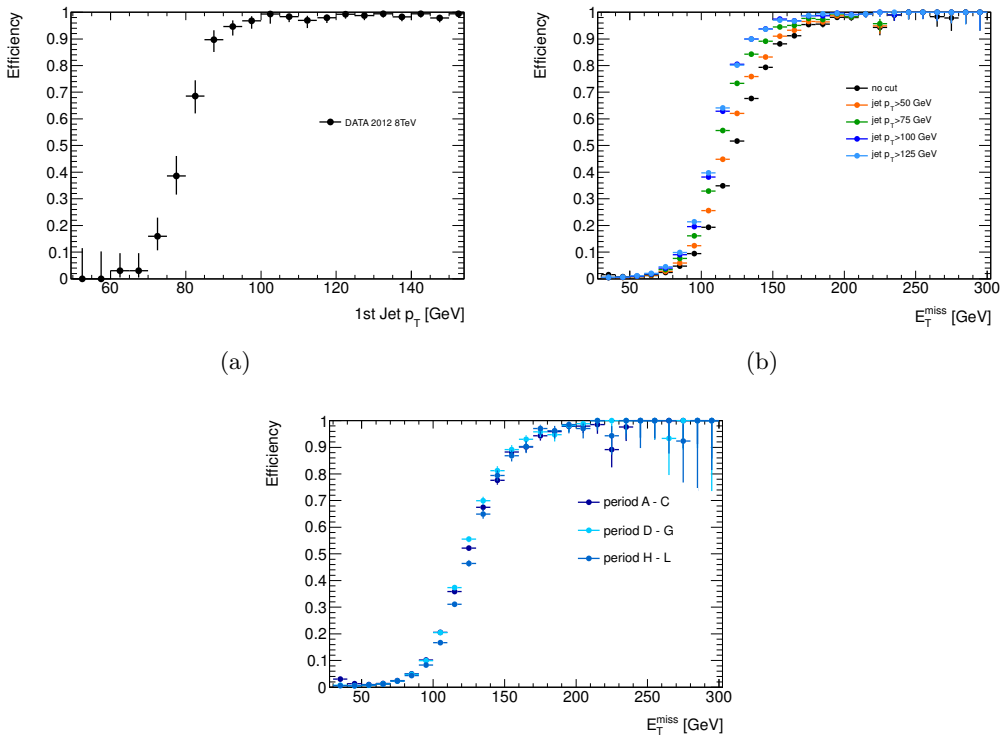

Figure 11.3.: Efficiency curves for jet p_T (a) and $E_{\mathrm{T}}^{\mathrm{miss}}$ (b) for *EF_j80_a4tchad_xe100_tclcw_veryloose* trigger, and efficiency curves for the $E_{\mathrm{T}}^{\mathrm{miss}}$ for different data taking periods (c), bootsrapped using the looser *EF_xe50_a4tchad* trigger. Efficiency curves shown after applied LCW jet calibration [227].

11.3.3. Event Cleaning

In order to obtain a representative data sample, the sources of events with fake missing energy due to non-collision backgrounds, bad calorimeter regions and fake muons need to be discarded. Same pre-selections are applied on the MC and data sample. Also, the non-removable non-collision backgrounds need to be estimated and their influence on the results of the analysis is evaluated in this section.

The non-collision background is the signal produced in the ATLAS detector in the processes which are not normal LHC collisions. The dominant sources of non-collision backgrounds are coherent noise in the LAr barrel and end-cap EM calorimeters, spike noise in the LAr hadronic end-cap calorimeters, cosmic-ray and beam-halo events where muons produce energetic photons in the calorimeter in the processes of bremsstrahlung, and beam-gas event where a proton collides with gas molecules in the volume of the beam pipe vacuum [227]. The event cleaning procedures for non collision backgrounds include the following:

- Vetoing events or full luminosity blocks in a time window around noise bursts in the Tile and LAr detector.
- Properties of the reconstructed jet are used to distinguish a jet originating from the p-p collision events, where non-collision background events can deposit real or fake energy in the calorimeters. Consequently bad jets with $p_T > 20$ GeV are rejected according ATLAS jet and $E_{\mathrm{T}}^{\mathrm{miss}}$ study recommendations [267].
- Negative energy cleaning is performed for the events which have a data corruption in the Tile calorimeter, which produces large negative cell or topo clusters energy. The cells with negative energy are normally not included in the jets by the reconstruction algorithm, which brings to large fake missing energy. A study showed that problematic events are successfully rejected with a cut of:

$$\frac{E_{\mathrm{T}}^{\mathrm{miss}\,CellOut}}{E_{\mathrm{T}}^{\mathrm{miss}}} \cos(\phi(E_{\mathrm{T}}^{\mathrm{miss}\,CellOut}) - \phi(E_{\mathrm{T}}^{\mathrm{miss}})) > 0.5 \tag{11.1}$$

  where the $E_{\mathrm{T}}^{\mathrm{miss}\,CellOut}$ is the negative energy deposited in the cells, which cannot be clustered in any object.
- A cut on charged fraction on a leading jet is used to reject cosmic events, beam background, jets not produced in a p-p collision, or detector noise where tracks are not expected but can have a accidental overlap with tracks from minimum bias events. The optimal cut value has been selected using the study performed on QCD MC samples and data [227]. Also, Tile hot cells, which were not masked in the MC event generation, have faulty events which are successfully removed with cuts on the jet charged fraction.
- The cut on timing is applied to reject remaining non-collision events. A cut on the energy weighted mean time of two leading jets after overlap removal is applied. Due to its low efficiency, the events failing this selection are used for a estimate on residual non-collision background contamination.

Residual non-collision background which remains after applying cuts of event cleaning, is estimated using the jet timing method. The jets originating from the p-p collisions are reconstructed with timing of 0 ns, and resolution of a few ns. However, jets originating from calorimeter noise, cosmic muons or beam background are more likely to be reconstructed out-of-time. The distribution of energy weighted mean time for the leading jets is used for the residual non-collision background estimate, which is defined as:

$$t_{N_j} = \frac{\sum_{i=0}^{N_j} t_i E_i}{\sum_{i=0}^{N_j} E_i} \tag{11.2}$$

where N_j is the number of considered leading jets in the event, t_i is the timing of the i-th jet, and E_i is the energy of the i-th jet. For a di-jet event, a cut on $|t_{N_j}| > 4$ ns successfully removes the non-collision background, and for higher jet multiplicity the $t_{N_j} > 4$ fully removes the non-collision background. The inverted cut on timing is used to perform an estimate of non-collision background in the signal region, which

was found to be negligible for a 2-6 jet multiplicity [227].

Dead calorimeter regions can strongly affect the reconstructed event topology, because they can lead to faulty jet energy reconstruction, jet energy response and resolution and fake missing transverse energy. For this reason, corrections on malfunctioning cells need to be placed, or the faulty events need to be discarded.

In this analysis there are two methods which estimate the energy which was not measured by the dead cells. The first method performs a correction using neighboring cells, with the assumption that the energy density is constant for all neighboring cells. This method is used by default in the jet p_T correction for all masked dead Tile cells and for isolated masked LAr cells before the $E_{\mathrm{T}}^{\mathrm{miss}}$ reconstruction. The second method performs a jet p_T correction on a jet by jet basis based on the jet profiling. From the MC simulation for the jet shape, the energy deposited in the dead calorimeter cells is estimated. The tool is run by default for all masked calorimeter cells, but it does not perform the jet energy nor missing transverse momenta correction. This method has the highest accuracy in the dead calorimeter cell energy deposition estimate.

In events with fake missing transverse energy due to dead calorimeter regions, faulty events are discarded. Here the multi-jet events can mimic signal due to the fake $E_{\mathrm{T}}^{\mathrm{miss}}$. In particular, for the dead Tile regions, a cut on $\Delta\phi(j_{1,2,3}, E_{\mathrm{T}}^{\mathrm{miss}})$ applied on the jets with $p_T > 40$ GeV successfully removes the fake $E_{\mathrm{T}}^{\mathrm{miss}}$ events [227].

Fake muons in the reconstruction can be caused by energetic jets which punch through the calorimeter and are detected in the muon system, or by badly measured inner detector tracks in jets which are wrongly matched to the muon spectrometer hits. They can cause a fake $E_{\mathrm{T}}^{\mathrm{miss}}$, and these events are vetoed if the muon does not satisfy the charge and momentum characteristics of a muon, or if the $E_{\mathrm{T}}^{\mathrm{miss}}$ contribution from the muon is large in the $E_{\mathrm{T}}^{\mathrm{miss}}$ of the event. Since this analysis uses no leptons, inefficiency of these cuts in the signal region is found to me negligible [227].

To summarize, after the trigger decision the event pre-selection is applied on the events. The events with jets which fail the quality criteria for the detector noise suppression and non-collision backgrounds, or they have no reconstructed primary vertex associated with five or more tracks are discarded [227].

11.4. Optimization for the NUHMG Model

The NUHMG model analysis was optimized in order to be compatible with the SUSY searches with a lepton veto, multiple jets and missing transverse momentum. It was optimized using multivariate technique and the fit setup assuming total integrated luminosity of 20.3 fb^{-1}. The optimization was performed in two steps. First step was done using the multivariate analysis. It was using MC signal and background samples and assuming 30% uncertainty on the background in the significance definition. The result is a ranked list of variable combinations with good signal separation, given with their range for further optimization. Second step was performed

using the background fit for the obtained optimal variable combination and their ranges. Here the MC samples and pseudo data for QCD were used, as described in the section 11.6, where the fit implementation was using control regions and signal and background uncertainties in the calculation. The multivariate analysis optimization was performed using 9 benchmark points, while the scan using the fit technique was performed with all 50 points of the NUHMG grid. The best performing cut flow using the fit was obtained for a pre-selection with 6 jets, high cut on $m_{\text{eff}}^{\text{incl}}$, relatively high cut on $\Delta\phi(j_{i>3}, E_{\text{T}}^{\text{miss}})$ and loose cut on transverse sphericity S_{T} . Improvements were set in place, where better fit stability was achieved without the usage of S_{T} , while obtaining similar expected exclusion. Further, high cut on $\Delta\phi(j_{i>3}, E_{\text{T}}^{\text{miss}})$ was traded for a very low cut on $E_{\text{T}}^{\text{miss}}$ $/m_{\text{eff}}^{\text{excl}}$ for a better QCD background removal.

Detailed optimization procedure is described in this section. The considered variables are defined in the section 11.4.1, NUHMG kinematic distributions are examined in 11.4.2, fast cut flow optimization using TMVA in 11.4.3, further optimization using the background fit in 11.4.4, and additional adjustments applied for the merging with the 0-lepton analysis in 11.4.5. Descriptions given in this section are taken and extended from [227].

11.4.1. SUSY Signal Separation Variables

NUHMG model has a jet multiplicity which peaks at 4 jets, which will be shown in the next section 11.4.2, while targeted final states include up to 8 jets and $E_{\text{T}}^{\text{miss}}$, described in the section 9.2. The model is explored in the analysis with a lepton veto, where channels with 2-6 jets and $E_{\text{T}}^{\text{miss}}$ are considered. Therefore, in this analysis optimization, a number of variables which exploit the event topology with high jet multiplicity and missing transverse energy for the signal separation from the SM background are considered. The main sources of background are the multi-jet, W+jets, Z+jets and $t\bar{t}$ background. The multi-jet background has a large cross-section, but SUSY signal can be well separated from it. Z($\rightarrow \nu\nu$)+jets background represents an irreducible background as it represents a true source of $E_{\text{T}}^{\text{miss}}$ with jets, but due to low cross-sections, it can be eliminated to a large extent. This leaves the W+jets and $t\bar{t}$ as the main sources of background in this analysis.

The variables used in the signal separation are defined as:

- N_{jet} - jet multiplicity is a powerful discriminating variable in SUSY searches, often used together with other cuts. It is defined in a inclusive way, where given jet multiplicity includes N_{jet} and higher number of jets. NUHMG model typically has a jet multiplicity with $N_{jet} \geq 4$.
- $E_{\text{T}}^{\text{miss}}$ - missing transverse momentum in the event. This analysis considers R-parity conserving SUSY models, and their decays have an invisible LSP or NLSP at the end of the decay chain, which results in missing transverse momentum. Due to large varieties of studied SUSY models, which consider various SUSY particles mass spectrum, the $E_{\text{T}}^{\text{miss}}$ can take values from rela-

tively low to very high values, and represents a good discriminant from all SM backgrounds for a large amount of models.

- $m_{\text{eff}}^{\text{incl}}$ - effective mass in the event, describes the total activity of the event. SUSY events typically have long decay chains and large p_T jets, and their m_{eff} is larger than for SM events. It is defined as the scalar sum of transverse momenta for all selected high p_T jets and leptons and the missing transverse energy, but since this analysis uses a lepton veto, the lepton term is equal to zero:

$$m_{\text{eff}}^{\text{incl}} = \sum_{i=1}^{N_{jet}} |p_T(i)| + E_{\text{T}}^{\text{miss}}. \tag{11.3}$$

  In this analysis the $m_{\text{eff}}^{\text{incl}}$ includes the N_{jet} number of jets defined by the channel, with p_T defined by the analysis selection, and in addition sums on all jets with $p_T > 40$ GeV in the event, i.e. the inclusive definition.
- H_{T} - scalar sum of jet p_T, in a similar way like $m_{\text{eff}}^{\text{incl}}$ represents the event activity, but does not rely on the size of the $E_{\text{T}}^{\text{miss}}$. It is defined as:

$$H_T = \sum_{i=1}^{N_{jet}} |p_T(i)|. \tag{11.4}$$

  It is a good discriminant against all SM backgrounds, but its performance needs to be evaluated and compared to other discriminating variables when considering a certain SUSY model. In this analysis H_{T} includes N_{jet} number of jets defined by the channel, with p_T defined by the analysis selection, and in addition sums on all jets with $p_T > 40$ GeV in the event, i.e. the inclusive definition.
- $E_{\text{T}}^{\text{miss}}$ $/m_{\text{eff}}^{\text{excl}}$ - ratio of $E_{\text{T}}^{\text{miss}}$ and $m_{\text{eff}}^{\text{excl}}$, represents a very good discriminating variable against multi-jet background. However, some SUSY models, like NUHMG, tend to have low $E_{\text{T}}^{\text{miss}}$, and only low cuts on $E_{\text{T}}^{\text{miss}}$ $/m_{\text{eff}}^{\text{excl}}$ can give good signal separation while maintaining sufficient signal statistics after performing the selection. Note that m_{eff} used in this context sums over N_{jets} number of jets used in the channel definition, with p_T defined by the analysis selection, i.e. exclusive definition.
- $E_{\text{T}}^{\text{miss}}$ $/\sqrt{H_{\text{T}}}$ - missing transverse momenta significance, is designed for a reduction of events with fake $E_{\text{T}}^{\text{miss}}$. It represents a measure of probability for $E_{\text{T}}^{\text{miss}}$ being higher than some threshold, for a given H_{T} . It is defined as ratio of $E_{\text{T}}^{\text{miss}}$ and $\sqrt{H_{\text{T}}}$, and it is mainly used for the multi-jet background reduction. Its performance needs to be compared to other discriminating variables when a certain SUSY model is studied. Note that H_{T} used in this context sums over N_{jets} number of jets used for the channel definition, with p_T defined by the analysis selection, i.e. exclusive definition.
- $\Delta\phi(j_{1,2,3}, E_{\text{T}}^{\text{miss}})$ and $\Delta\phi(j_{i>3}, E_{\text{T}}^{\text{miss}})$ - angle in the transverse plane between a jet and $E_{\text{T}}^{\text{miss}}$. They are a powerful discriminating variables, used to suppress

the multi-jet background. In the jet energy miss-measurement of a multi-jet event, a fake $E_{\mathrm{T}}^{\mathrm{miss}}$ is reconstructed in the direction of the jet. $\Delta\phi(j_{1,2,3}, E_{\mathrm{T}}^{\mathrm{miss}})$ is defined for up to first three jets in the event, while $\Delta\phi(j_{i>3}, E_{\mathrm{T}}^{\mathrm{miss}})$ is used for channels with 3-6 jets for all the jets in the event from the fourth.

- S_{T} - transverse sphericity, describes the event topology. SM events tend to have mostly back to back jets and leptons, while the rich cascade decays in SUSY events are produced from initial sparticles almost at rest, which decay in many directions, and therefore have jets and leptons distributed in all directions. Sphericity (S) is a variable which quantifies how much an event is shperical, and in ATLAS its transverse projection is considered. S_T, therefore, gives a measure of how much an event is spherical, with the projection to the transverse plane. An event which has two back to back events will have a $\mathrm{S}_T = 0$, while an event with many jets and leptons in all directions will have S_T close to 1. It is defined from the eigenvalues of the 2×2 sphericity tensor $S_{ij} = \sum_k p_{ki} p^{kj}$, where transverse momenta of all selected jets and leptons is included in the calculation:

$$S_T = \frac{2\lambda_2}{\lambda_1 + \lambda_2} \tag{11.5}$$

where $\lambda_1 > \lambda_2$ are the eigenvalues of the S_{ij} tensor [175]. SM events tend to have a large fraction of events with transverse sphericity close to 0, therefore, a cut on S_{T} is good for the SUSY signal separation.

11.4.2. NUHMG Strong Production Properties

The NUHMG model search is targeting a final state with multiple jets and missing transverse momentum. Firstly, jet multiplicity and $E_{\mathrm{T}}^{\mathrm{miss}}$ distributions are of interest. As this analysis is foreseen to be added to the search for $\tilde{q}$ and $\tilde{g}$ using final states with jets, missing transverse momentum and a veto on a lepton, already some optimization for more general searches have been done, and the NUHMG optimization needs to comply with requirements of jets p_T. Secondly, distributions of additional variables need to be investigated for improvements in the signal separation. In this section, distributions for the NUHMG signal and SM background will be given before applying the cut flow, but with already applied pre-cuts on trigger, event cleaning, lepton veto, $\Delta\phi(j_{1,2,3}, E_{\mathrm{T}}^{\mathrm{miss}}) > 0.2$, $E_{\mathrm{T}}^{\mathrm{miss}} > 160$ GeV, $p_T(jet1) > 130$ GeV and $p_T(jet2) > 60$ GeV.

In the figure 11.4 jet multiplicity, $E_{\mathrm{T}}^{\mathrm{miss}}$, $m_{\mathrm{eff}}^{\mathrm{incl}}$ and H_{T} distributions are shown for 3 NUHMG signal points and SM background. NUHMG model has a large jet multiplicity which peaks around 4 jets, and higher jet multiplicity can be a powerful discriminant against the SM background. As a typical R-parity conserving model, NUHMG signal has long $E_{\mathrm{T}}^{\mathrm{miss}}$ tails, and the $m_{\mathrm{eff}}^{\mathrm{incl}}$ and H_{T} distributions tend to take higher values than the SM background, and should be considered in the signal separation.

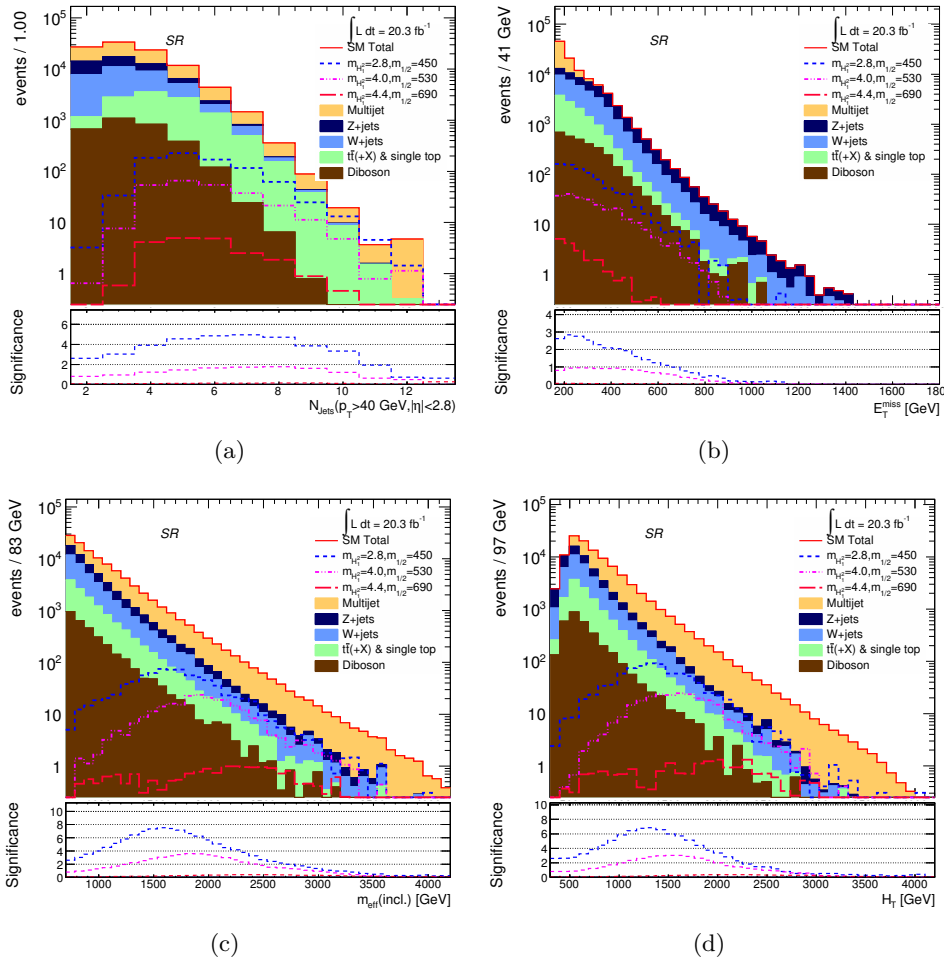

Figure 11.4.: NUHMG strong production distributions for N_{jet}, $E_{\mathrm{T}}^{\mathrm{miss}}$, $m_{\mathrm{eff}}^{\mathrm{incl}}$ and H_{T} . Pre-cuts on trigger, event cleaning, lepton veto, $\Delta\phi(j_{1,2,3}, E_{\mathrm{T}}^{\mathrm{miss}}) > 0.2$, $E_{\mathrm{T}}^{\mathrm{miss}} > 160$ GeV, $p_T(jet1) > 130$ GeV and $p_T(jet2) > 60$ GeV have been used. Significance is calculated using the formula 8.22.

NUHMG analysis needs to be added to a more general search for $\tilde{q}$ and $\tilde{g}$, where analysis is split into categorization according to jet multiplicity. Jets in the event are ordered by ascending jet p_T. Then for a channel of jet multiplicity N_{jets}, jets are selected such that the first jet $p_T(jet1) > 160$ GeV, and $p_T(jet) > 60$ GeV for the following jets, where in addition all remaining jets with $p_T > 40$ GeV are selected. In the figure 11.5 p_T distributions of first 6 jets for the NUHMG signal and SM are presented. First jet peaks around 450 GeV, so the cut on 160 GeV is in order. The 2-6 jets have sufficient signal events with $p_T > 60$ GeV. Therefore, this analysis can investigate channels with 4-6 jets.

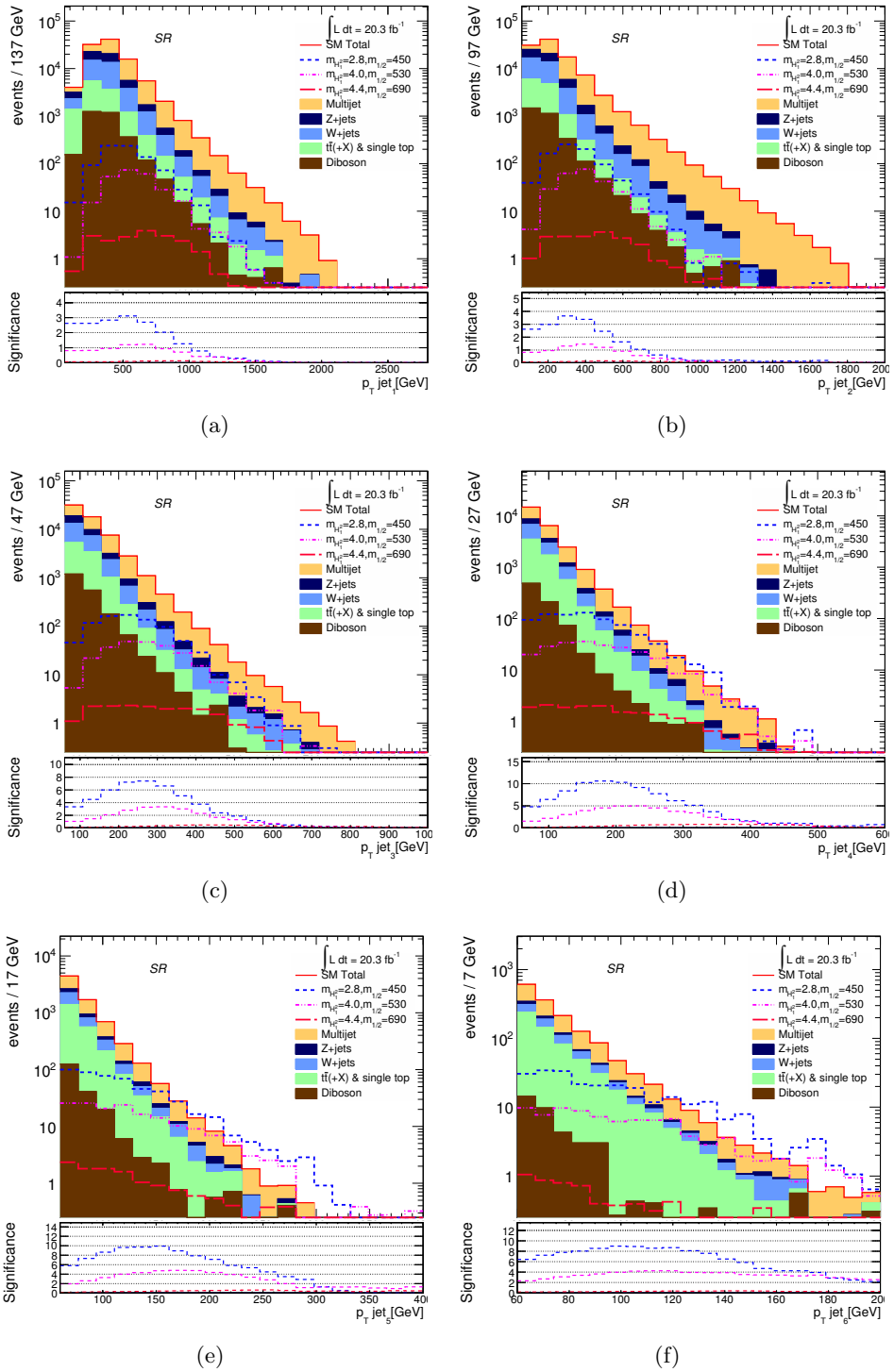

Figure 11.5.: NUHMG strong production distributions for jet p_T for the first 6 jets. Pre-cuts on trigger, event cleaning, lepton veto, $\Delta\phi(j_{1,2,3}, E_{\mathrm{T}}^{\mathrm{miss}}) > 0.2$, $E_{\mathrm{T}}^{\mathrm{miss}} > 160$ GeV, $p_T(jet1) > 130$ GeV and $p_T(jet2) > 60$ GeV have been used. Significance is calculated using the formula 8.22.

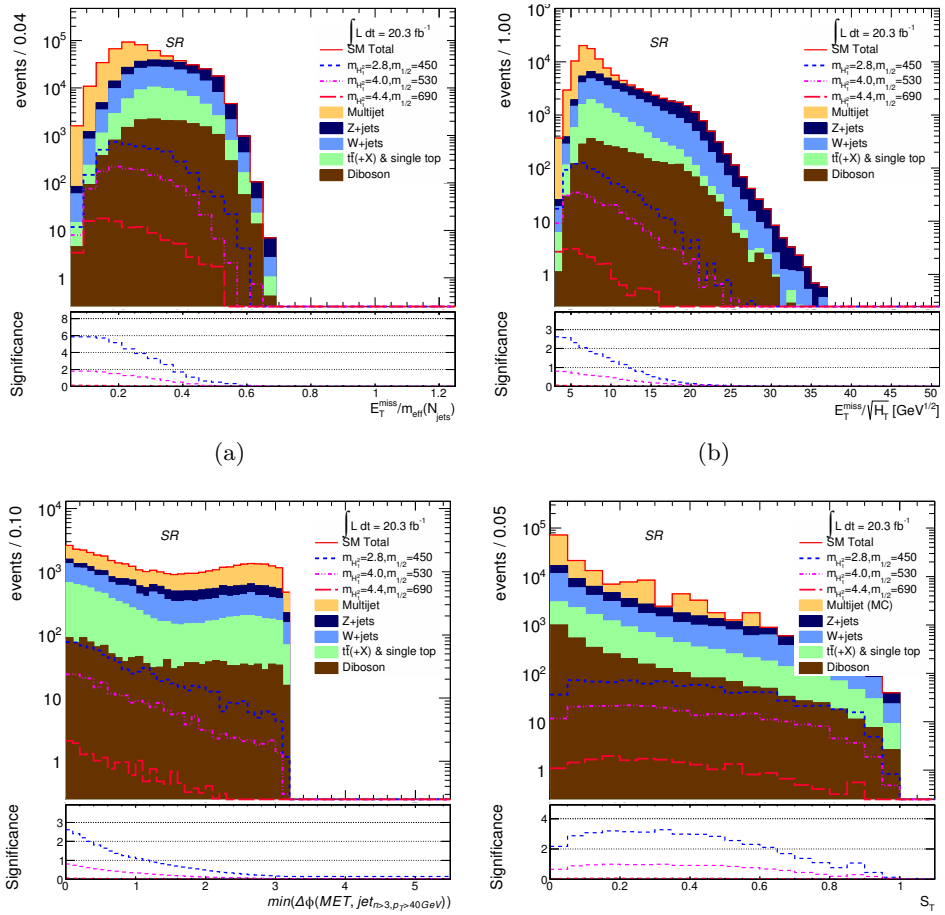

Figure 11.6.: NUHMG strong production distributions for $E_{\mathrm{T}}^{\mathrm{miss}}/m_{\mathrm{eff}}^{\mathrm{excl}}$, $E_{\mathrm{T}}^{\mathrm{miss}}/\sqrt{H_{\mathrm{T}}}$, $\Delta\phi(j_{i>3}, E_{\mathrm{T}}^{\mathrm{miss}})$ and S_{T}. Pre-cuts on trigger, event cleaning, lepton veto, $\Delta\phi(j_{1,2,3}, E_{\mathrm{T}}^{\mathrm{miss}}) > 0.2$, $E_{\mathrm{T}}^{\mathrm{miss}} > 160$ GeV, $p_T(jet1) > 130$ GeV and $p_T(jet2) > 60$ GeV have been used. Significance is calculated using the formula 8.22.

In order to improve signal separation, additional variables are considered. The NUHMG signal and SM background distributions for $E_{\mathrm{T}}^{\mathrm{miss}}/m_{\mathrm{eff}}^{\mathrm{excl}}$, $E_{\mathrm{T}}^{\mathrm{miss}}/\sqrt{H_{\mathrm{T}}}$, $\Delta\phi(j_{i>3}, E_{\mathrm{T}}^{\mathrm{miss}})$ and S_{T} are presented in the figure 11.6. Cutting on $E_{\mathrm{T}}^{\mathrm{miss}}/m_{\mathrm{eff}}^{\mathrm{excl}}$ and $E_{\mathrm{T}}^{\mathrm{miss}}/H_{\mathrm{T}}$ is not expected to bring improvement in signal separation, while $\Delta\phi(j_{i>3}, E_{\mathrm{T}}^{\mathrm{miss}})$ and S_{T} variables are expected to give improvement in a combination with other cuts. Therefore, in the NUHMG signal separation, a set of sensitive variables needs to be identified and the optimal cut flow needs to be chosen.

11.4.3. Fast Cut Flow Optimization Using TMVA

The NUHMG model is investigated in the m_{H1}^2 vs $m_{1/2}$ plane. To obtain better discovery and exclusion prospects 9 benchmark points were used. They were selected to cover typical B and C regions of the model, which are distributed parallel to the edge of the viable region, and with an increase in the masses of m_{H1}^2, see table 11.3. Three of these points are excluded or very close to the observed exclusion line obtained by general 0-lepton searches with 20.3 fb^{-1} [223]. Therefore, the new signal region was optimized to have a coverage higher than 3 benchmark points.

Point name	m_{H1}^2 (TeV^2)	$m_{1/2}$ (GeV)
NUHMG_2800000_450*	2.8	450
NUHMG_2800000_490*	2.8	490
NUHMG_2800000_530	2.8	530
NUHMG_4400000_570*	4.4	570
NUHMG_4400000_610	4.4	610
NUHMG_4400000_690	4.4	690
NUHMG_6000000_650	6.0	650
NUHMG_6000000_730	6.0	730
NUHMG_6000000_810	6.0	810

Table 11.3.: NUHMG model baseline points used for optimization. Points with (*) are excluded or very close to the observed exclusion line using standard 0-lepton setup with 20.3 fb^{-1} [223]. Improvement is viable for a coverage of more than 3 NUHMG points from this list.

The first part of the optimization was done using multivariate analysis in the TMVA [36] implementation. Instead of relying on the variable ranking of TMVA, variable combinations were run independently with TMVA using **Cuts method with Genetic Algorithm** for the minimization. For each variable combination the maximal significance was read out and the scan on the signal efficiency was performed, on which selection criteria were placed. In addition, the TMVA output for the cut flow was read out to obtain the range of the cuts of interesting variable combinations. The explanation of this method will be presented here.

The optimization was performed using the MC predictions of W+jets, Z+jets, diboson and $t\bar{t}$ backgrounds, and multi-jet pseudo-data background produced using the jet smearing method. Although the method has a possibility of performing optimization for each background separately, or combinations for selections of backgrounds expected to have dominant contribution, here all samples have been used

in the optimization.

First the variable combinations were prepared. For this $E_{\mathrm{T}}^{\mathrm{miss}}$, $E_{\mathrm{T}}^{\mathrm{miss}}$ $/m_{\mathrm{eff}}^{\mathrm{excl}}$, $m_{\mathrm{eff}}^{\mathrm{incl}}$, H_{T} , $E_{\mathrm{T}}^{\mathrm{miss}}/\sqrt{H_T}$, $\Delta\phi(j_{1,2,3}, E_{\mathrm{T}}^{\mathrm{miss}})$, $\Delta\phi(j_{i>3}, E_{\mathrm{T}}^{\mathrm{miss}})$ and S_{T} were used. In order to reduce the number of variable combinations, correlations of variables for signal and background were investigated. For correlations higher than 60% for each signal and background only one variable at a time was considered, i.e. a simple OR was used. Namely, these were H_{T} OR $m_{\mathrm{eff}}^{\mathrm{incl}}$, H_{T} OR $E_{\mathrm{T}}^{\mathrm{miss}}$ $/m_{\mathrm{eff}}^{\mathrm{excl}}$ and $E_{\mathrm{T}}^{\mathrm{miss}}$ OR $E_{\mathrm{T}}^{\mathrm{miss}}$ $/m_{\mathrm{eff}}^{\mathrm{excl}}$ OR $E_{\mathrm{T}}^{\mathrm{miss}}/\sqrt{H_T}$. The obtained number of variable combinations was 90.

In NUHMG model strong production the typical signature is expected to have at least 4 jets. Therefore, standard pre-cuts in the channels of at least 4, 5 and 6 jets were placed on the jet p_T (130, 60, 60, 60, 60, 60 GeV), $E_{\mathrm{T}}^{\mathrm{miss}}$ (160 GeV) and $\Delta\phi(j_{1,2,3}, E_{\mathrm{T}}^{\mathrm{miss}})$ (0.4). For each of 9 benchmark points all variable combinations for all 3 channels were run with the TMVA. In this way $90 \times 3 \times 9 = 2430$ variable-channel-point combinations were run with TMVA simultaneously.

Second, the TMVA implementation was run for each variable-channel-point combination with the Cuts method using the Genetic Algorithm for the minimization, for the specified variable ranges. From the obtained result the significance was read out using the simplified formula with 30% uncertainty for the background:

$$Z_A = \frac{S}{\sqrt{B + (\sigma_B B)^2}} \tag{11.6}$$

where S and B are number of signal and background events after all applied cuts, and σ_B is the assumed relative uncertainty for the background. The maximum significance and integrated significance were read out. In addition, the scan on the signal efficiency was performed. For each signal efficiency in the range 0.05 to 0.5 in steps of 0.05, the number of signal and background events, significance and the TMVA optimized cut flow were read out.

Third, the selection criteria were placed to obtain the good variable combinations, in two runs using $Z_A \geq 5$ and $Z_A \geq 3$ criteria. Firstly, the variable-channel-point combinations were selected for a maximum significance of 3(5), where the cases with integrated significance below 0.01 were rejected (sharp peaks). For the obtained combinations an efficiency scan was performed. Efficiencies with more than 1 signal event after applying all cuts were considered. For the signal efficiencies with significance higher than 3(5) cut flow was read out, and the maximum and minimum values for each cut were kept, providing an interesting range for a given cut on the variable in the given combination. Secondly, the list of points which passed the criteria for common variable-channel combination was made and ranked, see table 11.4. The maximum number of benchmark points passing the $Z_A \geq 5$ criteria was 5, and for $Z_A \geq 3$ criteria was 6.

	$Z_A \geq 5$		$Z_A \geq 3$
5 points	6j,$\Delta\phi(j_{i>3}, E_{\mathrm{T}}^{\mathrm{miss}})$,$m_{\mathrm{eff}}^{\mathrm{incl}}$,$E_{\mathrm{T}}^{\mathrm{miss}}$ /$m_{\mathrm{eff}}^{\mathrm{excl}}$,S_{T} * 6j,H_{T} ,$\Delta\phi(j_{i>3}, E_{\mathrm{T}}^{\mathrm{miss}})$,$E_{\mathrm{T}}^{\mathrm{miss}}/\sqrt{H_T}$,S_{T} 5j,H_{T} ,S_{T}	6 points	4j,H_{T} ,$E_{\mathrm{T}}^{\mathrm{miss}}/\sqrt{H_T}$,S_{T} 6j,H_{T} ,$E_{\mathrm{T}}^{\mathrm{miss}}$,S_{T} 6j,H_{T} ,$\Delta\phi(j_{1,2,3}, E_{\mathrm{T}}^{\mathrm{miss}})$,S_{T} 5j,H_{T} ,S_{T} 5j,H_{T} ,$\Delta\phi(j_{1,2,3}, E_{\mathrm{T}}^{\mathrm{miss}})$,$E_{\mathrm{T}}^{\mathrm{miss}}/\sqrt{H_T}$,S_{T} 6j,$\Delta\phi(j_{i>3}, E_{\mathrm{T}}^{\mathrm{miss}})$,$m_{\mathrm{eff}}^{\mathrm{incl}}$,$E_{\mathrm{T}}^{\mathrm{miss}}$ /$m_{\mathrm{eff}}^{\mathrm{excl}}$,S_{T} *
4 points	6j,H_{T} ,S_{T} 6j,H_{T} ,$\Delta\phi(j_{1,2,3}, E_{\mathrm{T}}^{\mathrm{miss}})$,S_{T} 5j,H_{T} ,$E_{\mathrm{T}}^{\mathrm{miss}}$,S_{T} 5j,H_{T} ,$\Delta\phi(j_{1,2,3}, E_{\mathrm{T}}^{\mathrm{miss}})$,$E_{\mathrm{T}}^{\mathrm{miss}}/\sqrt{H_T}$,S_{T} 4j,H_{T} ,$\Delta\phi(j_{1,2,3}, E_{\mathrm{T}}^{\mathrm{miss}})$,S_{T} 6j,$\Delta\phi(j_{1,2,3}, E_{\mathrm{T}}^{\mathrm{miss}})$,$\Delta\phi(j_{i>3}, E_{\mathrm{T}}^{\mathrm{miss}})$,$m_{\mathrm{eff}}^{\mathrm{incl}}$,$E_{\mathrm{T}}^{\mathrm{miss}}$ /$m_{\mathrm{eff}}^{\mathrm{excl}}$,S_{T} 6j,H_{T} ,$E_{\mathrm{T}}^{\mathrm{miss}}$,S_{T} 6j,H_{T} ,$\Delta\phi(j_{i>3}, E_{\mathrm{T}}^{\mathrm{miss}})$,S_{T}	5 points	6j,H_{T} ,$\Delta\phi(j_{i>3}, E_{\mathrm{T}}^{\mathrm{miss}})$,$E_{\mathrm{T}}^{\mathrm{miss}}/\sqrt{H_T}$,S_{T} 6j,H_{T} ,$\Delta\phi(j_{i>3}, E_{\mathrm{T}}^{\mathrm{miss}})$,$E_{\mathrm{T}}^{\mathrm{miss}}$,S_{T} 5j,H_{T} ,$E_{\mathrm{T}}^{\mathrm{miss}}/\sqrt{H_T}$,S_{T} 5j,H_{T} ,$\Delta\phi(j_{1,2,3}, E_{\mathrm{T}}^{\mathrm{miss}})$,$\Delta\phi(j_{i>3}, E_{\mathrm{T}}^{\mathrm{miss}})$,$E_{\mathrm{T}}^{\mathrm{miss}}$,S_{T} 4j,H_{T} ,$E_{\mathrm{T}}^{\mathrm{miss}}$,S_{T} 6j,$m_{\mathrm{eff}}^{\mathrm{incl}}$,$E_{\mathrm{T}}^{\mathrm{miss}}/\sqrt{H_T}$,S_{T} 6j,H_{T} ,$\Delta\phi(j_{i>3}, E_{\mathrm{T}}^{\mathrm{miss}})$,S_{T} 5j,H_{T} ,$E_{\mathrm{T}}^{\mathrm{miss}}$,S_{T} 4j,H_{T} ,S_{T} 4j,H_{T} ,$\Delta\phi(j_{1,2,3}, E_{\mathrm{T}}^{\mathrm{miss}})$,S_{T} 6j,$\Delta\phi(j_{i>3}, E_{\mathrm{T}}^{\mathrm{miss}})$,$m_{\mathrm{eff}}^{\mathrm{incl}}$,$E_{\mathrm{T}}^{\mathrm{miss}}/\sqrt{H_T}$,S_{T} 6j,$\Delta\phi(j_{1,2,3}, E_{\mathrm{T}}^{\mathrm{miss}})$,$m_{\mathrm{eff}}^{\mathrm{incl}}$,$E_{\mathrm{T}}^{\mathrm{miss}}$ /$m_{\mathrm{eff}}^{\mathrm{excl}}$,S_{T} 6j,$\Delta\phi(j_{1,2,3}, E_{\mathrm{T}}^{\mathrm{miss}})$,$m_{\mathrm{eff}}^{\mathrm{incl}}$,$E_{\mathrm{T}}^{\mathrm{miss}}/\sqrt{H_T}$,S_{T} 6j,$\Delta\phi(j_{1,2,3}, E_{\mathrm{T}}^{\mathrm{miss}})$,$\Delta\phi(j_{i>3}, E_{\mathrm{T}}^{\mathrm{miss}})$,$m_{\mathrm{eff}}^{\mathrm{incl}}$,$E_{\mathrm{T}}^{\mathrm{miss}}$ /$m_{\mathrm{eff}}^{\mathrm{excl}}$,S_{T} 6j,$\Delta\phi(j_{1,2,3}, E_{\mathrm{T}}^{\mathrm{miss}})$,$\Delta\phi(j_{i>3}, E_{\mathrm{T}}^{\mathrm{miss}})$,$m_{\mathrm{eff}}^{\mathrm{incl}}$,$E_{\mathrm{T}}^{\mathrm{miss}}$ /$m_{\mathrm{eff}}^{\mathrm{excl}}$ * 6j,$\Delta\phi(j_{1,2,3}, E_{\mathrm{T}}^{\mathrm{miss}})$,$\Delta\phi(j_{i>3}, E_{\mathrm{T}}^{\mathrm{miss}})$,$m_{\mathrm{eff}}^{\mathrm{incl}}$,$E_{\mathrm{T}}^{\mathrm{miss}}/\sqrt{H_T}$,S_{T}

Table 11.4.: Extensive list of interesting variable combinations obtained with TMVA optimization. 2430 variable combinations were tested using $E_{\mathrm{T}}^{\mathrm{miss}}$, $E_{\mathrm{T}}^{\mathrm{miss}}$ /$m_{\mathrm{eff}}^{\mathrm{excl}}$, $m_{\mathrm{eff}}^{\mathrm{incl}}$, H_{T} , $E_{\mathrm{T}}^{\mathrm{miss}}/\sqrt{H_T}$, $\Delta\phi(j_{1,2,3}, E_{\mathrm{T}}^{\mathrm{miss}})$, $\Delta\phi(j_{i>3}, E_{\mathrm{T}}^{\mathrm{miss}})$ and S_{T} variables with an OR for strongly correlated variables to reduce the number of combinations, using inclusive 4, 5 or 6 jet channels. Each variable combination was tested for maximum significance and then the scan was run for different TMVA testing signal efficiencies. In addition, cut flow for each efficiency was read out. There were 2 sets of criteria, first for $\mathrm{Z}_A \geq 5$ and second for $\mathrm{Z}_A \geq 3$ assuming 30% background uncertainty. Improvement compared to the standard 0-lepton searches would be reached for a coverage of more than 3 NUHMG points. Good performing candidates considered in this analysis are marked with (*).

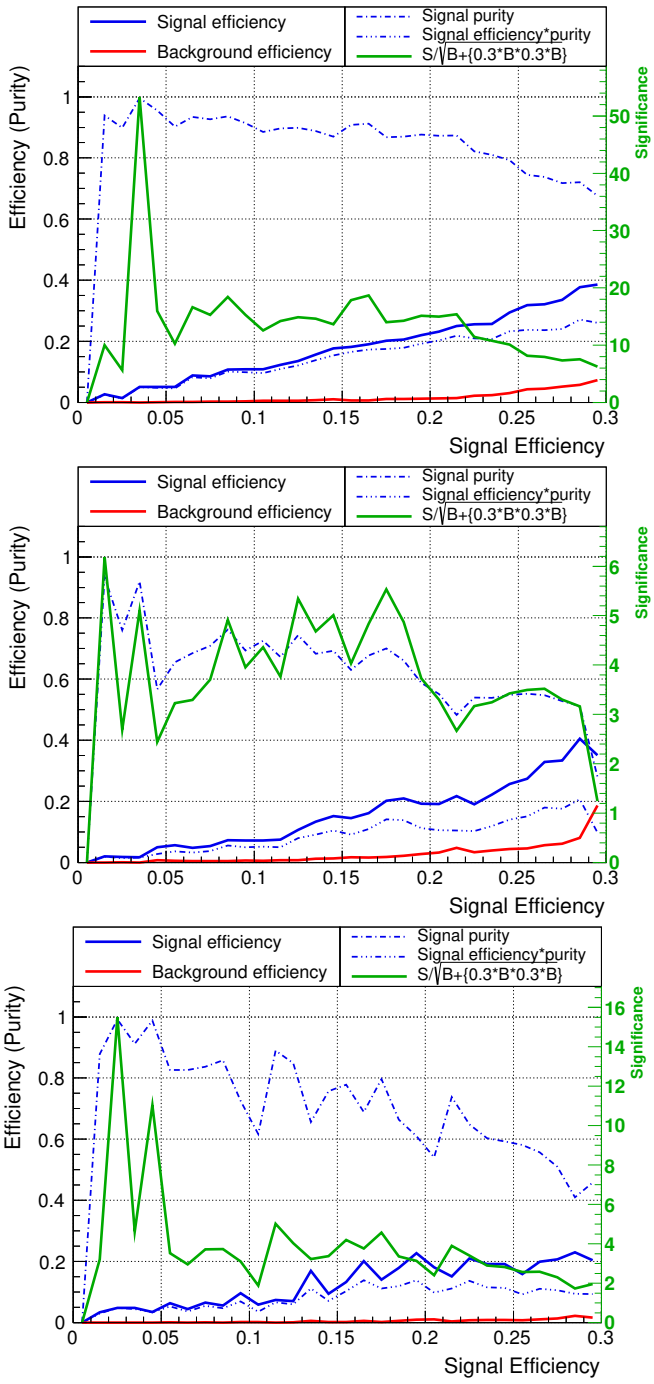

Figure 11.7.: TMVA optimization result for the 6-jet pre-selection using S_{T} , $\Delta\phi(j_{i>3}, E_{\mathrm{T}}^{\mathrm{miss}})$, $m_{\mathrm{eff}}^{\mathrm{incl}}$ and $E_{\mathrm{T}}^{\mathrm{miss}}$ $/m_{\mathrm{eff}}^{\mathrm{excl}}$ variables ('best for fit' scan selection) for the $m_{H1}^2 = 2.8$ TeV, $m_{1/2} = 450$ GeV, $m_{H1}^2 = 2.8$ TeV, $m_{1/2} = 490$ GeV and $m_{H1}^2 = 2.8$ TeV, $m_{1/2} = 530$ GeV points respectively. Significance of 5 can be achieved for 5 NUHMG points.

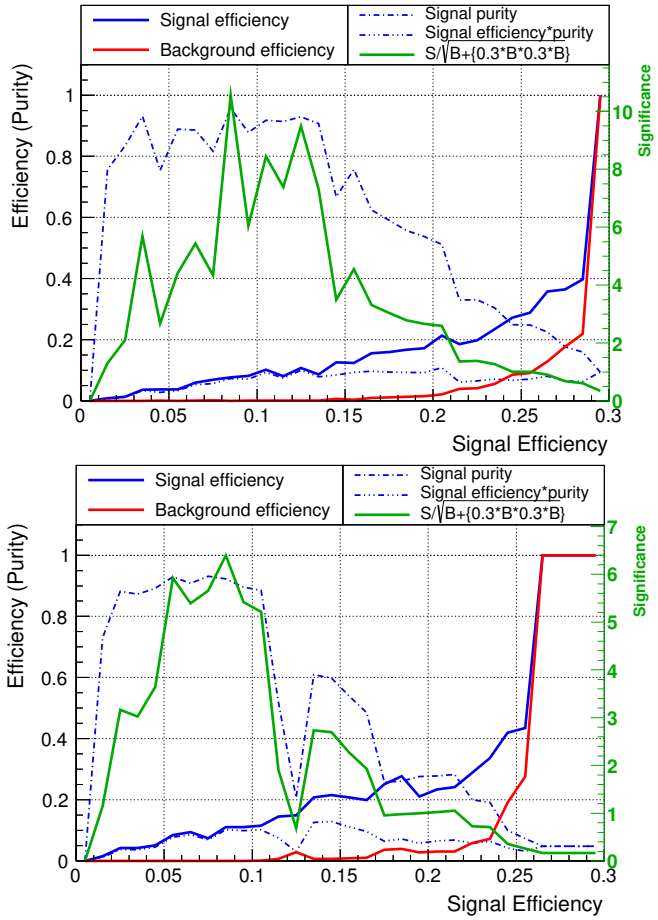

Figure 11.8.: TMVA optimization result for the 6-jet pre-selection using S_{T} , $\Delta\phi(j_{i>3}, E_{\mathrm{T}}^{\mathrm{miss}})$, $m_{\mathrm{eff}}^{\mathrm{incl}}$ and $E_{\mathrm{T}}^{\mathrm{miss}}$ $/m_{\mathrm{eff}}^{\mathrm{excl}}$ variables ('best for fit' scan selection) for the $m_{H1}^2 = 4.4$ TeV, $m_{1/2} = 570$ GeV and $m_{H1}^2 = 4.4$ TeV, $m_{1/2} = 610$ GeV points respectively. Significance of 5 can be achieved for 5 NUHMG points.

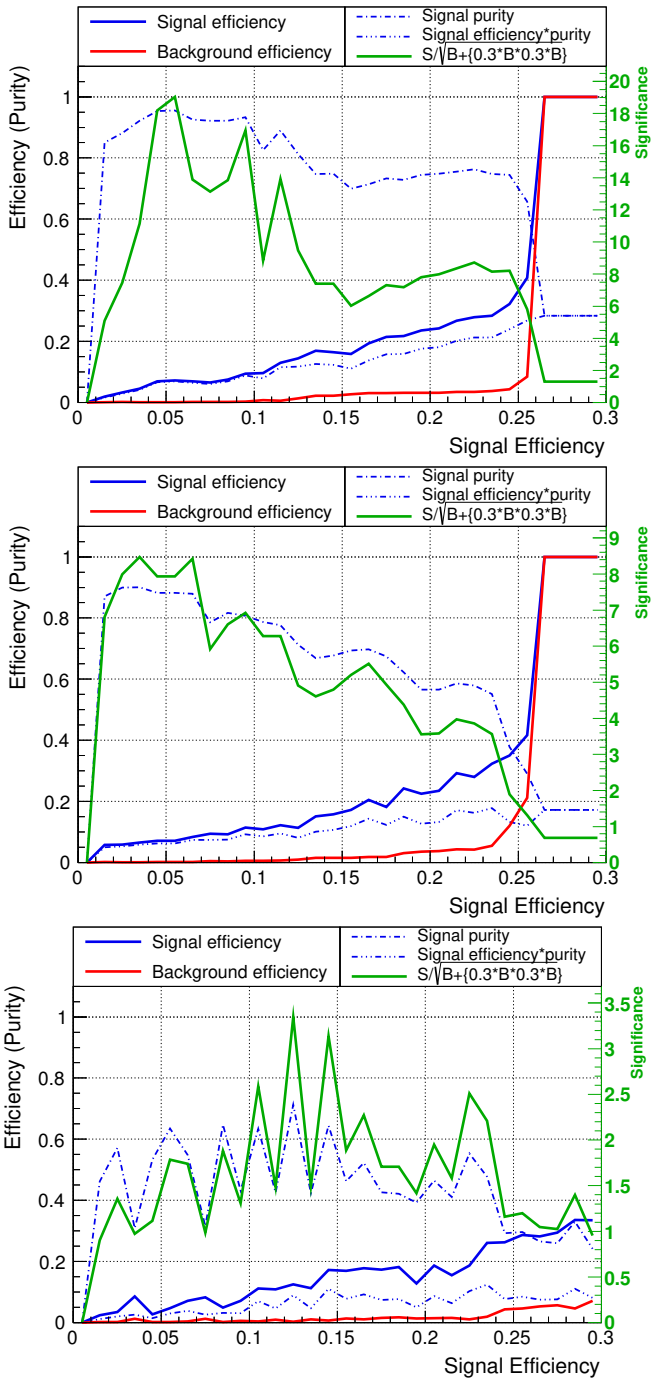

Figure 11.9.: TMVA optimization result for the 6-jet pre-selection using $m_{\text{eff}}^{\text{incl}}$, $E_{\text{T}}^{\text{miss}}$ $/m_{\text{eff}}^{\text{excl}}$, $\Delta\phi(j_{1,2,3}, E_{\text{T}}^{\text{miss}})$ and $\Delta\phi(j_{i>3}, E_{\text{T}}^{\text{miss}})$ variables ('final' selection) for the $m_{H1}^2 = 2.8$ TeV, $m_{1/2} = 450$ GeV, $m_{H1}^2 = 2.8$ TeV, $m_{1/2} = 490$ GeV and $m_{H1}^2 = 2.8$ TeV, $m_{1/2} = 530$ GeV points respectively. Significance of 3 can be achieved for 5 NUHMG points.

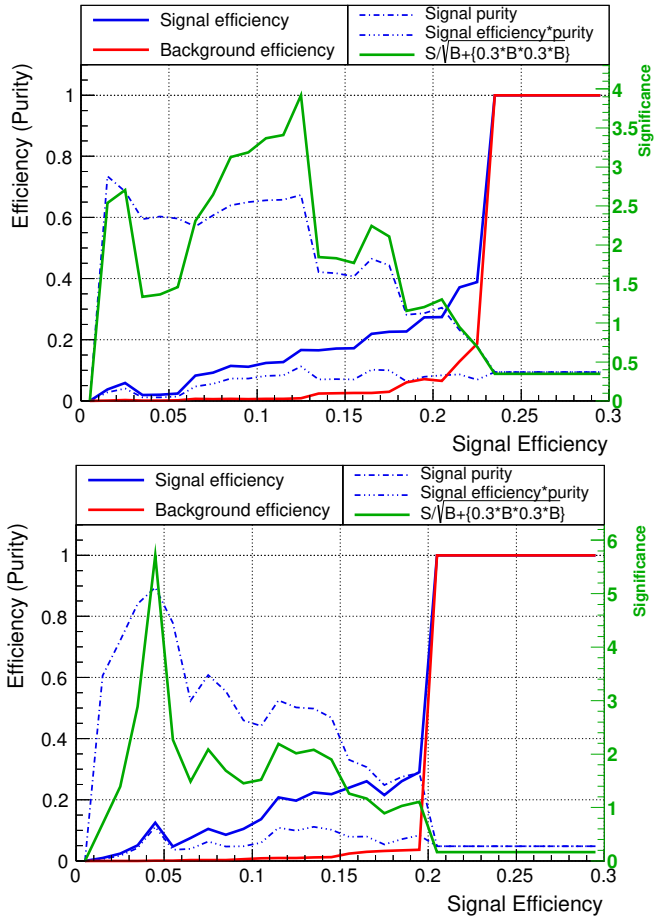

Figure 11.10.: TMVA optimization result for the 6-jet pre-selection using $m_{\text{eff}}^{\text{incl}}$, $E_{\text{T}}^{\text{miss}}$ $/m_{\text{eff}}^{\text{excl}}$, $\Delta\phi(j_{1,2,3}, E_{\text{T}}^{\text{miss}})$ and $\Delta\phi(j_{i>3}, E_{\text{T}}^{\text{miss}})$ variables ('final' selection) for the $m_{H1}^2 = 4.4$ TeV, $m_{1/2} = 570$ GeV and $m_{H1}^2 = 4.4$ TeV, $m_{1/2} = 610$ GeV points respectively. Significance of 3 can be achieved for 5 NUHMG points.

Two variable-channel combinations with the highest number of benchmark points passing the criteria on significance were considered. First uses a 6 jet channel, $\Delta\phi(j_{i>3}, E_{\mathrm{T}}^{\mathrm{miss}})$, $m_{\mathrm{eff}}^{\mathrm{incl}}$, $E_{\mathrm{T}}^{\mathrm{miss}}$ $/m_{\mathrm{eff}}^{\mathrm{excl}}$ and S_{T} and finds 5 NUHMG points for $Z_A \geq 5$ criteria. The second uses a 6 jet channel, $\Delta\phi(j_{1,2,3}, E_{\mathrm{T}}^{\mathrm{miss}})$, $\Delta\phi(j_{i>3}, E_{\mathrm{T}}^{\mathrm{miss}})$, $m_{\mathrm{eff}}^{\mathrm{incl}}$ and $E_{\mathrm{T}}^{\mathrm{miss}}$ $/m_{\mathrm{eff}}^{\mathrm{excl}}$ and finds 5 NUHMG points for $Z_A \geq 3$ criteria.

In the figures 11.7, 11.8, 11.9 and 11.10 the TMVA optimization results for these two variable-channel combinations and 5 points each, are shown. The signal efficiency on the x-axis is given for the training, while the efficiency and significance on the y-axis is given for the test sample. The solid green line represents the significance defined as 11.6. The solid blue and red line are signal and background efficiency respectively. The dashed blue line is signal purity defined as $S/(S+B)$, where S is the number of signal and B is the number of background events after the cuts. The dotted blue line is a product of signal efficiency and signal purity. The NUHMG points closer to the upper diagonal in the grid have a more uneven significance distribution, due to the fact that they have lower signal yields, and therefore it is more difficult to obtain high significance for them.

The obtained results showed linear performance for the signal efficiency in the range of up to about 30 %, i.e. the signal efficiency used in the train sample was about the same as the signal efficiency used in the test sample in the low signal efficiency range, which is sufficient for the SUSY searches where no high signal efficiency is expected.

The first variable-channel combination was used as a starting point in the optimization using the fit, and the second is the final variable-channel selection obtained in this analysis. The result of the TMVA optimization also includes the read out cut ranges for all variables for a given combination, and these are used in the next step of optimization described in the section 11.4.4.

11.4.4. Grid Optimization Using the Fit

In order to include all systematic and statistic uncertainties for the signal and background in the SR optimization, the fit method of the analysis with 0 leptons was used. The optimal cut flow was obtained from the selected variable-channel combination, chosen from the TMVA optimization result. In this step of optimization all 50 NUHMG grid points have been used.

The pre-cuts on the jet multiplicity, p_T, $E_{\mathrm{T}}^{\mathrm{miss}}$ and $\Delta\phi(j_{1,2,3}, E_{\mathrm{T}}^{\mathrm{miss}})$ were placed. The cuts on $\Delta\phi(j_{i>3}, E_{\mathrm{T}}^{\mathrm{miss}})$, $m_{\mathrm{eff}}^{\mathrm{incl}}$, $E_{\mathrm{T}}^{\mathrm{miss}}$ $/m_{\mathrm{eff}}^{\mathrm{excl}}$ and S_{T} were varied as shown in the table 11.5 for 81 signal region options. The best performing signal region using the criteria of lowest CL_S value was obtained, labeled as E31, see figure 11.11 and table 11.5 for ́best for fit' using $\Delta\phi(j_{i>3}, E_{\mathrm{T}}^{\mathrm{miss}}) > 0.6$, $m_{\mathrm{eff}}^{\mathrm{incl}} > 1500$ GeV, $E_{\mathrm{T}}^{\mathrm{miss}}$ $/m_{\mathrm{eff}}^{\mathrm{excl}} > 0.05$ and $S_{\mathrm{T}} > 0.1$, and further refinements were set in place.

	Variables	Fit scan	Best fit	Improved	Final
pre-cuts	jet multiplicity		≥ 6		
	p_T(jet1) [GeV]		>130		
	p_T(jet2-jet6) [GeV]		>60		
	$E_{\mathrm{T}}^{\mathrm{miss}}$ [GeV]		>160		
	$\Delta\phi(j_{1,2,3}, E_{\mathrm{T}}^{\mathrm{miss}})$		>0.4		
cuts	$\Delta\phi(j_{i>3}, E_{\mathrm{T}}^{\mathrm{miss}})$	[>0.4,>0.6,>0.8]	>0.6	>0.6	>0.2
	$m_{\mathrm{eff}}^{\mathrm{incl}}$ [GeV]	[>1200,>1500,>1800]	>1500	>1700	>1700
	$E_{\mathrm{T}}^{\mathrm{miss}}$ $/m_{\mathrm{eff}}^{\mathrm{excl}}$ (N_j)	[>0.05,>0.10,>0.15]	>0.05	-	>0.15
	S_{T}	[>0.1,>0.3,>0.5]	>0.1	-	-

Table 11.5.: Signal region optimization using the fit. Pre-cuts on the jet p_T, $E_{\mathrm{T}}^{\mathrm{miss}}$ and $\Delta\phi(j_{1,2,3}, E_{\mathrm{T}}^{\mathrm{miss}})$ were applied on the 6-jet selection and fit was run for a combination of cuts on $\Delta\phi(j_{i>3}, E_{\mathrm{T}}^{\mathrm{miss}})$, $m_{\mathrm{eff}}^{\mathrm{incl}}$, $E_{\mathrm{T}}^{\mathrm{miss}}$ $/m_{\mathrm{eff}}^{\mathrm{excl}}$ and S_{T} . Best for fit optimization combination of cuts was selected for further optimization. The removal of the $E_{\mathrm{T}}^{\mathrm{miss}}$ $/m_{\mathrm{eff}}^{\mathrm{excl}} > 0.05$ did not change the result, so it was not considered further in the analysis. The S_{T} was further removed as this did not change significantly the expected exclusion. This allowed for a higher cut on $m_{\mathrm{eff}}^{\mathrm{incl}}$, shown as 'improved' result in the table. As similar expected exclusion was obtained for low cut on $E_{\mathrm{T}}^{\mathrm{miss}}$ $/m_{\mathrm{eff}}^{\mathrm{excl}}$ and low cut on $\Delta\phi(j_{i>3}, E_{\mathrm{T}}^{\mathrm{miss}})$ this selection was chosen as the 'final' selection.

11.4.5. Addition of the 6jt+ Signal Region to the Analysis

As the best performing signal region had a very low cut on $E_{\mathrm{T}}^{\mathrm{miss}}$ $/m_{\mathrm{eff}}^{\mathrm{excl}}$ of 0.05, its removal was investigated. This showed that the analysis is not affected by the removal of this cut. Additionally, in order to achieve better fit stability, the removal of transverse sphericity cut was tested. This analysis showed that with omission of S_{T} cut the obtained CL_S values for each NUHMG point become higher, but the expected exclusion curve stays unchanged, while better fit stability is achieved for all NUHMG grid points.

Next, the distributions for parameters after placing all cuts except one, the so called N-1 or marginal distributions, with and without S_{T} cut were investigated. In the figure 11.12 marginal distributions for $\Delta\phi(j_{i>3}, E_{\mathrm{T}}^{\mathrm{miss}})$ (a,b) and $m_{\mathrm{eff}}^{\mathrm{incl}}$ (c,d) are shown. The S_{T} removes the multi-jet background. However, the $\Delta\phi(j_{i>3}, E_{\mathrm{T}}^{\mathrm{miss}})$ and $m_{\mathrm{eff}}^{\mathrm{incl}}$ show to be strong separating variables for both cases, with and without the S_{T} cut. The S_{T} distribution is also shown with and without the $\Delta\phi(j_{i>3}, E_{\mathrm{T}}^{\mathrm{miss}}) > 0.6$ cut. The high cut on $\Delta\phi(j_{i>3}, E_{\mathrm{T}}^{\mathrm{miss}})$ removes well all the backgrounds, but the S_{T} cut seems to remove both signal and background in the same amount. In addition, in order to preserve consistency with other SR in the 0 lepton analysis, the case without sphericity was favored. Therefore, in further analysis, the cut-flow without S_{T} is investigated.

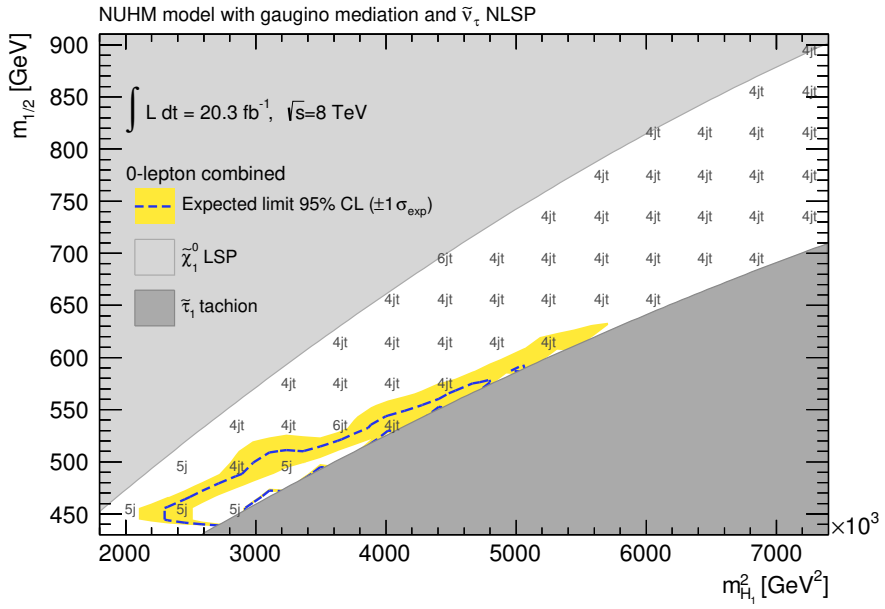

(a)

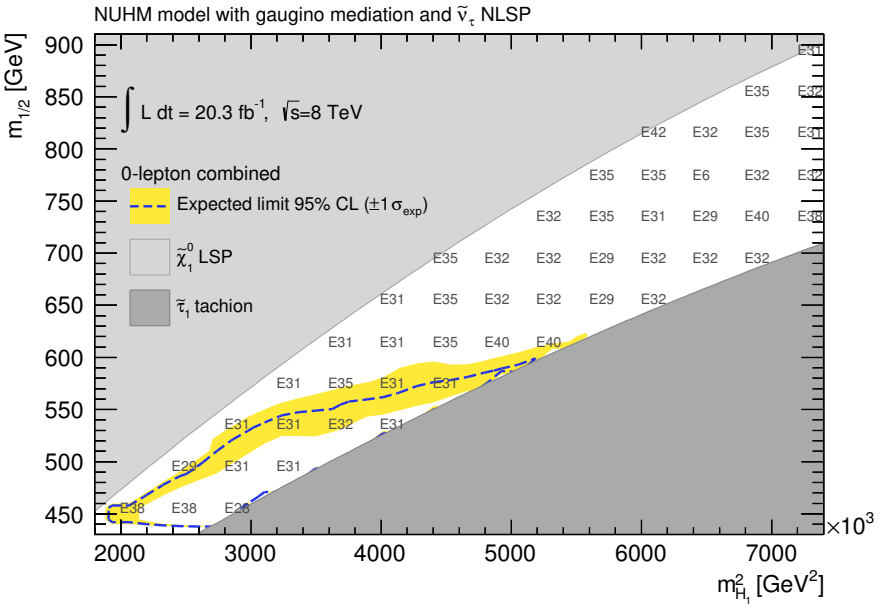

(b)

Figure 11.11.: Scan using the fit of analysis with 2-6 jets and missing transverse momenta. Expected exclusion without the new SR is shown at (a). Different cut values for $\Delta\phi(j_{i>3}, E_{\mathrm{T}}^{\mathrm{miss}})$, $m_{\mathrm{eff}}^{\mathrm{incl}}$, $E_{\mathrm{T}}^{\mathrm{miss}}$ /$m_{\mathrm{eff}}^{\mathrm{excl}}$ and S_{T} with the baseline 6-jet pre-selection were varied, and the SR with best CL_S value is shown at (b). The best performing signal region labeled E31, was selected for further refinement.

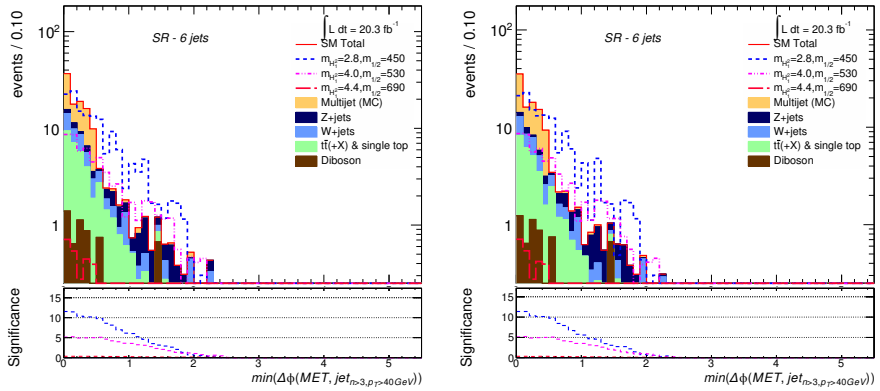

(a) $\Delta\phi(j_{i>3}, E_{\mathrm{T}}^{\mathrm{miss}})$: no S_{T}

(b) $\Delta\phi(j_{i>3}, E_{\mathrm{T}}^{\mathrm{miss}})$: $S_{\mathrm{T}} > 0.1$

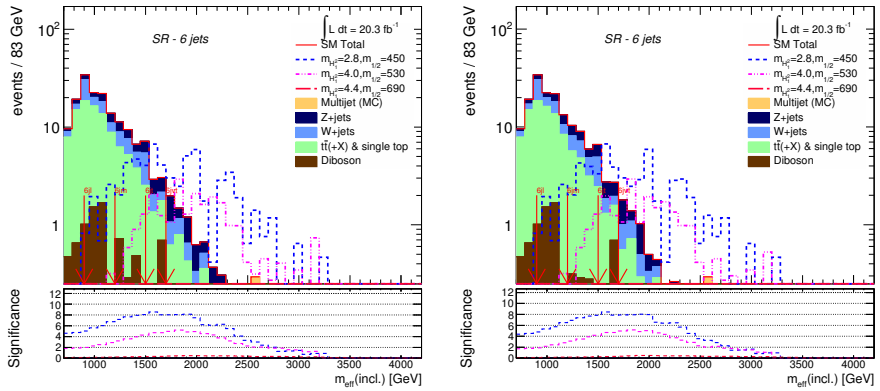

(c) $m_{\mathrm{eff}}^{\mathrm{incl}}$: no S_{T}

(d) $m_{\mathrm{eff}}^{\mathrm{incl}}$: $S_{\mathrm{T}} > 0.1$

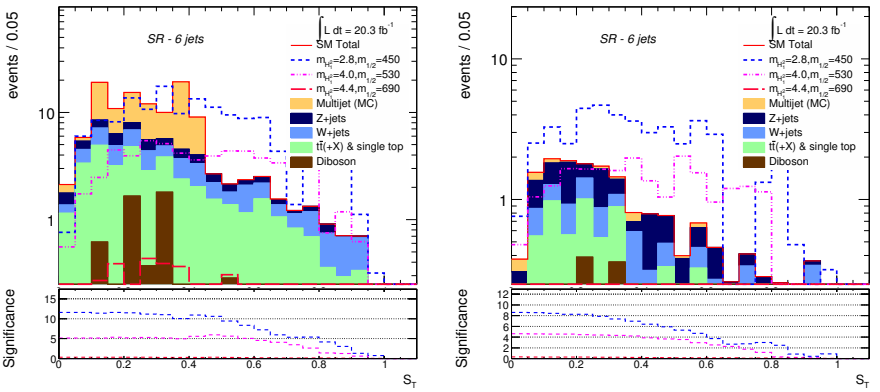

(e) S_{T} : no $\Delta\phi(j_{i>3}, E_{\mathrm{T}}^{\mathrm{miss}})$

(f) S_{T} : $\Delta\phi(j_{i>3}, E_{\mathrm{T}}^{\mathrm{miss}}) > 0.6$

Figure 11.12.: NUHMG strong production marginal distributions for $\Delta\phi(j_{i>3}, E_{\mathrm{T}}^{\mathrm{miss}})$ (a,b) and $m_{\mathrm{eff}}^{\mathrm{incl}}$ (c,d) for w/wo S_{T} , and S_{T} distribution for w/wo $\Delta\phi(j_{i>3}, E_{\mathrm{T}}^{\mathrm{miss}})$ cut. Pre-cuts on trigger, event cleaning, lepton veto, $\Delta\phi(j_{1,2,3}, E_{\mathrm{T}}^{\mathrm{miss}}) > 0.2$, $E_{\mathrm{T}}^{\mathrm{miss}} > 160$ GeV, $p_T(jet1) > 130$ GeV and $p_T(jet2) > 60$ GeV, cuts on $N_{jet} \geq 6$, $p_T(jet_1) > 130$ GeV, $p_T(jet_{2-6}) > 60$ GeV, $E_{\mathrm{T}}^{\mathrm{miss}} > 160$ GeV have been used. Significance is calculated using the formula 8.22.

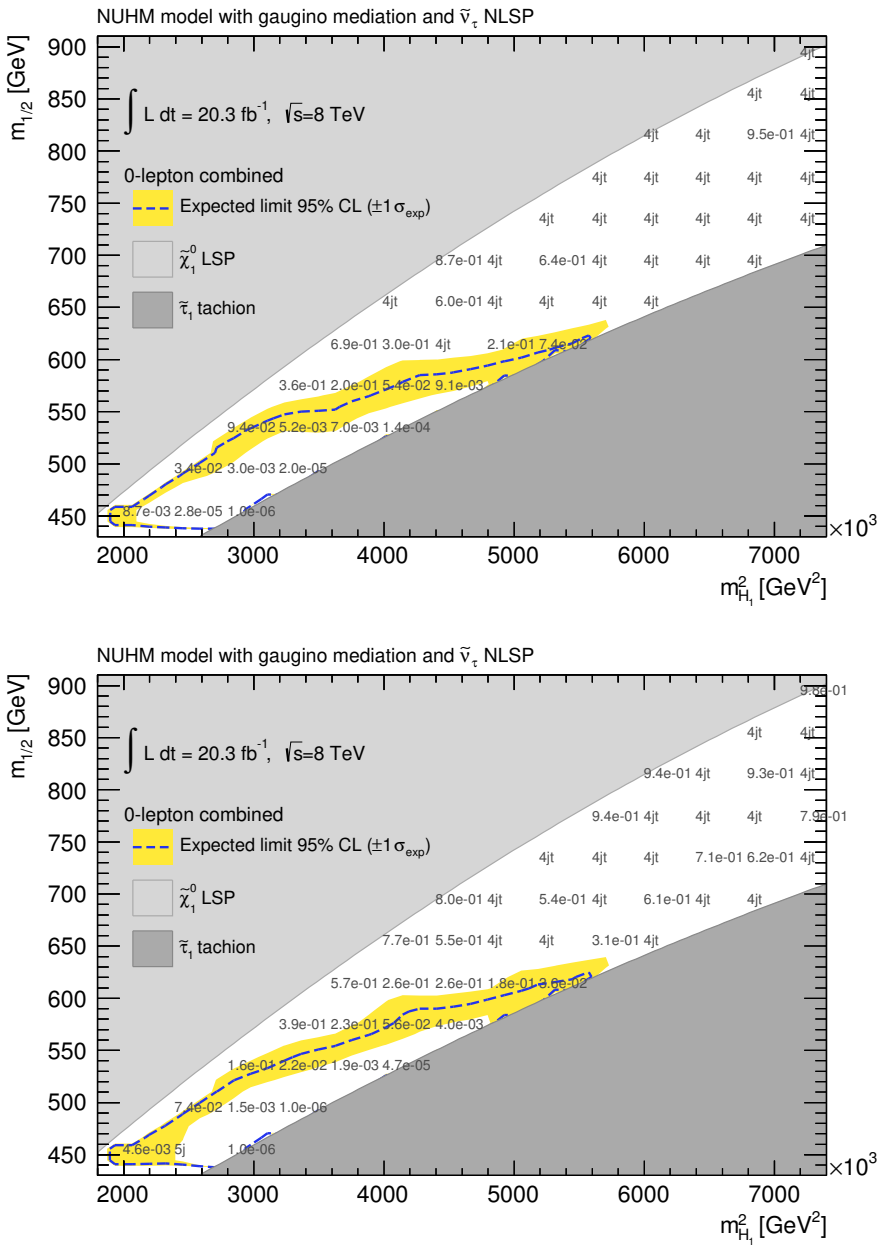

Figure 11.13.: Expected exclusion for NUHMG using the 'improved' (a) and 'final' (b) cut flow. The labels with letters show SR of the SR in the analysis with 0 leptons, while the values are the CL_S values for the new investigated SR. 'Improved' as better coverage in the low mass region, while 'final' is better in the high mass region. CL_S values are comparable for both cases, but worse than for the cut flow using S_T .

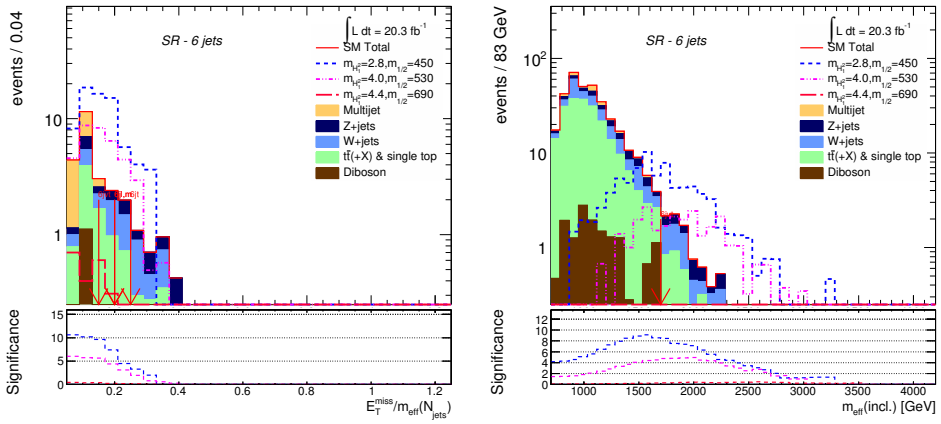

(a) $E_{\mathrm{T}}^{\mathrm{miss}}$ $/m_{\mathrm{eff}}^{\mathrm{excl}}$: $\Delta\phi(j_{i>3}, E_{\mathrm{T}}^{\mathrm{miss}}) > 0.2$ (b) $m_{\mathrm{eff}}^{\mathrm{incl}}$: $\Delta\phi(j_{i>3}, E_{\mathrm{T}}^{\mathrm{miss}}) > 0.2$

Figure 11.14.: NUHMG strong production marginal distributions for no S_{T} . No additional $E_{\mathrm{T}}^{\mathrm{miss}}$ $/m_{\mathrm{eff}}^{\mathrm{excl}}$ cut was used in the distributions. Pre-cuts on trigger, event cleaning, lepton veto, $\Delta\phi(j_{1,2,3}, E_{\mathrm{T}}^{\mathrm{miss}}) > 0.2$, $E_{\mathrm{T}}^{\mathrm{miss}} >$ 160 GeV, $p_T(jet1) > 130$ GeV and $p_T(jet2) > 60$ GeV, cuts on $N_{jet} \geq$ 6, $p_T(jet_1) > 130$ GeV, $p_T(jet_{2-6}) > 60$ GeV, $E_{\mathrm{T}}^{\mathrm{miss}} > 160$ GeV have been used. Significance is calculated using the formula 8.22.

The removal of S_{T} cut allowed placing a higher cut on $m_{\mathrm{eff}}^{\mathrm{incl}}$, and performance was investigated for different cut values for $m_{\mathrm{eff}}^{\mathrm{incl}}$. The best expected exclusion and CL_S values were obtained by placing $m_{\mathrm{eff}}^{\mathrm{incl}} > 1700$ GeV, see figure 11.13 (a) and table 11.5 for 'improved'. Next, the high cut on $\Delta\phi(j_{i>3}, E_{\mathrm{T}}^{\mathrm{miss}})$ was traded for a low cut on $E_{\mathrm{T}}^{\mathrm{miss}}$ $/m_{\mathrm{eff}}^{\mathrm{excl}}$ and cut on $\Delta\phi(j_{i>3}, E_{\mathrm{T}}^{\mathrm{miss}}) > 0.2$ typically used in the analysis with jets and $E_{\mathrm{T}}^{\mathrm{miss}}$. Although the CL_S values were a little bit worse, the expected exclusion had a very similar performance. The final selection was chosen with the 6-jet pre-selection and $E_{\mathrm{T}}^{\mathrm{miss}}$ $/m_{\mathrm{eff}}^{\mathrm{excl}} > 0.15$, $m_{\mathrm{eff}}^{\mathrm{incl}} > 1700$ GeV and $\Delta\phi(j_{i>3}, E_{\mathrm{T}}^{\mathrm{miss}})$ > 0.2, see figure 11.13 (a) and the table 11.5 for 'final'.

The fit obtained background content was also investigated. In the case of the 'improved' selection the background was dominated by the multi-jet background. The 'final' cut flow had background content dominated by W+jet and $t\bar{t}$. As there are large uncertainties on the multi-jet background, the 'final' cut flow was chosen. All control and validation regions were used as in the standard analysis with no leptons, 2-6 jets and $E_{\mathrm{T}}^{\mathrm{miss}}$.

In the 'final' cut flow marginal distributions were investigated as a cross-check. In the figure 11.14 marginal distributions for $E_{\mathrm{T}}^{\mathrm{miss}}$ $/m_{\mathrm{eff}}^{\mathrm{excl}}$ cut and $m_{\mathrm{eff}}^{\mathrm{incl}}$ cut are shown. The $E_{\mathrm{T}}^{\mathrm{miss}}$ $/m_{\mathrm{eff}}^{\mathrm{excl}}$ cut needs to be very low in order to allow for enough signal statistics, however, a cut of 1700 GeV in the $m_{\mathrm{eff}}^{\mathrm{incl}}$ distribution separates the SM background well.

In conclusion, the cut flow with $\Delta\phi(j_{i>3}, E_{\mathrm{T}}^{\mathrm{miss}}) > 0.2$, $E_{\mathrm{T}}^{\mathrm{miss}}$ $/m_{\mathrm{eff}}^{\mathrm{excl}} > 0.15$ and $m_{\mathrm{eff}}^{\mathrm{incl}} > 1700$ GeV had a good expected exclusion coverage for the whole NUHMG

grid, similar performance for the CL_S values, and irreducible background content not dominated by multi-jet background. In addition, it uses the standard variables of the 0 lepton search, which makes the CR design compatible with the 0 lepton search, therefore it was chosen as the optimal SR for the NUHMG grid analysis.

A note is in order concerning the transition from the optimal variable-channel combination obtained by the fast cut flow optimization with TMVA to the final selection. The result obtained with TMVA relies on the signal and background estimate obtained by MC, while the refined optimization using the fit incorporates all systematic uncertainties and CRs design. In addition, the method using the fit provides the final background content estimate in the SR, obtained by using the MC and data in CRs, which was considered in the selection of the optimal SR. Although the variable combination with 6 jets,$\Delta\phi(j_{i>3}, E_{\mathrm{T}}^{\mathrm{miss}})$,$m_{\mathrm{eff}}^{\mathrm{incl}}$,$E_{\mathrm{T}}^{\mathrm{miss}}$ /$m_{\mathrm{eff}}^{\mathrm{excl}}$,S_{T} was initially investigated for its prospects for a selection reaching significance of 5 sigma for 5 points used in the optimization, it was replaced with the variable combination with 6 jets,$\Delta\phi(j_{1,2,3}, E_{\mathrm{T}}^{\mathrm{miss}})$,$\Delta\phi(j_{i>3}, E_{\mathrm{T}}^{\mathrm{miss}})$,$m_{\mathrm{eff}}^{\mathrm{incl}}$,$E_{\mathrm{T}}^{\mathrm{miss}}$ /$m_{\mathrm{eff}}^{\mathrm{excl}}$. The later has prospects for significance of 3 sigma for 5 signal points obtained in optimization using TMVA. Namely, the method using TMVA obtained both variable-channel combinations in its ranking, i.e. the initial and the final variable combination are present in the table 11.4 marked with *. Therefore, the fast cut flow optimization using TMVA showed to help in finding a optimal SR when criteria for significance is considered, while refined optimization using the fit gave important information on the background content in the SR, and it provided better background estimate in the SR, as it included MC and data in CRs and full systematic uncertainty estimates.

11.5. Event Selection

The event selection used in the analysis with jets and missing transverse energy will be presented in this section. Special emphasis will be given on the 6jt+ signal region which was optimized for the NUHMG model.

11.5.1. Signal Regions Selection

The common event selection is performed using pre-selection cuts as explained in the section 11.3, which are followed by a number of signal region selection cuts that will be described in this section. As this analysis relies on good lepton reconstruction for the lepton veto and accurate missing transverse energy reconstruction, first the requirements on the data quality are applied by requesting a good run for all detector components. This is followed by the trigger decision selection which was described in the section 11.3.2. Next, to ensure event selection from a p-p collision, a request on a primary vertex is placed, by requiring at least 5 primary tracks in the event. Then the event cleaning requirements are placed, as described in the section 11.3.3, where events with faulty Tile or LAr events are removed, jets are required to have the right fraction of the transverse momentum of the jet carried by the charged

particle tracks, and jet energy deposited in the electromagnetic calorimeter, badly reconstructed muons are vetoed, corrupted Tile cells, cosmic and dead Tile drawer events are removed. Finally, as this analysis is based on the selection with no leptons, on the cleaned sample a veto on the lepton (e, μ) of good quality with $p_T > 10$ GeV is placed.

After the pre-selection, the cuts for 15 signal regions are applied, see table 11.6. Following the study on the trigger efficiency, to ensure that the events are in the plateau of the trigger which uses jets and $E_{\mathrm{T}}^{\mathrm{miss}}$, for all SR a cut on $E_{\mathrm{T}}^{\mathrm{miss}}$ of 160 GeV and a cut on the first jet p_T of 130 GeV are placed. The proceeding cuts for signal regions are optimized to have maximal reach in sensitivity for the grids in the $m_{\tilde{q}}$ vs $m_{\tilde{g}}$ plane. In particular, in the direct decays of $\tilde{q} \to q\tilde{\chi}_1^0$ one jet is produced, direct decays of $\tilde{g} \to q\bar{q}\tilde{\chi}_1^0$ produce two jets, while longer SUSY cascade decays can have $\tilde{\chi}_1^{\pm} \to qq'\tilde{\chi}_1^0$ in the decay chain and therefore more jets. Therefore, by examining processes of $\tilde{q}\ \tilde{q}$, $\tilde{q}\ \tilde{g}$ and $\tilde{g}\ \tilde{g}$ production, final states with two, three, four, five and six jet channels were considered, and dedicated optimizations were performed to obtain highest coverage. The lower jet multiplicity selections are targeting direct squark decays, while longer decay chains of gluino decays are used with higher jet multiplicity. The further jets p_T threshold is optimized for reducing the pile-up effect and good background rejection, and is set to 60 GeV. Additional cuts are placed for each signal region in order to reduce background and maintain SUSY signal in the selection, and they vary in the level of background rejection as 'very loose', 'loose', 'medium', 'tight' and 'very tight', labeled as l-, l, m, t, t+. In addition to these selections, signal regions which benefit from selecting a boosted W in the decay chain are in addition labeled with W.

Namely, for one-step $\tilde{g}\ \tilde{g}$ production grids, where $\tilde{\chi}_1^{\pm} \to W\tilde{\chi}_1^0$, the W boost is proportional to the $\tilde{\chi}_1^{\pm}$- $\tilde{\chi}_1^0$ mass difference, and variable x is defined as:

$$x = \frac{m_{\tilde{\chi}_1^{\pm}} - m_{\tilde{\chi}_1^0}}{m_{\tilde{q}(\tilde{g})} - m_{\tilde{\chi}_1^0}}. \tag{11.7}$$

The optimization in the high x region was performed considering a hadronically decaying W. The W is reconstructed as either a single high mass jet, or two resolved jets. The optimal signal regions selection with 2 resolved W jets (2(W $\to$ j)) is labeled 2jW, and with one resolved (W $\to$ jj) and one un-resolved W jet (W $\to$ j) is labeled 4jW, where jets invariant mass is required to be around the W mass peak of $60 < m_W < 100$ GeV.

In order to suppress the QCD background, all signal regions have a requirement on first three jets, if they exist, to have $\Delta\phi(j_{1,2,3}, E_{\mathrm{T}}^{\mathrm{miss}}) > 0.4$, where all jets with $p_T > 40$ GeV are considered. Signal regions with higher jet multiplicity, except the channels with W selection, have a looser requirement of $\Delta\phi(j_{i>3}, E_{\mathrm{T}}^{\mathrm{miss}}) > 0.2$ for the remaining jets, where all jets with $p_T > 40$ GeV are considered as well.

Further good QCD background suppression is done with variables which use the information on $E_{\mathrm{T}}^{\mathrm{miss}}$ and energy carried by the jets. In this respect, one of two

Requirement	Signal Region					
	2jl	**2jm**	**2jt**	**2jW**	**3j**	**4jW**
$E_{\mathrm{T}}^{\mathrm{miss}}$ [GeV] >	160					
$p_{\mathrm{T}}(j_1)$ [GeV] >	130					
$p_{\mathrm{T}}(j_2)$ [GeV] >	60					
$p_{\mathrm{T}}(j_3)$ [GeV] >	–				60	40
$p_{\mathrm{T}}(j_4)$ [GeV] >	–					40
$\Delta\phi(\mathrm{jet}_{1,2,(3)}, E_{\mathrm{T}}^{\mathrm{miss}})_{\mathrm{min}}$ >	0.4					
$\Delta\phi(\mathrm{jet}_{i>3}, E_{\mathrm{T}}^{\mathrm{miss}})_{\mathrm{min}}$ >	–					0.2
W candidates	–			$2(W \to j)$	–	$(W \to j) + (W \to jj)$
$E_{\mathrm{T}}^{\mathrm{miss}}/\sqrt{H_{\mathrm{T}}}$ [GeV$^{1/2}$] >	8	15		–		
$E_{\mathrm{T}}^{\mathrm{miss}}/m_{\mathrm{eff}}^{\mathrm{excl}}(N_{\mathrm{j}})$ >	–			0.25	0.3	0.35
$m_{\mathrm{eff}}^{\mathrm{incl}}$ [GeV] >	800	1200	1600	1800	2200	1100

Requirement	Signal Region								
	4jl-	**4jl**	**4jm**	**4jt**	**5j**	**6jl**	**6jm**	**6jt**	**6jt+**
$E_{\mathrm{T}}^{\mathrm{miss}}$ [GeV] >	160								
$p_{\mathrm{T}}(j_1)$ [GeV] >	130								
$p_{\mathrm{T}}(j_2)$ [GeV] >	60								
$p_{\mathrm{T}}(j_3)$ [GeV] >	60								
$p_{\mathrm{T}}(j_4)$ [GeV] >	60								
$p_{\mathrm{T}}(j_5)$ [GeV] >	–				60				
$p_{\mathrm{T}}(j_6)$ [GeV] >	–					60			
$\Delta\phi(\mathrm{jet}_{1,2,(3)}, E_{\mathrm{T}}^{\mathrm{miss}})_{\mathrm{min}}$ >	0.4								
$\Delta\phi(\mathrm{jet}_{i>3}, E_{\mathrm{T}}^{\mathrm{miss}})_{\mathrm{min}}$ >	0.2								
$E_{\mathrm{T}}^{\mathrm{miss}}/\sqrt{H_{\mathrm{T}}}$ [GeV$^{1/2}$] >	10		–						
$E_{\mathrm{T}}^{\mathrm{miss}}/m_{\mathrm{eff}}^{\mathrm{excl}}(N_{\mathrm{j}})$ >	–		0.4	0.25	0.2			0.25	0.15
$m_{\mathrm{eff}}^{\mathrm{incl}}$ [GeV] >	700	1000	1300	2200	1200	900	1200	1500	1700

Table 11.6.: Selection criteria used in the analysis with a lepton veto ($p_T > 10$ GeV) [31]. The signal regions are named after the jet multiplicity selection, and labeled 2j, 3j, 4j, 5j or 6j. In addition, according to the level of signal efficiency of 'very loose', 'loose', 'medium', 'tight' and 'very tight', the extension 'l-', 'l', 'm', 't' or 't+' is added. In addition, the SR 2jW and SR 4jW have a requirement of 60 GeV $< m(W_{\mathrm{cand}}) <$ 100 GeV used for resolved and unresolved W bosons. The $E_{\mathrm{T}}^{\mathrm{miss}}/m_{\mathrm{eff}}^{\mathrm{excl}}$ cut uses a value constructed from the leading N jets, but the $m_{\mathrm{eff}}^{\mathrm{incl}}$ cut includes all jets with $p_{\mathrm{T}} > 40$ GeV.

Point	$m(H_1^2)$=2.8 TeV $m_{1/2}$=450 GeV	$m(H_1^2)$=3.2 TeV $m_{1/2}$=490 GeV	$m(H_1^2)$=4.0 TeV $m_{1/2}$=530 GeV
Channel	6jt+	6jt+	6jt+
$N_{\text{generated}}$(unweighted)	19875	19913	19897
$N_{\text{generated}}$(weighted)	5581.4 (100.0)	5551.5 (100.0)	1531.6 (100.0)
Trigger	5581.4 (100.0)	5551.5 (100.0)	1531.6 (100.0)
Jet Cleaning	3496.1 (62.6)	3612.0 (65.1)	918.5 (60.0)
Vertex Cut	3493.3 (62.6)	3609.5 (65.0)	918.2 (59.9)
Cosmic Muon Veto	3475.0 (62.3)	3585.4 (64.6)	914.4 (59.7)
Bad Muon Veto	3474.4 (62.2)	3584.1 (64.6)	913.8 (59.7)
Bad $E_{\text{T}}^{\text{miss}}$ Muon Veto	3158.7 (56.6)	3290.7 (59.3)	842.5 (55.0)
Bad Tile Veto	3130.2 (56.1)	3269.0 (58.9)	835.7 (54.6)
Negative-cell Cleaning	3026.2 (54.2)	3132.1 (56.4)	813.4 (53.1)
0 Lepton	1856.4 (33.3)	1767.6 (31.8)	485.7 (31.7)
$E_T^{miss} > 160$ GeV	1107.2 (19.8)	903.1 (16.3)	334.4 (21.8)
$p_T(j_1) > 130$ GeV	1101.7 (19.7)	883.7 (15.9)	334.4 (21.8)
$p_T(j_2) > 60$ GeV	1101.7 (19.7)	880.8 (15.9)	334.4 (21.8)
$p_T(j_3) > 60$ GeV	1090.3 (19.5)	835.9 (15.1)	332.6 (21.7)
$p_T(j_4) > 60$ GeV	998.5 (17.9)	713.4 (12.9)	314.0 (20.5)
$p_T(j_5) > 60$ GeV	668.1 (12.0)	465.8 (8.4)	218.9 (14.3)
$p_T(j_6) > 60$ GeV	347.3 (6.2)	223.5 (4.0)	121.5 (7.9)
$\Delta\phi(j_{1,2,3}, E_T^{miss}) > 0.4$	248.0 (4.4)	155.6 (2.8)	88.0 (5.7)
$\Delta\phi(j_{i>3} > 40GeV, E_T^{miss}) > 0.2$	177.7 (3.2)	117.2 (2.1)	64.1 (4.2)
$E_{\text{T}}^{\text{miss}}/m_{\text{eff}}^{\text{excl}} > 0.15$	106.8 (1.9)	67.2 (1.2)	35.4 (2.3)
$m_{\text{eff}}^{\text{incl}} > 1.7$ TeV	42.0 (0.8)	34.0 (0.6)	24.0 (1.6)

Table 11.7.: Cut flow for the 6jt+ SR for three NUHMG parameter-space points normalized to 20.3 fb^{-1}. Absolute efficiency in brackets (%).

types of cuts are placed, based on the optimization results for each signal region. The $E_{\text{T}}^{\text{miss}}/m_{\text{eff}}^{\text{excl}}$ cut takes values on the range from 0.15 to 0.40, while the cut on $E_{\text{T}}^{\text{miss}}/\sqrt{H_T}$ is in the range from 8 to 15. Both variables use information on the jets used for defining the channel of the analysis, i.e. jet $p_T > 60$ GeV.

The final cut placed on all signal regions is mainly for further QCD reduction, and it is computed as the scalar sum of all jets with $p_T > 40$ GeV and missing transverse energy, labeled as $m_{\text{eff}}^{\text{incl}}$. It is in the range from 800 to 2200 GeV.

The dominant sources of backgrounds remaining in the signal region selection originate from W+jets, Z+jets, $t\bar{t}$, single t and multiple jets. The major contribution within the W+jets background comes from W $\rightarrow \tau\nu$ events with τ decaying hadronically, and smaller contributing from W $\rightarrow e\nu, \mu\nu$ events. The Z+jets contribute to the irreducible background with Z $\rightarrow \nu\bar{\nu}$ which have a large $E_{\text{T}}^{\text{miss}}$. The top quark pair backgrounds can have large $E_{\text{T}}^{\text{miss}}$ in decays like tt $\rightarrow b\bar{b}\tau\nu qq'$ when τ decays hadronically, where these events can pass the signal region selections at non-negligible rate. Finally, the multi-jet background can pass signal region selection in cases where jets are miss-reconstructed, so fake $E_{\text{T}}^{\text{miss}}$ is large, or in the semi leptonic decays of third generation quarks where $E_{\text{T}}^{\text{miss}}$ is present.

The cut flow for the 6jt+ SR is shown in the figure 11.7 for three NUHMG parameter-space points. The trigger is fully efficient, but about 30-40% of events are filtered out by the jet cleaning cut. This cut is known to remove more events for models which have low $E_{\mathrm{T}}^{\mathrm{miss}}$. Therefore, this is well justified by the typical kinematics of a NUHMG model event, which is characterized by lots of events with very low $E_{\mathrm{T}}^{\mathrm{miss}}$, which would be removed by higher $E_{\mathrm{T}}^{\mathrm{miss}}$ cut later on in any case. Further event cleaning for cosmic muons, bad muon reconstruction, and detector corrections remove additional 5-10 % of events. The lepton veto is a strong selection cut which removes around 20% of events. The cut on $E_{\mathrm{T}}^{\mathrm{miss}}$ additionally removes 10-15% of events, but effectively removes the background events. As NUHMG model has a peak jet multiplicity for 4 jets, the next cuts on first 4 jet p_T are not strong in removing the signal events, but are effective in the background rejection, while cuts on fifth and sixth jet p_T remove more signal events but tailor the signal to background ratio towards higher significance. Strong QCD removal is obtained by the $\Delta\phi(j_{1,2,3}, E_{\mathrm{T}}^{\mathrm{miss}})$ and $\Delta\phi(j_{i>3}, E_{\mathrm{T}}^{\mathrm{miss}})$ cuts. Finally, good signal to background ratio is obtained by the cuts on $E_{\mathrm{T}}^{\mathrm{miss}}$ $/m_{\mathrm{eff}}^{\mathrm{excl}}$ and $m_{\mathrm{eff}}^{\mathrm{incl}}$ which remove a lot of signal events, but at the same time remove remaining W+jets, Z+jets and $t\bar{t}$ backgrounds in the SR. The obtained absolute signal efficiency after the cut flow is around 1% or below.

11.5.2. Control Regions Selection

The backgrounds in the analysis are estimated in a consistent way by using control regions (CR). For each signal region there are four orthogonal control regions defined (CRγ, CRQ, CRW and CRT) which provide independent data samples used for the background estimate, see table 11.8. In total there are 60 CR used in the analysis. They are designed to contain a large enough statistics, negligible SUSY signal contamination and low systematic uncertainty contribution in the signal region count estimate, which is achieved by reverting the cut on $m_{\mathrm{eff}}^{\mathrm{incl}}$ used in the SR selection.

CR	SR background	CR process	CR selection
CRγ	$Z(\to \nu\nu)$+jets	γ+jets	Isolated photon
CRQ	Multi-jets	Multi-jets	SR with reversed requirements on (i) $\Delta\phi(j_{1,2,3}, E_{\mathrm{T}}^{\mathrm{miss}})$ and (ii) $E_{\mathrm{T}}^{\mathrm{miss}}/m_{\mathrm{eff}}^{\mathrm{excl}}(N_{\mathrm{j}})$ or $E_{\mathrm{T}}^{\mathrm{miss}}/\sqrt{H_{\mathrm{T}}}$
CRW	$W(\to \ell\nu)$+jets	$W(\to \ell\nu)$+jets	30 GeV $< m_{\mathrm{T}}(\ell, E_{\mathrm{T}}^{\mathrm{miss}}) <$ 100 GeV, b-veto
CRT	$t\bar{t}$ and single-t	$t\bar{t} \to b\bar{b}qq'\ell\nu$	30 GeV $< m_{\mathrm{T}}(\ell, E_{\mathrm{T}}^{\mathrm{miss}}) <$ 100 GeV, b-tag

Table 11.8.: Details of control regions used in the analysis [31]. For each control region the targeted background in the SR, the process in the CR and the selection in the CR are shown. The high-purity leptons (photons) in the CR have a 25 (130) GeV threshold.

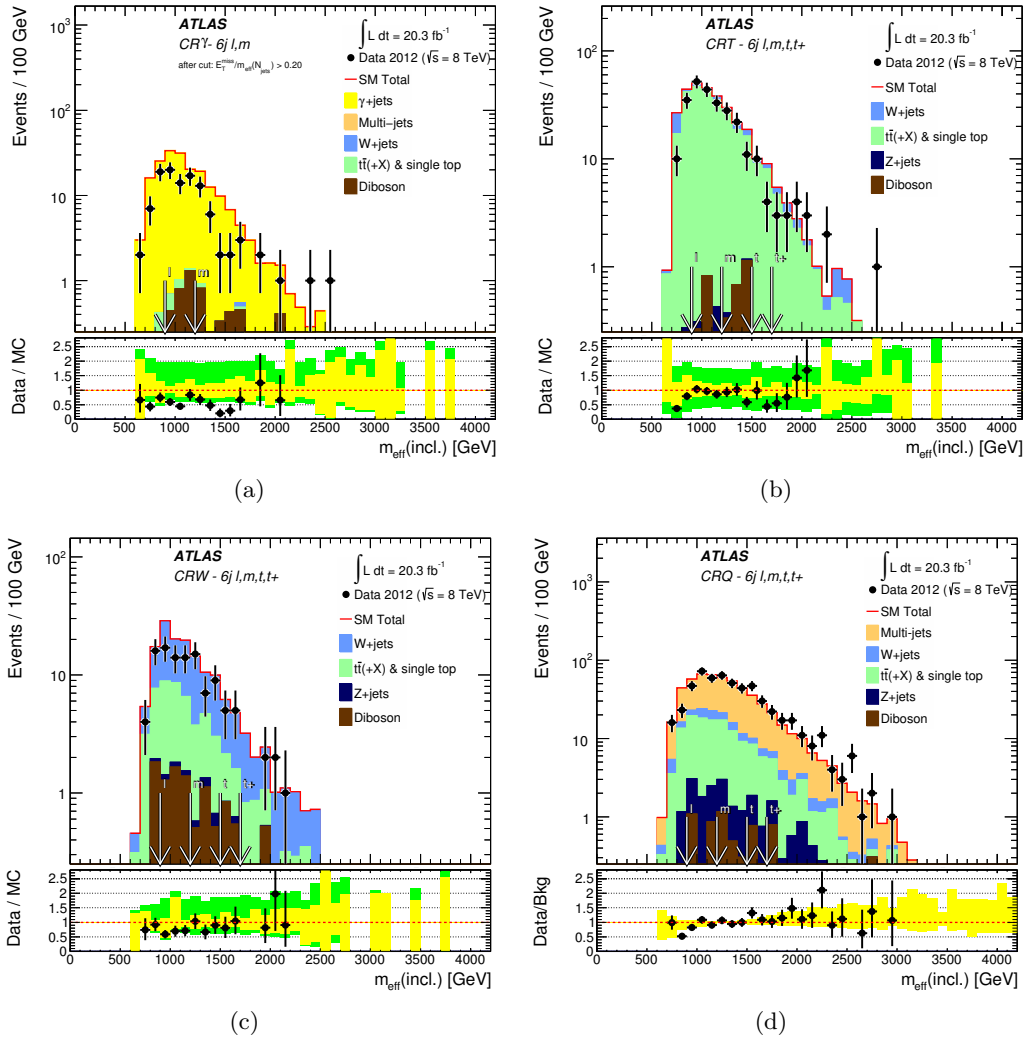

Figure 11.15.: Observed $m_{\text{eff}}^{\text{incl}}$ distributions in the CRγ (a), CRW (b), CRZ (c) and CRQ (excluding requirement on $E_{\text{T}}^{\text{miss}}/m_{\text{eff}}^{\text{excl}}$) (d) control regions for the six-jet channel [227]. The CRγ, CRW and CRZ distributions are given for MC background expectations normalized to the cross-section and integrated luminosity. The CRQ distribution is given for the data-driven estimation used in the analysis. In the lower plots the yellow error band denotes experimental and MC statistical uncertainty, while the green band in addition includes the theoretical modeling uncertainty. The arrows denote the $m_{\text{eff}}^{\text{incl}}$ cut requirements for six-jet loose, medium, tight and very-tight signal regions.

CRγ is used for the Z($\rightarrow \nu\nu$)+jets background estimate. The γ+jets events are selected with a photon threshold of $p_T(\gamma) > 130$ GeV. For a $p_T(\gamma) > m_Z$ the kinematics of events resembles the Z+jets events [227], and the photon p_T can be replaced by the missing transverse momentum to estimate the Z($\rightarrow \nu\nu$)+ jets background. The uncertainites on the photon isolation, parton distribution functions and photon miss-identification are included in the analysis in the estimate for the Z($\rightarrow \nu\nu$)+jets background, see more details in the section 11.7.2.

CRQ selects events rich with multi-jet events in the region similar to the SR, with reverting the cuts on $\Delta\phi(j_{1,2,3}, E_{\mathrm{T}}^{\mathrm{miss}})$, which selects multi-jet events with fake $E_{\mathrm{T}}^{\mathrm{miss}}$ and $E_{\mathrm{T}}^{\mathrm{miss}}$ from neutrinos in the heavy quark decay, and $E_{\mathrm{T}}^{\mathrm{miss}}$ $/m_{\mathrm{eff}}^{\mathrm{excl}}$ or $E_{\mathrm{T}}^{\mathrm{miss}}$ $/\sqrt{H_T}$ which separate this CR from the W+jets and $t\bar{t}$ events in which the boosted W decays into hadronic τ giving a low $\Delta\phi(j_{1,2,3}, E_{\mathrm{T}}^{\mathrm{miss}})$ topology. However, in order to minimize effects of extrapolation from CR to the SR, in addition a lower cut is placed on these two variables.

CRW and CRT target the events of W($\rightarrow l\nu$)+jets and combined semi-leptonic $t\bar{t}$ with single-t, respectively. The CRW uses a selection with a b-jet veto, while CRT has a b-jet tag requirement. Each CR selects a high purity lepton with $p_T(l)$ > 25 GeV which has a transverse mass with $E_{\mathrm{T}}^{\mathrm{miss}}$ $m_T(l, E_{\mathrm{T}}^{\mathrm{miss}})$ in the range from 30 to 100 GeV. A study showed that in W($\rightarrow l\nu$)+jets and semi-leptonic $t\bar{t}$ samples about 75% events in the SR have a jet faked by the lepton, coming from electron miss-identification or hadronically decaying τ leptons. Therefore, to estimate the W($\rightarrow l\nu$)+jets and combined $t\bar{t}$ with single-t background the reconstructed lepton is treated as a jet to recompute jet dependent variables like $\Delta\phi(j_i, E_{\mathrm{T}}^{\mathrm{miss}})$ and $m_{\mathrm{eff}}^{\mathrm{incl}}$ in the event for estimates. However, these CR do not use cuts on $\Delta\phi(j_i, E_{\mathrm{T}}^{\mathrm{miss}})$, $E_{\mathrm{T}}^{\mathrm{miss}}$ $/m_{\mathrm{eff}}^{\mathrm{excl}}$ of $E_{\mathrm{T}}^{\mathrm{miss}}$ $/\sqrt{H_T}$, with the exception of SR 2jl, in order to increase the statistics. For the same purpose, the $m_{\mathrm{eff}}^{\mathrm{incl}}$ cut is loosened to 1300 GeV in CRW and CRT for the SR 6jt.

In the figure 11.15 the $m_{\mathrm{eff}}^{\mathrm{incl}}$ distribution for CRγ, CRQ, CRW and CRT for the 6 jet channel are shown, where the inverted cut on $m_{\mathrm{eff}}^{\mathrm{incl}}$ is added to obtain values for each dedicated SR selection, and the SR 6jt+ $m_{\mathrm{eff}}^{\mathrm{incl}}$ cut is labeled as 't+' in the plots. The MC distributions are to an extent harder than the data, which is corrected by the normalization factors obtained by the fit.

11.5.3. Validation Regions Selection

The background estimates are cross-checked in the validation regions (VR), designed to have minimal signal contamination. The results on validation for the 6jt+ SR are shown in the section 11.8.2. There is a number of VR designed per each SR, dedicated for different physics processes, and they are defined as:

- VRZ is designed to validate CRγ estimate of the Z($\rightarrow \nu\nu$)+jets events by selecting Z($\rightarrow ll$)+jets events. Two opposite sign same flavor high-purity leptons are selected and their invariant mass is requested to be around the Z mass

peak, from 66 to 116 GeV. Second validation region, VRZf is similar to VRZ, but with additional cuts on $E_{\mathrm{T}}^{\mathrm{miss}}$ $/m_{\mathrm{eff}}^{\mathrm{excl}}$ and $\Delta\phi(j_i, E_{\mathrm{T}}^{\mathrm{miss}})$.

- VRWf uses cuts as CRW to validate events where lepton is miss-reconstructed as a jet, but adds the cuts on $\Delta\phi(j_i, E_{\mathrm{T}}^{\mathrm{miss}})$ and $E_{\mathrm{T}}^{\mathrm{miss}}$ $/m_{\mathrm{eff}}^{\mathrm{excl}}$ or $E_{\mathrm{T}}^{\mathrm{miss}}$ $/\sqrt{H_T}$. VRWM takes the selection as CRW, but considers identified lepton as missing particle (M) instead of being treated as a jet. VRWMf is very similar to VRWM, but adds cuts on $\Delta\phi(j_i, E_{\mathrm{T}}^{\mathrm{miss}})$ and $E_{\mathrm{T}}^{\mathrm{miss}}$ $/m_{\mathrm{eff}}^{\mathrm{excl}}$ or $E_{\mathrm{T}}^{\mathrm{miss}}$ $/\sqrt{H_T}$.

- VRTf uses cuts as CRT to validate events where lepton is identified as a jet, but adds cuts on $\Delta\phi(j_i, E_{\mathrm{T}}^{\mathrm{miss}})$ and $E_{\mathrm{T}}^{\mathrm{miss}}$ $/m_{\mathrm{eff}}^{\mathrm{excl}}$ or $E_{\mathrm{T}}^{\mathrm{miss}}$ $/\sqrt{H_T}$. VRTM takes the selection as CRT, but considers identified lepton as missing particle (M) instead of being treated as a jet. VRTMf is very similar to VRTM, but adds cuts on $\Delta\phi(j_i, E_{\mathrm{T}}^{\mathrm{miss}})$ and $E_{\mathrm{T}}^{\mathrm{miss}}$ $/m_{\mathrm{eff}}^{\mathrm{excl}}$ or $E_{\mathrm{T}}^{\mathrm{miss}}$ $/\sqrt{H_T}$. VRT2L is sensitive to fully leptonic $t\bar{t}$ processes and is similar to VRZ. It requires two opposite sign same flavor high-purity leptons but their mass is requested to be higher than 116 GeV, away from the Z mass peak.

- VRWT+ is used to test lepton charge asymmetry. The selection is placed in a same way as for CRW+CRT but keeping only positively charged leptons. Similarly, the VRWT- takes the CRW+CRT and selects negatively charged leptons. The VRWTf+ and VRWT- take in addition cuts on $\Delta\phi(j_i, E_{\mathrm{T}}^{\mathrm{miss}})$ and $E_{\mathrm{T}}^{\mathrm{miss}}$ $/m_{\mathrm{eff}}^{\mathrm{excl}}$ or $E_{\mathrm{T}}^{\mathrm{miss}}$ $/\sqrt{H_T}$.

- VRQi are designed to verify multi-jet background estimates, and they are orthogonal to CRQ and SR, as presented in the figure 11.16. VRQ1 is sensitive to $E_{\mathrm{T}}^{\mathrm{miss}}$ $/m_{\mathrm{eff}}^{\mathrm{excl}}$ extrapolation and is defined as CRQ with a modified cut on $E_{\mathrm{T}}^{\mathrm{miss}}$ $/m_{\mathrm{eff}}^{\mathrm{excl}}$ which is the same as for SR. VRQ2 is sensitive to the $\Delta\phi(j_i, E_{\mathrm{T}}^{\mathrm{miss}})$ extrapolation and is defined as CRQ with a modified cut on $\Delta\phi(j_i, E_{\mathrm{T}}^{\mathrm{miss}})$ which is the same as for SR. VRQ3 and VRQ4 give additional validation by adding intermediate cuts between CR and SR, but taking modified cut on $\Delta\phi(j_i, E_{\mathrm{T}}^{\mathrm{miss}})$ with $0.2 < \Delta\phi(j_{1,2,3}, E_{\mathrm{T}}^{\mathrm{miss}}) < 0.4$ and $0.1 < \Delta\phi(j_{i>3}, E_{\mathrm{T}}^{\mathrm{miss}}) < 0.2$.

- The remaining VR are for validating τ lepton estimates. VRWTau is designed to test $\mathrm{W}(\rightarrow \tau\nu)$+jets background estimate, and requires cuts as for SR with modified cut on $\Delta\phi(j_i, E_{\mathrm{T}}^{\mathrm{miss}})$ which takes values $0.2 < \Delta\phi(j_{1,2,3}, E_{\mathrm{T}}^{\mathrm{miss}}) < 0.4$ and $0.1 < \Delta\phi(j_{i>3}, E_{\mathrm{T}}^{\mathrm{miss}}) < 0.2$ and no b-tagged jets. VRttbarTau is designed to test $t\bar{t} \rightarrow \tau\nu$+jets background and is similar to VRWTau with a difference of requesting at least one b-tagged jet.

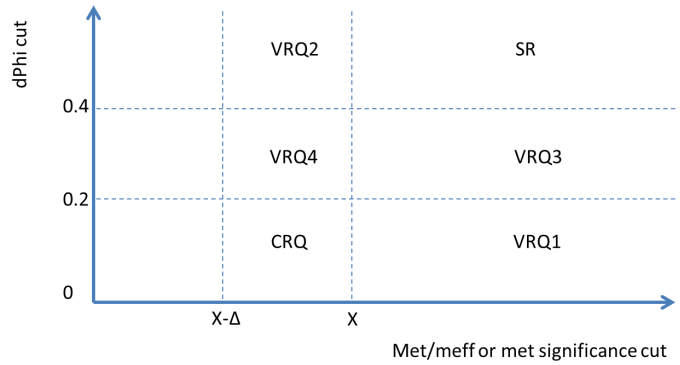

Figure 11.16.: Validation regions for multi-jet background definition in the $E_{\mathrm{T}}^{\mathrm{miss}}/m_{\mathrm{eff}}^{\mathrm{excl}}$ or $E_{\mathrm{T}}^{\mathrm{miss}}/\sqrt{H_T}$ vs $\Delta\phi(j_i, E_{\mathrm{T}}^{\mathrm{miss}})$ plane [227].

11.6. Background Estimation

The background determination in the SR is done in couple of steps. As the control regions are designed to be dominated by certain processes, the initial estimate of each process is done by using the control regions CRQ, CRW, CRT, CRγ and CRZ, to perform estimates of QCD multi-jet, W+jets, $t\bar{t}$, γ+jets for the Z($\rightarrow \nu\nu$)+jets and Z+jets processes respectively. They are used to extrapolate these estimates to the SR. The QCD multi-jet background estimation is done using the jet smearing method, described in the section 11.6.1, while all other background estimates are explained in the section 11.6.2. A fit is performed simultaneously for all processes in order to match the MC counts to the data using all CR selections. The obtained normalization is applied to the MC estimate in the CR and propagated to the SR estimate. These are used further for the statistical analysis in the signal and background or background only hypothesis. This procedure is described in the section 11.6.2.

11.6.1. QCD Multi-jet Background Estimation

In this analysis the multi-jet background is determined in a fully data driven way, using the jet smearing method. The $E_{\mathrm{T}}^{\mathrm{miss}}$ in the QCD multi-jet background can originate from jet miss-measurement and neutrinos in heavy flavor jets. The jet-smearing method includes both of these effects, and provides QCD multi-jet distributions minimally dependent on the MC prediction. The multi-jet background estimation in CRs is used to obtain transfer factors, included in the likelihood fit, and give predictions in the SRs. A short description of this method will be given in this section.

The jet smearing method uses the so-called jet response function, which quantifies the fluctuation in the jet p_T measurement, where more details about the

method can be found in [268, 269]. The low $E_{\mathrm{T}}^{\mathrm{miss}}$ events from the data are selected, because their reconstruction is closest to the 'true' particle level jets. Then the jet fluctuation is added by smearing out the four-vector of the jets, to obtain the QCD pseudo data. Typically, this method is used to determine transfer factors from the e.g. low $\Delta\phi(j_{1,2,3}, E_{\mathrm{T}}^{\mathrm{miss}})$ QCD CR to the higher $\Delta\phi(j_{1,2,3}, E_{\mathrm{T}}^{\mathrm{miss}})$ in the SRs. The jet-smearing method is performed in four steps:

1. Select low $E_{\mathrm{T}}^{\mathrm{miss}}$ seed events in data using single jet triggers to be used in steps 3 and 4.

2. Define MC response function by comparing the generator level p_T to the reconstructed, for different jet p_T slices and b-tag and b-jet selection.

3. Modify the response function (2) by smearing the seed events from data (1) until an agreement is reached between the smeared response function and data in CRs.

4. Smear jets from the seed events (1) using the data constrained smearing function (3) to obtain distributions of key variables in the CRs and SRs, which produces low and high $E_{\mathrm{T}}^{\mathrm{miss}}$ events.

The seed events are selected using a single jet trigger with jet p_T thresholds as shown in the table 11.2. An additional cut on the leading offline reconstructed jet p_T is placed to ensure that selected events are in the trigger platoe. To ensure that the jets are well measured, i.e. the response fluctuations are small, an additional cut on $E_{\mathrm{T}}^{\mathrm{miss}}$ $/\sqrt{H_{\mathrm{T}}}$ is placed. For b-jets an additional higher cut on $E_{\mathrm{T}}^{\mathrm{miss}}$ $/\sqrt{H_{\mathrm{T}}}$ per b-jet is placed, to ensure that the fraction of b-jets before and after the seed selection remains unchanged, so that no bias is introduced to the seeds with less b-jets.

MC response function R is obtained by matching truth and reconstructed jets in the multi-jet QCD MC sample, and it is defined as:

$$R = \frac{p_T(reco)}{p_T(truth)} \tag{11.8}$$

and it is binned in $p_T = 20$ GeV bin size, see figure 11.17 (a) (black line labeled as MC Response Map). The jet response is dependent on the jet kinematics. It is p_T dependent since hadronic showers can have large fluctuations, some of the deposited energy can be outside of the jet reconstruction algorithm cone, and some jets can produce a 'punch through' to the muon system. Also, due to the fact that ATLAS uses different detector technologies in different η regions, jet response is η dependent. Since heavy flavor jets can contain neutrinos, the jet response differs for the b-jet veto and the b-jet selection. The MC response function can be modeled by the Gaussian function in the core region (blue line) and non-Gaussian function in the low side tail region (black line). In order to obtain the turning point between

these two regions, the Crystal Ball function is used (red line). The b-tagged and b-vetoed response functions are measured each.

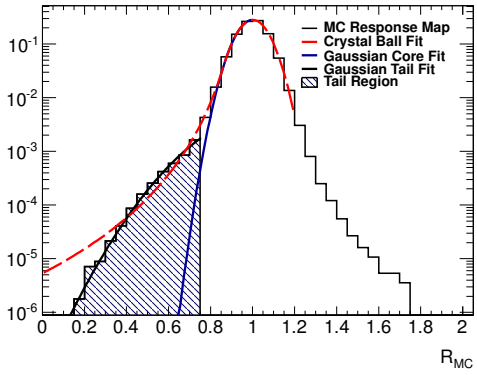

(a)

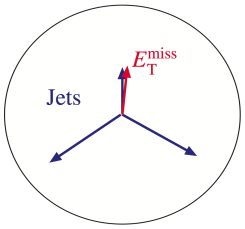

(b)

Figure 11.17.: MC response function in the jet p_T slice 200-220 GeV. The MC response function is modeled in the core and low-tail region, where the core has a Gaussian distribution(a). The Crystal Ball function is used to determine the turning point for the two regions. The data 'seed event' jets are smeared to obtain agreement of MC event distributions and data [268, 269].

Modification of the MC response is performed by seed event smearing, in order to obtain jet response that matches the data. The seed events are used to produce pseudo-data which is compared to the data. For the multi-jet selection, each jet four-vector is multiplied by a random value using the jet response function for a given jet p_T, and the jet response function is modified until agreement of pseudo-data and data is reached. Then the $E_{\mathrm{T}}^{\mathrm{miss}}$ in the smeared event is:

$$\vec{E}_{\mathrm{T}}^{\mathrm{miss}\prime} = \vec{E}_{\mathrm{T}}^{\mathrm{miss}\,seed} + \sum_i \vec{p}_T(j_i) - \sum_i \vec{p}'_T(j_i) \tag{11.9}$$

where the prime denotes the values after smearing.

The jet smearing is performed in two ways:

- Additional Gaussian smearing in the core region, to widen the jet response. A p_T dependent Gaussian is used, and a jet from a seed event is multiplied by a random number from a Gaussian of mean one and width $\sigma_{correction}(p_T)$, determined in the di-jet analysis.

- Non-Gaussian jet response low-side tail shape modification, which is essential for $E_{\mathrm{T}}^{\mathrm{miss}}$ modeling. It accounts for events which have a large jet reconstruction fluctuation. Events with high $E_{\mathrm{T}}^{\mathrm{miss}}$ are required, where the $E_{\mathrm{T}}^{\mathrm{miss}}$ is associated

with one jet, and a multi-jet selection is used, in the so called 'Mercedes' analysis.

Di-jet analysis accounts for jet fluctuation in the pure di-jet events, which manifests in the jet p_T asymmetry. It takes a selection of exactly two jets with back-to back topology and small $E_{\mathrm{T}}^{\mathrm{miss}}$. It uses the jet p_T asymmetry, defined for first two jets as:

$$A(p_{T1}, p_{T2}) = \frac{p_{T1} - p_{T2}}{p_{T1} + p_{T2}} \tag{11.10}$$

which is considered for MC and data. The asymmetry A is measured for p_T bins, and each bin is fitted with the Gaussian. If the MC jet asymmetry width σ_A is narrower than in the data, the MC jets are smeared by the p_T dependent value $\sigma_{correction}(p_T)$. It is required that the corrected response $\sigma_{total}(p_T)$ matches the response of data ($\sigma_{total}(p_T) = \sigma_{data}(p_T)$) and the $\sigma_{correction}(p_T)$ is obtained from:

$$\left(\frac{\sigma_{total}(p_T)}{p_T}\right)^2 = \left(\frac{\sigma_{MC}(p_T)}{p_T}\right)^2 + \sigma_{correction}(p_T)^2 \tag{11.11}$$

with the usage of the σ_A fit parameters obtained for the MC and data.

Additional refinement to this method is performed using the ϕ smearing method, where the MC jets are in addition smeared by a rotation in the ϕ angle, to account for the difference in the phi distribution of MC jets after the smearing by the p_T. The $\Delta\phi$ correction is obtained in a same procedure as for the asymmetry case. The method is performed for each, the b-jet veto and the b-jet selection using jet p_T slices.

'Mercedes' analysis considers the non-Gaussian jet response low-side tail, and is essential in producing high $E_{\mathrm{T}}^{\mathrm{miss}}$ pseudo-data. It is performed after the di-jet analysis jet smearing, with a selection of at least three jets, where one jet is associated with $E_{\mathrm{T}}^{\mathrm{miss}}$. This is realized for jets forming a typical 'Mercedes' sign, see figure 11.17 (b). Then the response function for these jets is given by:

$$R_2 \simeq \frac{\vec{p}_T^{\,j} \cdot (\vec{p}_T^{\,j} + \vec{E}_{\mathrm{T}}^{\mathrm{miss}})}{|\vec{p}_T^{\,j} + \vec{E}_{\mathrm{T}}^{\mathrm{miss}}|^2} \tag{11.12}$$

where $\vec{p}_T^{\,j}$ is transverse momenta of the reconstructed jet associated with $E_{\mathrm{T}}^{\mathrm{miss}}$. The non-Gaussian response needs to be modified in order to achieve agreement of pseudo-data and data. First the low side tail region needs to be defined, by finding the turning point from the core Gaussian to the low side tail region. This is achieved by using the Crystal Ball function on each jet response jet p_T slice. From the fit parameters, the turning point is found and low side tail region is defined. Second, the low side tail is best fitted in the with the Gaussian in the newly defined tail region, and width of the low side tail σ_{tail} is multiplied by a $\Delta\sigma_{tail}$ to obtain agreement of the smeared sample with the data in the R_2 distribution. This procedure is performed for each, b-jet and b-veto selection. Additional check was performed using $|\eta|$ slices,

to account for R_2 dependence on $|\eta|$.

The jet smearing was performed using the di-jet and 'Mercedes' analysis to obtain the QCD pseudo-data. Jet smearing is also performed to account for the systematic uncertainties for the upward and downward fluctuation. The MC for other SM backgrounds together with the QCD pseudo data was compared to the data in the QCD CRs. The performance was validated for m_{eff} , $E_{\text{T}}^{\text{miss}}$ $/m_{\text{eff}}$ and $\Delta\phi(j_{1,2,3}, E_{\text{T}}^{\text{miss}})$ distributions for 2-6 jet multiplicity, and uniform ratio is obtained for all distributions. The QCD pseudo data is further included in the likelihood fit in the analysis, where additional normalization is performed, and estimate of the QCD background in the SR is obtained.

11.6.2. Electroweak Background Estimation

The Z+jets, W+jets and $t\bar{t}$ backgrounds are determined from MC and data, using the technique which will be described in the section 11.7.1, while diboson background is determined from MC only. In this section details about MC and their comparison to data will be given.

The fake lepton background in CRW, CRT and VRZ have shown to be lower than 4% mainly due to the fact that it decreases quickly with $E_{\text{T}}^{\text{miss}}$ [270]. The fake photon background was estimated to be less than 5 % of the total SM prediction in the CRγ region [271]. Therefore, these backgrounds can be neglected in this analysis [227].

For CRγ, VRZ, CRW and CRT the default and alternative MC generator performance have been compared, the MC generators used in this analysis have been presented in the table 11.1. It has been shown that MC produced with SHERPA agrees well with data in terms of rate and shape in the CRγ and VRZ. However, using SHERPA in CRγ gives higher number of events for high jet multiplicity (N_{jet} > 5), while ALPGEN gives a beeter agreement. Therefore, the difference between these two generators is included in the analysis as additional source of uncertainty. In CRW both SHERPA and ALPGEN tend to over estimate the event rate in the W p_T distribution. In addition, for very high jet multiplicitites, SHERPA predicts too many events with respect to data in CRW, while ALPGEN is providing a slightly better agreement with data in the jet-multiplicity distributions. Therefore, the difference of these two generator predictions is added to the analysis as additional systematic uncertainty. The $t\bar{t}$ background in the CRT using the default PowHeg+PYTHIA and alternative MC@NLO+HERWIG generators tend to over estimate the data. In this analysis the default MC using the PowHeg+PYTHIA with the Perugia2011C tune is used, which in addition uses $p_T(t\bar{t})$ reweighing. A dedicated analysis showed that good agreement of MC and data is achieved for up to 7 jet multiplicity, which gives good confidence in the usage of this method. As the diboson represents a minor background in this analysis, its estimate has been taken directly from MC distributions, together with its theoretical uncertainty. To the contrary of all other backgrounds it is not included in the fit as a free parameter, see more about the statistical procedure in the next section 11.7.1.

11.7. Statistical Treatment and Systematic Uncertainties

The background determination and statistical tests are performed at the same time in this analysis. Details about the statistical treatment are given in the section 11.7.1 and considered systematic uncertainties are described in the section 11.7.2.

11.7.1. Statistical Treatment

This analysis uses a profile likelihood approach in the background determination and new physics statistical tests, using the MC predictions and observed number of events in the SR and multiple CR. This method allows for CR correlations due to cross contamination and common systematic uncertainties of different SM (or SUSY) processes to be taken into account. In the background determination the combined fit with log likelihood is used, as described in the section 8.3. The statistical test uses profile log likelihood ratio, as described in the section 8.2. There are three results that are computed, called the **background only fit** (background fit), **model independent fit** (discovery fit) and the **SUSY model-exclusion fit** (exclusion fit). In this section more details on the fit and statistical tests used in this analysis will be given.

The **likelihood function** is constructed for each channel, i.e. SR with its dedicated CRs. The counts in these regions are treated as Poisson distributions for each SM and SUSY sample, labeled as P_{SR},P_{CRY},P_{CRQ},P_{CRW} and P_{CRT}, for control regions dedicated for samples of Z+jets, QCD jets, W+jets and $t\bar{t}$ respectively. The systematic uncertainties are included as nuisance parameters and are assumed to have Gausian distribution. The likelihood for each channel for a tested μ value is therefore:

$$L(\mathbf{n}|\mu, s, \mathbf{b}, \theta) = P_{SR} \times P_{CR\gamma} \times P_{CRQ} \times P_{CRW} \times P_{CRT} \times C_{syst} \tag{11.13}$$

where the term C_{syst} represents the pdf-s which constrain the systematic uncertainties, and more details about the treatment of systematic uncertainties will be given in the section 11.7.2. The $\mathbf{n}$ represents the measured number of events for each region, $\mathbf{b}$ is the expected number of background events for control regions, and θ are the nuisance parameters that parametrize the systematic uncertainties, e.g. luminosity or jet energy scale. The s is the expected number of signal events taken from MC when the exclusion fit is used.

The expected number of background events $\mathbf{b}$ for each region i like SR, CR or VR and sample j are taken from MC for W+jets, Z+jet and $t\bar{t}$, while for the QCD jets the estimate is taken from pseudo data generated using the jet smearing method.

The μ value for the signal is fixed to $\mu_s = 0$ in the background-only and model independent and $\mu_s = 1$ in the SUSY model-exclusion fit. The μ_j for the background samples j (W+jets,Z+jets,$t\bar{t}$,QCD jets) have an initial value of 1, and are determined by the selected type of fit (background-only, model independent, SUSY model-exclusion). Other minor backgrounds like diboson and single t are taken from

MC and are treated as fixed.

The expected number of events λ for each SR, CR or VR i and samples j, is given by:

$$\lambda_i(\mu, s_i, \mathbf{b}, \theta) = s_i(\theta)\mu_s + \sum_{j}^{W,Z,t\bar{t},QCD} b_{i,j}(\theta)\mu_j + b_i^{VV}(\theta) \tag{11.14}$$

where the s_i is the expected number of events for a given SR, CR or VR, the $b_i^{VV}(\theta)$ term denotes minor backgrounds like diboson, which are taken from MC.

For a given set of SR, CR and VR (i.e. channel), the background fit obtains the so called **transfer factors** (TF) as the main result, i.e. the ratios of expected number of events in the SR and CR for a given SM sample:

$$TF = \frac{N_{SR}^{MC}}{N_{CR}^{MC}} \tag{11.15}$$

The number of events in the signal region for a sample j is initially given by:

$$N_{SR}^{pred} = N_{CR}^{data} \times \frac{N_{SR}^{MC}}{N_{CR}^{MC}} \tag{11.16}$$

where the N_{CR}^{data} is the number of observed events in the CR, and the initial value for the TF before the fit is given by the ratio of expected number of events in the SR and CR. Next, the background estimates are normalized coherently across all CR-s for a given channel using the inter-CR TF, so the fit obtained TF allow for the total number of expected and observed events to match in all CR. The final result is the central expected TF value for each sample, i.e. SM process, together with their associated correlated and uncorrelated uncertainties. By using this technique some of the systematic uncertainties cancel out to a large extent, like systematic uncertainty from jet energy scale (JES) and theoretical uncertainties in the MC cross-section calculation of SM processes. The analysis uses similar kinematic selections for the CRs and SR in order to reduce residual uncertainties correlated between them.

The **Z**($\rightarrow \nu\nu$)**+jets** process represents an important background in this study, as it mimics the signal and is a source of large systematic uncertainty. For this reason an improved background determination of this process has been used. In a standard setup, a control sample of γ + jets in the CRγ is used to estimate the Z($\rightarrow \nu\nu$)+jets sample. For $p_T(\gamma) > m_Z$ these kinematics are similar, and the p_T of the photon is considered as a $E_{\mathrm{T}}^{\mathrm{miss}}$. The Z($\rightarrow ll$)+jets events strongly resemble Z($\rightarrow \nu\nu$)+jets events, but have low statistics. The γ+jets have high statistics, but need a correction on the cross-section of the process. Therefore, the improved estimate on the number of events for the Z($\rightarrow \nu\nu$)+jets process has a correction κ to the γ+jets MC:

$$N_{SR}^{Z\nu\nu,pred} = N_{CR\gamma}^{\gamma+jets,data} \times \frac{N_{SR}^{Z\nu\nu,MC}}{N_{CR\gamma}^{\gamma+jets,MC} \times \kappa} \tag{11.17}$$

and the κ correction is given as ratio of normalization factors in CRγ and CRZ for γ+jets and Z($\rightarrow ll$)+jets processes:

$$\kappa = \frac{N_{CR\gamma VL}^{\gamma+jets,data} \times N_{CRZVL}^{Zll,MC}}{N_{CR\gamma VL}^{\gamma+jets,MC} \times N_{CRZVL}^{Zll,data}} = \frac{(N_{CR\gamma VL}^{data} - N_{CR\gamma VL}^{bkg,MC}) \times N_{CRZVL}^{Zll,MC}}{N_{CR\gamma VL}^{\gamma+jets,MC} \times (N_{CRZVL}^{data} - N_{CRZVL}^{bkg,MC})} \tag{11.18}$$

where CRs are designed to be very loose, i.e. CRγVL and CRZVL, and a correction to the data estimate is placed by subtracting the remaining background, estimated by the MC, i.e. $N_{CR\gamma VL}^{bkg,MC}$ and $N_{CRZVL}^{bkg,MC}$. The κ value is measured for Sherpa (nominal) and Alpgen (alternative) MC generators, which reduces the theoretical uncertainty on the Z($\rightarrow \nu\nu$)+jets background due to differences in the MC generator distributions, by a large amount. However, the uncertainty on the κ correction measurements needs to be included in the fit, and is treated as additional uncertainty on the Z($\rightarrow \nu\nu$)+jets background, see more details on the systematic uncertainties treatment in the next section 11.7.2, and the Z($\rightarrow \nu\nu$)+jets background estimate method description in [227].

The multi-jet TF-s are obtained with the data-driven method, where a resolution function is applied to well measured multi-jet events to account for uncertainty coming from jet energy miss-measurement and heavy-flavor semileptonic decays on $E_{\mathrm{T}}^{\mathrm{miss}}$, as explained in detail in the section 11.6.1. The TF for the other SM processes use MC information.

The **background-only fit** is performed in order to determine compatibility of event yields from the SR with the SM prediction. It uses data from the CRs in the likelihood fit, in order to constrain all nuisance parameters and determine normalization for each background TF. For each background component a dedicated CR is used, and the predicted yields in the CR are fitted to the values obtained from the data. It is assumed that new physics does not contribute to the yields. The background-only fit is therefore used for the estimation of the expected yields in the SR, but also in VRs in order to gain confidence in the background estimation. The statistics test quantifies the agreement of data with the SM-only hypothesis with the one-sided p_0 value. All event yield tables in this thesis are given for the background-only fit.

The **model-independent fit** is performed if no excess of data has been observed in order to determine upper limits on the on the number of new physics signal events in each SR. Namely, this is a upper limit on the visible cross-section for BSM physics processes ($\langle\varepsilon\sigma\rangle$) and it is defined as the product of acceptance, reconstruction efficiency and production cross-section. The likelihood for the model-independent fit includes the number of observed events in the SR, in addition to the event yields from the CR, as done in the background-only fit. The signal strength μ is fixed to be non-negative, and added as a free parameter in the fit, and normalization on the TFs for each background are set as free parameters in the fit. The possible contamination of CR by the new physics events is neglected.

The **SUSY model-exclusion fit** can be used to set limits on the signal cross-

sections for a given SUSY model (assuming signal strength $\mu = 1$), if no excess of data has been observed. The normalization on each background TF and on the signal are free parameters in the fit. For the case of discovery, the fit obtained signal strength μ_{sig}, i.e. the signal normalization factor, can give confidence in a certain signal hypothesis test. The likelihood is constructed using the yields in the CRs and in the SR, as in the model-independent fit, with additionally taking into account the presence of the signal events in the CRs, theoretical and experimental uncertainties of the SUSY cross-section and kinematic distributions. Also, the correlations between signal and background systematic uncertainties are included in the likelihood. Here the CL_s statistical test is used to produce exclusion curves for the SUSY signal exclusion plots.

In the analysis test statistics pdf need to be used for the likelihood fit, p-value and CL_s computation. For the analysis optimization and first estimates the Asimov test statistics is used, as described in the chapter 8.2.1. The public results of the discovery test and a selection of signal points for a cross-check in model-independent and SUSY model-exclusion fits use the toy MC pdf-s. The low count channels use toy MC pdf as well. The background-only test is performed for a q statistics and p-value is calculated for the observed statistics q_{obs} as $p_b = P(q \leq q_{obs}|b)$. The SUSY model-exclusion uses the $CL_s = p_{s+b}/(1 - p_b)$ as explained in the chapter 8.2.1, while the result for the model-independent fit as a result obtains the optimal μ value.

11.7.2. Systematic Uncertainties

In the likelihood function, the systematic uncertainties are included with the probability density function $C_{syst}(\theta^{\mathbf{0}}, \theta)$ for nominal values $\theta^{\mathbf{0}}$ of nuisance parameters and θ values around them, which are varied when the likelihood is maximized. The C_{syst} is simplified by taking each $\theta_i^0 = 0$ and normalizing their constraining pdf-s for θ_i. For e.g. luminosity is modeled by the Gaussian distribution with $\theta_{lumi}^0 = 0$ and $\theta_{lumi} = \pm 1$, which corresponds to one sigma deviation. Therefore, for independent nuisance parameters the C_{syst} is a product of Gaussian probability distributions:

$$C_{syst}(\theta^{\mathbf{0}}, \theta) = \prod_{i \in SU} G(\theta_i^0, \theta_i) \tag{11.19}$$

where SU are all considered systematic uncertainties.

There are four ways to consider nuisance parameter correlations, included in the likelihood for the systematic uncertainty treatment. First, they can be fully correlated across different regions and samples (e.g. luminosity, JES, JER, see more details below). Second, fully correlated across different regions but independent per sample (e.g. theoretical uncertainties). Third, fully uncorrelated variables with one parameter per bin (e.g. statistical errors). Fourth, partially correlated (e.g. diboson theoretical uncertainty). The systematic uncertainties with impact lower than the luminosity uncertainty are neglected.

Name	Characteristic scale	L Treatment	Comment
Luminosity	2.8%	Fully correlated	Pure MC estimates
MC statistics		Uncorrelated	All MC samples
Experimental Uncertainties			
JES			
JER			
Soft $E_{\mathrm{T}}^{\mathrm{miss}}$ scale	5%	Fully corr.	
Soft $E_{\mathrm{T}}^{\mathrm{miss}}$ resolution	2%		
Lepton/photon efficiency	$5-7\%$ for γ		For photons, CRY only
b-tagging			Only in CRW and CRT
Theoretical uncertainties			
Pile-Up	$\langle\mu\rangle \times [0.9, 1.1]$	Fully corr.	All MC samples
Total cross-section	Diboson	Partially corr.	Pure MC estimates
μ_R/μ_F scale variation	$\mu \times [0.5, 2.0]$	Corr. per process	W+jets/Z+jets/γ+jets
Matching scale variation	$p_T(j, min) = [15, 25]$ GeV	Corr. per process	W+jets/Z+jets/γ+jets
Number of extra partons	Decreased by 1	Corr. per process	W+jets/Z+jets/γ+jets
Generator comparison	ALPGEN vs SHERPA	Corr. per process	W+jets/Z+jets/γ+jets
W + heavy flavor	$\simeq 25-50\%$	Corr. per process	W+jets
γ+jets κ correction	$\simeq 6\%$	Corr. per process	γ+jets
Generator comparison	MC@NLO vs POWHEG-BOX	Corr. per process	$t\bar{t}$
$t\bar{t}$ diff. cross-section	vary weights	Corr. per process	$t\bar{t}$
Multi-jets method (Gaus.)		Corr. per process	QCD
Multi-jets method (Tails)		Corr. per process	QCD

Table 11.9.: Details on systematic uncertainties used in the likelihood fit. They are included as nuisance parameters in the fit, and can be treated as uncorrelated and partially or fully correlated per physics sample and selection region [227].

In the table 11.9 the details of systematics treatment in the likelihood fit are shown. The systematic on luminosity is treated as fully correlated across different regions and samples. Due to high precision in luminosity determination it takes a value of 2.8%, and uncertainty is used only with the pure MC estimates. The MC statistics is treated as uncorrelated for all MC samples. The uncertainties due to experimental uncertainties are included in the fit. The jet energy scale (JES) uncertainty is determined using the test-beam, simulation and in-situ measurements as described in [185, 272]. In this analysis one nuisance parameter for JES is used, and this systematic uncertainty is treated as fully correlated across all MC samples. The 17 JES nuisance parameters were varied up and down, and the sum in quadrature of up and down variations has been compared to the summary variation case. Good agreement has been found for different jet multiplicities, and using one nuisance parameter in the JES uncertainty estimation can be applied in the 6jt+ selection. The study has been performed using the simplified model of $\tilde{q}\tilde{q}$ production on the up and down JES variations. The JES nuisance parameters included effects on a number of partons, calibration effects, pileup, flavor composition and b-jet energy scale. Using one nuisance parameter and its uncertainty using summary up and down variations has been found to be a good estimate of the JES uncertainty for this analysis [227]. The jet energy resolution (JER) was estimated using a technique described in [273], and treated as fully correlated across all MC samples. As this analysis relies on the reconstruction of large number of jets, the JES and JER uncertainties are expected

to be large. However, due to the usage of transfer factors in the background determination, using the equation 11.15, these uncertainties cancel out to a large extent, and these uncertainties are not dominant. The effect of pile-up due to high instantaneous luminosity is varied for $\langle\mu\rangle$ in the 0.9 - 1.1 range, and added to the JES and JER calculation. It is fully correlated across all MC samples. The effect on scale and resolution from the low-p_T calorimeter activity, included in the $E_{\mathrm{T}}^{\mathrm{miss}}$ calculation but not coming from jets and baseline leptons, is treated as fully correlated across all MC samples, and is estimated to be 7% and 2% respectively. The uncertainty on the lepton and photon reconstruction efficiency is used fully correlated for photons in the CRY, and is estimated to be 5-7%. The effect of b-tagging/veto efficiency systematic uncertainty is used in CRW and CRT as fully correlated.

The uncertainties of theoretical MC modeling are taken into account. The uncertainty on the cross-section calculation is used only for the pure MC estimates, in particular for the diboson sample, and is partially correlated, per process. The W+jets, Z+jets and γ+jets backgrounds have a refined systematic uncertainty estimation which includes uncertainty from the factorization and renormalization scales, determined by shifting the scale by a factor of two, and are correlated per process. Also, matching scale, number of extra partons and uncertainties determined by the different generator comparison are included correlated per process. For the Z($\rightarrow ll$)+jets in addition to these uncertainties, the κ correction is used on the nominal and alternative MC estimates, which improves the MC and data agreement in the CRs and reduces the overall systematic uncertainty for this background. The uncertainty on the κ correction, in addition to other uncertainties, accounts for photon isolation and miss-identification, and effects of different parton distribution functions, and is estimated to be around 6%. Most of the systematic uncertainties for κ cancel out, and the dominant contribution arises primarily from the photon selection, and there are smaller effects on the lepton selection, QCD and other background uncertainties in the dedicated CRs. Uncertainty on the κ correction is incorporated as additional uncertainty on the Z($\rightarrow ll$)+jets background estimation, correlated per process. Additional uncertainty arising from W+heavy flavor background, is found to be 25%-50%, and is included as correlated per process, but is highly reduced by the usage of the TF in the analysis.

The uncertainties for the diboson sample on scale and PDF uncertainties are found to be $\leq$ 50 % for each SR, and a uniform 50% uncertainty is applied for this case. The $t\bar{t}$ uncertainties are added correlated per process for different generators and difference in cross-section calculation correlated per process. The QCD background systematic uncertainties are determined as the uncertainties from the jet-smearing method, which is determined by varying the width and tails of the jet resolution function, which are both added correlated per process. The uncertainties from PDF modeling have shown to be negligible for each MC sample. The breakdown of systematic obtained by the background-only fit is shown in the section 11.8.1 in the table 11.13.

The SUSY model analysis includes theoretical uncertainties on the signal cross-

section and systematic uncertainties on the signal acceptance. It has been shown that initial state radiation (ISR) strongly affects the signal acceptance for SUSY models with small mass splittings between the strongly interacting states ($\tilde{q}$ and $\tilde{g}$) and the LSP/NLSP ($\tilde{\chi}_1^{\pm}$ or $\tilde{\nu}_\tau$). The systematic uncertainty arising from ISR was studied using MC samples by varying the value of α_s, renormalization and factorization scales and the MADGRAPH/PYTHIA matching scales. For mass splittings of Δm < 100 GeV this uncertainty was ranging 10-40% for different SR, the uncertainty was shown not to depend on the SUSY particles masses for a fixed Δm, while for fixed SUSY particle masses Δm falls approximately exponentially [31]. The NUHMG model for all studied points has a larger mass splitting of $\Delta m > 900$ GeV, see figures 10.2 and 10.3 , and the uncertainty from ISR has a small effect for this grid.

11.8. Results and Interpretation

This section describes the results of the SR 6jt+ and NUHMG model using the 20.3 fb−1 of ATLAS 8 TeV data. First the background only fit performance is estimated in the section 11.8.1. Next, the validation of the background estimation is set in place, as described in the section 11.8.2. The results are presented in the section 11.8.3. As no significant excess of data compared to the SM expectation is observed, the results interpretation is shown in the section 11.8.4, and the performance of the 0-lepton NUHMG model analysis is compared to the one-lepton analysis in the section 11.8.5.

11.8.1. Background Fit Performance

The background-only fit is run to obtain background normalization factors, gain confidence in background determination using validation and to perform the statistical test for the background-only hypothesis. In this section the performance of this fit will be presented.

The free parameters in the fit are scaling factors for the background samples and the nuisance parameters θ. The results for the background-only fit for the 6jt+ channel CRs and SR are shown in the table 11.10. The statistical uncertainites for dedicated CR are derived from the number of events and the correlations between the CRs. After the fit dominant contribution of irreducible background in the SR comes from the top background, while the multi-jet, W+jets, Z+jets and diboson background have smaller contributions in the SR.

In the table 11.11 scaling factor values are shown. The W+jets and Z+jets backgrounds have the highest scaling factors, which is due to two reasons. First, the W/Z+jet background modeling for the large jet multiplicity predicts more events than seen in data. This tendency has been observed ATLAS wide, and is explained in the section 11.6.2. This effect is included in the analysis with theoretical uncertainties on these backgrounds. Second, the $E_{\mathrm{T}}^{\mathrm{miss}}$ $/m_{\mathrm{eff}}^{\mathrm{excl}}$ cut strongly reduces the W/Z+jets background in the CRW/Z, which manifests in large statistical uncertain-

SR6jt+ channel	CRW	CRT	CRY	CRQ	SR
Observed events	5	16	5	53	6
Fitted bkg events	5.05 ± 1.82	16.01 ± 4.10	4.99 ± 2.23	53.01 ± 7.29	4.94 ± 1.56
Fitted Diboson events	1.10 ± 0.55	0.20 ± 0.10	0.65 ± 0.33	1.01 ± 0.50	0.20 ± 0.10
Fitted γ+jets events	0.00 ± 0.00	0.00 ± 0.00	4.19 ± 2.26	0.00 ± 0.00	0.00 ± 0.00
Fitted Multi-jet events	0.00 ± 0.00	0.00 ± 0.00	0.00 ± 0.00	43.25 ± 8.36	$0.25^{+0.39}_{-0.25}$
Fitted $t\bar{t}$ events	3.20 ± 2.81	15.55 ± 4.59	0.13 ± 0.12	8.09 ± 4.83	3.67 ± 1.75
Fitted W+jets events	$0.67^{+3.21}_{-0.67}$	$0.26^{+1.26}_{-0.26}$	0.00 ± 0.00	$0.22^{+1.09}_{-0.22}$	$0.25^{+1.23}_{-0.25}$
Fitted Z+jets events	0.08 ± 0.07	$0.00^{+0.00}_{-0.00}$	0.01 ± 0.01	$0.44^{+0.80}_{-0.44}$	$0.57^{+0.79}_{-0.57}$
MC exp. SM events	13.19	17.92	16.16	38.89	9.16
MC exp. Diboson events	1.11	0.20	0.66	1.01	0.21
MC exp. γ+jets events	0.00	0.00	15.34	0.00	0.00
MC exp. Multi-jet events	0.00	0.00	0.00	25.88	0.15
MC exp. $t\bar{t}$ events	2.95	14.27	0.12	7.46	3.38
MC exp. W+jets events	8.82	3.44	0.00	2.95	3.36
MC exp. Z+jets events	0.30	0.01	0.04	1.59	2.07

Table 11.10.: SR6jt+ background fit results for the CRW, CRT, CRY, CRQ and SR regions, for an integrated luminosity of 20.3 fb^{-1} fb^{-1} [227]. Nominal MC expectations (normalized to MC cross-sections) are given for comparison. The errors shown for CRs are the statistical plus systematic, while for the SR they are systematic uncertainties only.

Sample	Scaling factor
Z+jets	0.27 $\pm$0.15
W+jets	0.1 $\pm$0.7
$t\bar{t}$	1.09 $\pm$0.38
Multi-jets	1.67 $\pm$0.32

Table 11.11.: Scaling factors in the 6jt+ channel for Z+jets, W+jets, $t\bar{t}$ and multi-jet background obtained by the background-only fit.

ties. Therefore, this effect is included in the analysis via uncertainties on the scaling factors. The Z+jets background has an additional refinement which reduces its systematic uncertainty, as explained in the section 11.7.1, which contributes to the fact that this scaling factor is smaller than the W+jets case. However, in the validation procedure, these backgrounds show good performance in the background-only fit, and good agreement is reached for all VRW/Z pulls, see section 11.8.2 and figure 11.20. Therefore, W/Z+jets background estimates can be considered reliable.

In order to gain confidence in the quality of the background determination and fitting procedure, cross-checks on the nuisance parameters and size of correlations are set in place for the background-only fit. In the profile log-likelihood fit, the

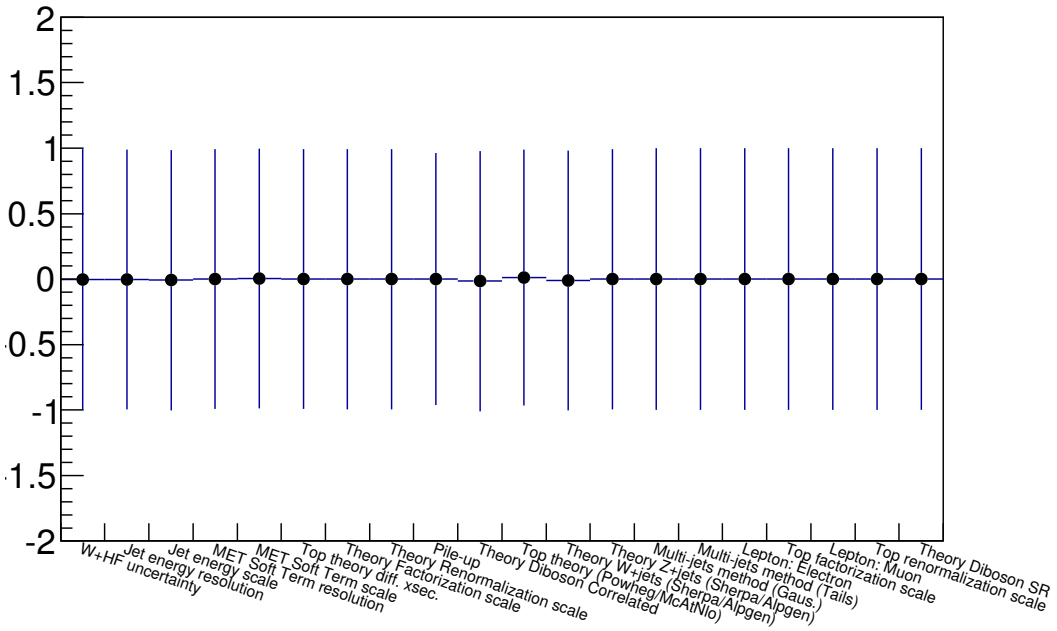

Figure 11.18.: Nuisance parameter values obtained by the background-only fit for the 6jt+ channel [227]. All nuisance parameters have width around 1, therefore there is no profiling of the nuisance parameters by the fit.

nuisance parameters are modeled with the Gaussian distribution with a mean value and width equal to 1 as an initial value. Their final fit-obtained values are shown in the figure 11.18. The fit-obtained values are very close to the initial value of 1, i.e. there are no large changes by the fit for all nuisance parameters width, therefore there is no profiling of nuisance parameters, which gives confidence in the fit quality. The map of correlations for the SR 6jt+ obtained for the background-only fit between different systematic uncertainties are shown in the figure 11.19. There are no strong correlations except for the case of top theoretical uncertainty correlated with CR statistics of W+jets and multi-jet background, and correlations between top CR statistics with CR statistics of W+jets and multi-jet background. This is well understood by the top background population in CRW and CRQ and its large theoretical uncertainty, and is included in the systematic uncertainty calculation.

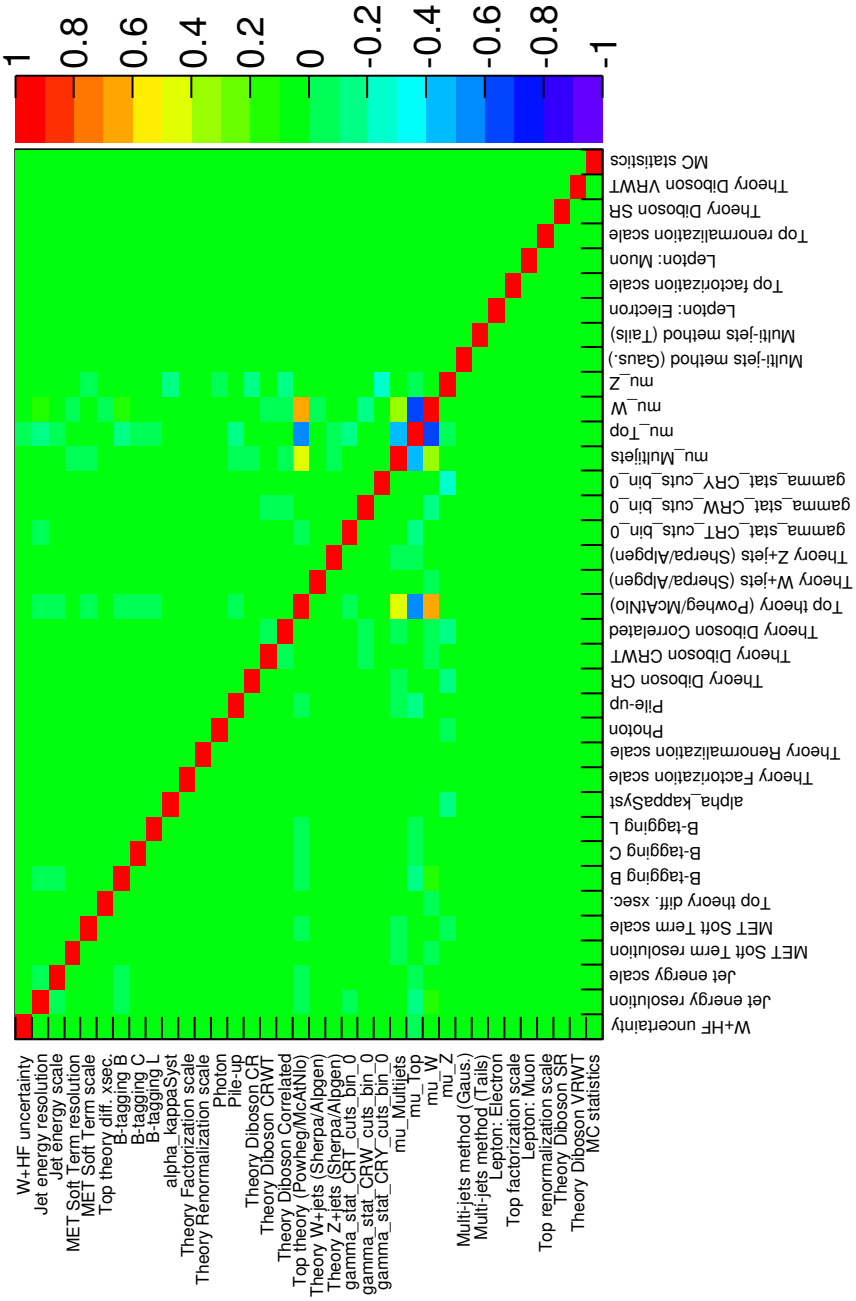

Figure 11.19.: Correlations matrix for the nuisance parameters used in the profile log-likelihood fit obtained by the background-only fit setup for the SR 6jt+ [227].

11.8.2. Validation

The most powerful test of background determination procedure using the fit is obtained by comparing the number of events observed in data with the expected number of events determined by the background-only fit in VRs. More precisely, the background-only fit is run and the predictions obtained by the fit are compared to the observed number of events in each VR. A set of 19 VRs are used for the 6jt+ channel, where each VR is dedicated for a cross-check of different physics process, which are defined in the section 11.5.3.

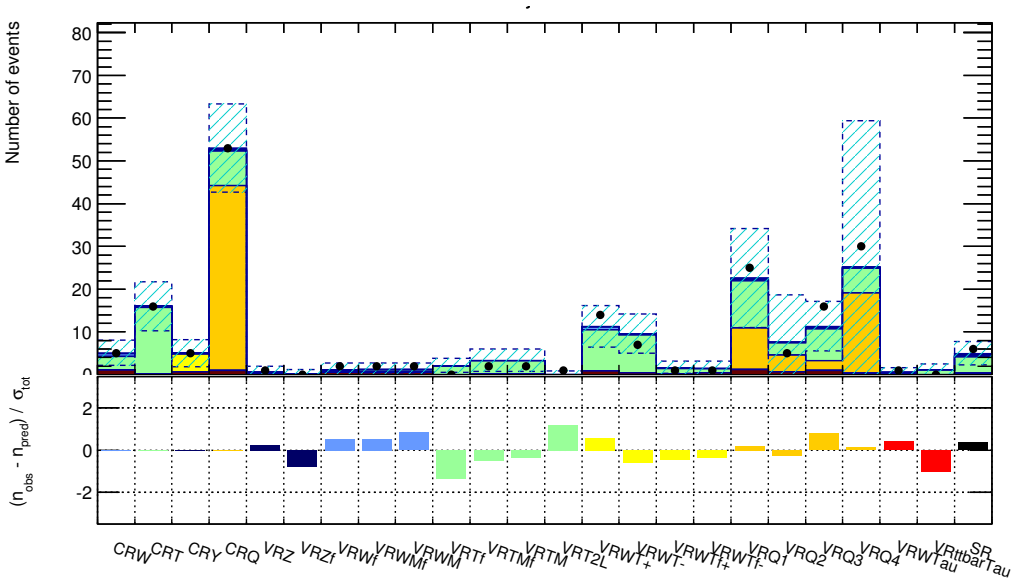

Figure 11.20.: Observed versus expected number of events in all VRs for the 6jt+ channel [227]. Event counts are shown in the upper plot, where dark blue is the Z+jets, light blue is the W+jets, light green is the top, light yellow is the W+top, and dark yellow is the QCD background prediction, and the black dots are the observed number of events. The dashed blue area represents the total uncertainty for the predicted number of events, including statistical and fitted background uncertainty. The lower plot shows 'pull' results, using the same coloring scheme, where σ_{tot} is the total uncertainty in the VR, including statistical and fitted background uncertainty. Note that σ_{tot} is correlated between VRs.

The validation results are typically presented with the so called 'pull' distributions, see figure 11.20. The 'pull' for a given VR is defined as:

$$\frac{n_{obs} - n_{pred}}{\sigma_{tot}} \tag{11.20}$$

where n_{obs} and n_{pred} are the number of observed and predicted number of events in the VR, respectively. The σ_{tot} is the total uncertainty in the VR, and is given by:

$$\sigma_{tot} = \sigma_{stat} \otimes \Delta n_{pred} \tag{11.21}$$

where Δn_{pred} is the uncertainty on the background prediction in the VR obtained by the fit, while σ_{stat} is the statistical uncertainty on the predicted number of events in the VR, computed as an upper and lower 68% CL of a Poisson distribution centered around n_{pred}. In more detail, the values of 'pull' in relevant VRs for the 6jt+ channel are shown in the table 11.12. All VRs pulls have less than 1.4 sigma deviation from the central value. Therefore, SR 6jt+ has good performance in all VR, which gives good confidence in the procedure of background determination using the fit. One should note that uncertainties are correlated and VRs are not necessarily mutually exclusive.

SR	VRZz	VRWf	VRMWf	VRWTau	VRTf	VRMTf	VRttbarTau	VRQ1	VRQ4
6jt+	-0.8	0.5	0.5	0.4	-1.4	-0.5	-1.0	0.2	0.1

Table 11.12.: Difference of number of events observed in data and SM MC expectations obtained by the fit, divided by the total uncertainty of the prediction ('pull'), in relevant VRs for the 6jt+ channel [31].

11.8.3. Results

As the background-only fit performance in the SR 6jt+ was validated, the results of this SR can be examined. First the dominant contributions to systematic uncertainties and the kinematic variable distributions will be examined. Then the yields in the SR and their statistical interpretation will be explored in the section.

The treatment of systematic uncertainties have been described in the section 11.7.2, and in the table 11.13 breakdown of dominant systematic uncertainties for the SR 6jt+ is shown. The CR statistics uncertainty arises for the limited statistics in the CRs. The uncertainty on the JES, JER, including the uncertainty on low-p_T calorimeter activity not associated with jets or leptons, i.e. the $E_{\mathrm{T}}^{\mathrm{miss}}$ soft term, are together labeled as Jet/MET in the table. The uncertainty related to theoretical modeling of SM background samples are estimated using the comparison of TFs for each sample produced by different generator. The theoretical uncertainty on the renormalization and factorization scales is estimated by increasing and decreasing the relevant scales by factor of two. The uncertainty on the PDF modeling has been tested for each background process and found to be negligible. The diboson scale and PDF uncertainties have been taken to be 50% with a uniform distribution. The uncertainties of b-jet tag/veto, pile-up and other minor backgrounds are included in the table under the label 'other'.

The overall systematic uncertainty is estimated to be 33%. The dominant contribution is arising from the top quark CR statistics with 22.4 %. In a similar way,

Channel	**6jt+**
Total bkg	4.9
Total bkg unc.	±1.6 [33%]
CR stats: Z/γ^*+jets	±0.31 [6.3%]
CR stats: W+jets	±0.7 [14.3%]
CR stats: top quark	±1.1 [22.4%]
CR stats: multi-jets	±0.04 [0.8%]
MC statistics	±0.4 [8.2%]
Jet/MET	±0.29 [5.9%]
Leptons	±0.32 [6.5%]
Z/γ TF	±0.04 [0.8%]
Theory: Z/γ^*+jets	±0.7 [14.3%]
Theory: W+jets	±0.08 [1.6%]
Theory: top quark	±0.5 [10.2%]
Theory: diboson	±0.1 [2.0%]
Theory: scale unc.	±0.5 [10.2%]
Multi-jets method	±0.4 [8.2%]
Other	±0.03 [0.6%]

Table 11.13.: Breakdown of the dominant systematic uncertainties on background estimates obtained by the fit, in the SR 6jt+. Uncertainties relative to the expected total background yield are shown in parenthesis. 'CR stats' labels the uncertainties arising from a statistical uncertainty of a dedicated CR for a given physics process. Note that the individual uncertainties can be correlated, and do not necessarily add up quadratically to the total background uncertainty [31].

the W+jets background CR statistics uncertainties are as high as 14.3 %. The theoretical uncertainties in the Z/γ^*+jets sample are as high as 14.3 %, and are arising from their $E_{\mathrm{T}}^{\mathrm{miss}}$ contribution in the SR due to the low $E_{\mathrm{T}}^{\mathrm{miss}}$ /$m_{\mathrm{eff}}^{\mathrm{excl}}$ cut of 6jt+. The theoretical uncertainty on the top quark background modeling is 10.2 %, while the scale uncertainty is 10.2 %. Jet/MET is not very high in this SR, and is 5.9 %. Namely, by using the transfer factor technique in the background determination, these large uncertainties cancel out. The MC statistics uncertainty in the SR is 8.2 %. The multi-jets background has a relatively low contribution of 8.2 % due to the successful QCD background removal in the SR selection. Note that the individual uncertainties can be correlated, and do not necessarily add up quadratically to the total background uncertainty.

In the figure 11.21 the observed $E_{\mathrm{T}}^{\mathrm{miss}}$ /$m_{\mathrm{eff}}^{\mathrm{excl}}$ (excluding requirement on $m_{\mathrm{eff}}^{\mathrm{incl}}$) and $m_{\mathrm{eff}}^{\mathrm{incl}}$ distributions for the SR 6jt+ are shown. The distributions are given for before the normalization. The distributions show good agreement of data and MC prediction within the statistical and systematic uncertainty, and no significant excess of data has been observed in the SR 6jt+.

The event yields in the SR 6jt+ are presented in the figure 11.22 for pure MC prediction before the fit (a) and values obtained by the fit (b). Before the fit MC prediction has large $t\bar{t}$, W+jets and Z+jets contribution, while multi-jets and diboson contributions are very small. The fit performs scaling down of W+jets and Z+jets backgrounds, as explained in the section 11.8.1. The uncertainties on modeling of these backgrounds are included in the fit as nuisance parameters, and good performance in the validation regions is obtained for all VRW/Z, see more details in the section 11.8.2. The multi-jet contribution is scaled up by a small amount, while diboson is unchanged since it is taken from the MC prediction. A good agreement of data with the SM prediction in the SR 6jt+ is seen.

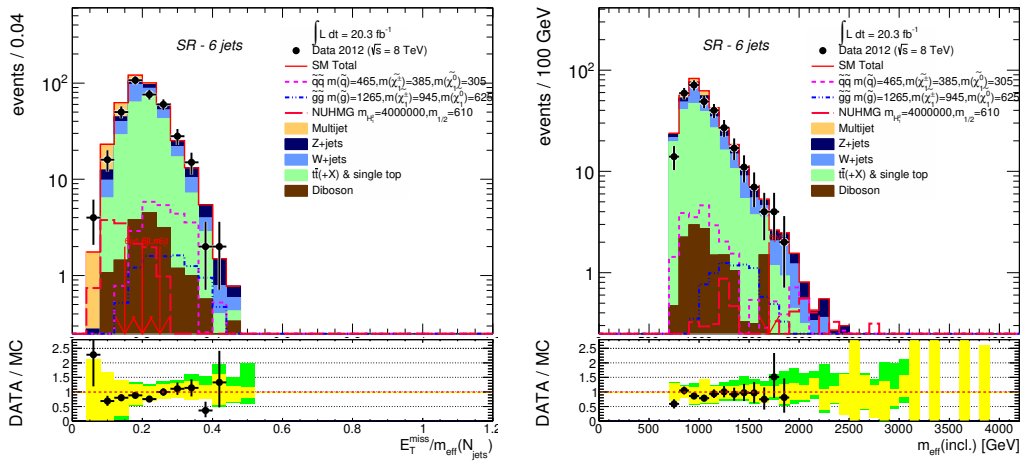

(a) (b)

Figure 11.21.: Observed $E_{\mathrm{T}}^{\mathrm{miss}}/m_{\mathrm{eff}}^{\mathrm{excl}}$ (excluding requirement on $m_{\mathrm{eff}}^{\mathrm{incl}}$) (a) and $m_{\mathrm{eff}}^{\mathrm{incl}}$ (b) distributions in the SR of the 6jt+ channel [31]. The distributions are given for MC background expectations normalized to the cross-section and integrated luminosity for all background samples, except for the multi-jet background distribution, which is given for the data-driven estimation used in the analysis. In the lower plots the yellow error band denotes experimental and MC statistical uncertainty, while the green band in addition includes the theoretical modeling uncertainty. The arrows denote the cut requirements for six-jet loose, tight and very-tight signal regions.

The details of event yield in the SR 6jt+ are shown in the table 11.14. The background only fit obtained expected number of SM background events in the signal region is 4.9±1.6, where the number of observed events is 6. Also, the 95%

CL model independent upper limits for the visible cross-section on the new physics ($\langle\epsilon\sigma\rangle^{95}_{\rm obs}$) are calculated using 5000 MC pseudo-experiments and asymptotic test statistics calculation, and are 0.39 fb and 0.36 fb respectively. The 95% upper limit on the observed number of signal events is 7.9 and 7.3 for the MC pseudo-experiments and asymptotic estimate, while the upper limit for expected number of signal events is $6.6^{+2.6}_{-1.6}$ and $6.4^{+3.2}_{-2.0}$ for the MC pseudo-experiments and asymptotic calculation estimate. Finally, the p-value for the background-only hypothesis is p_0=0.36 and the equvivalent Gausian significance is Z=0.4. The number of observed events in the SR 6jt+ is slighlty higher than the expected background estimation, but the excess is not significant and the data is in agreement with the SM prediction. In addition, no significant exess is seen in any of the SR in the search with 2-6 jets and $E_{\rm T}^{\rm miss}$, and good agreement between the data and the expected number of events are observed in all SR, see more details in [31]. Therefore, the results can be interpreted in a number of SUSY models, where a dedicated interpretation in the NUHMG will be shown in the next section 11.8.4

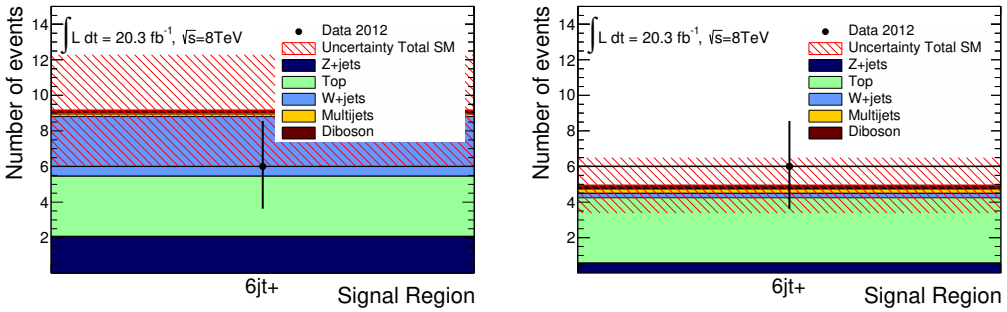

(a) (b)

Figure 11.22.: Event yields in the SR 6jt+ before (a) and after (b) the background-only fit.

11.8.4. Interpretation

No statistically significant excess of data in the SRs has been observed, and limits on the physics BSM are set. In more detail, the 95% CL exclusion limits are set using the CL_S prescription [212] explained in the section 8.2.1. The test statistics was generated using asymptotic formulae [207], and all 0-lepton analyses results were cross-checked using 5000 MC pseudo-experiments for a few signal points. All SR selections were run for each NUHMG grid point using the SUSY-model exclusion fit, as explained in 11.7.1. The SR with best expected sensitivity is selected to derive the observed limit, where asymptotic formulae are used to obtain these results. In addition, the observed SUSY-model exclusion limits are calculated for $\pm\sigma$ variation

Signal Region	**6jt+**
MC expected events	
Diboson	0.21
Z/γ^*+jets	2.1
W+jets	3.4
$t\bar{t}$(+EW) + single top	3.4
Fitted background events	
Diboson	0.2 ± 0.1
Z/γ^*+jets	$0.6^{+0.8}_{-0.6}$
W+jets	$0.3^{+1.2}_{-0.3}$
$t\bar{t}$(+EW) + single top	3.7 ± 1.7
Multi-jets	$0.3^{+0.4}_{-0.3}$
Total bkg	4.9 ± 1.6
Observed	6
$\langle\epsilon\sigma\rangle^{95}_{\text{obs}}$ [fb]	0.39
$\langle\epsilon\sigma\rangle^{95}_{\text{obs}}$ [fb] (asymptotic)	0.36
S^{95}_{obs}	7.9
S^{95}_{obs} (asymptotic)	7.3
S^{95}_{exp}	$6.6^{+2.6}_{-1.6}$
S^{95}_{exp} (asymptotic)	$6.4^{+3.2}_{-2.0}$
p_0 (Z)	0.36 (0.4)

Table 11.14.: Number of events observed in the signal region 6jt+ and background expectations shown for MC estimates and normalized by the fit [31]. The uncertainty on the total background yield is quoted symmetric. The 95% CL upper limits on the visible cross-section ($\langle\epsilon\sigma\rangle^{95}_{\text{obs}}$), the observed number of signal events (S^{95}_{obs}) and the number of signal events (S^{95}_{exp}) given the expected number (and $\pm 1\sigma$ excursions on the expectation) of background events are given using 5000 MC pseudo-experiments and asymptotic formulae. The quoted p-value (p_0) is given for the background-only hypothesis, and the equivalent Gaussian significance (Z) is given in the brackets.

on the theoretical systematic uncertainty on the cross-section calculation for each signal point. The expected SUSY-model exclusion limits are calculated using the mean expected background estimate for the SR as the nominal event yield.

In the figure 11.23 the expected and observed SUSY-model exclusion is shown for the NUHMG model. All grid points around and inside the expected exclusion line have the 6jt+ SR as the best performing expected sensitivity SR. The observed SUSY-model exclusion line is below the expected due to the excess in the observation, but is within the $\pm 1\sigma$ systematic uncertainty of the expected exclusion. The excluded region has a good coverage in the low $m_{1/2}$ region which has a more compact mass spectrum, up to $m_{1/2} = 530$ GeV. In the high mass range better exclusion

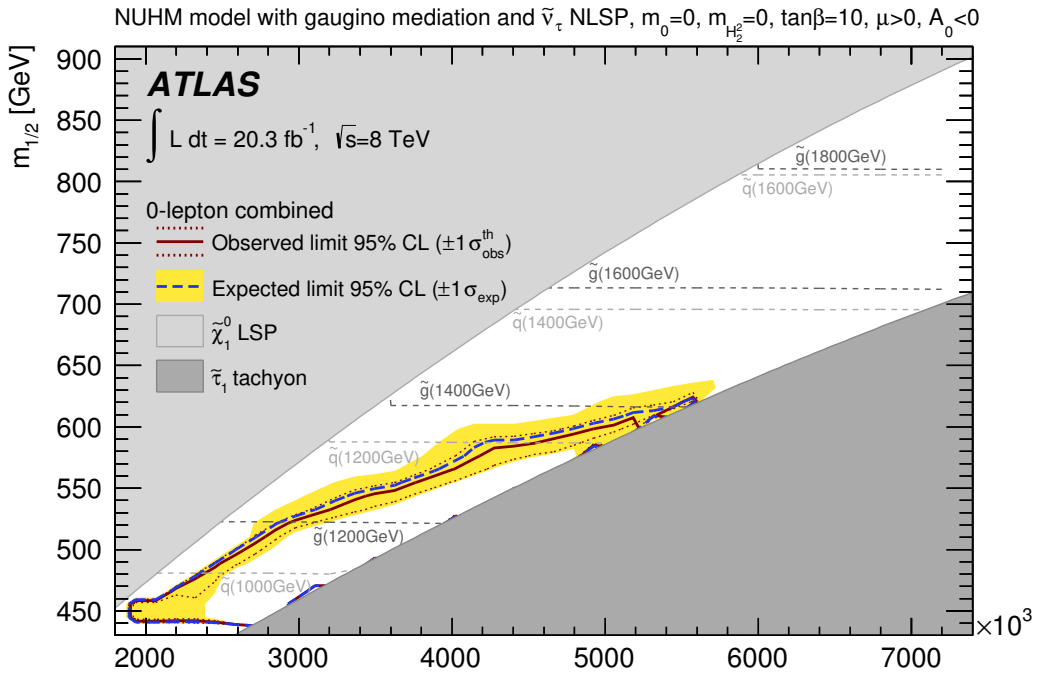

Figure 11.23.: Expected and observed NUHMG SUSY-model exclusion using the CL_S technique [31]. The best expected sensitivity SR is the 6jt+ for all grid points within the exclusion. The expected $\pm 1\sigma_{exp}$ exclusion includes experimental and theoretical uncertainties on the signal and background. The observed $\pm 1\sigma^{th}_{obs}$ variations are calculated for theoretical uncertainty on the cross-section calculation for each point.

is obtained for the lower $m_{1/2}$ points, i.e. closer to the lower diagonal, and observed exclusion line reaches up to $m_{1/2} = 620$ GeV and $m^2_{H_1} = 5.4$ TeV^2. In the grid the $m_{\tilde{q}}$ and $m_{\tilde{g}}$ masses grow linearly with $m_{1/2}$, and observed excluded masses for $\tilde{q}$ and $\tilde{g}$ are up to about 1250 and 1400 GeV respectively.

In addition to NUHMG model interpretation, the SR 6jt+ showed good performance in the models where final state has high jet multiplicity and low $E_{\mathrm{T}}^{\mathrm{miss}}$, which is typical for a longer $\tilde{g}$ decay chains. Therefore, the performance of SR 6jt+ can be inspected on two models commonly studied in the search with 2-6 jets and missing transverse momentum. First, the slice of mSUGRA/CMSSM [94–99] models with $\tan\beta = 30$, $A_0 = -2m_0$ and $\mu > 0$ is studied, where SUSY signal events were obtained using Herwig++ 2.5.2. Second, the simplified model for pair produced gluino pair with intermediate $\tilde{\chi}^{\pm}_1$ each decaying into two quarks, a W boson and $\tilde{\chi}^0_1$ (one-step decay). The $\tilde{\chi}^0_1$ mass is set to 60 GeV for this grid. Here the SUSY signal samples are generated using HERWIG++ 2.5.2 interfaced to PYTHIA 6.426.

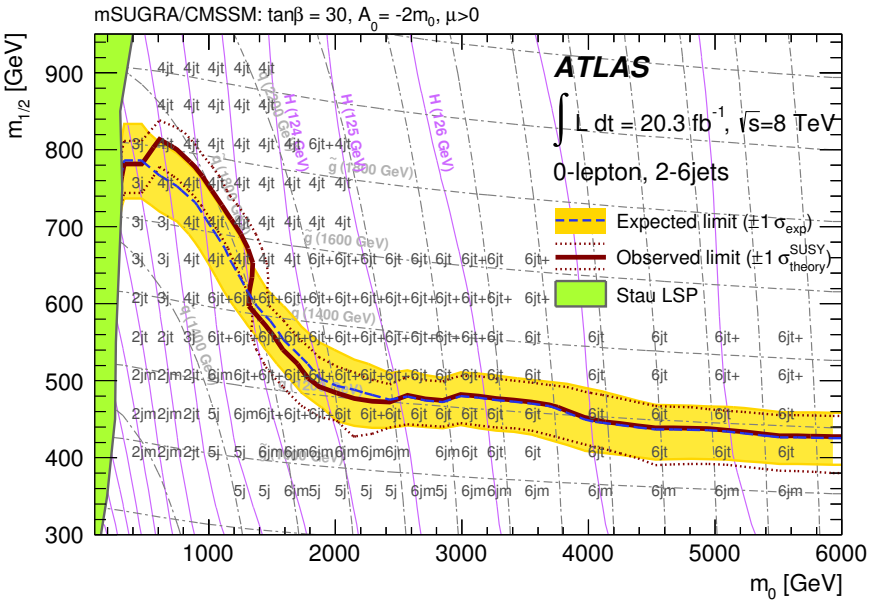

Figure 11.24.: Expected and observed mSUGRA/CMSSM SUSY-model exclusion using the CL_S technique [31]. The expected $\pm 1\sigma_{exp}$ exclusion includes experimental and theoretical uncertainties on the signal and background. The observed $\pm 1\sigma_{obs}^{th}$ variations are calculated for theoretical uncertainty on the cross-section calculation for each point.

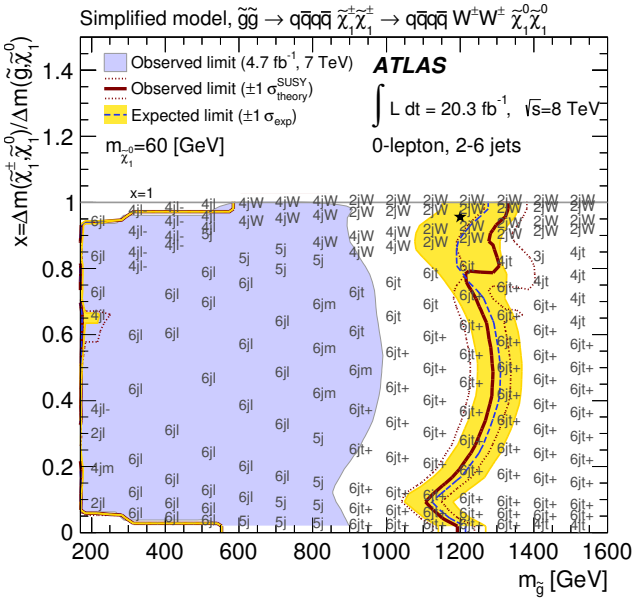

Figure 11.25.: Expected and observed simplified model $\tilde{g}\ \tilde{g}$ production one-step decay SUSY-model exclusion using the CL_S technique [31]. The expected $\pm 1\sigma_{exp}$ exclusion includes experimental and theoretical uncertainties on the signal and background. The observed $\pm 1\sigma_{obs}^{th}$ variations are calculated for theoretical uncertainty on the cross-section calculation for each point.

In the figures 11.24 and 11.25 the expected and observed SUSY-model exclusions using the CL_S technique are presented for these two grids. In the mSUGRA/CMSSM model for $1200 < m_0 < 2300$ GeV range the best performing expected sensitivity SR is the 6jt+. For the simplified model of $\tilde{g}\tilde{g}$ one-step decay the best performing expected sensitivity SR is the 6jt+ for the low $X = \Delta m(\tilde{\chi}_1^{\pm}, \tilde{\chi}_1^0)/\Delta m(\tilde{g}, \tilde{\chi}_1^0)$ region. For X=0.1 the observed exclusion is up to about 1100 GeV for the $\tilde{g}$ masses. In the region of $0.3 < X < 0.8$ the best performing expected sensitivity SR is 6jt+ as well, and the observed exclusion reaches $m_{\tilde{g}}$ of about 1350 GeV, however, in this region similar performance can be obtained with the SR 6jt as well.

11.8.5. Comparison to Analysis with One Lepton, Jets and Missing Transverse Momentum

In order to show compatibility of the NUHMG search using the lepton veto to other analyses, a similar search has been performed on this grid, by the search with one lepton. It was using a selection with one high p_T lepton of $p_T > 25$ GeV, 3-6 jets and missing transverse momenta. It targets $\tilde{q}$ or $\tilde{g}$ pair production. There was no dedicated optimization performed for the NUHMG model. In this section details of the search with one high p_T lepton will be given, where more information can be found in [38], and a comparison of these two searches will be presented.

The final states of the analysis with one high p_T lepton target pair produced $\tilde{g}$ and $\tilde{q}$ (assuming degenerate first two generations), with decay chains via $\tilde{\chi}_1^{\pm}$ and/or $\tilde{\chi}_1^0$ or $\tilde{l}$. The $\tilde{\chi}_1^{\pm}$ decays into W boson and the $\tilde{\chi}_1^0$, $\tilde{\chi}_2^0$ or $\tilde{l}$, $\tilde{\chi}_2^0$ decays into Z boson and $\tilde{\chi}_1^0$, or via $\tilde{l}$ into leptons and $\tilde{\chi}_1^0$. Also, $\tilde{t}$ mediated final states are also considered, see figure 11.26. The analysis with one high p_T lepton requires exactly one lepton, 3-6 jets, and missing transverse momentum.

In addition to the analysis with 0 leptons, this analysis uses these variables:

- $m_{\text{eff}}^{\text{incl}}$ - effective mass in the event, as defined at 11.3 with the lepton term different from zero. It is a scalar sum of transverse momenta for all selected high p_T jets and leptons and the missing transverse energy:

$$m_{\text{eff}}^{\text{incl}} = \sum_{i=1}^{N_l} |p_T(i)| + \sum_{j=1}^{N_{jet}} |p_T(j)| + E_{\text{T}}^{\text{miss}}. \tag{11.22}$$

- M_T - transverse mass of the lepton and $\mathbf{p}_T^{miss}$. It is defined as:

$$M_T = \sqrt{2p_T^l E_{\text{T}}^{\text{miss}}(1 - cos[\Delta\phi(\vec{l}, \mathbf{p}_T^{miss})])} \tag{11.23}$$

  where $\Delta\phi(\vec{l}, \mathbf{p}_T^{miss})$ is the angle between the lepton and $\mathbf{p}_T^{miss}$. It is good for the $W \to l\nu$ background rejection.

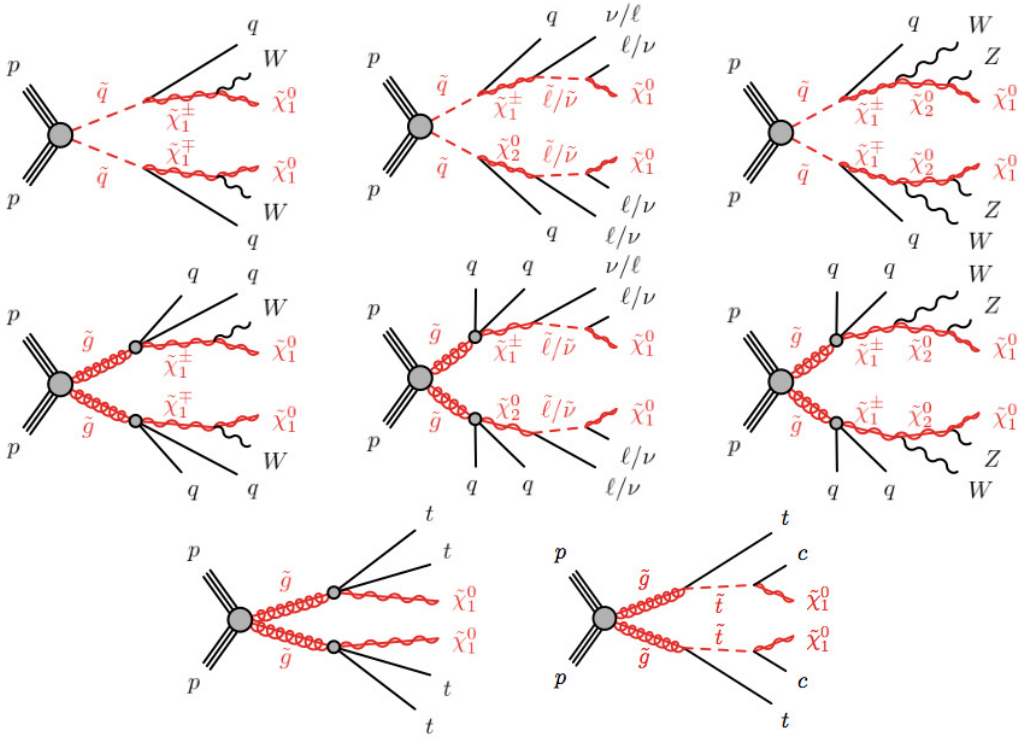

Figure 11.26.: Targeted final states in the analysis using one high p_T lepton, multiple jets and missing transverse momentum [38].

	Single-bin (binned) hard single-lepton		
	3-jet	**5-jet**	**6-jet**
N_ℓ	1 electron or muon		
$p_T(l)$ (GeV)	> 25		
Lepton veto	$p_T{}^{2^{\text{nd}}\text{lepton}} < 10$ GeV		
N_{jet}	≥ 3	≥ 5	≥ 6
$p_T{}^{\text{jet}}$(GeV)	$> 80, 80, 30$	$> 80, 50, 40, 40, 40$	$> 80, 50, 40, 40, 40, 40$
Jet veto	($p_T{}^{5^{\text{th}}\text{jet}} < 40$ GeV)	($p_T{}^{6^{\text{th}}\text{jet}} < 40$ GeV)	–
$E_{\text{T}}^{\text{miss}}$ (GeV)	>500 (300)	>300	>350 (250)
M_T (GeV)	> 150	> 200 (150)	> 150
$E_{\text{T}}^{\text{miss}}/m_{\text{eff}}^{\text{excl}}$	> 0.3	–	–
$m_{\text{eff}}^{\text{incl}}$ (GeV)	> 1400 (800)		> 600
Binned variable	($m_{\text{eff}}^{\text{incl}}$ in 4 bins)		($E_{\text{T}}^{\text{miss}}$ in 3 bins)
Bin width	(200 GeV, 4^{th} is inclusive)		(100 GeV, 3^{rd} is inclusive)

Table 11.15.: Selection criteria for the single-lepton SRs aimed for the $\tilde{q}$ or $\tilde{g}$ pair production. There are two sets of requirements using the single-bin and binned signal regions, where the selection for the binned case is in brackets. Electron and muon channels are targeted independently, see more details in [38].

Signal region	$\langle\epsilon\sigma\rangle^{95}_{\text{obs}}$[fb]	S^{95}_{obs}	S^{95}_{exp}	CL_B	$p(s=0)$
Single-bin hard single-lepton channel					
3-jet	0.40	8.2	$7.8^{+3.3}_{-2.2}$	0.59	0.41
3-jet (electron)	0.29	5.9	$6.2^{+2.1}_{-2.0}$	0.39	0.50
3-jet (muon)	0.35	7.0	$5.7^{+2.1}_{-1.5}$	0.72	0.27
5-jet	0.28	5.7	$7.2^{+3.1}_{-1.9}$	0.26	0.50
5jet (electron)	0.29	6.0	$5.8^{+2.2}_{-1.2}$	0.55	0.50
5-jet (muon)	0.20	4.0	$5.4^{+1.6}_{-1.4}$	0.10	0.49
6-jet	0.22	4.5	$6.0^{+2.2}_{-1.6}$	0.10	0.50
6-jet (electron)	0.24	4.8	$5.3^{+1.6}_{-1.3}$	0.32	0.50
6-jet (muon)	0.16	3.2	$4.9^{+1.4}_{-1.3}$	0.08	0.50

Table 11.16.: Single lepton analysis upper limits using the model independent fit, for 95% CL upper limit on the visible cross-section ($\langle\epsilon\sigma\rangle^{95}_{\text{obs}}$) and number of signal events (S^{95}_{obs}). 95% CL upper limit in the expected number of signal events S^{95}_{exp}, confidence level observed for the background-only hypothesis CL_B, and the discovery p-value ($p(s=0)$, for less observed events than expected p(s=0) = 0.5) [38].

For the SRs there are two sets of selections defined, see table 11.15. They all require a electron or a muon with $p_T > 25$ GeV, with a veto on more leptons in order to be orthogonal to other analyses. They have requirements of 3, 5 or 6 jets, and place cuts on $E_{\text{T}}^{\text{miss}}$, M_T and $E_{\text{T}}^{\text{miss}}$ $/m_{\text{eff}}^{\text{excl}}$. First is a single bin selection. It is optimized for the discovery, and it is also used to set limits on the visible cross-section. Second is the binned SR, which exploits the signal shape when model dependent limits are set. The binned variable in the 3-jet and 5-jet channel is $m_{\text{eff}}^{\text{incl}}$ with 4 steps of 200 GeV, while the 6-jet channel is using $E_{\text{T}}^{\text{miss}}$ with 3 steps of 100 GeV, where for all binned SRs the last bin is inclusive. The binned SR requirements have relaxed values with respect to single-bin SRs. The binned SRs have exclusive jet selection, by placing a jet veto, in order to be orthogonal and allow for a statistical combination of these SRs.

More details about the used samples, pre-selection, CRs, VRs, background determination and analysis procedure can be found in [38]. The number of observed events in each SR has been found to be consistent with the SM expectations. The model independent 95% CL upper limit in the observed/expected cross-section and number of events, CL_B and p-value for the background only hypothesis are shown in the table 11.16.

As no significant excess of data in any SR has been observed, exclusion limits have been set for the NUHMG model. The 95% CL expected and observed exclusion limits are shown in the figure 11.27. In the low mass region the expected and observed exclusion does not reach the upper diagonal. In the high mass range better exclusion is obtained for the lower $m_{1/2}$ points, and expected exclusion line reaches up to $m_{1/2}$ = 500 GeV and $m^2_{H_1}$ = 3.3 TeV^2, while the observed reaches up to $m_{1/2}$ = 580 GeV

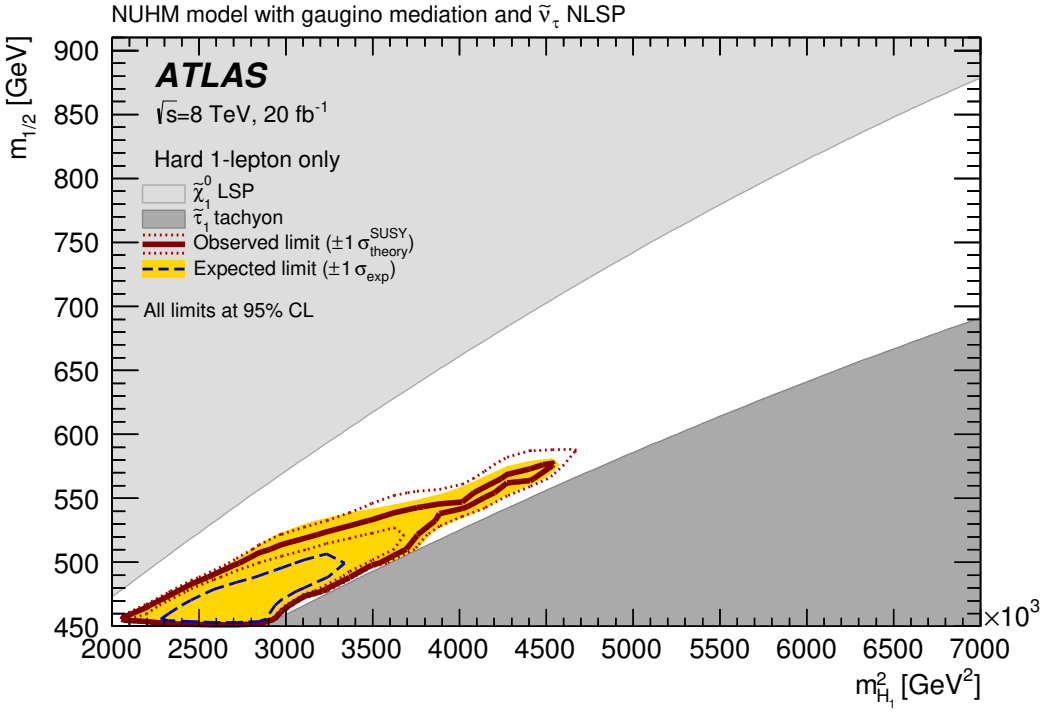

Figure 11.27.: Expected and observed NUHMG SUSY-model exclusion for one-lepton analysis [38]. The $\pm 1\sigma_{exp}$ includes experimental and theoretical, while $\pm 1\sigma_{obs}^{th}$ includes theoretical uncertainty on the cross-section calculation.

and $m_{H_1}^2 = 4.5$ TeV^2, but does not reach the lower diagonal in the high $m_{1/2}$ region.

In order to compare sensitivity of two analyses, the expected exclusion at 95% CL is compared for the 0-lepton and one-lepton searches, see figure 11.28. The one-lepton expected line has about 100 GeV in $m_{1/2}$ and 1 TeV in $m_{H_1}^2$ smaller reach. In addition, the 1 sigma deviation on the expected exclusion due to experimental uncertainities is much higher for the one-lepton case, see figures 11.23 and 11.27. The observed 95% CL line of the 0-lepton analysis is below the expected due to small excess in the observed number of events in the data. In the one-lepton analysis, the observed line is higher than the expected due to the smaller number of observed events in the SRs than predicted. In each analysis this deviation is within the 1 sigma experimental uncertainty of the expected exclusion, see figures 11.23 and 11.27. In all regions 0-lepton analysis expected and observed exclusion is higher than in the one-lepton analysis, however, the searches show compatible exclusion. As these two analyses have orthogonal selections, the statistical combination of the 0-lepton and one-lepton searches is in preparation, and is driven by the 0-lepton analysis due to its higher sensitivity for the NUHMG model.

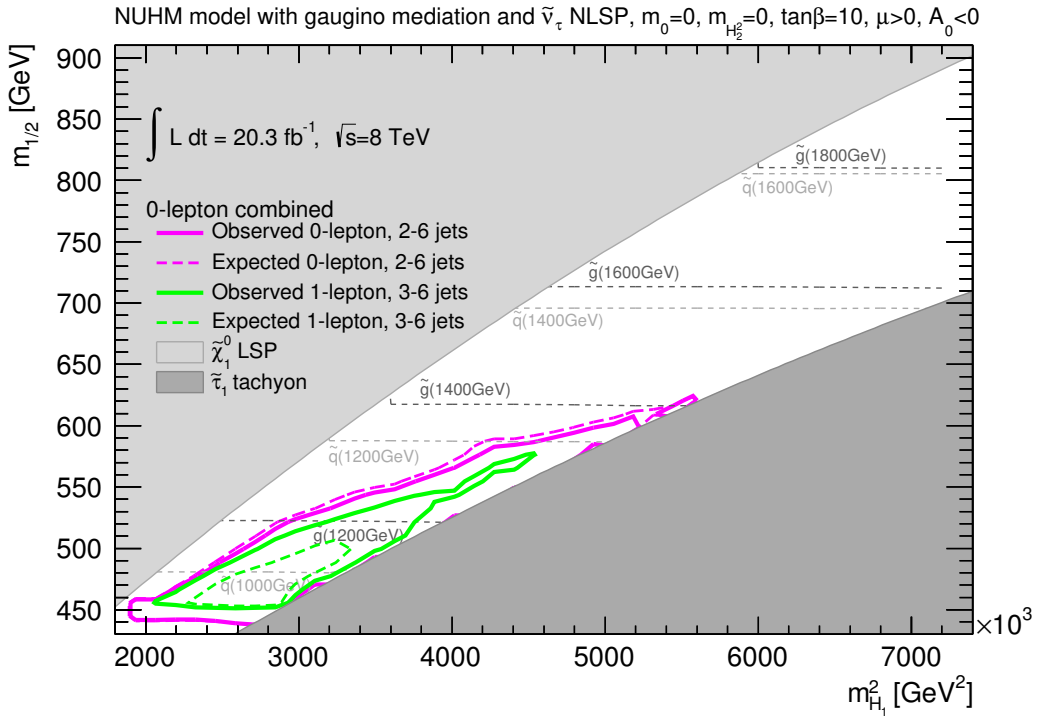

Figure 11.28.: Expected and observed NUHMG SUSY-model exclusion comparison for 0-lepton and one-lepton analyses. The expected $\pm 1\sigma_{exp}$ exclusion includes experimental and theoretical uncertainties on the signal and background. The observed $\pm 1\sigma^{th}_{obs}$ variations are calculated for theoretical uncertainty on the cross-section calculation for each point.

12. Conclusion

In this thesis the 8 TeV physics analyses of NUHMG and NUHM SUSY models were performed using 20.3 fb^{-1} of ATLAS data. Firstly, the NUHMG analysis [28] was done by optimizing a dedicated signal region for this model and adding it to the search for $\tilde{q}$ and $\tilde{g}$ with 2-6 jets, missing energy and a lepton veto. The new signal region named 6jt+ showed good expected sensitivity for the NUHMG model, and it performed well in the models which predict multiple jets and missing transverse energy in the 0-lepton searches. Good agreement in the number of events in the data compared to the SM prediction has been observed, and 95% CL exclusion limits have been set, where the expected and observed 95% CL exclusion limits agree within 1 sigma uncertainty. An additional search for the NUHMG model has been performed in the analysis with one lepton, multiple jets and missing energy as a cross-check. The 0- and one-lepton search showed compatible sensitivity, and a statistical combination of these two analyses is in preparation, where the result is driven by the 0-lepton exclusion limits. Secondly, the NUHM model analysis is well motivated in the framework of Radiatively Driven Natural SUSY [30]. The analysis of this model was performed with the direct gaugino production, with a statistical combination of searches using final states with 2, 3, and 4 leptons, without dedicated optimization for this model, and exclusion limits have been set as no significant excess of data has been seen.

The NUHMG model is well motivated in SUSY searches due to its compact mass spectrum, additional allowed decays of sleptons and gauginos, and $\tilde{\nu}_\tau$ NLSP. It was found that a search with multiple jets and missing energy has good prospects, because the leptons have very low p_T, and a search with a lepton veto is a good selection.

NUHMG analysis has been optimized in three steps. In the first step, a newly developed method for fast signal region optimization with Rectangular Cuts method of TMVA with the Genetic Algorithm, was used. It performs TMVA optimization for ∼10 discriminating variables, several jet multiplicity channels and 9 NUHMG points. This leads to ∼2400 variable-channel-point combinations, from which the optimal variable combinations are ranked for the successful performance, using the MC predictions on the signal and SM background, and approximated significance definition. In the second step, for the selected variable combination, a scan using a fit, with data in control regions, full systematic uncertainties, for all 50 signal points, is performed to select the optimal cut values. In the third step, the optimal cut flow is adjusted and re-evaluated to be compatible with the 0-lepton analysis control and validation regions design. The background is estimated using the background fit, and the CL_S value for all NUHMG grid points is used for the comparison of analyses

performance. The resulting signal region uses 6 jets, low cut on $E_{\mathrm{T}}^{\mathrm{miss}}$ $/m_{\mathrm{eff}}$ and high cut on m_{eff} , and has been named 6jt+.

The analysis on 20.3 fb^{-1} of 8 TeV ATLAS data showed good agreement in the number of events observed in the data and predicted by the SM. Therefore, 95% CL exclusion limits have been set for a number of models. The best performance for the NUHMG model was obtained using the 6jt+ signal region. The observed number of data events in this signal region is 6 for expected 4.9±1.4 SM events, where the observed limit is within 1 sigma uncertainty of the expected exclusion. The observed excluded masses for $\tilde{q}$ and $\tilde{g}$ are up to about 1250 and 1400 GeV respectively. This was the first experimental result for the NUHMG model. Also, the 6jt+ signal region showed good performance in the SUSY models with large jet multiplicity and low missing energy, i.e. the compact mass spectrum regions, and therefore it extends the general SUSY searches. Additional search for NUHMG model has been performed with the analysis using one lepton, multiple jets and missing energy. Each, the 95% CL expected and observed exclusion are lower for the one-lepton analysis compared to the 0-lepton analysis, but they show compatibility. A statistical combination of these two searches is in preparation and is driven by the 0-lepton exclusion.

The NUHM model has a very good motivation in current SUSY searches, and it was interpreted using the ATLAS multilepton searches. The model has two degrees of freedom more compared to CMSSM models, and allows for a SUSY parameter space where it is compatible with the Higgs mass constrain. In addition, as $\tilde{q}$ and $\tilde{g}$ masses have been excluded by the LHC searches up to ∼1.7 TeV, it can accommodate this constrain as well, with the low level of electroweak fine tuning. This framework has been named Radiatively Driven Natural SUSY. The dominant production is direct gaugino production, and a search using a statistical combination of 2, 3 and 4 lepton searches was performed for NUHM. The statistical combination is driven by the 3 lepton search, which showed the highest sensitivity. The model dependent observed exclusion showed smaller exclusion reach than the expected, where the difference is higher than 1 sigma, in the high $m_{1/2}$ range where the gaugino mass spectrum becomes compact. The 95% CL observed exclusion reaches about 300 GeV in $m_{1/2}$, and extends to highest tested values of 500 GeV in the μ direction. This is the first RNS NUHM exlusion at the LHC.

In addition to physics searches, the assurance of data taking is of great importance. For this reason, the ATLAS trigger online monitoring represents an important task, and a program called Trigger Presenter (TriP) was prepared for shifters and experts in the ATLAS control room. The program is lightweight, it collects data in different ways and presents the information on Level 1, Level 2 and Event Filter triggers, High Level Trigger PC farms and global information in a user friendly graphical user interface. The program was extensively used in integration tests before, and at the first LHC startup. Today a new version of this program is in use.

In this thesis various aspects of physics searches and analysis optimization have been presented. The results on NUHMG and NUHM models exclusion represent the first exclusions of these models at the LHC, and therefore due to their physics

motivation an important result. In addition, a program implemented and used in the online monitoring represents an important part of the ATLAS data taking and data quality assurance.

13. Outlook

Direct searches for new physics represent an important aspect in understanding the nature, and have a good motivation be continued in the following LHC data taking and future high energy experiments. Future SUSY analyses should have complete and wide coverage, but also include most recent measurements, and explore models that fit the observations. The analyses described in this thesis were extending the SUSY searches and exploring well motivated models. In future searches, the aspects of these analyses need to be further explored and refined.

The NUHMG analysis with the newly developed 6jt+ signal region showed good sensitivity in the compact mass region in $\tilde{q}$ and $\tilde{g}$ production searches with longer decay chains in 8 TeV searches with 20.3 fb^{-1}. With the increasing exclusion reach of direct SUSY searches, the compact mass region is one of the scenarios where additional improvements are needed. However, for more compact regions, the jet p_T is lower, which makes the analysis more difficult. On the other hand, with higher c.m.e. p-p collisions, the $\tilde{q}$ and $\tilde{g}$ production cross-sections increase faster than the SM background, and higher coverage is viable with a dedicated analysis. Therefore, in order to allow for better coverage of these searches, compact mass spectrum and signatures with lots of jets and $E_{\mathrm{T}}^{\mathrm{miss}}$ will represent an important search in the future LHC data taking, and dedicated analyses should be set in place.

As the parameter space of MSSM is being strongly excluded by the current LHC searches, the next step for future analyses can be the Next-to-MSSM. This SUSY model with higher complexity predicts more Higgs particles, and more gauginos. Due to presence of higher number of SUSY particles, the mass spectrum can be more compact, and signature with higher object multiplicity will be of interest for future searches. Therefore, analysis with high jet multiplicity will be needed also for the models with higher complexity.

The NUHM was explored in the Radiatively Driven Natural SUSY framework, and future analyses of this model will represent a well motivated search at higher c.m.e. at the LHC and future colliders. In this model the $\tilde{q}$ masses are in the order of a few TeV, and at 8 TeV the dominant production is the gaugino production. However, at 13 TeV and higher c.m.e. the $\tilde{q}$ and $\tilde{g}$ production cross-section increase in larger amount than the electroweak, in the low $\mu \sim 150$ GeV region. Then the search using the strong production can give good sensitivity even using lower integrated luminosity. Also, the analysis using the gaugino production at 13 TeV and higher integrated luminosity $\sim 100\ fb^{-1}$ will give an additional good sensitivity in the higher $m_{1/2}$ region. Due to the good motivation of this model, the search for RNS with NUHM model will represent a very important search at 13 TeV.

In order to obtain the data-set with good quality assurance, in addition to physics

searches, various aspects of data taking need to be taken into account, and programs for online monitoring will be a great asset in future data taking.

Having in mind the complexity of the SM predictions and measurements and aspects of physics beyond the SM, the searches for new physics are of great importance in understanding the nature. With the current experimental results, theoretical modeling, running high energy data taking experiments, advanced computing resources, highly developed techniques for signal and background estimation and separation, these searches are viable at the LHC and future experiments. It is a wonderful opportunity to be able to contribute to this global goal.

A. NUHM and Radiatively Driven Natural SUSY Analysis

The NUHM model within the Radiatively-driven Natural SUSY framework (RNS) was motivated in the section 4. In this section the 8 TeV analysis of the model will be shown. First the NUHM scans were performed in order to find viable regions with the Higgs mass, LEP and LHC constrains, and the compatibility of these findings with the RNS NUHM grid proposal will be shown in the section A.1. Second the SUSY mass spectrum using the RNS NUHM, dominant productions, branching fractions and final states will be examined in the section A.2. Third, details of the NUHM grid mass spectrum and cross sections will be shown in the section A.3. Finally, the results of the NUHM grid interpretation using 20.3 fb^{-1} of 8 TeV ATLAS data, within the searches for the electroweak production using 2, 3 and 4 leptons will be presented in the section A.4. Descriptions given in this section are taken and extended from [274].

A.1. NUHM Scans Compatibility with RNS

Good motivation for NUHM model within the RNS framework was examined in the section 4. The NUHM parameter space proposed in [30] was chosen for the analysis using $m_0 = 5$ TeV, $\tan\beta = 15$, $A_0 = -1.6m_0$, $m_A = 1$ TeV in the $m_{1/2}$ vs μ plane. However, prior to this choice for the NUHM grid, detailed scans were performed to find a viable region in NUHM parameter-space where the Higgs mass constrain is preserved, the points are viable for the LEP limits on gaugino masses constrain, the $\tilde{q}$,$\tilde{g}$ and $\tilde{t}$ are not excluded by previous LHC measurements, and the $\tilde{\chi}_1^0$ is the LSP. A compatibility of these scans findings with the RNS NUHM grid proposal will be presented at the end of this section.

The NUHM SUSY mass spectrum and LO cross-sections were generated using the same setup as described in the section 9.1. The SUSY and Higgs mass spectrum and mixing angles have been computed using SOFTSUSY 3.3.4 [154], while the SUSY and Higgs particle decays have been calculated using SUSY-HIT [156] as an interface to decay calculators SDECAY 1.3 [158] and HDECAY 3.302 [157] respectively. The high mass compactification scale is set to be $M_X = M_{GUT} = 1.987\times10^{16}$ GeV. At this stage of analysis cross-sections were calculated at LO using PYTHIA 6.426 [159] using PDF set CTEQ6L1.

Extensive NUHM grid scans were performed in order to find viable parameter space regions with m_h and LEP constrain and with $\tilde{\chi}_1^0$ LSP. Each point was obtained

for $A_0 = 0$, and then the A_0 scan was performed in order to obtain $122.5 \leq m_h \leq 127.5$ GeV. In this setup, the considered grid plane was in μ vs $m_{1/2}$, and additional scans on $\tan\beta$, m_0 and m_A were done. Scans were performed in a wider range than the final proposal, see table A.1 for details. The cross sections, branching fractions and mass spectrum were examined. In the following are the scan details and a short list of conclusions:

- A_0 **scan** into negative values to obtain m_h constrain. It is run for all scans:
  - Higgs mass constrain always obtained for about $A_0 \sim$ -2m_0.
  - Therefore, select $A_0 \sim -2m_0$.
- $\tan\beta$ **scan** in the range [10, 50] with step 10 (μ = 300GeV, $m_{1/2}$ = 500GeV, m_0 = 3 TeV, $\tan\beta$ = 10, m_A = 1 TeV):
  - For higher $\tan\beta$ in the mass spectrum $\tilde{l}$ have higher mass spread, but gaugino sector is not affected.
  - $\tilde{t}$ always light, but gaugino production higher than strong production.
  - At very high $\tan\beta = 50$ number of viable points drops.
  - Gaugino cross-sections not affected by the $\tan\beta$ scan.
  - Therefore, $\tan\beta$ should be below 50, gaugino production will not be affected by $\tan\beta$.
- m_0 **scan** in the range [1, 5] TeV with step 1 TeV ($\mu = 300$GeV, $m_{1/2} = 500$GeV, $m_0 = 4$ TeV, $\tan\beta = 10$, $m_A = 1$ TeV):
  - For higher m_0 $\tilde{q}$ masses shift to very high values, $\tilde{t}$ always in the same mass range, but gaugino production gets more dominant for higher m_0.
  - Number of viable points better for $m_0 > 1$ TeV.
  - Gaugino production cross-section not affected by the m_0 scan.
  - Therefore, as the gaugino production is dominant, any high value of m_0 can be chosen.
- m_A **scan** for 0.6 and 1 TeV:
  - Higher number of viable points obtained with 1 TeV.
  - Therefore, fix $m_A = 1$ TeV.

In conclusion, the RNS NUHM choice of low $\tan\beta = 15$ agrees with $\tan\beta < 50$ value obtained by the scans. The high m_0 produces high $\tilde{q}$ and $\tilde{g}$ masses, which allows for gaugino production to become dominant. Therefore, RNS $m_0 = 5$ TeV is in agreement with favored high values of $m_0 > 1$ TeV obtained by the scans, since the dominant gaugino production is not affected by this parameter. The value of A_0 = -1.6 m_0 is in agreement with the scan findings of $A_0 \sim -2m_0$, and sets the m_h to be around 125 GeV. Also, the choice of $m_A = 1$ TeV agrees with the value obtained

Fixed parameters	sign(μ) > 0
RNS NUHM	m_0 = 5 TeV, tan β = 15, A_0 = -1.6m_0, m_A = 1 TeV 100 $\leq \mu \leq$ 500 GeV, step 50 GeV 100 $\leq m_{1/2} \leq$ 500 GeV, step 50 GeV
LSP and LEP limit checks	$\tilde{\chi}_1^0$ LSP $\tilde{\chi}_1^0$> 46 GeV $\tilde{\chi}_1^{\pm}$> 94 GeV
Higgs mass constrain	$A_0 < 0$, varied to obtain 122.5 $\leq m_h \leq$ 127.5 GeV, step 10 GeV
Grid scan range	0.1$\leq \mu \leq$ 2.2 TeV, step 0.2 TeV 0.1$\leq m_{1/2} \leq$3 TeV, step 0.2 TeV
Scan details	10 $\leq$ tan $\beta \leq$ 50, step 10 μ = 300GeV, $m_{1/2}$ = 500GeV, m_0 = 3 TeV, tan β = 10, m_A = 1 TeV
	1 $\leq m_0 \leq$ 5 TeV, step 1 TeV μ = 300GeV, $m_{1/2}$ = 500GeV, m_0 = 4 TeV, tan β = 10, m_A = 1 TeV
	600 $\leq m_A \leq$ 1000 GeV, step 400 GeV

Table A.1.: RNS NUHM and NUHM grid scan parameters. Grid is prepared in μ vs $m_{1/2}$ parameter space. In the scans the $\tilde{\chi}_1^0$ LSP and LEP limits [39] checks were performed, together with the Higgs mass constrain [222].

by the scans. Therefore, the NUHM grid scans are in complete agreement with the RNS NUHM parameters. Due to low level of electroweak fine tuning for $\mu \lesssim 500$ GeV, viable cross-section at 8 TeV p-p collisions up to $m_{1/2} \lesssim 500$ GeV, and LEP limits requiring $\mu \gtrsim 100$ GeV and $m_{1/2} \gtrsim 100$ GeV, the RNS NUHM was chosen for the analysis, as shown in the table A.1.

A.2. NUHM Final States

In this section the typical mass spectrum, dominant production channels, branching fractions and final states will be examined for the RNS NUHM model.

An example of the mass spectrum and dominant decay modes for one NUHM point μ = 300 GeV, $m_{1/2}$ = 300 GeV is given in the table A.2. The $\tilde{q}$, $\tilde{b}$ and $\tilde{t}_2$ masses are very high $\gtrsim$ 3 TeV, which means their direct production at 8 TeV will be suppressed. The $\tilde{t}_1$ is of the order 1.5 TeV, and $\tilde{g}$ has a low mass below 1 TeV, but their production is not dominant. Gauginos have low masses of a few 100 GeV, and their direct production is dominant. $\tilde{\chi}_1^0$ LSP has a mass higher than 100 GeV. Therefore, in this analysis, production and decays of gauginos are of interest. The dominant decay modes are:

- $\tilde{\chi}_4^0 \rightarrow \tilde{\chi}_1^\pm$W
- $(\tilde{\chi}_4^0, \tilde{\chi}_3^0, \tilde{\chi}_2^0) \rightarrow \tilde{\chi}_1^0$Z
- $(\tilde{\chi}_4^0, \tilde{\chi}_3^0) \rightarrow \tilde{\chi}_1^0$h
- $(\tilde{\chi}_2^\pm, \tilde{\chi}_1^\pm) \rightarrow (\tilde{\chi}_2^0, \tilde{\chi}_1^0)$ W
- $\tilde{\chi}_2^\pm \rightarrow \tilde{\chi}_1^\pm$Z.

Therefore, searches for electroweak production of gauginos with W, Z or h in the final state have good prospects.

	Mass (GeV)	Decay Modes
$\tilde{\ell}_\mathrm{L}$	5075	$\tilde{\chi}_1^\pm \nu_l$(34%), $\tilde{\chi}_2^\pm \nu_l$(27%), $\tilde{\chi}_2^0 l$(24%), $\tilde{\chi}_4^0 l$(8%), $\tilde{\chi}_1^0 l$(7%)
$\tilde{\nu}_l$	5074	$\tilde{\chi}_1^\pm l$(44%), $\tilde{\chi}_2^\pm l$(17%), $\tilde{\chi}_2^0 \nu_l$(15%), $\tilde{\chi}_4^0 \nu_l$(13%), $\tilde{\chi}_1^0 \nu_l$(11%)
$\tilde{\tau}_2$	5005	$\tilde{\chi}_1^\pm \nu_\tau$(32%), $\tilde{\chi}_2^\pm \nu_\tau$(26%), $\tilde{\chi}_2^0 \tau$(24%), $\tilde{\chi}_4^0 \tau$(8%), $\tilde{\chi}_1^0 \tau$(7%)
$\tilde{\nu}_\tau$	5004	$\tilde{\chi}_1^\pm \tau$(44%), $\tilde{\chi}_2^\pm \tau$(18%), $\tilde{\chi}_2^0 \nu_\tau$(14%), $\tilde{\chi}_4^0 \nu_\tau$(13%), $\tilde{\chi}_1^0 \nu_\tau$(11%)
$\tilde{\ell}_\mathrm{R}$	4822	$\tilde{\chi}_1^0 l$(95%)
$\tilde{\tau}_1$	4673	$\tilde{\chi}_1^0 \tau$(82%)
$\tilde{q}_\mathrm{R}$	5100	$\tilde{g}\ q$(99%)
$\tilde{q}_\mathrm{L}$	4948	$\tilde{g}\ q$(95%)
$\tilde{b}_2$	4786	$\tilde{g}\ b$(95%)
$\tilde{t}_2$	3458	$\tilde{g}\ t$(71%), $\tilde{\chi}_3^0 t$(7%), $\tilde{\chi}_4^0 t$(6%), $\tilde{t}_1 h$(8%)
$\tilde{b}_1$	3452	$\tilde{g}\ b$(76%), $\tilde{\chi}_2^\pm t$(12%), $\tilde{\chi}_4^0 b$(7%)
$\tilde{t}_1$	1480	$\tilde{g}\ t$(58%), $\tilde{\chi}_2^\pm b$(14%), $\tilde{\chi}_3^0 t$(11%), $\tilde{\chi}_4^0 t$(7%), $\tilde{\chi}_1^\pm b$(7%)
$\tilde{g}$	848	$\tilde{\chi}_2^\pm bt$(30%), $\tilde{\chi}_1^\pm bt$(21%), $\tilde{\chi}_1^0 tt$(12%), $\tilde{\chi}_2^0 tt$(8%), $\tilde{\chi}_3^0 tt$(9%), $\tilde{\chi}_4^0 tt$(7%)
$\tilde{\chi}_4^0$	356	$\tilde{\chi}_1^\pm W$(84%), $\tilde{\chi}_1^0 h$(13%), $\tilde{\chi}_1^0 Z$(3%)
$\tilde{\chi}_2^\pm$	354	$\tilde{\chi}_2^0 W$(54%), $\tilde{\chi}_1^\pm Z$(32%), $\tilde{\chi}_1^0 W$(14%)
$\tilde{\chi}_3^0$	312	$\tilde{\chi}_1^0 Z$(94%), $\tilde{\chi}_1^0 h$(6%)
$\tilde{\chi}_2^0$	234	$\tilde{\chi}_1^0 Z$(100%)
$\tilde{\chi}_1^\pm$	233	$\tilde{\chi}_1^0 W$(100%)
$\tilde{\chi}_1^0$	131	LSP

Table A.2.: NUHM point $\mu = 300$ GeV, $m_{1/2} = 300$ GeV mass spectrum and branching ratios. Direct gluino, squark and slepton production suppressed due to their high masses. Only direct gaugino production and decays are relevant for this grid at 8 TeV searches. Squark, slepton and sneutrino masses given for the average of the first two generations respectively, as they are almost degenerate. l = (e,μ), q = (u,d,c,s).

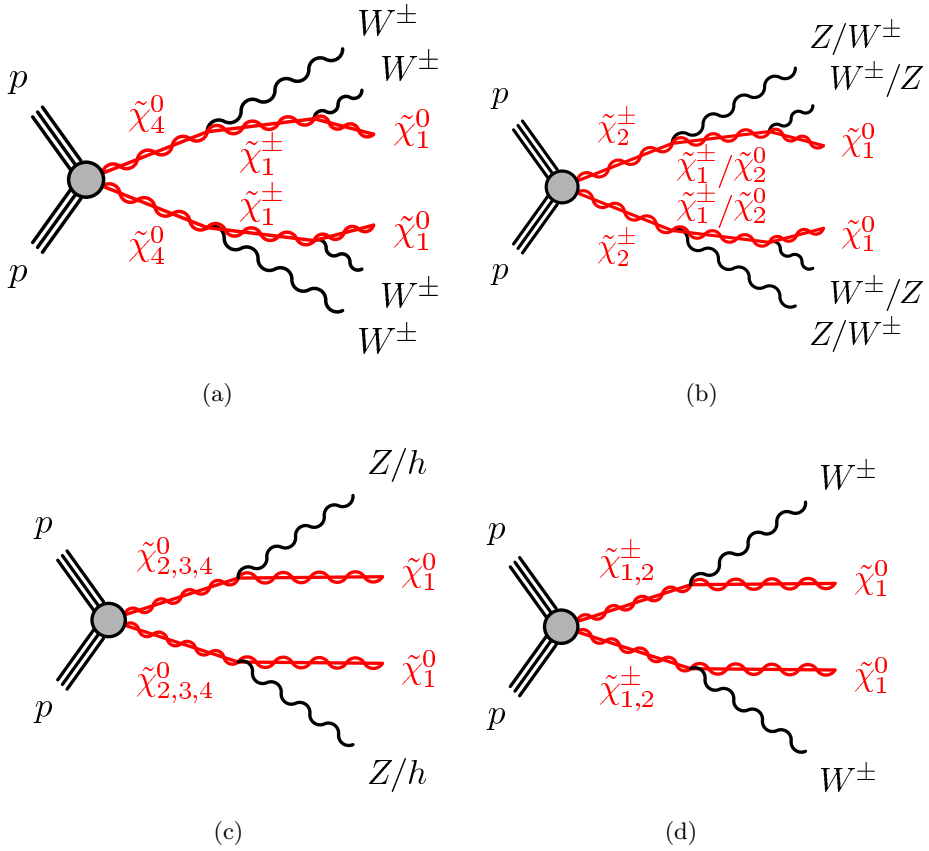

Figure A.1.: Targeted NUHM final states. Due to low branching fraction of the strong production, direct gaugino production is dominant. Typical final states include 4W and $E_{\mathrm{T}}^{\mathrm{miss}}$ (a), 2W2Z and $E_{\mathrm{T}}^{\mathrm{miss}}$ (b), 2Z/h and $E_{\mathrm{T}}^{\mathrm{miss}}$ (c) or 2W and $E_{\mathrm{T}}^{\mathrm{miss}}$ (d). l = (e,μ), q = (u,d,c,s).

In the figure A.1 targeted final states of 4W with $E_{\mathrm{T}}^{\mathrm{miss}}$, 2W2Z with $E_{\mathrm{T}}^{\mathrm{miss}}$, 2W with $E_{\mathrm{T}}^{\mathrm{miss}}$ and 2Z/h with $E_{\mathrm{T}}^{\mathrm{miss}}$ are presented for the direct gaugino production. Therefore, in this analysis, final states with 2, 3, and 4 leptons are of interest.

The mass spectrum of three NUHM points are shown in the figure A.2 for comparison. A distinguishable property of NUHM is the compact and low gaugino sector. The $\tilde{g}$ is always lighter than the $\tilde{t}_1$ and $\tilde{q}$. For increasing $m_{1/2}$ gauginos become heavier, and for increasing μ gaugino mass spectrum becomes more compact, which makes the analysis more difficult. The $\tilde{t}_1$ mass is somewhat low compared to previous LHC exclusion limits of $\sim$ 1 TeV [35], however these searches were done using the strong production. Therefore, NUHM represents an interesting scenario for LHC searches due to its low and compact gaugino sector and not yet excluded $\tilde{t}_1$using the direct gaugino production.

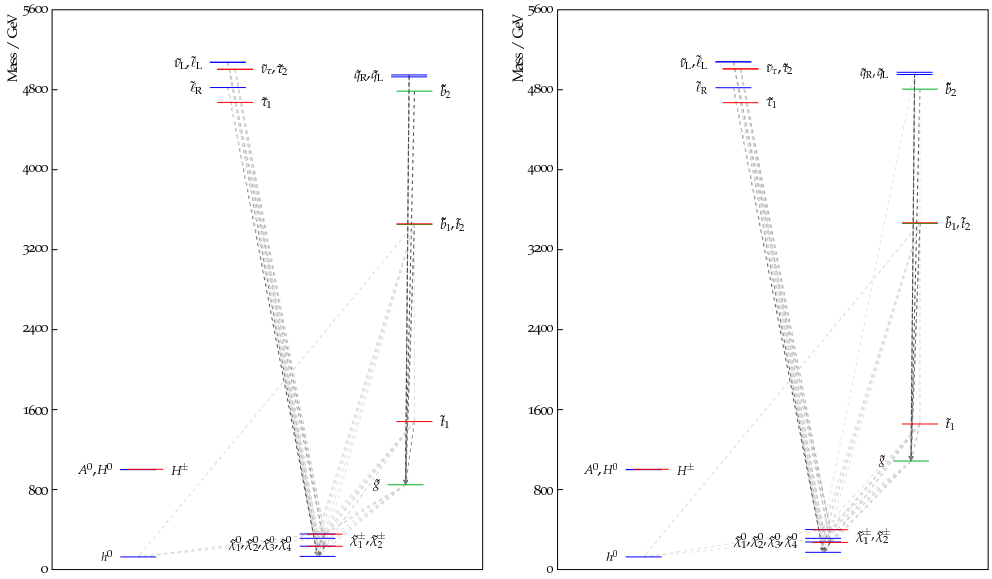

(a) $\mu = 300$ GeV, $m_{1/2} = 300$ GeV

(b) $\mu = 300$ GeV, $m_{1/2} = 400$ GeV

(c) $\mu = 400$ GeV, $m_{1/2} = 300$ GeV

Figure A.2.: Mass spectrum and branching ratio lines for NUHM points. With increasing $m_{1/2}$ gauginos become heavier (compare (a) and (b)). For increasing μ gaugino mass spectrum becomes more compact (compare (a) and (c)). Thickness of the gray lines scaled to the value of the branching ratio. Sparticle mass spectrum plots are obtained using the PySLHA [218].

A.3. NUHM Grid Properties

The NUHM grid was produced for 81 SUSY parameter space points, using the RNS NUHM specifications shown in the table A.1. The LEP constrain was not used, as this is the first exclusion of this model. The mass spectrum and the cross-section of the grid is presented in this section.

The Les Houches accord files for the points were produced using the setup described in the section A.1. The event generation was performed using the HERWIG++ 2.5.2 [170] event generator with the CTEQ6L1 [233] tune, for the direct gaugino production. The two lepton generator filter was used, within $|\eta| < 2.7$, for the electrons and muons of $p_T > 5$ GeV, and leptonic taus of $p_T > 15$ GeV, while maintaining the hadronic taus.

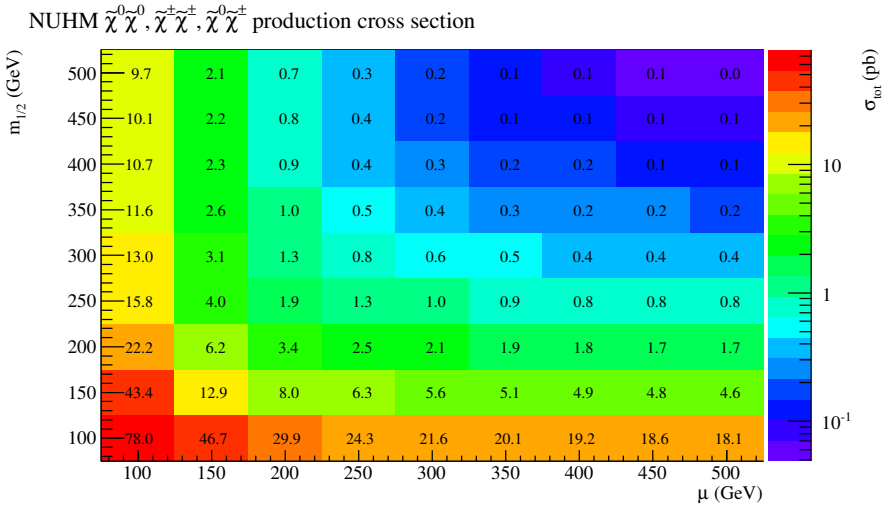

Figure A.3.: NUHM grid direct gaugino production NLL+NLO cross-section obtained following the prescription from [224] using NLL-fast [198] and PROSPINO 2.1 [191] used in the analysis. It includes all productions of $\tilde{\chi}^0\tilde{\chi}^0$, $\tilde{\chi}^\pm\tilde{\chi}^\pm$ and $\tilde{\chi}^0\tilde{\chi}^\pm$ for all gaugino generations.

The mass spectrum of NUHM for fixed $\mu = 150$ GeV and $m_{1/2} = 150$ is shown in the figure A.4. For increasing $m_{1/2}$ the gaugino masses increase, but the mass spectrum becomes more compact, which makes the analysis more difficult for increasing $m_{1/2}$. $\tilde{g}$ mass is increasing in a same way as gauginos, and for $m_{1/2} > 500$ GeV it becomes higher than $\tilde{t}_1$, while $\tilde{q}$ and $\tilde{t}$ masses do not change in large amount. As the $\tilde{q}$ and $\tilde{t}$ masses are very high, their production is negligible at 8 TeV searches, while $\tilde{g}$ production falls steeply for high $m_{1/2}$. For increasing μ the gaugino masses increase, and the mass difference of gauginos always has > 30 GeV mass gap, which leaves leptons with high p_T for the detection at all μ values. The increasing μ does not affect the $\tilde{g}$, $\tilde{q}$ and $\tilde{t}$ masses.

The production cross-section used in the analysis was calculated for all gaugino

production processes at NLL + NLO following the prescription from [224], using NLL-fast [198] and PROSPINO 2.1 [191]. In the figure A.3 total gaugino production cross-section for all NUHM points, without generator filter efficiency applied, are presented. As expected, for increasing μ the cross-section is almost unchanged, but for increasing $m_{1/2}$ the gaugino production cross-section falls steeply. It should be noted that for most of the NUHM grid, excluding only the low $\mu, m_{1/2}$ points, gaugino production represents almost 100% of the total cross-section.

A.4. NUHM 8 TeV Data Analysis

The NUHM model analysis was performed without a dedicated optimization, using the analyses of electroweak production with 2, 3 and 4 leptons [275–277]. In addition to 0-lepton and 1-lepton analyses, these searches use the following variables:

- $E_{\mathrm{T}}^{\mathrm{miss}\ ,rel}$ - corrected $E_{\mathrm{T}}^{\mathrm{miss}}$ definition, defined as:

$$E_{\mathrm{T}}^{\mathrm{miss,rel}} = \begin{cases} E_{\mathrm{T}}^{\mathrm{miss}} & ,\Delta\phi_{l,j} \geq \pi/2, \\ E_{\mathrm{T}}^{\mathrm{miss}} \times \sin\Delta\phi_{l,j} & ,\Delta\phi_{l,j} < \pi/2 \end{cases} \tag{A.1}$$

  where $\Delta\phi_{l,j}$ is the azimuthal angle between the $\mathbf{p_T}^{miss}$ direction and the nearest e, μ, central b-jet or central light-flavor jet. It is aimed to suppress events with significantly miss-measured jets and leptons.

- m_{T2} - 'stransverse' mass is calculated for two leptons and $\mathbf{p_T}^{miss}$ using the $\mathbf{q_T}$ transverse vector, which is used to minimize the larger of two transverse masses m_T in the m_{T2} definition:

$$m_T(\mathbf{p}_T, \mathbf{q}_T) = \sqrt{2(p_T q_T - \mathbf{p}_T \mathbf{q}_T)} \tag{A.2}$$

$$m_{T2} = \min_{\mathbf{q_T}}[\max(m_T(\mathbf{p_T}^{l1}, \mathbf{q_T}), m_T(\mathbf{p_T}^{l2}, \mathbf{p_T}^{miss} - \mathbf{q_T}))] \tag{A.3}$$

  where $\mathbf{p}_T^{l1}$ and $\mathbf{p}_T^{l2}$ are transverse momenta of two leptons. In SM events with two W bosons which decay leptonically, the $\mathbf{p}_T^{miss}$ originates from neutrinos, and the m_{T2} has an end-point around the W mass. For the signal, the LSP contributes to the $\mathbf{p}_T^{miss}$, and m_{T2} end-point is shifted by a value correlated to the $\tilde{l}$ or $\tilde{\chi}_1^{\pm}$and LSP mass difference.

- m_{xy} - invariant mass of two objects, which for signal events can take values that differ from the W and Z mass.

The NUHM model interpretation is performed using a statistical combination where the following signal regions were included in the fit, see table A.3:

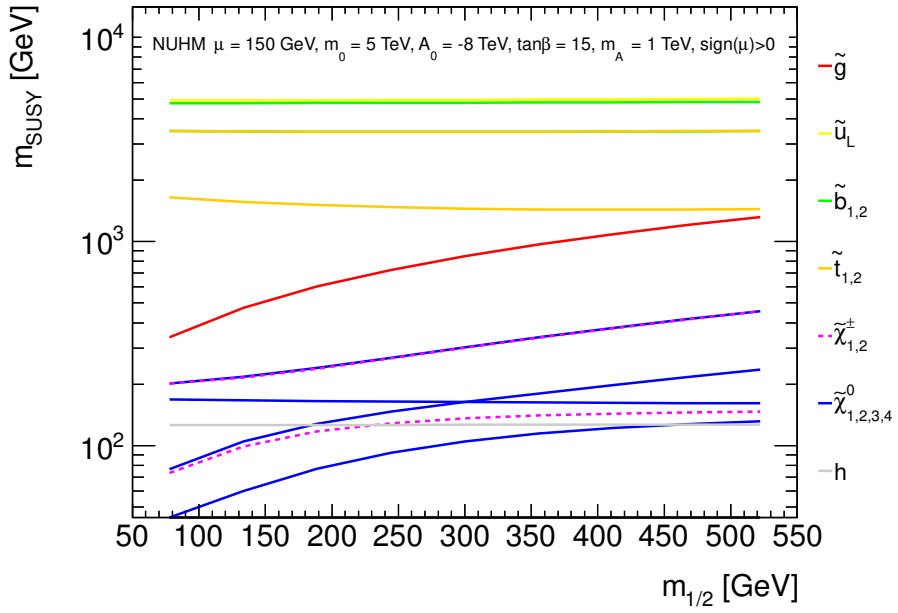

(a) $\mu = 150$ GeV

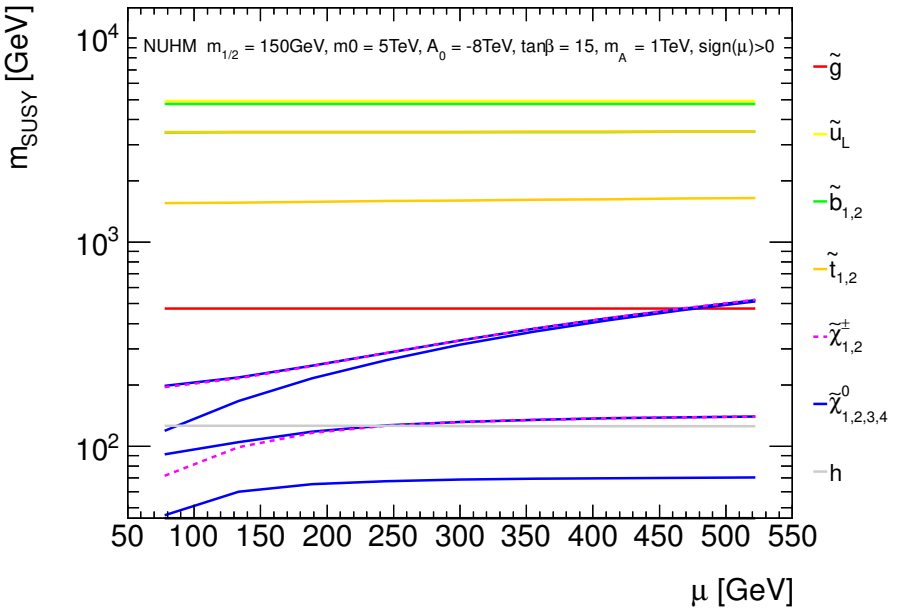

(b) $m_{1/2} = 150$ GeV

Figure A.4.: NUHM model sparticle masses for fixed $\mu = 150$ GeV (a) and $m_{1/2} = 150$ GeV (b).

- **2 Lepton**: Signal region with the best expected sensitivity is selected for each point, using the SRWWa, SRWWb, SRWWc, SR-mT90, SRmT120 and SRZJets, defined in [275].
- **3 Lepton**: Statistical combination of signal regions SR0a, SR0b, SR1 and SR2a, defined in [276].
- **4 Lepton**: Statistical combination of signal regions SR0noZa, SR1noZa, SR2noZa, SR0Z, SR1Z and SR2Z, defined in [277].

	SR	m_{T2}^{90}	m_{T2}^{120}	WWa	WWb	WWc	Zjets
2 Lepton [276]	lepton flavor	DF,SF	DF,SF	DF,SF	DF,SF	DF,SF	SF
	central light jets	0	0	0	0	0	≥ 2
	central b-jets	0	0	0	0	0	0
	forward jets	0	0	0	0	0	0
	$\lvert m_{ll} - m_Z \rvert$(GeV)	> 10	> 10	> 10	> 10	> 10	< 10
	m_{ll} (GeV)	-	-	< 120	< 170	-	-
	$E_{\mathrm{T}}^{\mathrm{miss},rel}$ (GeV)	-	-	> 80	-	-	> 80
	$p_{T,ll}$ (GeV)	-	-	> 80	-	-	> 80
	m_{T2} (GeV)	> 90	> 120	-	> 90	> 100	-
	ΔR_{ll}	-	-	-	-	-	[0.3,1.5]
	m_{jj} (GeV)	-	-	-	-	-	[50,100]

	SR	0τa	0τb	1τ	2τa
3 Lepton [276]	Flavor/sign	$l^+l^-l, l^+l^-l^{'}$	$l^{\pm}l^{\mp}l^{'\mp}$	$\tau^{\pm}l^{\mp}l^{\mp}, \tau^{\pm}l^{\mp}l^{'\mp}$	$\tau\tau l$
	b-tagged jet	veto	veto	veto	veto
	$E_{\mathrm{T}}^{\mathrm{miss}}$ (GeV)	binned	> 50	> 50	> 50
	Other	m_{SFOS} binned m_T binned	$p_T^{3^{rd}l}$>20 $\Delta\phi_{ll^{'}}^{min} \leq 1.0$	$p_T^{2^{nd}l}$>30 $\sum p_T^l > 70$ $m_{l\tau} < 120$ m_{ee} Z veto	m_{T2}^{max}>100

	SR	0noZa	1noZa	2noZa	0Z	1Z	2Z
4 Lepton [277]	N(l)	≥ 4	=3	=2	≥ 4	=3	=2
	N(τ)	≥ 0	$\geq$1	$\geq$2	≥ 0	$\geq$1	$\geq$2
	Z-veto	SFOS SFOS+l SFOS+SFOS	SFOS SFOS+l	SFOS SFOS	-	-	-
	Z-requirement	-	-	-	SFOS	SFOS	SFOS
	$E_{\mathrm{T}}^{\mathrm{miss}}$ (GeV)	> 50	> 50	> 75	> 75	> 100	> 75

Table A.3.: Signal region selection used in the 2, 3 and 4 lepton statistical combination analysis. One best expected signal region for 2 lepton analysis is used, and all listed 3 and 4 lepton signal regions. More details about samples, control and validation region selection, and individual analyses results can be found in [275–277]. DF, SF and SFOS denote different flavor, same flavor and same flavor opposite sign, respectively.

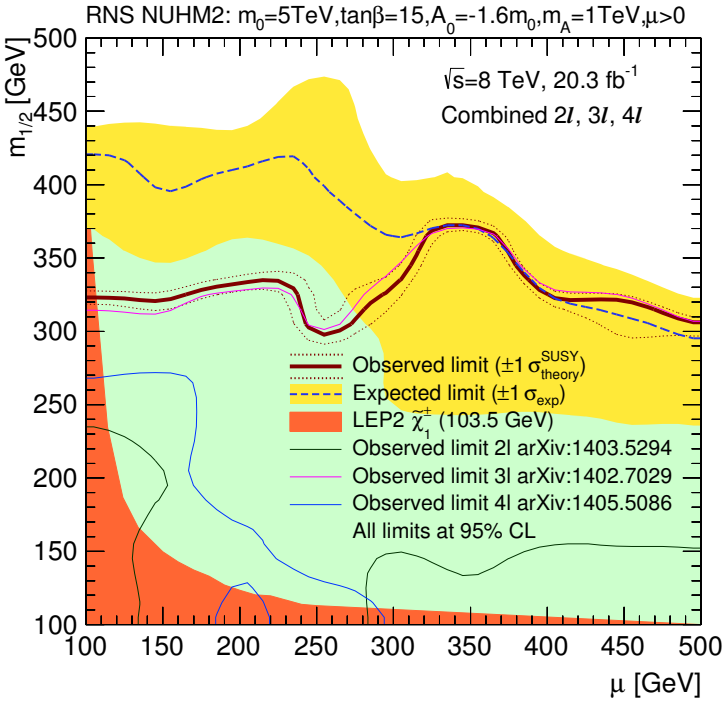

Figure A.5.: RNS NUHM exclusion for a statistical combination of 2, 3 and 4 lepton analyses [274].

The analysis was performed using a statistical combination including one signal region with the best expected sensitivity for the 2 lepton analysis, and all listed signal regions for the 3 and 4 lepton analysis. See more details about each analyses samples, control and validation regions and selections in [275–277]. Fit performance showed no additional profiling compared to single analyses, which gives good confidence in its performance.

No significant excess of data in any of the analyses has been seen, and exclusion limits have been set. The statistical combination exclusion limits for NUHM are driven by the 3 lepton analysis, which showed highest expected sensitivity. The 95% CL expected and observed exclusion limits using the 2, 3 and 4 lepton analyses and their statistical combination are shown in the figure A.5 [274]. The observed 95% CL exclusion in the low μ region has a downward fluctuation compared to the expected 95% CL exclusion higher than 1 sigma. This effect has been observed also in the 3 lepton analysis, which is the dominant analysis in this statistical combination. The observed 95% CL exclusion reaches about 300 GeV in $m_{1/2}$, while in μ direction it extends up to the highest examined value of 500 GeV.

B. Online Monitoring of the Trigger in ATLAS with TriP

A program called **Trigger Presenter** (TriP) was designed in order to accommodate requirements for the online monitoring of the ATLAS trigger. In the section 6.7 the ATLAS Trigger and Data acquisition system were described. In the section B.1 details about the program implementation, and its usage in B.2, will be provided. Trigger Presenter was extensively used in the ATLAS control room during the ATLAS integration test runs during 2008. and at the LHC startup in September 2008. A new version of the program called Trigger Rate Presenter (TRP) is in use today.

B.1. Trigger Presenter Implementation

In order to provide a tool for online monitoring and diagnostics for the shifter and a trigger expert, the Trigger Presenter was designed. It is aimed at monitoring of Level 1 and HLT rates. Also, in order to ensure stable running of HLT algorithms, the monitoring of the HLT PC farms is performed. In this section the requirements for the program and details about its implementation will be given.

A number of requirements needs to be met in the design of the TriP:

- High scalability: there is a couple aspects in which the program is required to be scalable. First, the trigger menu can be changed for each data taking run. Then the number of Level 1 trigger items and Level 2 and Event Filter trigger chains can significantly vary, depending on the run conditions. Second, the HLT farms have a highly configurable structure which can be changed for each run. Also, the possibility of adding PCs to the HLT farm needs to be considered in both of these aspects.

- Flexible structure: at Level 2 and Event Filter, the number of trigger chains and for each chain a number of steps can differ, and they can be changed for each run. Also, the HLT PC farm structure is defined by the configuration, where the complete organization and grouping of PCs can be changed for each run.

- Accessible levels of information: the summary information needs to be monitored, but in case of problems, there should be a possibility to navigate down to the lowest level of structure for the trigger rates and PC farms.

- History of all information: as the time and presence of a problem can provide good diagnostics, the history of all information needs to be stored, and accommodated with the current structure.
- Simple warning system: as the program provides rates, additional warning system using thresholds is used. A simple warning system with green - orange - red for OK - WARNING - ERROR levels of rates is set in place. For this dedicated algorithm checks are used.
- User friendly graphical user interface: as the program is used by the shifter and expert, it is required to be easy to read but also provide all available information.
- Lightweight program: as the program receives large amounts of information, and multiple monitoring tools are used in the control room, the program needs to have low memory consumption.

Trigger and Data Acquisition (TDAQ) system of ATLAS is running on about 2000 commodity computing nodes. Multiple software applications for tasks of event rejection, event building, recording, task control and event monitoring are executed on each node. In order to ensure high performance of of the TDAQ, a system for exchanging control and monitoring information is used, called Information Service (IS). In addition, some monitoring tasks require a usage of histograms, and for this a dedicated system is used, called the Online Histogramming (OH) [278]. Typically, the TDAQ information, e.g. trigger rates or CPU usage of the node, are published to the IS or OH, and monitoring software reads this information and presents it in a user friendly way.

The information published by the TDAQ to the IS and OH needs to be summed up and evaluated. This is done by two systems, the Gatherer and the Data Quality Monitoring Framework (DQMF), see figure B.1. Gatherer is a system that sums up specified information from IS or OH and produces summary result for a given configuration. DQMF is a system for evaluation of summed up values. For each trigger and detector system, information is evaluated by dedicated algorithms executed by the DQMF, where warning and error signals are produced for specified thresholds and test algorithms, calculated by DQMF using the IS, OH and the ATLAS detector status information from the Conditions Data Base. The evaluated information is further published to the IS, or automatically sent as warnings to the Run Control system, and evaluation flags are saved to the Conditions Database [152].

The information and the data quality flag published to the IS are read out by the monitoring system, where it subscribes to the information using the naming convention for the IS [278]. The information published to the OH is read out in a similar way. A dedicated convention has been developed for the HLT published rates, trigger chain names and steps. In the figure B.2 an example of HLT chain names and event counts convention used by the OH is shown, the so called HLT Steering file, produced for Level 2 and Event Filter [150]. The axis holds the chain

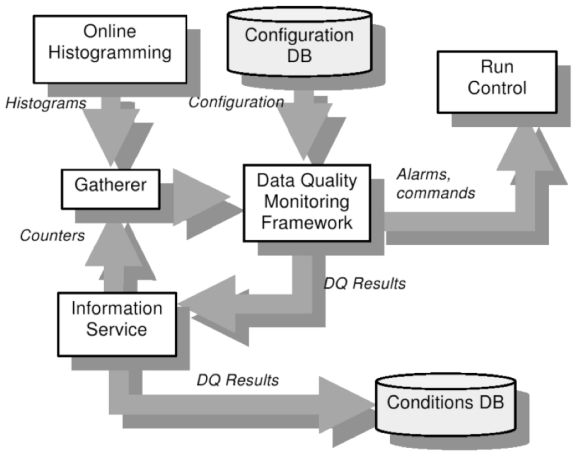

Figure B.1.: Data Quality Monitoring information for ATLAS using Information Service (IS), Online Histogramming (OH), Gatherer and Data Quality Monitoring Framework (DQMF) [152]. Information published by TDAQ to the IS or OH is summed up by the Gatherer. Data quality flag is assigned by the DQMF, using in addition the information on the ATLAS detector components status from the Conditions Data Base, and published back to the IS and Run Control.

names, and the first column gives the summary information for the whole Level 2 or Event Filter. In the first row the input rates for Level 2 or Event Filter are shown, and higher rows show chain rates at next steps. The -1 represents end of a chain. Step names for a given chain are read out from the Conditions DB. The last two rows hold after the pre-scale rate, and after the pass-through rate. Pre-scale is used for some chains in order to reduce their bandwidth, while pass-through allows for a minimal number of events to be accepted if the rate for the chain is low. From this information rates for all chains and summary information are calculated by the Trigger Presenter.

The information for trigger components from IS and OH is received, mapped and presented in different ways in TriP. The details of the information receiving and TriP class implementations are given here, see figure B.3 for the TriP classes:

- **Level 1**: The Level 1 information about the trigger item names, rates before and after pre-scale and forced accept are received from the IS and mapped into structure by the **TDataManagerLvl1** class implementation. The maximal number of trigger items is 256 which is a hardware limit, but not all need to be used in each run. The mapped information consists of **TLevel1Data** class, which consists of multiple **TPItem** class objects which summarize the rate information in **TItem** and additional information about the used pre-scales. In addition the summary information is calculated and the history information is stored during the run.

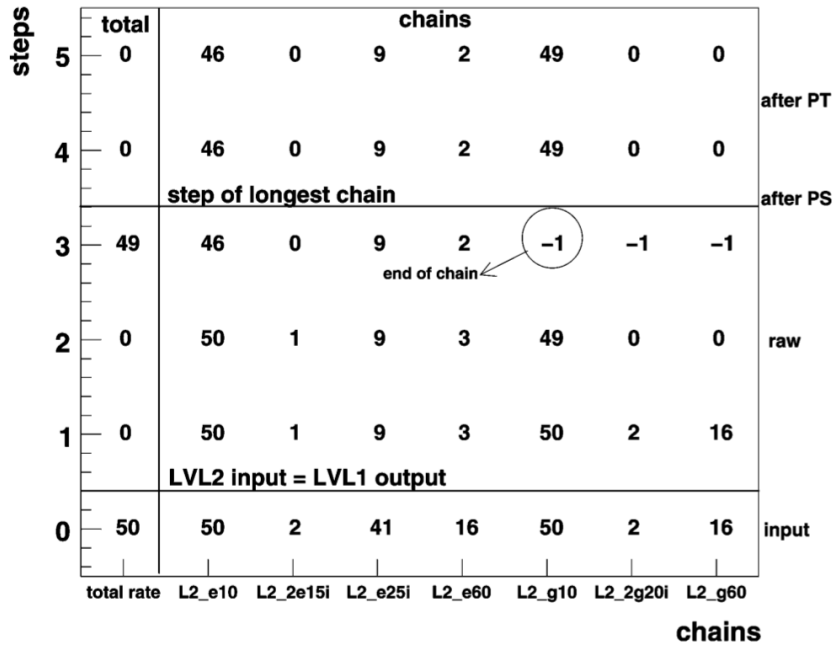

Figure B.2.: Convention for the Data Quality Monitoring of High Level Trigger [150], the so-called HLT Steering file. Axis represent the chain names, first column is the summary information for the whole Level 2 or Event Filter. First row is the input number of events, and higher rows show the number events for a given step, where -1 represents end of the chain. Last two rows show the after the pre-scale and after the pass-through number of events. From this input rates are calculated in the TriP.

- **Level 2 and Event Filter**: The Level 2 and Event Filter trigger chains information is received from OH each. The rates and the DQMF flag information is received and mapped into structure by the **TDataManager** class. A convention for the chain steps and their DQM flag is used. The mapped information consists of **TLevelData** class which contains multiple **TChain** objects which further contain **TStep** objects. The summary information is calculated and the rate history is stored during the run.
- **HLT Farms**: The HLT farms information is read out from IS and mapped into structure by the **TFarmManager** class. Level 2 and Event Filter farms have different types of substructure. The HLT farm can be changed by the configuration and the number of substructure segments can significantly vary, while the number of structure levels is kept. One should note that HLT is using more than 16000 processing tasks (PT). Level 2 can have multiple segments **L2_Segment**, which contain multiple sub-segments **L2_Subsegment**,

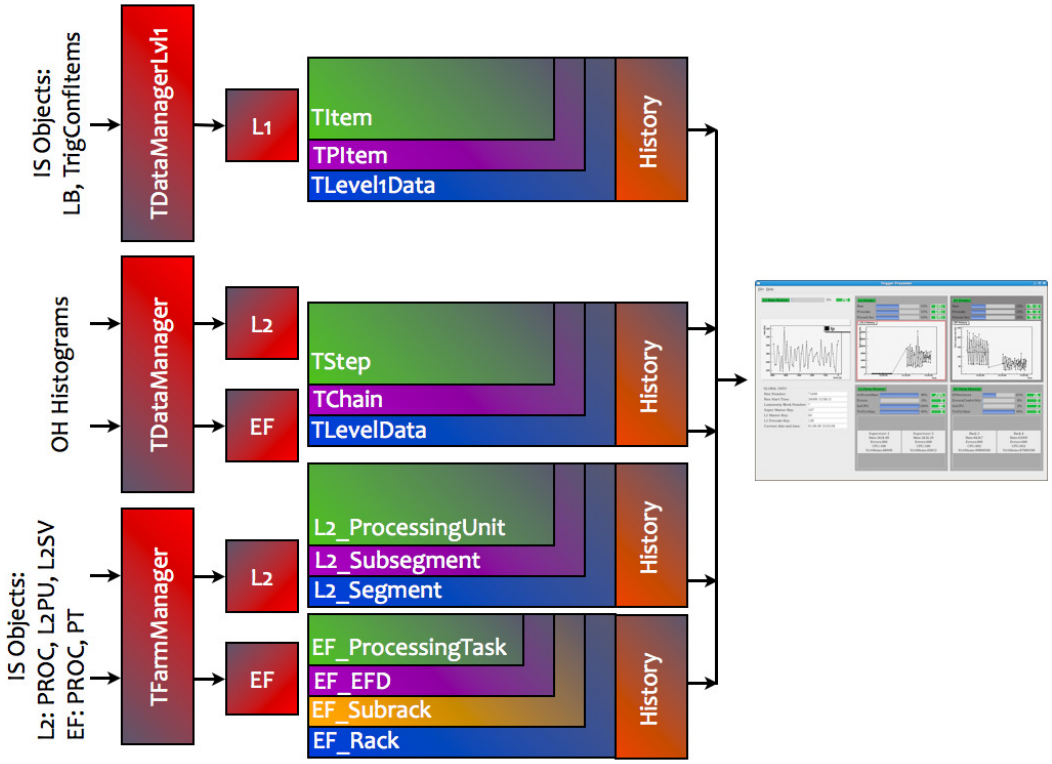

Figure B.3.: Trigger Presenter (TriP) classes implementation for Level 1, Level 2 and Event Filter trigger information, HLT PC farm and global information.

which further consist of more processing units **L2_ProcessingUnit**. Event Filter can have multiple racks **EF_Rack**, which contain more sub-racks **EF_Subrack**, which further have more EFDs **EF_EFD** and they consist of more processing tasks **EF_ProcessingTask**. The information on the rate, number of errors, CPU and memory usage is read out and mapped to corresponding classes, and the summary information is calculated and the history information is stored during the run.

- **Global Information**: In addition to trigger information, the global information about the run status, run number, luminosity block and time are shown. These are read out from IS and from the local computer.

TriP is designed as a plug-in for the Online Histogram Presenter (OHP) [279] in order to make use of the information receiving from the OH. In order to perform reading out of large amounts of data, a design using the semaphore is implemented, where retrieving of different blocks of information is performed one at a time. The blocks of information are read at 10s intervals.

Figure B.4.: Trigger Presenter (TriP) main panel.

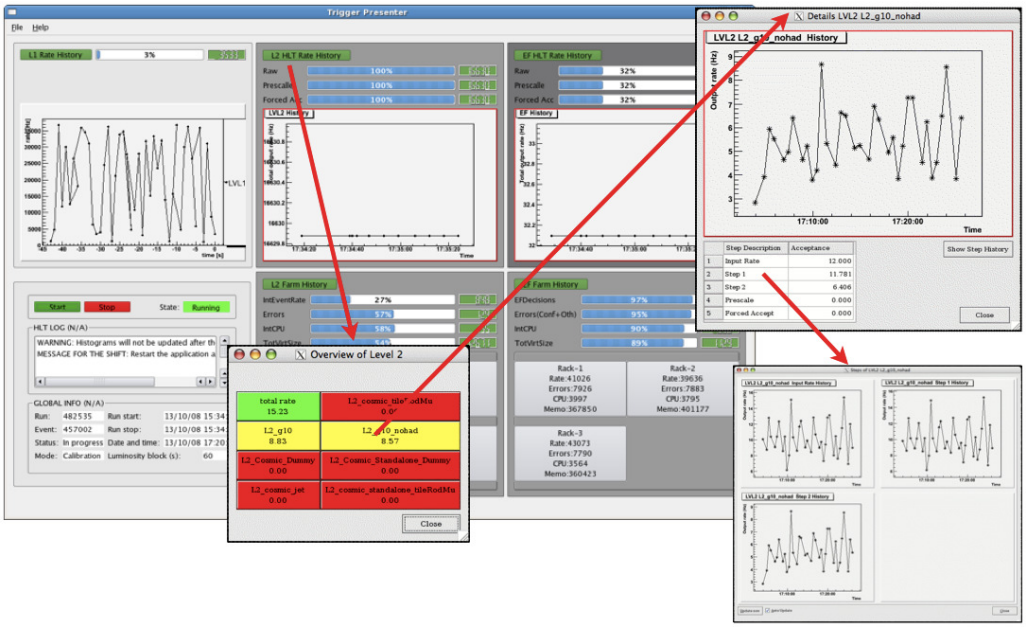

Figure B.6.: Trigger Presenter (TriP) Level 2 and Event Filter details.

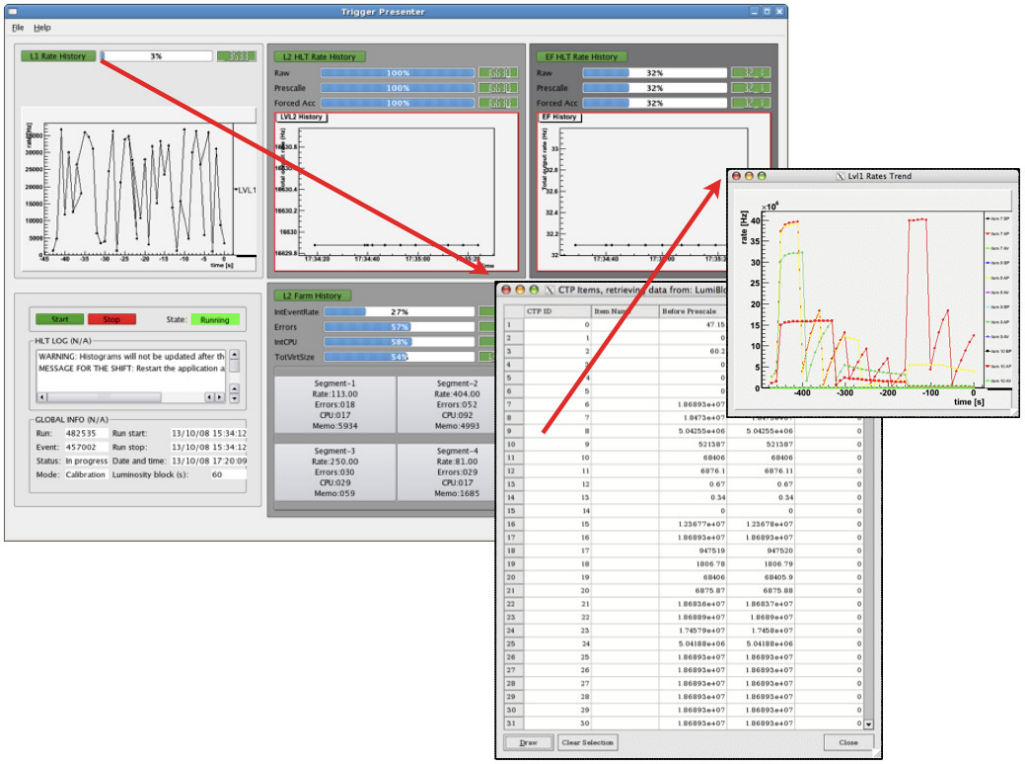

Figure B.5.: Trigger Presenter (TriP) Level 1 details.

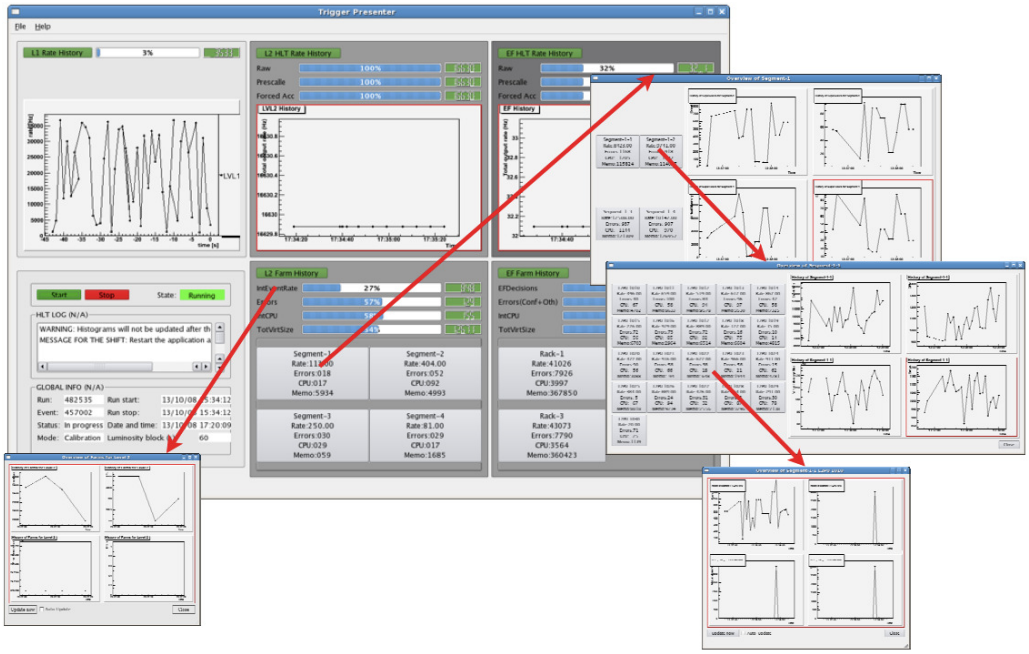

Figure B.7.: Trigger Presenter (TriP) HLT farm details.

B.2. Graphical User Interface

The read out, mapped and stored history information in TriP is presented in a user friendly graphical user interface. In the figure B.4 the main panel is shown. On the upper left the Level 1 summary and history information are shown. On the upper middle and right is the same for Level 2 and Event Filter. The the global information is on the lower left, while the HLT farm information is on the lower middle and right. The user can navigate by clicking on the Level 1 button to get the list of trigger items and their rate information, see figure B.5. By clicking on a trigger item and holding shift for selecting multiple trigger items, and clicking on the Draw button, the history of the selected rate is shown.

By clicking on the Level 2 or Event Filter button, the clickable list of trigger chains with their rate information is obtained, see figure B.6. By clicking on a trigger chain button, step and history information is obtained, and by further clicking on Show Step History, their history of rates is shown in a new panel.

By clicking on a Level 2 Farm or Event Filter Farm button, summary history information is obtained, see figure B.7. By clicking on a Level 2 segment, the user can navigate through sub-segments to the processing units rate and their history. By clicking on Event Filter Rack button, the user can navigate via sub-rack, EFD to the processing task rates and their history.

Bibliography

[1] S.L. Glashow. Partial Symmetries of Weak Interactions. *Nucl.Phys.*, 22:579–588, 1961. doi:10.1016/0029-5582(61)90469-2.

[2] S. Weinberg. A Model of Leptons. *Phys.Rev.Lett.*, 19:1264–1266, 1967. doi:10.1103/PhysRevLett.19.1264.

[3] A. Salam. Weak and Electromagnetic Interactions. *Conf.Proc.*, C680519:367–377, 1968. URL: http://inspirehep.net/record/53083?ln=en.

[4] M. Gell-Mann. A Schematic Model of Baryons and Mesons. *Phys.Lett.*, 8:214–215, 1964. doi:10.1016/S0031-9163(64)92001-3.

[5] G. Zweig. An SU3 Model for Strong Interaction Symmetry and its Breaking; Version 2, February 1964. URL: https://cds.cern.ch/record/570209/?ln=en.

[6] H. Fritzsch et al. Advantages of the Color Octet Gluon Picture. *Phys.Lett.*, B47:365–368, 1973. doi:10.1016/0370-2693(73)90625-4.

[7] D. J. Gross and F. Wilczek. Ultraviolet Behavior of Nonabelian Gauge Theories. *Phys.Rev.Lett.*, 30:1343–1346, 1973. doi:10.1103/PhysRevLett.30.1343.

[8] H. D. Politzer. Reliable Perturbative Results for Strong Interactions? *Phys.Rev.Lett.*, 30:1346–1349, 1973. doi:10.1103/PhysRevLett.30.1346.

[9] M. J. G. Veltman and G. Hooft. Example of a gauge field theory. *Utrecht University Repository*, pages 1–38, June 1972. URL: http://dspace.library.uu.nl/handle/1874/4802.

[10] G. Aad et al. (ATLAS Collaboration). Observation of a New Particle in the Search for the Standard Model Higgs Boson with the ATLAS Detector at the LHC. *Physics Letters B*, 716(1):1 – 29, 2012. URL: http://www.sciencedirect.com/science/article/pii/S037026931200857X, doi:http://dx.doi.org/10.1016/j.physletb.2012.08.020.

[11] S. Chatrchyan et al. (CMS Collaboration). Observation of a New Boson at a Mass of 125 GeV with the CMS Experiment at the LHC. *Physics Letters B*, 716(1):30 – 61, 2012. URL: http://www.sciencedirect.com/science/article/pii/S0370269312008581, doi:http://dx.doi.org/10.1016/j.physletb.2012.08.021.

[12] L. Evans and P. Bryant. The LHC Machine. *Journal of Instrumentation*, 3(08):S08001, 2008. URL: http://stacks.iop.org/1748-0221/3/i=08/a=S08001.

[13] CERN press office. LHC Sets New World Record, November 2009. URL: http://press.web.cern.ch/press-releases/2009/11/lhc-sets-new-world-record.

[14] G. Aad et al. (ATLAS Collaboration). The ATLAS Experiment at the CERN Large Hadron Collider. *JINST*, 3:S08003, 2008. doi:10.1088/1748-0221/3/08/S08003.

[15] S. Chatrchyan et al. (CMS Collaboration). The CMS Experiment at the CERN LHC. *JINST*, 3:S08004, 2008. doi:10.1088/1748-0221/3/08/S08004.

[16] A. A. Jr. Alves et al. (LHCb Collaboration). The LHCb Detector at the LHC. *JINST*, 3:S08005, 2008. doi:10.1088/1748-0221/3/08/S08005.

[17] K. Aamodt et al. (ALICE Collaboration). The ALICE Experiment at the CERN LHC. *JINST*, 3:S08002, 2008. doi:10.1088/1748-0221/3/08/S08002.

[18] M. H. Seymour and M. Marx. Monte Carlo Event Generators, 2013. arXiv:1304.6677, doi:10.1007/978-3-319-05362-2_8.

[19] H. Miyazawa. Baryon Number Changing Currents. *Prog. Theor. Phys.*, 36 (6):1266–1276, 1966. doi:10.1143/PTP.36.1266.

[20] P. Ramond. Dual Theory for Free Fermions. *Phys. Rev.*, D3:2415–2418, 1971. doi:10.1103/PhysRevD.3.2415.

[21] Yu. A. Gol'fand and E. P. Likhtman. Extension of the Algebra of Poincare Group Generators and Violation of p Invariance. *JETP Lett.*, 13:323–326, 1971. [Pisma Zh.Eksp.Teor.Fiz.13:452-455,1971]. URL: https://inspirehep.net/record/68412.

[22] A. Neveu and J. H. Schwarz. Factorizable Dual Model of Pions. *Nucl. Phys.*, B31:86–112, 1971. doi:10.1016/0550-3213(71)90448-2.

[23] A. Neveu and J. H. Schwarz. Quark Model of Dual Pions. *Phys. Rev.*, D4:1109–1111, 1971. doi:10.1103/PhysRevD.4.1109.

[24] J.L. Gervais and B. Sakita. Field Theory Interpretation of Supergauges in Dual Models. *Nucl. Phys.*, B34:632–639, 1971. doi:10.1016/0550-3213(71)90351-8.

[25] D. V. Volkov and V. P. Akulov. Is the Neutrino a Goldstone Particle? *Phys. Lett.*, B46:109–110, 1973. doi:10.1016/0370-2693(73)90490-5.

[26] J. Wess and B. Zumino. A Lagrangian Model Invariant Under Supergauge Transformations. *Phys. Lett.*, B49:52, 1974. doi:10.1016/0370-2693(74)90578-4.

[27] J. Wess and B. Zumino. Supergauge Transformations in Four-Dimensions. *Nucl. Phys.*, B70:39–50, 1974. doi:10.1016/0550-3213(74)90355-1.

[28] L. Covi and S. Kraml. Collider Signatures of Gravitino Dark Matter with a Sneutrino NLSP. *JHEP*, 08:015, 2007. arXiv:hep-ph/0703130, doi:10.1088/1126-6708/2007/08/015.

[29] J. R. Ellis et al. Exploration of the MSSM with Nonuniversal Higgs Masses. *Nucl.Phys.*, B652:259–347, 2003. arXiv:hep-ph/0210205, doi:10.1016/S0550-3213(02)01144-6.

[30] H. Baer et al. Radiatively-driven Natural Supersymmetry at the LHC. *JHEP*, 1312:013, 2013. URL: http://arxiv.org/abs/1310.7291, arXiv:1310.4858, doi:10.1007/JHEP12(2013)013.

[31] G. Aad et al. (ATLAS Collaboration). Search for Squarks and Gluinos with the ATLAS Detector in Final States with Jets and Missing Transverse Momentum using $\sqrt{s} = 8$ TeV Proto–Proton Collision Data. *JHEP*, 2014. arXiv:1405.7875.

[32] LEPSUSYWG, ALEPH, DELPHI, L3 and OPAL Collaboration. Lep limits: Charginos, large m0. *note LEPSUSYWG/01-03.1*, 2004. URL: http://lepsusy.web.cern.ch/lepsusy/Welcome.html.

[33] G. Aad et al. (ATLAS Collaboration). Measurement of the Higgs Boson Mass from the $H \to \gamma\gamma$ and $H \to ZZ^* \to 4\ell$ Channels with the ATLAS Detector using 25 fb^{-1} of pp Collision Data. *Phys.Rev.*, D90:052004, 2014. arXiv:1406.3827, doi:10.1103/PhysRevD.90.052004.

[34] S. Chatrchyan et al. (CMS Collaboration). Precise Determination of the Mass of the Higgs Boson and Studies of the Compatibility of its Couplings with the Standard Model, 2014. URL: https://cds.cern.ch/record/1728249?ln=en.

[35] G. Aad et al. (ATLAS Collaboration). ATLAS Combined Summary Plot - Supersymmetry, 2014. URL: https://atlas.web.cern.ch/Atlas/GROUPS/PHYSICS/CombinedSummaryPlots/SUSY/ATLAS_SUSY_Summary/ATLAS_SUSY_Summary.eps [cited June 2014].

[36] A. Hoecker et al. TMVA: Toolkit for Multivariate Data Analysis. *PoS*, ACAT:040, 2007. arXiv:physics/0703039.

[37] G. Aad et al. (ATLAS Collaboration, ATLAS Statistics Forum). The CLs Method. , 07 2011. URL: https://twiki.cern.ch/twiki/pub/AtlasProtected/StatisticsTools/CLsInfo.pdf [cited 27. 08. 2014.].

[38] G. Aad et al. (ATLAS Collaboration). Search for Squarks and Gluinos in Events with Isolated Leptons, Jets and Missing Transverse Momentum at $\sqrt{s} = 8$ TeV with the ATLAS Detector. *JHEP*, 2015. arXiv:1501.03555.

[39] K. A. Olive et al. (Particle Data Group). The Review of Particle Physics, 2014. URL: http://pdg.lbl.gov/.

[40] F. Englert and R. Brout. Broken Symmetry and the Mass of Gauge Vector Mesons. *Phys. Rev. Lett.*, 13:321–323, Aug 1964. URL: http://link.aps.org/doi/10.1103/PhysRevLett.13.321, doi:10.1103/PhysRevLett.13.321.

[41] P. W. Higgs. Broken Symmetries, Massless Particles and Gauge Fields. *Physics Letters*, 12(2):132 – 133, 1964. URL: http://www.sciencedirect.com/science/article/pii/0031916364911369, doi:http://dx.doi.org/10.1016/0031-9163(64)91136-9.

[42] P. W. Higgs. Broken Symmetries and the Masses of Gauge Bosons. *Phys. Rev. Lett.*, 13:508–509, Oct 1964. URL: http://link.aps.org/doi/10.1103/PhysRevLett.13.508, doi:10.1103/PhysRevLett.13.508.

[43] G.S. Guralnik et al. Global conservation laws and massless particles. *Phys. Rev. Lett.*, 13:585–587, Nov 1964. URL: http://link.aps.org/doi/10.1103/PhysRevLett.13.585, doi:10.1103/PhysRevLett.13.585.

[44] P. W. Higgs. Spontaneous Symmetry Breakdown without Massless Bosons. *Phys. Rev.*, 145:1156–1163, May 1966. URL: http://link.aps.org/doi/10.1103/PhysRev.145.1156, doi:10.1103/PhysRev.145.1156.

[45] T. W. B. Kibble. Symmetry Breaking in Non-Abelian Gauge Theories. *Phys. Rev.*, 155:1554–1561, Mar 1967. URL: http://link.aps.org/doi/10.1103/PhysRev.155.1554, doi:10.1103/PhysRev.155.1554.

[46] M. Bustamante et al. Beyond the Standard Model for Montaneros, 2009. arXiv:0911.4409.

[47] F. Halzen and A. D. Martin. *Quarks and Leptons: An Introductory Course in Modern Particle Physics*. John Wiley and Sons, New York, 1984.

[48] H. W. Baer and X. Tata. *Weak Scale Supersymmetry: From Superfields to Scattering Events*. Cambridge Univ. Press, Cambridge, 2006. URL: https://inspirehep.net/record/728103.

[49] J. R. Ellis. Higgs Physics, 2013. arXiv:1312.5672.

[50] G. Aad et al. (ATLAS Collaboration). Standard Model Total Production Cross Section Measurements, July 2014. URL: https://atlas.web.cern.ch/Atlas/GROUPS/PHYSICS/CombinedSummaryPlots/SM/ATLAS_a_SMSummary_TotalXsect/ATLAS_a_SMSummary_TotalXsect.png.

[51] G. Aad et al. (ATLAS Collaboration). Inclusive Jet Cross Section Measurements, July 2014. URL: https://atlas.web.cern.ch/Atlas/GROUPS/PHYSICS/CombinedSummaryPlots/SM/ATLAS_h_SMSummary_InclJetsFiducialRatio/ATLAS_h_SMSummary_InclJetsFiducialRatio.png.

[52] S. Chatrchyan et al. (CMS and LHCb Collaboration). Observation of the Rare $B_s^0 \to \mu^+\mu^-$ decay from the Combined Analysis of CMS and LHCb Data. *Nature*, 522:68–72, 2015. arXiv:1411.4413, doi:10.1038/nature14474.

[53] S. Chatrchyan et al. (CMS Collaboration). Combination of Standard Model Higgs boson Searches and Measurements of the Properties of the New Boson with a Mass Near 125 GeV. Technical Report CMS-PAS-HIG-12-045, CERN, Geneva, 2012. URL: https://cds.cern.ch/record/1494149/files/HIG-12-045-pas.pdf.

[54] G. Aad et al. (ATLAS Collaboration). Observation of an Excess of Events in the Search for the Standard Model Higgs Boson in the H to ZZ to 4l Channel with the ATLAS Detector. Technical Report ATLAS-CONF-2012-169, CERN, Geneva, Dec 2012. URL: https://cds.cern.ch/record/1499628?ln=en.

[55] G. Aad et al. (ATLAS Collaboration). Higgs Boson Production Signal Strengths. , December 2014. URL: https://atlas.web.cern.ch/Atlas/GROUPS/PHYSICS/CombinedSummaryPlots/HIGGS/ATLAS_HIGGS_mu_Summary_simple/ATLAS_HIGGS_mu_Summary_simple.pdf.

[56] G. Aad et al. (ATLAS and CMS Collaboration). Combined Measurement of the Higgs Boson Mass in pp Collisions at $\sqrt{s} = 7$ and 8 TeV with the ATLAS and CMS Experiments. *Phys. Rev. Lett.*, 114:191803, May 2015. URL: http://link.aps.org/doi/10.1103/PhysRevLett.114.191803, doi:10.1103/PhysRevLett.114.191803.

[57] V. Chachatryan et al. (CMS Collaboration). Constraints on the Spin-Parity and Anomalous HVV Couplings of the Higgs Boson in Proton Collisions at 7 and 8 TeV, 2014. arXiv:1411.3441.

[58] G. Aad et al. (ATLAS Collaboration). Evidence for the Spin-0 Nature of the Higgs Boson using ATLAS Data. *Phys.Lett.*, B726:120–144, 2013. arXiv:1307.1432, doi:10.1016/j.physletb.2013.08.026.

[59] J. Bernon et al. Status of Higgs Couplings After Run 1 of the LHC. *Phys.Rev.*, D90(7):071301, 2014. arXiv:1409.1588, doi:10.1103/PhysRevD.90.071301.

[60] M. Baak et. al. (The Gfitter Group). . Electroweak Fit. , July 2014. URL: http://project-gfitter.web.cern.ch/project-gfitter/.

[61] M. Baak et. al. (The Gfitter Group). The Electroweak Fit of the Standard Model after the Discovery of a New Boson at the LHC. *Eur.Phys.J.*, C72:2205, 2012. arXiv:1209.2716, doi:10.1140/epjc/s10052-012-2205-9.

[62] The Planck Collaboration. The Planck Cosmic Recipe, March 2013. URL: http://sci.esa.int/planck/51557-planck-new-cosmic-recipe/.

[63] S. P. Martin. A Supersymmetry Primer. *Adv.Ser.Direct.High Energy Phys.*, 21:1–153, 2010. arXiv:hep-ph/9709356, doi:10.1142/9789814307505_0001.

[64] J. R. Ellis. The Beautiful Physics of LHC Run 2, 2014. arXiv:1412.2666.

[65] S. Weinberg. Implications of Dynamical Symmetry Breaking. *Phys. Rev.*, D13:974–996, 1976. doi:10.1103/PhysRevD.13.974.

[66] E. Gildener. Gauge Symmetry Hierarchies. *Phys. Rev.*, D14:1667, 1976. doi:10.1103/PhysRevD.14.1667.

[67] S. Weinberg. Implications of Dynamical Symmetry Breaking: An Addendum. *Phys. Rev.*, D19:1277–1280, 1979. doi:10.1103/PhysRevD.19.1277.

[68] L. Susskind. Dynamics of Spontaneous Symmetry Breaking in the Weinberg-Salam Theory. *Phys. Rev.*, D20:2619–2625, 1979. doi:10.1103/PhysRevD.20.2619.

[69] S. Dimopoulos and H. Georgi. Softly Broken Supersymmetry and SU(5). *Nucl. Phys.*, B193:150, 1981. doi:10.1016/0550-3213(81)90522-8.

[70] E. Witten. Dynamical Breaking of Supersymmetry. *Nucl. Phys.*, B188:513, 1981. doi:10.1016/0550-3213(81)90006-7.

[71] M. Dine et al. Supersymmetric Technicolor. *Nucl. Phys.*, B189:575–593, 1981. doi:10.1016/0550-3213(81)90582-4.

[72] S. Dimopoulos and S. Raby. Supercolor. *Nucl. Phys.*, B192:353, 1981. doi:10.1016/0550-3213(81)90430-2.

[73] N. Sakai. Naturalness in Supersymmetric Guts. *Zeit. Phys.*, C11:153, 1981. doi:10.1007/BF01573998.

[74] R.K. Kaul and P. Majumdar. Cancellation of Quadratically Divergent Mass Corrections in Globally Supersymmetric Spontaneously Broken Gauge Theories. *Nucl. Phys.*, B199:36, 1982. doi:10.1016/0550-3213(82)90565-X.

[75] U. Amaldi et al. Comparison of Grand Unified Theories with Electroweak and Strong Coupling Constants Measured at LEP. *Phys. Lett.*, B260:447–455, 1991. doi:10.1016/0370-2693(91)91641-8.

[76] S. Dimopoulos et al. Supersymmetry and the Scale of Unification. *Phys. Rev.*, D24:1681–1683, 1981. doi:10.1103/PhysRevD.24.1681.

[77] L. E. Ibanez and G. G. Ross. Low-Energy Predictions in Supersymmetric Grand Unified Theories. *Phys. Lett.*, B105:439, 1981. doi:10.1016/0370-2693(81)91200-4.

[78] M. B. Einhorn and D. R. T. Jones. The Weak Mixing Angle and Unification Mass in Supersymmetric SU(5). *Nucl. Phys.*, B196:475, 1982. doi:10.1016/0550-3213(82)90502-8.

[79] W. J. Marciano and G. Senjanovic. Predictions of Supersymmetric Grand Unified Theories. *Phys. Rev.*, D25:3092, 1982. doi:10.1103/PhysRevD.25.3092.

[80] C. Giunti et al. Running Coupling Constants and Grand Unification Models. *Mod. Phys. Lett.*, A6:1745–1755, 1991. doi:10.1142/S0217732391001883.

[81] J. R. Ellis et al. Probing the Desert Using Gauge Coupling Unification. *Phys. Lett.*, B260:131–137, 1991. doi:10.1016/0370-2693(91)90980-5.

[82] P. Langacker and M. X. Luo. Implications of Precision Electroweak Experiments for M(t), rho(0), sin**2-Theta(W) and Grand Unification. *Phys. Rev.*, D44:817–822, 1991. doi:10.1103/PhysRevD.44.817.

[83] O. Lahav and A. R. Liddle. The Cosmological Parameters 2014. *PDG*, 2014. arXiv:1401.1389.

[84] The Planck Collaboration. The Planck Dark Matter All-sky Map, April 2013. URL: http://sci.esa.int/planck/51604-all-sky-map-of-dark-matter-distribution-in-the-universe/.

[85] D. Buttazzo et al. Investigating the Near-Criticality of the Higgs Boson. *JHEP*, 1312:089, 2013. arXiv:1307.3536, doi:10.1007/JHEP12(2013)089.

[86] Rudolf Haag et al. All Possible Generators of Supersymmetries of the S-Matrix. *Nuclear Physics B*, 88(2):257 – 274, 1975. URL: http://www.sciencedirect.com/science/article/pii/0550321375902795, doi:http://dx.doi.org/10.1016/0550-3213(75)90279-5.

[87] S. Coleman and J. Mandula. All Possible Symmetries of the *S* Matrix. *Phys. Rev.*, 159:1251–1256, Jul 1967. URL: http://link.aps.org/doi/10.1103/PhysRev.159.1251, doi:10.1103/PhysRev.159.1251.

[88] J. Wess and B. Zumino. Supergauge Transformations in Four Dimensions. *Nuclear Physics B*, 70(1):39 – 50, 1974. URL: http://www.sciencedirect.com/science/article/pii/0550321374903551, doi:http://dx.doi.org/10.1016/0550-3213(74)90355-1.

[89] P. Fayet. Supersymmetry and Weak, Electromagnetic and Strong Interactions. *Phys. Lett.*, B64:159, 1976. doi:10.1016/0370-2693(76)90319-1.

[90] P. Fayet. Spontaneously Broken Supersymmetric Theories of Weak, Electromagnetic and Strong Interactions. *Phys. Lett.*, B69:489, 1977. doi:10.1016/0370-2693(77)90852-8.

[91] G. R. Farrar and P. Fayet. Phenomenology of the Production, Decay, and Detection of New Hadronic States Associated with Supersymmetry. *Phys. Lett.*, B76:575–579, 1978. doi:10.1016/0370-2693(78)90858-4.

[92] P. Fayet. Relations Between the Masses of the Superpartners of Leptons and Quarks, the Goldstino Couplings and the Neutral Currents. *Phys. Lett.*, B84:416, 1979. doi:10.1016/0370-2693(79)91229-2.

[93] S. S. AbdusSalam et al. Benchmark Models, Planes, Lines and Points for Future SUSY Searches at the LHC. *Eur.Phys.J.*, C71:1835, 2011. arXiv:1109.3859, doi:10.1140/epjc/s10052-011-1835-7.

[94] A. Chamseddine et al. Locally Supersymmetric Grand Unification. *Phys. Rev. Lett.*, 49:970–974, Oct 1982. URL: http://link.aps.org/doi/10.1103/PhysRevLett.49.970, doi:10.1103/PhysRevLett.49.970.

[95] R. Barbieri et al. Gauge Models with Spontaneously Broken Local Supersymmetry. *Physics Letters B*, 119(46):343 – 347, 1982. URL: http://www.sciencedirect.com/science/article/pii/0370269382906852, doi:http://dx.doi.org/10.1016/0370-2693(82)90685-2.

[96] L. Ibanez. Locally Supersymmetric SU(5) Grand Unification. *Physics Letters B*, 118(13):73 – 78, 1982. URL: http://www.sciencedirect.com/science/article/pii/0370269382906049, doi:http://dx.doi.org/10.1016/0370-2693(82)90604-9.

[97] L. Hall and et al. Supergravity as the Messenger of Supersymmetry Breaking. *Phys. Rev. D*, 27:2359–2378, May 1983. URL: http://link.aps.org/doi/10.1103/PhysRevD.27.2359, doi:10.1103/PhysRevD.27.2359.

[98] N. Ohta. Grand Unified Theories Based on Local Supersymmetry. *Prog.Theor.Phys.*, 70:542, 1983. doi:10.1143/PTP.70.542.

[99] G. L. Kane et al. Study of Constrained Minimal Supersymmetry. *Phys.Rev.*, D49:6173–6210, 1994. arXiv:hep-ph/9312272, doi:10.1103/PhysRevD.49.6173.

[100] L. Randall and R. Sundrum. Out of this World Supersymmetry Breaking. *Nucl.Phys.*, B557:79–118, 1999. arXiv:hep-th/9810155, doi:10.1016/S0550-3213(99)00359-4.

[101] G. F. Giudice et.al. Gaugino Mass without Singlets. *JHEP*, 9812:027, 1998. arXiv:hep-ph/9810442, doi:10.1088/1126-6708/1998/12/027.

[102] M. Dine and W. Fischler. A Phenomenological Model of Particle Physics Based on Supersymmetry. *Phys. Lett.*, B110:227, 1982. doi:10.1016/0370-2693(82)91241-2.

[103] L. Alvarez-Gaume et al. Low-Energy Supersymmetry. *Nucl. Phys.*, B207:96, 1982. doi:10.1016/0550-3213(82)90138-9.

[104] C. R. Nappi and B. A. Ovrut. Supersymmetric Extension of the SU(3) x SU(2) x U(1) Model. *Phys. Lett.*, B113:175, 1982. doi:10.1016/0370-2693(82)90418-X.

[105] M. Dine and A. E. Nelson. Dynamical Supersymmetry Breaking at Low-energies. *Phys. Rev.*, D48:1277–1287, 1993. arXiv:hep-ph/9303230, doi:10.1103/PhysRevD.48.1277.

[106] M. Dine et al. Low-energy Dynamical Supersymmetry Breaking Simplified. *Phys. Rev.*, D51:1362–1370, 1995. arXiv:hep-ph/9408384, doi:10.1103/PhysRevD.51.1362.

[107] M. Dine et al. New Tools for Low-energy Dynamical Supersymmetry Breaking. *Phys. Rev.*, D53:2658–2669, 1996. arXiv:hep-ph/9507378, doi:10.1103/PhysRevD.53.2658.

[108] Z. Chacko et al. Gaugino Mediated Supersymmetry Breaking. *JHEP*, 0001:003, 2000. arXiv:hep-ph/9911323, doi:10.1088/1126-6708/2000/01/003.

[109] T. G. Rizzo. SUSY Without Prejudice at Linear Colliders, 2008. arXiv:0812.1229.

[110] R. Barbier, C. Berat, M. Besancon, M. Chemtob, A. Deandrea, et al. R-parity violating supersymmetry. *Phys.Rept.*, 420:1–202, 2005. arXiv:hep-ph/0406039, doi:10.1016/j.physrep.2005.08.006.

[111] Stefano Porto, Gudrid A. Moortgat-Pick, and Krzysztof Rolbiecki. Towards discrimination of MSSM and NMSSM scenarios at colliders. 2014. arXiv:1404.1053.

[112] D. Alves et al. Simplified Models for LHC New Physics Searches. *J.Phys.*, G39:105005, 2012. arXiv:1105.2838, doi:10.1088/0954-3899/39/10/105005.

[113] S. Dimopoulos et al. Maximally Natural Supersymmetry, 2014. arXiv:1404.7554.

[114] T. Plehn. PROSPINO2 Cross-Section for 8 TeV LHC. URL: http://www.thphys.uni-heidelberg.de/~plehn/index.php?show=prospino&visible=tools.

[115] H. Baer et al. Post-LHC7 Fine-Tuning in the mSUGRA/CMSSM Model with a 125 GeV Higgs Boson. *Phys.Rev.*, D87(3):035017, 2013. arXiv:1210.3019, doi:10.1103/PhysRevD.87.035017.

[116] E. Komatsu, E. et. all (WMAP Collaboration). Seven-Year Wilkinson Microwave Anisotropy Probe (WMAP) Observations: Cosmological Interpretation. *Astrophys.J.Suppl.*, 192:18, 2011. arXiv:1001.4538, doi:10.1088/0067-0049/192/2/18.

[117] LEP SUSY Working Group (ALEPH, DELPHI L3, OPAL). Lep2 susy results. LEPSUSYWG/01-03.1. URL: http://lepsusy.web.cern.ch/lepsusy/Welcome.html.

[118] First Evidence for the Decay $B_s^0 \to \mu^+\mu^-$. *Phys.Rev.Lett.*, 110(2):021801, 2013. arXiv:1211.2674, doi:10.1103/PhysRevLett.110.021801.

[119] G. W. Bennett et. all (Muon g-2 Collaboration). Measurement of the Negative Muon Anomalous Magnetic Moment to 0.7 ppm. *Phys.Rev.Lett.*, 92:161802, 2004. arXiv:hep-ex/0401008, doi:10.1103/PhysRevLett.92.161802.

[120] G. Aad et al. (ATLAS Collaboration). Search for Squarks and Gluinos with the ATLAS Detector in Final States with Jets and Missing Transverse Momentum using 4.7 fb^{-1} of $\sqrt{s} = 7$ TeV Proton-Proton Collision Data. *Phys.Rev.*, D87(1):012008, 2013. arXiv:1208.0949, doi:10.1103/PhysRevD.87.012008.

[121] S. Chatrchyan et al. (CMS Collaboration). Search for Supersymmetry at the LHC in Events with Jets and Missing Transverse Energy. *Phys.Rev.Lett.*, 107:221804, 2011. arXiv:1109.2352, doi:10.1103/PhysRevLett.107.221804.

[122] H. N. Brown et. al (Muon g-2 Collaboration). Precise Measurement of the Positive Muon Anomalous Magnetic Moment. *Phys. Rev. Lett.*, 86:2227–2231, Mar 2001. URL: http://link.aps.org/doi/10.1103/PhysRevLett.86.2227, doi:10.1103/PhysRevLett.86.2227.

[123] J. Quevillon. Higgs Physics Beyond the Standard Model, PhD Thesis, 2014. URL: https://inspirehep.net/record/1326222.

[124] T. Falk et al. Heavy Sneutrinos as Dark Matter. *Phys.Lett.*, B339:248–251, 1994. arXiv:hep-ph/9409270, doi:10.1016/0370-2693(94)90639-4.

[125] G. Aad et al. (ATLAS Collaboration). A Particle Consistent with the Higgs Boson Observed with the ATLAS Detector at the Large Hadron Collider. *Science*, 338:1576–1582, 2012. doi:10.1126/science.1232005.

[126] T. Moroi et al. Cosmological Constraints on the Light Stable Gravitino. *Physics Letters B*, 303(34):289 – 294, 1993. URL: http://www.sciencedirect.com/science/article/pii/0370269393914340, doi:http://dx.doi.org/10.1016/0370-2693(93)91434-O.

[127] M. Bolz et al. Thermal Production of Gravitinos. *Nucl.Phys.*, B606:518–544, 2001. arXiv:hep-ph/0012052, doi:10.1016/S0550-3213(01)00132-8,10.1016/j.nuclphysb.2007.09.020.

[128] J. Pradler and F. D. Steffen. Thermal Gravitino Production and Collider Tests of Leptogenesis. *Phys.Rev.*, D75:023509, 2007. arXiv:hep-ph/0608344, doi:10.1103/PhysRevD.75.023509.

[129] P. S. Bhupal Dev et al. Constraining Non-thermal and Thermal Properties of Dark Matter, 2013. arXiv:1311.5297.

[130] M. Kawasaki et al. Big-Bang Nucleosynthesis and Hadronic Decay of Long-lived Massive Particles. *Phys.Rev.*, D71:083502, 2005. arXiv:astro-ph/0408426, doi:10.1103/PhysRevD.71.083502.

[131] F. D. Steffen. Gravitino Dark Matter and Cosmological Constraints. *JCAP*, 0609:001, 2006. arXiv:hep-ph/0605306, doi:10.1088/1475-7516/2006/09/001.

[132] M. Pospelov. Particle Physics Catalysis of Thermal Big Bang Nucleosynthesis. *Phys.Rev.Lett.*, 98:231301, 2007. arXiv:hep-ph/0605215, doi:10.1103/PhysRevLett.98.231301.

[133] K. Kohri and F. Takayama. Big Bang Nucleosynthesis with Long Lived Charged Massive Particles. *Phys.Rev.*, D76:063507, 2007. arXiv:hep-ph/0605243, doi:10.1103/PhysRevD.76.063507.

[134] M. Kaplinghat and A. Rajaraman. Big Bang Nucleosynthesis with Bound States of Long-lived Charged Particles. *Phys.Rev.*, D74:103004, 2006. arXiv:astro-ph/0606209, doi:10.1103/PhysRevD.74.103004.

[135] H. Hamaguchi et al. Stau-catalyzed Li-6 Production in Big-Bang Nucleosynthesis. *Phys.Lett.*, B650:268–274, 2007. arXiv:hep-ph/0702274, doi:10.1016/j.physletb.2007.05.030.

[136] J. Pradler and F. D. Steffen. Constraints on the Reheating Temperature in Gravitino Dark Matter Scenarios. *Phys.Lett.*, B648:224–235, 2007. arXiv:hep-ph/0612291, doi:10.1016/j.physletb.2007.02.072.

[137] K. Jedamzik. Big Bang Nucleosynthesis Constraints on Hadronically and Electromagnetically Decaying Relic Neutral Particles. *Phys.Rev.*, D74:103509, 2006. arXiv:hep-ph/0604251, doi:10.1103/PhysRevD.74.103509.

[138] R. H. Cyburt et al. Bound-State Effects on Light-Element Abundances in Gravitino Dark Matter Scenarios. *JCAP*, 0611:014, 2006. arXiv:astro-ph/0608562, doi:10.1088/1475-7516/2006/11/014.

[139] J. L. Diaz-Cruz et al. On the Feasibility of a Stop NLSP in Gravitino Dark Matter Scenarios. *JHEP*, 0705:003, 2007. arXiv:hep-ph/0701229, doi:10.1088/1126-6708/2007/05/003.

[140] J. L. Feng et al. SuperWIMP Gravitino Dark Matter from Slepton and Sneutrino Decays. *Phys.Rev.*, D70:063514, 2004. arXiv:hep-ph/0404198, doi:10.1103/PhysRevD.70.063514.

[141] T. Kanzaki et al. Cosmological Constraints on Gravitino LSP Scenario with Sneutrino NLSP. *Phys.Rev.*, D75:025011, 2007. arXiv:hep-ph/0609246, doi:10.1103/PhysRevD.75.025011.

[142] D. E. Kaplan et al. Supersymmetry Breaking Through Transparent Extra Dimensions. *Phys.Rev.*, D62:035010, 2000. arXiv:hep-ph/9911293, doi:10.1103/PhysRevD.62.035010.

[143] J. R. Ellis et al. No Scale Supersymmetric Guts. *Nucl.Phys.*, B247:373–395, 1984. doi:10.1016/0550-3213(84)90555-8.

[144] K. Inoue et al. Vanishing Squark and Slepton Masses in a Class of Supergravity Models. *Phys.Rev.*, D45:328–337, 1992. doi:10.1103/PhysRevD.45.328.

[145] C Lefevre. LHC: the Guide (English Version). . URL: http://cds.cern.ch/record/1165534?ln=en.

[146] V. Parma and L. Rossi. Performance of the LHC Magnet System. , May 2009. URL: https://accelconf.web.cern.ch/accelconf/pac2009/papers/tu1rai03.pdf.

[147] CERN PhotoLab, Life at CERN. Passage of Particles Through the Detector, 2008. URL: https://cdsweb.cern.ch/record/1096081 [cited 2012-01-29].

[148] K. Kordas et al. (ATLAS Collaboration). The ATLAS Data Acquisition and Trigger: Concept, Design and Status. *Nucl.Phys.Proc.Suppl.*, 172:178–182, 2007. doi:10.1016/j.nuclphysbps.2007.08.004.

[149] P. Jenni et al. (ATLAS Collaboration). *ATLAS High-Level Trigger, Data-Acquisition and Controls: Technical Design Report*. Technical Design Report ATLAS. CERN, Geneva, 2003. URL: http://cds.cern.ch/record/616089?ln=en.

[150] N. Berger et al. (ATLAS Collaboration). The High-Level-Trigger Steering of the ATLAS Experiment. Technical Report ATL-COM-DAQ-2007-020, CERN, Geneva, Jun 2007. Conference Record RT07 TNS IEEE 2007. URL: http://ieeexplore.ieee.org/stamp/stamp.jsp?arnumber=4448451.

[151] J. Mamuzic et al. (ATLAS Collaboration). Status of the ATLAS Trigger System for LHC Startup. In *NSS '08. IEEE*, pages 2188–2192, Oct 2008. doi:10.1109/NSSMIC.2008.4774786.

[152] A. Corso-Radu et al. (ATLAS Collaboration). Data Quality Monitoring Framework for ATLAS Experiment: Performance Achieved with Colliding Beams at LHC. *J.Phys.Conf.Ser.*, 119(ATL-DAQ-PROC-2011-007):042034, Jan 2011. doi:10.1088/1742-6596/119/4/042034.

[153] G. Aad et al. (ATLAS Collaboration). Athena Framework. . URL: http://atlas-computing.web.cern.ch/atlas-computing/packages/athenaCore/athenaCore.php.

[154] B. C. Allanach. SOFTSUSY: a Program for Calculating Supersymmetric Spectra. *Comput. Phys. Commun.*, 143:305–331, 2002. arXiv:hep-ph/0104145, doi:10.1016/S0010-4655(01)00460-X.

[155] P. Skands et al. SUSY Les Houches Accord: Interfacing SUSY Spectrum Calculators, Decay Packages, and Event Generators. *JHEP*, 0407:036, 2004. arXiv:hep-ph/0311123v4, doi:10.1088/1126-6708/2004/07/036.

[156] A. Djouadi et al. Decays of Supersymmetric Particles: the program SUSY-HIT (SUspect-SdecaY-Hdecay-InTerface). *Acta Phys. Polon.*, B38:635–644, 2007. arXiv:hep-ph/0609292.

[157] A. Djouadi et al. HDECAY: A Program for Higgs Boson Decays in the Standard Model and its Supersymmetric Extension. *Comput.Phys.Commun.*, 108:56–74, 1998. arXiv:hep-ph/9704448, doi:10.1016/S0010-4655(97)00123-9.

[158] M. Muhlleitner et al. SDECAY: A Fortran Code for the Decays of the Supersymmetric Particles in the MSSM. *Comput.Phys.Commun.*, 168:46–70, 2005. arXiv:hep-ph/0311167, doi:10.1016/j.cpc.2005.01.012.

[159] T. Sjostrand et al. PYTHIA 6.4 Physics and Manual. *JHEP*, 05:10–31, 2006. arXiv:hep-ph/0603175, doi:10.1088/1126-6708/2006/05/026.

[160] MCnet. *Monte Carlo Tools*, 2009. arXiv:0911.5286.

[161] L. Loennblad. Terascale Monte Carlo School, 2008. URL: https://indico.desy.de/conferenceOtherViews.py?view%20=standard&confId=708 [cited 2012-01-29].

[162] T. Sjostrand. Introduction to Monte Carlo Event Generators, 2010. URL: http://home.thep.lu.se/~torbjorn/talks/karlsruhe10a.pdf.

[163] D. Bourilkov et al. LHAPDF: PDF use from the Tevatron to the LHC. *TeV4LHC workshop*, 2006. arXiv:hep-ph/0605240.

[164] Z. Was. TAUOLA for Simulation of Tau Decay and Production: Perspectives for Precision Low Energy and LHC Applications. *Nucl.Phys.Proc.Suppl.*, 218:249–255, 2011. arXiv:1101.1652, doi:10.1016/j.nuclphysbps.2011.06.040.

[165] E. Barberio and Z. Was. PHOTOS: A Universal Monte Carlo for QED Radiative Corrections. Version 2.0. *Comput.Phys.Commun.*, 79:291–308, 1994. doi:10.1016/0010-4655(94)90074-4.

[166] T. Gleisberg et al. Event Generation with SHERPA 1.1. *JHEP*, 0902:007, 2009. arXiv:0811.4622, doi:10.1088/1126-6708/2009/02/007.

[167] M. L. Mangano et al. ALPGEN, a Generator for Hard Multiparton Processes in Hadronic Collisions. *JHEP*, 0307:001, 2003. arXiv:hep-ph/0206293.

[168] S. Alioli et al. NLO Vector-boson Production Matched with Shower in POWHEG. *JHEP*, 0807:060, 2008. arXiv:0805.4802, doi:10.1088/1126-6708/2008/07/060.

[169] B. C. Allanach et al. SUSY Les Houches Accord 2. *Comput.Phys.Commun.*, 180:8–25, 2009. arXiv:0801.0045, doi:10.1016/j.cpc.2008.08.004.

[170] G. Corcella et al. HERWIG 6.5 Release Note, 2002. arXiv:hep-ph/0210213.

[171] S. Frixione et al. Matching NLO QCD and Parton Showers in Heavy Flavor Production. *JHEP*, 0308:007, 2003. arXiv:hep-ph/0305252, doi:10.1088/1126-6708/2003/08/007.

[172] J. Alwall et al. MadGraph 5 : Going Beyond. *JHEP*, 1106:128, 2011. arXiv:1106.0522, doi:10.1007/JHEP06(2011)128.

[173] Asai, M. Geant4-a Simulation Toolkit. *Trans.Amer.Nucl.Soc.*, 95:757, 2006. URL: https://inspirehep.net/record/737974.

[174] G. Aad et al. (ATLAS Collaboration). The ATLAS Simulation Infrastructure. *Eur.Phys.J.*, C70:823–874, 2010. arXiv:1005.4568, doi:10.1140/epjc/s10052-010-1429-9.

[175] G. Aad et al. (ATLAS Collaboration). Expected Performance of the ATLAS Experiment - Detector, Trigger and Physics. *CERN*, pages 1513–1694, 2009. arXiv:0901.0512.

[176] G. Aad et al. (ATLAS Collaboration). Electron Efficiency Measurements with the ATLAS Detector Using the 2012 LHC Proton-Proton Collision Data, Jun 2014. URL: https://inspirehep.net/record/1299450.

[177] G. Aad et al. (ATLAS Collaboration). Measurement of the Muon Reconstruction Performance of the ATLAS Detector using 2011 and 2012 LHC Proton-Proton Collision Data. *Eur.Phys.J.*, C74(11):3130, 2014. arXiv:1407.3935, doi:10.1140/epjc/s10052-014-3130-x.

[178] G. Aad et al. (ATLAS Collaboration). Performance of Missing Transverse Momentum Reconstruction in ATLAS studied in Proton-Proton Collisions recorded in 2012 at 8 TeV, Aug 2013. URL: https://inspirehep.net/record/1260962.

[179] G. Aad et al. (ATLAS Collaboration). Pile-up Subtraction and Suppression for Jets in ATLAS, Aug 2013. URL: https://inspirehep.net/record/1260963.

[180] T. Cornelissen et al. (ATLAS Collaboration). Concepts, Design and Implementation of the ATLAS New Tracking (NEWT). *CERN Document Server*, (ATL-SOFT-PUB-2007-007. ATL-COM-SOFT-2007-002), Mar 2007. URL: https://inspirehep.net/record/1197243.

[181] S. Hassani et al. (ATLAS Collaboration). A Muon Identification and Combined Reconstruction Procedure for the ATLAS Detector at the LHC using the (MUONBOY, STACO, MuTag) Reconstruction Packages. *NIM A*, 572(1):77 – 79, 2007. URL: http://www.sciencedirect.com/science/article/pii/S0168900206019863, doi:http://dx.doi.org/10.1016/j.nima.2006.10.340.

[182] G. Aad et al. (ATLAS Collaboration). Performance of the Reconstruction and Identification of Hadronic Tau Decays in ATLAS with 2011 Data, Oct 2012. URL: https://inspirehep.net/record/1204341.

[183] G. Aad et al. (ATLAS Collaboration). Identification and Energy Calibration of Hadronically Decaying Tau Leptons with the ATLAS Experiment in *pp* Collisions at $\sqrt{s}$=8 TeV, 2014. arXiv:1412.7086.

[184] W. Lampl et al. (ATLAS Collaboration). Calorimeter Clustering Algorithms: Description and Performance, 2008. URL: http://inspirehep.net/record/807147.

[185] G. Aad et al. (ATLAS Collaboration). Jet Energy Measurement with the ATLAS Detector in Proton-Proton Collisions at $\sqrt{s} = 7$ TeV. *Eur.Phys.J.*, C73:2304, 2013. arXiv:1112.6426, doi:10.1140/epjc/s10052-013-2304-2.

[186] M. Cacciari et al. The Antikt Jet Clustering Algorithm. *JHEP*, 04(063):063, 2008. arXiv:0802.1189, doi:10.1088/1126-6708/2008/04/063.

[187] G. Aad et al. (ATLAS Collaboration). Tagging and Suppression of Pileup Jets with the ATLAS Detector, May 2014. URL: http://inspirehep.net/record/1295764.

[188] G. Aad et al. (ATLAS Collaboration). Commissioning of the ATLAS High-performance b-tagging Algorithms in the 7 TeV Collision Data. Technical Report ATLAS-CONF-2011-102, CERN, Geneva, Jul 2011. URL: https://cds.cern.ch/record/1369219?ln=en.

[189] Giacinto Piacquadio and Christian Weiser. A new Inclusive Secondary Vertex Algorithm for b-jet Tagging in ATLAS. *J.Phys.Conf.Ser.*, 119:032032, 2008. doi:10.1088/1742-6596/119/3/032032.

[190] G. Aad et al. (ATLAS Collaboration). Performance of Missing Transverse Momentum Reconstruction in Proton-Proton Collisions at 7 TeV with ATLAS. *Eur.Phys.J.*, C72:1844, 2012. arXiv:1108.5602, doi:10.1140/epjc/s10052-011-1844-6.

[191] W. Beenakker et al. PROSPINO: A Program for the Production of Supersymmetric Particles in Next-to-leading Order QCD. *arXiv*, 1996. arXiv:hep-ph/9611232.

[192] W. Beenakker et al. The Production of Charginos / Neutralinos and Sleptons at Hadron Colliders. *Phys. Rev. Lett.*, 83:3780–3783, 1999. arXiv:hep-ph/9906298, doi:10.1103/PhysRevLett.83.3780.

[193] M. Spira. Higgs and SUSY Particle Production at Hadron Colliders, 2002. arXiv:hep-ph/0211145.

[194] T. Plehn. Measuring the MSSM Lagrangean. *Czech. J. Phys.*, 55:B213–B220, 2005. arXiv:hep-ph/0410063.

[195] W. Beenakker et al. Squark and Gluino Production at Hadron Colliders. *Nucl. Phys.*, B492:51–103, 1997. arXiv:hep-ph/9610490, doi:10.1016/S0550-3213(97)00084-9.

[196] W. Beenakker et al. Stop Production at Hadron Colliders. *Nucl. Phys.*, B515:3–14, 1998. arXiv:hep-ph/9710451, doi:10.1016/S0550-3213(98)00014-5.

[197] R. Van Der Leeuw et al. (ATLAS Collaboration). Systematic Uncertainties in mSUGRA NLO Cross-section Calculations at sqrt(s) = 7 TeV. Technical Report ATL-COM-PHYS-2010-466, CERN, Geneva, August 2010. URL: https://cds.cern.ch/record/1276000?

[198] Rwth Aachen Group. NLL-Fast, 2013. URL: http://web.physik.rwth-aachen.de/service/wiki/bin/view/Kraemer/SquarksandGluinos [cited 04.06.2014].

[199] A. Kulesza and L. Motyka. Threshold Resummation for Squark-Antisquark and Gluino-Pair Production at the LHC. *Phys.Rev.Lett.*, 102:111802, 2009. arXiv:0807.2405, doi:10.1103/PhysRevLett.102.111802.

[200] A. Kulesza and L. Motyka. Soft Gluon Resummation for the Production of Gluino-Gluino and Squark-Antisquark Pairs at the LHC. *Phys.Rev.*, D80:095004, 2009. arXiv:0905.4749, doi:10.1103/PhysRevD.80.095004.

[201] W. Beenakker et al. Soft-gluon Resummation for Squark and Gluino Hadroproduction. *JHEP*, 0912:041, 2009. arXiv:0909.4418, doi:10.1088/1126-6708/2009/12/041.

[202] W. Beenakker et al. Squark and Gluino Hadroproduction. *Int.J.Mod.Phys.*, A26:2637–2664, 2011. arXiv:1105.1110, doi:10.1142/S0217751X11053560.

[203] T. Hastie et al. *Elements of Statistical Learning*. Springer, 2009. URL: http://statweb.stanford.edu/~tibs/ElemStatLearn/.

[204] G. Aad et al. (ATLAS Collaboration). Calibration of the Performance of b-tagging for c and Light-flavour Jets in the 2012 ATLAS Data: Internal Note, Jul 2014. URL: https://cds.cern.ch/record/1741020?ln=en.

[205] P. Speckmayer et al. The Toolkit for Multivariate Data Analysis, TMVA 4. *J.Phys.Conf.Ser.*, 219:032057, 2010. doi:10.1088/1742-6596/219/3/032057.

[206] A. L. Read. Presentation of Search Results: The CL(s) Technique. *J.Phys.*, G28:2693–2704, 2002. doi:10.1088/0954-3899/28/10/313.

[207] G. Cowan et al. Asymptotic Formulae for Likelihood-Based Tests of New Physics. *Eur.Phys.J.*, C71:1554, 2011. arXiv:1007.1727, doi:10.1140/epjc/s10052-011-1554-0.

[208] A. Wald. Tests of Statistical Hypothesis Concerning Several Parameters When the Number of Observations is Large. *Transactions of the American Mathematical Society*, 54(3):426–482, November 1943. URL: http://dx.doi.org/10.2307/1990256, doi:10.2307/1990256.

[209] S. S. Wilks. The Large-Sample Distribution of the Likelihood Ratio for Testing Composite Hypotheses. *The Annals of Mathematical Statistics*, 9(1):60–62, 03 1938. URL: http://dx.doi.org/10.1214/aoms/1177732360, doi:10.1214/aoms/1177732360.

[210] K. Cranmer et al. (ATLAS Collaboration). Recommendations and Discussion for Optimizing a Blind Analysis. (Private correspondence), 06 2012.

[211] K. Cranmer et al. (ATLAS Collaboration). Extensions to the Frequentist Recommendation, 08 2014. URL: https://twiki.cern.ch/twiki/pub/AtlasProtected/StatisticsTools/ExtendedStatForumRecommendations.pdf [cited 2014-08-27].

[212] G. Aad et al. (ATLAS Collaboration, ATLAS Statistics Forum). Friquentist Limit Recommendation, June 2011. URL: https://svnweb.cern.ch/trac/atlasphys/browser/Physics/StatForum/FrequentistRecommendation/doc/Frequentist_Limit_Recommendation.pdf [cited 08.08.2014.].

[213] M. Baak et al. (ATLAS Collaboration). HistFitter Software Framework for Statistical Data Analysis, 2014. arXiv:1410.1280.

[214] K. Cranmer et al. (ROOT Collaboration). HistFactory: A Tool for Creating Statistical Models for use With RooFit and RooStats, 2012. URL: https://cds.cern.ch/record/1456844?ln=en.

[215] R. Brun and F. Rademakers. ROOT - An Object Oriented Data Analysis Framework. *NIM A*, 389(1–2):81 – 86, 1997. New Computing Techniques in Physics Research. URL: http://www.sciencedirect.com/science/article/pii/S016890029700048X, doi:10.1016/S0168-9002(97)00048-X.

[216] W. Verkerke and D. P. Kirkby. The RooFit Toolkit for Data Modeling, 2003. arXiv:physics/0306116.

[217] L. Moneta et al. The RooStats Project. *PoS*, ACAT2010:057, 2010. arXiv:1009.1003.

[218] Andy Buckley. PySLHA: a Pythonic Interface to SUSY Les Houches Accord Data, 2013. arXiv:1305.4194.

[219] M. Abdullah et al. Flavored Gauge Mediation, A Heavy Higgs, and Supersymmetric Alignment. *JHEP*, 1306:057, 2013. arXiv:1209.4904, doi:10.1007/JHEP06(2013)057.

[220] J. L. Evans et al. Relatively Heavy Higgs Boson in More Generic Gauge Mediation. *Phys.Lett.*, B705:342–348, 2011. arXiv:1107.3006, doi:10.1016/j.physletb.2011.10.031.

[221] J. L. Evans et al. A 125GeV Higgs Boson and Muon g-2 in More Generic Gauge Mediation. *Phys.Rev.*, D85:095004, 2012. arXiv:1201.2611, doi:10.1103/PhysRevD.85.095004.

[222] G. Aad et al. (ATLAS Collaboration). Measurements of Higgs Boson Production and Couplings in Diboson Final States with the ATLAS Detector at the LHC. *Phys.Lett.*, B726:88–119, 2013. arXiv:1307.1427, doi:10.1016/j.physletb.2013.08.010.

[223] G. Aad et al. (ATLAS Collaboration). Search for Squarks and Gluinos with the ATLAS Detector in Final States with Jets and Missing Transverse Momentum and 20.3 fb^{-1} of $\sqrt{s} = 8$ TeV Proton-Proton Collision Data, May 2013. URL: https://inspirehep.net/record/1260927.

[224] M. Kramer et al. Supersymmetry Production Cross Sections in pp Collisions at $\sqrt{s} = 7$ TeV, 2012. arXiv:1206.2892.

[225] P. Nadolsky et al. Implications of CTEQ Global Analysis for Collider Observables. *Phys. Rev.*, D78:013004, 2008. arXiv:0802.0007, doi:10.1103/PhysRevD.78.013004.

[226] A. D. Martin et al. Parton Distributions for the LHC. *Eur.Phys.J.*, C63:189–285, 2009. arXiv:0901.0002, doi:10.1140/epjc/s10052-009-1072-5.

[227] G. Aad et al. (ATLAS Collaboration). Search for Squarks and Gluinos with the ATLAS Detector in Final States with Jets and Missing Transverse Momentum and 20.3 fb-1 of sqrt(s) = 8 TeV Proton-Proton Collision Data: Supporting Documentation, May 2014. URL: https://cds.cern.ch/record/1595965?

[228] G. Aad et al. (ATLAS Collaboration). The ATLAS Integrated Luminosity, 2013. URL: https://twiki.cern.ch/twiki/bin/view/AtlasPublic/LuminosityPublicResults [cited 13 June 2014].

[229] T. Sjostrand et al. A Brief Introduction to PYTHIA 8.1. *Comput.Phys.Commun.*, 178:852–867, 2008. arXiv:0710.3820, doi:10.1016/j.cpc.2008.01.036.

[230] S. Catani et al. Vector Boson Production at Hadron Colliders: a Fully Exclusive QCD Calculation at NNLO. *Phys.Rev.Lett.*, 103:082001, 2009. arXiv:0903.2120, doi:10.1103/PhysRevLett.103.082001.

[231] H. L. Lai et al. New Parton Distributions for Collider Physics. *Phys.Rev.*, D82:074024, 2010. arXiv:1007.2241, doi:10.1103/PhysRevD.82.074024.

[232] G. Aad et al. (ATLAS Collaboration). First Tuning of HERWIG/JIMMY to ATLAS Data, Oct 2010. URL: https://inspirehep.net/record/1196714.

[233] J. Pumplin et al. New Generation of Parton Distributions with Uncertainties from Global QCD Analysis. *JHEP*, 07:012, 2002. arXiv:hep-ph/0201195.

[234] G. Corcella et al. HERWIG 6: An Event Generator for Hadron Emission Reactions with Interfering Gluons (Including Supersymmetric Processes). *JHEP*, 0101:010, 2001. arXiv:hep-ph/0011363.

[235] P. Nason. A New Method for Combining NLO QCD with Shower Monte Carlo Algorithms. *JHEP*, 0411:040, 2004. arXiv:hep-ph/0409146, doi:10.1088/1126-6708/2004/11/040.

[236] S. Frixione et al. Matching NLO QCD Computations with Parton Shower Simulations: the POWHEG Method. *JHEP*, 0711:070, 2007. arXiv:0709.2092, doi:10.1088/1126-6708/2007/11/070.

[237] S. Alioli et al. A General Framework for Implementing NLO Calculations in Shower Monte Carlo Programs: the POWHEG BOX. *JHEP*, 1006:043, 2010. arXiv:1002.2581, doi:10.1007/JHEP06(2010)043.

[238] M. Czakon et al. Total Top-Quark Pair-Production Cross Section at Hadron Colliders Through $O(\alpha_S^4)$. *Phys.Rev.Lett.*, 110:252004, 2013. arXiv:1303.6254, doi:10.1103/PhysRevLett.110.252004.

[239] M. Czakon and A. Mitov. Top++: A Program for the Calculation of the Top-Pair Cross-Section at Hadron Colliders. *Comput.Phys.Commun.*, 185:2930, 2014. arXiv:1112.5675, doi:10.1016/j.cpc.2014.06.021.

[240] B. Cooper et al. Importance of a Consistent Choice of Alpha(s) in the Matching of AlpGen and Pythia. *Eur.Phys.J.*, C72:2078, 2012. arXiv:1109.5295, doi:10.1140/epjc/s10052-012-2078-y.

[241] P. Z. Skands. Tuning Monte Carlo Generators: The Perugia Tunes. *Phys.Rev.*, D82:074018, 2010. arXiv:1005.3457, doi:10.1103/PhysRevD.82.074018.

[242] S. Frixione and B. R. Webber. Matching NLO QCD Computations and Parton Shower Simulations. *JHEP*, 0206:029, 2002. arXiv:hep-ph/0204244.

[243] B. P. Kersevan and E. Richter-Was. The Monte Carlo Event Generator AcerMC Versions 2.0 to 3.8 with Interfaces to PYTHIA 6.4, HERWIG 6.5 and ARIADNE 4.1. *Comput.Phys.Commun.*, 184:919–985, 2013. arXiv:hep-ph/0405247, doi:10.1016/j.cpc.2012.10.032.

[244] N. Kidonakis. Next-to-next-to-leading-order Collinear and Soft gluon Corrections for t-channel Single Top Quark Production. *Phys.Rev.*, D83:091503, 2011. arXiv:1103.2792, doi:10.1103/PhysRevD.83.091503.

[245] N. Kidonakis. NNLL Resummation for s-channel Single Top Quark Production. *Phys.Rev.*, D81:054028, 2010. arXiv:1001.5034, doi:10.1103/PhysRevD.81.054028.

[246] N. Kidonakis. Two-loop Soft Anomalous Dimensions for Single top Quark Associated Production with a W- or H-. *Phys.Rev.*, D82:054018, 2010. arXiv:1005.4451, doi:10.1103/PhysRevD.82.054018.

[247] A. Lazopoulos et al. Next-to-leading order QCD Corrections to $t\bar{t}Z$ Production at the LHC. *Phys.Lett.*, B666:62–65, 2008. arXiv:0804.2220, doi:10.1016/j.physletb.2008.06.073.

[248] M. V. Garzelli et al. t $\bar{t}$ W^{+-} and t $\bar{t}$ Z Hadroproduction at NLO accuracy in QCD with Parton Shower and Hadronization Effects. *JHEP*, 1211:056, 2012. arXiv:1208.2665, doi:10.1007/JHEP11(2012)056.

[249] J. M. Campbell and R. K. Ellis. $t\bar{t}W^{+-}$ Production and Decay at NLO. *JHEP*, 1207:052, 2012. arXiv:1204.5678, doi:10.1007/JHEP07(2012)052.

[250] J. M. Campbell and R. K. Ellis. An Update on Vector Boson Pair Production at Hadron Colliders. *Phys.Rev.*, D60:113006, 1999. arXiv:hep-ph/9905386, doi:10.1103/PhysRevD.60.113006.

[251] J. M. Campbell et al. Vector Boson Pair Production at the LHC. *JHEP*, 1107:018, 2011. arXiv:1105.0020, doi:10.1007/JHEP07(2011)018.

[252] G. Aad et al. (ATLAS Collaboration). Measurements of Top Quark Pair Relative Differential Cross-sections with ATLAS in pp Collisions at $\sqrt{s} = 7$ TeV. *Eur.Phys.J.*, C73(1):2261, 2013. arXiv:1207.5644, doi:10.1140/epjc/s10052-012-2261-1.

[253] G. Aad et al. (ATLAS Collaboration). Measurement of Top-Quark Pair Differential Cross-sections in the l+jets Channel in pp Collisions at $\sqrt{s} = 7$ TeV using the ATLAS Detector, 2013. URL: https://inspirehep.net/record/1260978.

[254] G. Aad et al. (ATLAS Collaboration). ATLAS Tunes of PYTHIA 6 and Pythia 8 for MC11, Jul 2011. URL: https://inspirehep.net/record/1196788.

[255] G. Aad et al. (ATLAS Collaboration). Further ATLAS Tunes of PYTHIA6 and Pythia 8, Nov 2011. URL: https://inspirehep.net/record/1196924.

[256] S. Agostinelli et. al. Geant4-a Simulation Toolkit. *NIM A*, 506(3):250 – 303, 2003. URL: http://www.sciencedirect.com/science/article/pii/S0168900203013688, doi:http://dx.doi.org/10.1016/S0168-9002(03)01368-8.

[257] M. Cacciari and G. P. Salam. Dispelling the N^3 Myth for the k_t Jet-finder. *Phys.Lett.*, B641:57–61, 2006. arXiv:hep-ph/0512210, doi:10.1016/j.physletb.2006.08.037.

[258] M. Cacciari and G. P. Salam. Pileup Subtraction using Jet Areas. *Phys.Lett.*, B659:119–126, 2008. arXiv:0707.1378, doi:10.1016/j.physletb.2007.09.077.

[259] C. Issever et al. An Improved Weighting Algorithm to Achieve Software Compensation in a Fine Grained LAr Calorimeter. *NIM A*, 545(3):803 – 812, 2005. URL: http://www.sciencedirect.com/science/article/pii/S016890020500745X, doi:http://dx.doi.org/10.1016/j.nima.2005.02.010.

[260] G. Aad et al. (ATLAS Collaboration). Jet Energy Scale and its Systematic Uncertainty in Proton-Proton Collisions at sqrt(s)=7 TeV with ATLAS 2011 Data, Jan 2013. URL: https://inspirehep.net/record/1229978.

[261] G. Aad et al. (ATLAS Collaboration). Measuring the b-tag Efficiency in a Top-pair Sample with 4.7 fb-1 of Data from the ATLAS Detector, Jul 2012. URL: https://inspirehep.net/record/1204320.

[262] G. Aad et al. (ATLAS Collaboration). Electron Reconstruction and Identification Efficiency Measurements with the ATLAS Detector using the 2011 LHC Proton-Proton Collision Data. *Eur.Phys.J.*, C74(7):2941, 2014. arXiv:1404.2240, doi:10.1140/epjc/s10052-014-2941-0.

[263] G. Aad et al. (ATLAS Collaboration). Muon Reconstruction Efficiency and Momentum Resolution of the ATLAS Experiment in Proton-Proton Collisions at $\sqrt{s} = 7$ TeV in 2010. *Eur.Phys.J.*, C74(9):3034, 2014. arXiv:1404.4562, doi:10.1140/epjc/s10052-014-3034-9.

[264] G. Aad et al. (ATLAS Collaboration). Recommendations of the Physics Objects and Analysis Harmonisation Study Groups 2014, May 2014. URL: https://cds.cern.ch/record/1700874.

[265] G. Aad et al. (ATLAS Collaboration). Measurements of the Photon Identification Efficiency with the ATLAS Detector using 4.9 fb1 of pp Collision Data Collected in 2011, Aug 2012. URL: https://inspirehep.net/record/1204294.

[266] G. Aad et al. (ATLAS Collaboration). Search for Squarks and Gluinos using Final States with Jets and Missing Transverse Momentum with the ATLAS Detector in $\sqrt{s} = 7$ TeV Proton-Proton Collisions. *Phys.Lett.*, B701:186–203, 2011. arXiv:1102.5290, doi:10.1016/j.physletb.2011.05.061.

[267] G. Aad et al. (ATLAS Collaboration). Selection of Jets Produced in Proton-Protonroton Collisions with the ATLAS Detector Using 2011 Data, Mar 2012. URL: https://cds.cern.ch/record/1430034.

[268] S. Owen. Multijet Background Estimation for Supersymmetry Searches Using the ATLAS Detector at the Large Hadron Collider, 2012. URL: http://etheses.whiterose.ac.uk/2854/.

[269] S. Owen et al. (ATLAS Collaboration). Data-driven Estimation of the QCD Multijet Background to SUSY Searches with Jets and Missing Transverse Momentum at ATLAS using Jet Smearing: Internal Note, Aug 2011. URL: https://cds.cern.ch/record/1374670?ln=en.

[270] G. Aad et al. (ATLAS Collaboration). Search for Squarks and Gluinos using Final States with Jets And Missing Transverse Momentum with the ATLAS

Experiment in sqrt(s) = 7 TeV Proton-Proton Collisions: Supporting Documentation. Technical Report ATL-COM-PHYS-2012-426, CERN, Geneva, Apr 2012. URL: https://cds.cern.ch/record/1442313?ln=en.

[271] G. Aad et al. (ATLAS Collaboration). Measurement of the Inclusive Isolated Prompt Photon Cross Section in pp Collisions at $\sqrt{s} = 7$ TeV with the ATLAS Detector using 4.6 fb^{-1}: Internal Note, Jun 2012. URL: https://cds.cern.ch/record/1453853?ln=en.

[272] G. Aad et al. (ATLAS Collaboration). Single Hadron Response Measurement and Calorimeter Jet Energy Scale Uncertainty with the ATLAS Detector at the LHC. *Eur.Phys.J.*, C73:2305, 2013. arXiv:1203.1302, doi:10.1140/epjc/s10052-013-2305-1.

[273] G. Aad et al. (ATLAS Collaboration). Jet Energy Resolution in Proton-Proton Collisions at $\sqrt{s} = 7$ TeV Recorded in 2010 with the ATLAS Detector. *Eur.Phys.J.*, C73:2306, 2013. arXiv:1210.6210, doi:10.1140/epjc/s10052-013-2306-0.

[274] G. Aad et al. (ATLAS Collaboration). Search for Electroweak SUSY Production in sqrt(s) = 8 TeV p p Collisions with the ATLAS Detector. *in preparation for JHEP*, 2015.

[275] G. Aad et al. (ATLAS Collaboration). Search for Direct Production of Charginos, Neutralinos and Sleptons in Final States with Two Leptons and Missing Transverse Momentum in *pp* Collisions at $\sqrt{s} = 8$ TeV with the ATLAS Detector. *JHEP*, 1405:071, 2014. arXiv:1403.5294, doi:10.1007/JHEP05(2014)071.

[276] G. Aad et al. (ATLAS Collaboration). Search for Direct Production of Charginos and Neutralinos in Events with Three Leptons and Missing Transverse Momentum in $\sqrt{s} = 8$TeV *pp* Collisions with the ATLAS Detector. *JHEP*, 1404:169, 2014. arXiv:1402.7029, doi:10.1007/JHEP04(2014)169.

[277] G. Aad et al. (ATLAS Collaboration). Search for Supersymmetry in Events with Four or More Leptons in $\sqrt{s} = 8$ TeV pp Collisions with the ATLAS Detector. *Phys.Rev.*, D90:052001, 2014. arXiv:1405.5086, doi:10.1103/PhysRevD.90.052001.

[278] S. Kolos et al. High-performance scalable Information Service for the ATLAS experiment. Technical Report ATL-DAQ-PROC-2012-007, CERN, Geneva, May 2012. URL: https://cds.cern.ch/record/1451245.

[279] Andrea Dotti, Paolo Adragna, D C Cimino, Massimo Della Pietra, Roberto Ferrari, Gabriella Gaudio, Chiara Roda, D Salvatore, Wainer R Vandelli, and Pasquale Federico Zema. OHP: An Online Histogram Presenter for the ATLAS

experiment. Technical Report ATL-DAQ-CONF-2006-006. ATL-COM-DAQ-2006-014, CERN, Geneva, Mar 2006. URL: https://cds.cern.ch/record/937506.

List of Figures

2.1. The Higgs potential [49]. 12
2.2. Standard Model total production cross section measurements compared to corresponding theoretical expectations at NLO order or higher. The data set and integrated luminosity used in the measurement are indicated in the figure [50]. 16
2.3. The observed local p_0 as a function of m_H for the ATLAS [10](a) and CMS [11](b) experiment using the combined $H \to \gamma\gamma$ and $H \to ZZ^* \to 4l$ processes. The dashed curves represent the median expected local p-value, and the solid lines are the experimental results. There is a 7σ and around 6σ signal-like peak for the ATLAS and CMS respectively. The c.m.e and integrated luminosity are indicated on the plots. 17
2.4. Production strengths for a Higgs boson of mass $m_H = 125.36$ GeV, normalized to the SM expectations. Best fit values are shown with the black line, the total $\pm 1\sigma$ uncertainty is indicated in green [55]. 18
2.5. Global SM fit to electroweak data comparison to the Higgs mass measurement [60]. The discrepancy between the fit obtained and the fit on the ATLAS and CMS data is consistent with $\Delta\chi^2 \sim 1.2\sigma$ level. 19

3.1. One-loop quantum corrections to the Δm_H^2 due to the fermionic (left) and scalar boson (right) loop [46]. 22
3.2. Gauge coupling strengths in SM do not evolve to a unified value (a), shown for the LEP measurements, but unify when SUSY is introduced (b) [46]. 23
3.3. All-sky map of dark matter distribution in the universe (a) and the 'cosmic recipe' (b) obtained by the Planck measurements [84]. . . . 24
3.4. Quadratic Higgs self coupling λ (a) and electroweak vacuum stability (b). The $\lambda < 0$ for a values of quadratic Higgs self coupling higher than the cut-off scale. In the m_t vs m_H plane, for the world average masses and accuracy, the electroweak vacuum is in the meta stable region [85]. 25
3.5. Running of renormalization group equations, an example of mSUGRA /CMSSM model. Parameters m_0 and $m_{1/2}$ are given at the high GUT scale, and the SUSY particle masses are obtained at the electroweak scale [46]. 35

3.6. Average production cross-sections for different production channels at 8 TeV, obtained by the Prospino 2.1 [114]. 39
3.7. Experimental and theoretical constrains for mSUGRA/CMSSM model using $\tan\beta = 10$ (a) and $\tan\beta = 50$ (b) [115]. Green shaded area represents WMAP cosmological constrains [116], blue shaded area is the LEP2 chargino limit [117], dashed blue line is the LHCb $B_S \to \mu^+\mu^-$ limit [118], orange shaded area is favored by g-2 anomaly measurements [119], black solid line are exclusion limits from direct LHC measurements [120, 121], and red line represents the amount of fine tuning [115]. 40

4.1. Maximal h mass vs $\tan\beta$ for various SUSY models. Random scan for SUSY parameters was performed, and the m_h was measured. The m_h^{max} is defined as the value for which 99% of scan points have m_h smaller than it [123]. 42
4.2. Radiatively-driven natural SUSY using NUHM model for $m_0 = 5$ TeV, $\tan\beta = 15$, $A_0 = -1.6m_0$, $m_A = 1$ TeV. The red line shows the Δ_{EW}, the solid blue is the 8 TeV LHC reach, in dashed and dot-dashed is the 14 TeV LHC reach, the black solid line shows the ILC reach. The blue and gray shaded area are LEP2 and LEP1 exclusion limits for gauginos, and light gray area has $\Omega^{std}_{\tilde{\chi}^0_1}h^2 < 0.12$ [30]. . . . 44

5.1. Fyenman diagram for a $\tilde{\nu}_\tau$ NLSP decay into $\tilde{G}$ LSP and ν_τ. 47
5.2. SUSY breaking for gaugino mediation. In the bulk, SUSY breaking couples directly to gauginos, while coupling between matter fields and SUSY breaking sector is forbidden due to their location in the extra dimensions [142]. 49
5.3. NUHMG model for $\tan\beta = 10$, $m_0 = 0$, $m^2_{H_2} = 0$, $A_0 = 0$ and $|\mu| = 1$ has three regions which differ in sparticle mass order as A ($m_{\tilde{\tau}_1} > m_{\tilde{\chi}^0_1} > m_{\tilde{\nu}_\tau}$), B ($m_{\tilde{\chi}^0_1} > m_{\tilde{\tau}_1} > m_{\tilde{\nu}_\tau}$) and C ($m_{\tilde{\chi}^0_1} > m_{\tilde{l}} > m_{\tilde{\tau}_1} > m_{\tilde{\nu}_\tau}$). Orange area has a satisfied $\tilde{\nu}_\tau$ NLSP, light gray is where $\tilde{\tau}_1$ NLSP is not viable, while dark gray has a $\tilde{\tau}_1$ NLSP excluded by LEP limit. Left white area has a $\tilde{\tau}_1$ satisfied NLSP, while right white area is where $\tilde{\chi}^0_1$ is the LSP/NLSP, which are not considered in this model. Dashed blue equidistant lines represent the mass difference for $m_{\tilde{\tau}_1} - m_{\tilde{\nu}_\tau}$ in GeV. Region below white dash-dotted line satisfies BBN bounds for any $\tilde{G}$ mass [28]. 51
5.4. Feynman diagram for a dominant three-body decay of $\tilde{\tau}_1$ into $\tilde{\nu}_\tau$ with the W exchange [28]. 52

6.1. Large Hadron Collider accelerator complex [145]. The protons are accelerated in steps via Linac2 (50 MeV), PS Booster (1.4 GeV), PS (25 GeV), SPS (450 GeV) and LHC (4 TeV in this thesis, 7 TeV design). 54

6.2. Passage of particles through the ATLAS detector. Charged particles like electron, muon and proton leave a track in the inner detector. The electron and photon leave a shower in the Electromagnetic Calorimeter, while proton and neutron leave a hadronic shower in the hadronic calorimeter, muon is detected by the muon spectrometer, and neutrino is reconstructed as missing energy in the transverse plane [147]. 59
6.3. Schematic view of the ATLAS detector. Inner detector consists of Pixel, Semiconductor Tracker and Transition Radiation Tracker, and it is placed inside the solenoid magnet. Liquid Argon and Tile calorimeters are outside of the solenoid magnet. Toroid magnet is placed around the calorimeters. Muon spectrometers are placed within and outside of the toroid magnet [14]. 60
6.4. Inner detector components have a design of barrel and end-caps placed inside the solenoid magnet. Closest to the beam-line are the Pixel and Silicon micro-strip tracker (SCT), surrounded by the Transition radiation tracker (TRT) [14]. 62
6.5. Calorimetry at the ATLAS experiment is placed outside the solenoid magnet. It consists of electromagnetic and hadronic Liquid Argon (LAr), and Tile calorimeters in the barrel and end-cap regions [14]. 63
6.6. Muon Detector system at the ATLAS experiment consists of Monitored Drift Tubes (MDT) and Cathode Strip Chambers (CSC) for precision measurements, and Resistive Plate Chambers (RPC) and Thin Gap Chambers (TGC) for fast triggering [14]. 64
6.7. Three level trigger system at the ATLAS experiment. The input bunch crossing rate of $\sim$40 MHz is reduced to $<$ 75 kHz by the hardware based Level 1 trigger, where regions of interest (RoI) are built with latency of 2.5 μs using the reduced detector information from calorimeters and muon detectors. The software based Level 2 and Event Filter triggers reduce the event rate in two steps, to a few kHz by the Level 2 with latency of 10 ms by adding the tracking information in the RoI, and finally to a few hundreds of Hz by the event filter with latency of less than 1s using the full detector information in the RoI [149]. 65
6.8. Trigger chains of the ATLAS High-Level Trigger steering algorithm. The trigger decision is performed in a step-wise, seeded and consecutive way. The boxes represent algorithm tests which start from Level 1 decision. Multiple algorithms are run at Level 2 using the information in the RoI. Similar procedure is performed at the Event Filter using the full detector information. [150]. 66
6.9. Trigger and data acquisition system at the ATLAS experiment [14]. 67

7.1. PYTHIA, the multi purpose event generator, performs calculation through consecutive steps, [161, 162]. First the incoming p-p beams properties are determined using parton densities. Next, the hard subprocess is calculated using matrix elements, and the initial and final state radiation are added. Then the multiple parton-parton interactions with their initial and final state radiation are calculated. Finally, the color strings are formed, the hadronisation and the decays of unstable particles are calculated. 73
7.2. Electron (a) [176], muon (b) [177] i $E_{\mathrm{T}}^{\mathrm{miss}}$ (c) [178] reconstruction efficiency, and jet energy scale uncertainty (d) [178] for 8 TeV 2012 ATLAS data. The muon reconstruction efficiency shown for inner detector muons. $E_{\mathrm{T}}^{\mathrm{miss}}$ shown for after pile-up suppression. Fractional jet energy scale as a function of anti-kt jets p_T with R=0.4 calibrated using LCW+JES calibration scheme, for average pile-up conditions. 79

8.1. TMVA Factory and Reader class implementation. The user provides a script with specifications for the MVA method and discriminating variables for the training sample. The event weighing, samples distribution preparation is performed. The specified MVA methods are trained, and the result is tested and evaluated by Factory for all specified MVA methods simultaneously. The user also provides a script for the Reader, including used variables and MVA methods, and the event classification is performed for all specified MVA methods simultaneously [36]. 91
8.2. Minimization algorithms schematic representation [205]. 92
8.3. Test statistics t_μ distribution and p-value (a) and significance Z relation to p-value for the Gaussian distribution $\varphi(x) = (1/\sqrt{2\pi})e^{-x^2/2}$ (b) [207]. 97
8.4. Sensitivity of an experiment. The median q_μ statistics assuming strength parameter μ' relation to p-value in the pdf for q_μ assuming strength parameter μ [207]. 101
8.5. Test statistics q distribution under s + b and b only hypothesis for good (a) and poor sensitivity (b) [37]. (Note that test statistics here are represented by Gaussian distributions, while in practice they satisfy the chi-square distribution.) 103

9.1. NUHMG points mass spectrum and branching ratio lines. Mass order for $\tilde{\chi}_1^0$, $\tilde{e}$ and $\tilde{\tau}$ differs for increasing $m_{H_1}^2$, where $\tilde{\ell}_{\rm L}$ and $\tilde{\tau}_1$ masses shift in comparison to $\tilde{\chi}_1^0$. Region A ($m_{\tilde{\ell}_{\rm L}} > m_{\tilde{\tau}} > m_{\tilde{\chi}_1^0} > m_{\tilde{\nu}_\tau}$) is not presented as it is very close to the diagonal, while regions B ($m_{\tilde{\ell}_{\rm L}} > m_{\tilde{\chi}_1^0} > m_{\tilde{\tau}} > m_{\tilde{\nu}_\tau}$) and C ($m_{\tilde{\chi}_1^0} > m_{\tilde{\ell}_{\rm L}} > m_{\tilde{\tau}} > m_{\tilde{\nu}_\tau}$) are present in a) and b) figures respectively. Thickness of the gray lines is scaled to the value of the branching ratio. ($\tan\beta = 10$, $m_0 = 0$, $m_{H_2}^2 = 0$, $A_0 < 0$, sign(μ) > 0,$\tilde{l} = (\tilde{e}$,$\tilde{\mu}$), $\tilde{q} = (\tilde{u}$,$\tilde{d}$,$\tilde{c}$,$\tilde{s})$.) Sparticle mass spectrum plots are obtained using the PySLHA [218]. 111

9.2. NUHMG model cross-section for the strong production processes, with included $\tilde{q}$ -gaugino and $\tilde{g}$ -gaugino production. For all squark generations anti-squark production is included, and $\tilde{\chi}$ denotes all $\tilde{\chi}^0$ and $\tilde{\chi}^\pm$ generations. Total includes the processes of $\tilde{t}\tilde{t}, \tilde{q}\tilde{q}, \tilde{q}\tilde{g}, \tilde{g}\tilde{g}, \tilde{b}\tilde{b}, \tilde{\chi}\tilde{q}, \tilde{\chi}\tilde{g}$ production. 112

9.3. Targeted NUHMG final states with multiple jets and $E_{\rm T}^{\rm miss}$. $\tilde{g}$ pair production with up to 8 jets and $E_{\rm T}^{\rm miss}$ (a), $\tilde{q}$ pair production with up to 6 jets and $E_{\rm T}^{\rm miss}$ (b), and $\tilde{t}_1$ pair production with 2 b-jets, up to 4 light jets and $E_{\rm T}^{\rm miss}$ (c). Same final state using a lepton veto can be used when soft τ or l is present. If no b-tag is applied, $\tilde{t}_1$ pair production with multiple jets can be found as well. l = (e,μ), q = (u,d,c,s). 115

10.1. NUHMG grid scan using $\tilde{\nu}_\tau$ NLSP selection and LEP limits constrain with the scan on the Higgs mass constrain. First the satisfying points for $A_0 = 0$, are selected for the grid, shown in red at a). Next, the scan into negative values of A_0 was performed and the point with highest m_h was selected. The best obtained Higgs mass is shown at b) and the corresponding value of A_0 is shown at c). All grid points, shown as circled, satisfy the LEP limits for $\tilde{\chi}_1^0$, $\tilde{\chi}_1^\pm$and $\tilde{\tau}_1$mass for both A_0 = 0 and after the $A_0 < 0$ scan, shown at d), e) and f) respectively for the $A_0 < 0$ case. (*) The m_h represents the obtained h mass for each point in the grid, maximized to be close to the experimental Higgs mass measurement $\sim$ 125.5 GeV. 119

10.2. NUHMG grid check for $\tilde{g}$, $\tilde{q}$ and $\tilde{t}_1$masses. For all points $\tilde{q}$, $\tilde{g}$ and $\tilde{t}_1$ masses run with $m_{1/2}$ parameter. $\tilde{q}$ and $\tilde{g}$ masses are in the 1-2 TeV range, shown at a) and b), and $\tilde{t}_1$ has masses below 1 TeV, shown at c). $\tilde{\nu}_\tau$ mass shown at d). 120

10.3. NUHMG model sparticle masses for $m_{H_1^2}$ and fixed $m_{1/2} = 530$ GeV (a) and for $m_{1/2}$ and fixed $m_{H_1}^2 = 4$ TeV^2 (b). 121

10.4. NUHMG (left) and mSUGRA (right) typical points cross section (a) and branching fractions (b) at LO obtained with PYTHIA 6.4.22 [159] at different c.m.e. Given for the mSUGRA point (SU3) with tanβ=6, sign(μ)>0, m_0=100 GeV, $m_{1/2}$=300 GeV, A_0=-300 GeV, and NUHMG point with tanβ=10, sign(μ)>0, m_0=0, $m_{1/2}$=350 GeV, m_{H_2}=0, m_{H_1}=1.5 TeV, A_0=0 parameters. 123
10.6. NUHMG grid strong production cross-section at NLL+NLO obtained following the prescription from [224] using NLL-fast [198] and PROSPINO 2.1 [191] used in the analysis. It includes production processes of $\tilde{q}\ \tilde{q}$,$\tilde{g}\ \tilde{g}$,$\tilde{q}\ \tilde{g}$,$\tilde{b}\tilde{b}$,$\tilde{t}\ \tilde{t}$, $\tilde{\chi}\tilde{g}$ and $\tilde{\chi}\tilde{q}$. $\tilde{\chi}$ denotes all generations of $\tilde{\chi}^0$ and $\tilde{\chi}^{\pm}$. All cross-sections include both squark and anti-squark production. 124
10.5. NUHMG grid cross section at LO obtained with PYTHIA 6.4.26 [159] used for the estimate of yields in the 8 TeV search. Total cross section (a), $\tilde{q}\ \tilde{q}$, $\tilde{g}\ \tilde{g}$, $\tilde{q}\ \tilde{g}$, $\tilde{t}\tilde{t}$ and $\tilde{b}\tilde{b}$ production cross section (b), branching fraction of the $\tilde{q}\ \tilde{g}$ (all generations) production (c) and estimated number of $\tilde{q}\ \tilde{g}$ (all generations) signal events for 21 fb^{-1} and assumed signal efficiency of 3.5 % (d) are shown. All cross-sections include both squark and anti-squark production. 125

11.1. Targeted final states in the search with no leptons, jets and missing transverse momenta. Feynman diagrams of direct decays of $\tilde{q}\ \tilde{q}$ (a) and $\tilde{g}\ \tilde{g}$ (b), and one step decays via $\tilde{\chi}_1^{\pm}$ for $\tilde{q}\ \tilde{q}$ (b) and $\tilde{g}\ \tilde{g}$ (c) are shown. 128
11.2. Details of the data sample at 8 TeV p-p collisions used in the analysis. The collected integrated luminosity in 2012 was 20.3 fb^{-1} (a), mean number of p-p interactions per bunch crossing was 20.7 (b), and average the peak instantaneous luminosity per LHC fill in 2012 was 7×10^{33}cm^{2}s^{-1} (c) [228]. 130
11.3. Efficiency curves for jet p_T (a) and $E_{\mathrm{T}}^{\mathrm{miss}}$ (b) for $EF\_j80\_a4tchad\_xe100\_tclcw\_veryloose$ trigger, and efficiency curves for the $E_{\mathrm{T}}^{\mathrm{miss}}$ for different data taking periods (c), bootsrapped using the looser $EF\_\ xe50\_a4tchad$ trigger. Efficiency curves shown after applied LCW jet calibration [227]. 136
11.4. NUHMG strong production distributions for N_{jet}, $E_{\mathrm{T}}^{\mathrm{miss}}$, $m_{\mathrm{eff}}^{\mathrm{incl}}$ and H_{T} . Pre-cuts on trigger, event cleaning, lepton veto, $\Delta\phi(j_{1,2,3}, E_{\mathrm{T}}^{\mathrm{miss}}) > 0.2$, $E_{\mathrm{T}}^{\mathrm{miss}} > 160$ GeV, $p_T(jet1) > 130$ GeV and $p_T(jet2) > 60$ GeV have been used. Significance is calculated using the formula 8.22. . . 142
11.5. NUHMG strong production distributions for jet p_T for the first 6 jets. Pre-cuts on trigger, event cleaning, lepton veto, $\Delta\phi(j_{1,2,3}, E_{\mathrm{T}}^{\mathrm{miss}}) > 0.2$, $E_{\mathrm{T}}^{\mathrm{miss}} > 160$ GeV, $p_T(jet1) > 130$ GeV and $p_T(jet2) > 60$ GeV have been used. Significance is calculated using the formula 8.22. . . 143

11.6. NUHMG strong production distributions for $E_{\mathrm{T}}^{\mathrm{miss}}/m_{\mathrm{eff}}^{\mathrm{excl}}$, $E_{\mathrm{T}}^{\mathrm{miss}}/\sqrt{H_{\mathrm{T}}}$, $\Delta\phi(j_{i>3}, E_{\mathrm{T}}^{\mathrm{miss}})$ and S_{T}. Pre-cuts on trigger, event cleaning, lepton veto, $\Delta\phi(j_{1,2,3}, E_{\mathrm{T}}^{\mathrm{miss}}) > 0.2$, $E_{\mathrm{T}}^{\mathrm{miss}} > 160$ GeV, $p_T(jet1) > 130$ GeV and $p_T(jet2) > 60$ GeV have been used. Significance is calculated using the formula 8.22. 144

11.7. TMVA optimization result for the 6-jet pre-selection using S_{T}, $\Delta\phi(j_{i>3}, E_{\mathrm{T}}^{\mathrm{miss}})$, $m_{\mathrm{eff}}^{\mathrm{incl}}$ and $E_{\mathrm{T}}^{\mathrm{miss}}/m_{\mathrm{eff}}^{\mathrm{excl}}$ variables ('best for fit' scan selection) for the $m_{H1}^2 = 2.8$ TeV, $m_{1/2} = 450$ GeV, $m_{H1}^2 = 2.8$ TeV, $m_{1/2} = 490$ GeV and $m_{H1}^2 = 2.8$ TeV, $m_{1/2} = 530$ GeV points respectively. Significance of 5 can be achieved for 5 NUHMG points. 148

11.8. TMVA optimization result for the 6-jet pre-selection using S_{T}, $\Delta\phi(j_{i>3}, E_{\mathrm{T}}^{\mathrm{miss}})$, $m_{\mathrm{eff}}^{\mathrm{incl}}$ and $E_{\mathrm{T}}^{\mathrm{miss}}/m_{\mathrm{eff}}^{\mathrm{excl}}$ variables ('best for fit' scan selection) for the $m_{H1}^2 = 4.4$ TeV, $m_{1/2} = 570$ GeV and $m_{H1}^2 = 4.4$ TeV, $m_{1/2} = 610$ GeV points respectively. Significance of 5 can be achieved for 5 NUHMG points. 149

11.9. TMVA optimization result for the 6-jet pre-selection using $m_{\mathrm{eff}}^{\mathrm{incl}}$, $E_{\mathrm{T}}^{\mathrm{miss}}/m_{\mathrm{eff}}^{\mathrm{excl}}$, $\Delta\phi(j_{1,2,3}, E_{\mathrm{T}}^{\mathrm{miss}})$ and $\Delta\phi(j_{i>3}, E_{\mathrm{T}}^{\mathrm{miss}})$ variables ('final' selection) for the $m_{H1}^2 = 2.8$ TeV, $m_{1/2} = 450$ GeV, $m_{H1}^2 = 2.8$ TeV, $m_{1/2} = 490$ GeV and $m_{H1}^2 = 2.8$ TeV, $m_{1/2} = 530$ GeV points respectively. Significance of 3 can be achieved for 5 NUHMG points. 150

11.10. TMVA optimization result for the 6-jet pre-selection using $m_{\mathrm{eff}}^{\mathrm{incl}}$, $E_{\mathrm{T}}^{\mathrm{miss}}/m_{\mathrm{eff}}^{\mathrm{excl}}$, $\Delta\phi(j_{1,2,3}, E_{\mathrm{T}}^{\mathrm{miss}})$ and $\Delta\phi(j_{i>3}, E_{\mathrm{T}}^{\mathrm{miss}})$ variables ('final' selection) for the $m_{H1}^2 = 4.4$ TeV, $m_{1/2} = 570$ GeV and $m_{H1}^2 = 4.4$ TeV, $m_{1/2} = 610$ GeV points respectively. Significance of 3 can be achieved for 5 NUHMG points. 151

11.11. Scan using the fit of analysis with 2-6 jets and missing transverse momenta. Expected exclusion without the new SR is shown at (a). Different cut values for $\Delta\phi(j_{i>3}, E_{\mathrm{T}}^{\mathrm{miss}})$, $m_{\mathrm{eff}}^{\mathrm{incl}}$, $E_{\mathrm{T}}^{\mathrm{miss}}/m_{\mathrm{eff}}^{\mathrm{excl}}$ and S_{T} with the baseline 6-jet pre-selection were varied, and the SR with best CL_S value is shown at (b). The best performing signal region labeled E31, was selected for further refinement. 154

11.12. NUHMG strong production marginal distributions for $\Delta\phi(j_{i>3}, E_{\mathrm{T}}^{\mathrm{miss}})$ (a,b) and $m_{\mathrm{eff}}^{\mathrm{incl}}$ (c,d) for w/wo S_{T}, and S_{T} distribution for w/wo $\Delta\phi(j_{i>3}, E_{\mathrm{T}}^{\mathrm{miss}})$ cut. Pre-cuts on trigger, event cleaning, lepton veto, $\Delta\phi(j_{1,2,3}, E_{\mathrm{T}}^{\mathrm{miss}}) > 0.2$, $E_{\mathrm{T}}^{\mathrm{miss}} > 160$ GeV, $p_T(jet1) > 130$ GeV and $p_T(jet2) > 60$ GeV, cuts on $N_{jet} \geq 6$, $p_T(jet_1) > 130$ GeV, $p_T(jet_{2-6}) > 60$ GeV, $E_{\mathrm{T}}^{\mathrm{miss}} > 160$ GeV have been used. Significance is calculated using the formula 8.22. 155

11.13. Expected exclusion for NUHMG using the 'improved' (a) and 'final' (b) cut flow. The labels with letters show SR of the SR in the analysis with 0 leptons, while the values are the CL_S values for the new investigated SR. 'Improved' as better coverage in the low mass region, while 'final' is better in the high mass region. CL_S values are comparable for both cases, but worse than for the cut flow using S_{T} . 156
11.14. NUHMG strong production marginal distributions for no S_{T} . No additional $E_{\mathrm{T}}^{\mathrm{miss}}$ $/m_{\mathrm{eff}}^{\mathrm{excl}}$ cut was used in the distributions. Pre-cuts on trigger, event cleaning, lepton veto, $\Delta\phi(j_{1,2,3}, E_{\mathrm{T}}^{\mathrm{miss}}) > 0.2$, $E_{\mathrm{T}}^{\mathrm{miss}}$ > 160 GeV, $p_T(jet1) > 130$ GeV and $p_T(jet2) > 60$ GeV, cuts on $N_{jet} \geq 6$, $p_T(jet_1) > 130$ GeV, $p_T(jet_{2-6}) > 60$ GeV, $E_{\mathrm{T}}^{\mathrm{miss}} > 160$ GeV have been used. Significance is calculated using the formula 8.22. 157
11.15. Observed $m_{\mathrm{eff}}^{\mathrm{incl}}$ distributions in the CRγ (a), CRW (b), CRZ (c) and CRQ (excluding requirement on $E_{\mathrm{T}}^{\mathrm{miss}}$ $/m_{\mathrm{eff}}^{\mathrm{excl}}$) (d) control regions for the six-jet channel [227]. The CRγ, CRW and CRZ distributions are given for MC background expectations normalized to the cross-section and integrated luminosity. The CRQ distribution is given for the data-driven estimation used in the analysis. In the lower plots the yellow error band denotes experimental and MC statistical uncertainty, while the green band in addition includes the theoretical modeling uncertainty. The arrows denote the $m_{\mathrm{eff}}^{\mathrm{incl}}$ cut requirements for six-jet loose, medium, tight and very-tight signal regions. 163
11.16. Validation regions for multi-jet background definition in the $E_{\mathrm{T}}^{\mathrm{miss}}$ $/m_{\mathrm{eff}}^{\mathrm{excl}}$ or $E_{\mathrm{T}}^{\mathrm{miss}}$ $/\sqrt{H_T}$ vs $\Delta\phi(j_i, E_{\mathrm{T}}^{\mathrm{miss}})$ plane [227]. 166
11.17. MC response function in the jet p_T slice 200-220 GeV. The MC response function is modeled in the core and low-tail region, where the core has a Gaussian distribution(a). The Crystal Ball function is used to determine the turning point for the two regions. The data 'seed event' jets are smeared to obtain agreement of MC event distributions and data [268, 269]. 168
11.18. Nuisance parameter values obtained by the background-only fit for the 6jt+ channel [227]. All nuisance parameters have width around 1, therefore there is no profiling of the nuisance parameters by the fit. 179
11.19. Correlations matrix for the nuisance parameters used in the profile log-likelihood fit obtained by the background-only fit setup for the SR 6jt+ [227]. 180

11.20. Observed versus expected number of events in all VRs for the 6jt+ channel [227]. Event counts are shown in the upper plot, where dark blue is the Z+jets, light blue is the W+jets, light green is the top, light yellow is the W+top, and dark yellow is the QCD background prediction, and the black dots are the observed number of events. The dashed blue area represents the total uncertainty for the predicted number of events, including statistical and fitted background uncertainty. The lower plot shows 'pull' results, using the same coloring scheme, where σ_{tot} is the total uncertainty in the VR, including statistical and fitted background uncertainty. Note that σ_{tot} is correlated between VRs. 181
11.21. Observed $E_{\mathrm{T}}^{\mathrm{miss}}/m_{\mathrm{eff}}^{\mathrm{excl}}$ (excluding requirement on $m_{\mathrm{eff}}^{\mathrm{incl}}$) (a) and $m_{\mathrm{eff}}^{\mathrm{incl}}$ (b) distributions in the SR of the 6jt+ channel [31]. The distributions are given for MC background expectations normalized to the cross-section and integrated luminosity for all background samples, except for the multi-jet background distribution, which is given for the data-driven estimation used in the analysis. In the lower plots the yellow error band denotes experimental and MC statistical uncertainty, while the green band in addition includes the theoretical modeling uncertainty. The arrows denote the cut requirements for six-jet loose, tight and very-tight signal regions. 184
11.22. Event yields in the SR 6jt+ before (a) and after (b) the background-only fit. 185
11.23. Expected and observed NUHMG SUSY-model exclusion using the CL_S technique [31]. The best expected sensitivity SR is the 6jt+ for all grid points within the exclusion. The expected $\pm 1\sigma_{exp}$ exclusion includes experimental and theoretical uncertainties on the signal and background. The observed $\pm 1\sigma_{obs}^{th}$ variations are calculated for theoretical uncertainty on the cross-section calculation for each point. 187
11.24. Expected and observed mSUGRA/CMSSM SUSY-model exclusion using the CL_S technique [31]. The expected $\pm 1\sigma_{exp}$ exclusion includes experimental and theoretical uncertainties on the signal and background. The observed $\pm 1\sigma_{obs}^{th}$ variations are calculated for theoretical uncertainty on the cross-section calculation for each point. . 188
11.25. Expected and observed simplified model $\tilde{g}\ \tilde{g}$ production one-step decay SUSY-model exclusion using the CL_S technique [31]. The expected $\pm 1\sigma_{exp}$ exclusion includes experimental and theoretical uncertainties on the signal and background. The observed $\pm 1\sigma_{obs}^{th}$ variations are calculated for theoretical uncertainty on the cross-section calculation for each point. 188
11.26. Targeted final states in the analysis using one high p_T lepton, multiple jets and missing transverse momentum [38]. 190

11.27. Expected and observed NUHMG SUSY-model exclusion for one-lepton analysis [38]. The $\pm 1\sigma_{exp}$ includes experimental and theoretical, while $\pm 1\sigma_{obs}^{th}$ includes theoretical uncertainty on the cross-section calculation. 192
11.28. Expected and observed NUHMG SUSY-model exclusion comparison for 0-lepton and one-lepton analyses. The expected $\pm 1\sigma_{exp}$ exclusion includes experimental and theoretical uncertainties on the signal and background. The observed $\pm 1\sigma_{obs}^{th}$ variations are calculated for theoretical uncertainty on the cross-section calculation for each point. 193

A.1. Targeted NUHM final states. Due to low branching fraction of the strong production, direct gaugino production is dominant. Typical final states include 4W and $E_{\mathrm{T}}^{\mathrm{miss}}$ (a), 2W2Z and $E_{\mathrm{T}}^{\mathrm{miss}}$ (b), 2Z/h and $E_{\mathrm{T}}^{\mathrm{miss}}$ (c) or 2W and $E_{\mathrm{T}}^{\mathrm{miss}}$ (d). l = (e,μ), q = (u,d,c,s). 205
A.2. Mass spectrum and branching ratio lines for NUHM points. With increasing $m_{1/2}$ gauginos become heavier (compare (a) and (b)). For increasing μ gaugino mass spectrum becomes more compact (compare (a) and (c)). Thickness of the gray lines scaled to the value of the branching ratio. Sparticle mass spectrum plots are obtained using the PySLHA [218]. 206
A.3. NUHM grid direct gaugino production NLL+NLO cross-section obtained following the prescription from [224] using NLL-fast [198] and PROSPINO 2.1 [191] used in the analysis. It includes all productions of $\tilde{\chi}^0\tilde{\chi}^0$, $\tilde{\chi}^{\pm}\tilde{\chi}^{\pm}$ and $\tilde{\chi}^0\tilde{\chi}^{\pm}$ for all gaugino generations. 207
A.4. NUHM model sparticle masses for fixed μ = 150 GeV (a) and $m_{1/2}$ = 150 GeV (b). 209
A.5. RNS NUHM exclusion for a statistical combination of 2, 3 and 4 lepton analyses [274]. 211

B.1. Data Quality Monitoring information for ATLAS using Information Service (IS), Online Histogramming (OH), Gatherer and Data Quality Monitoring Framework (DQMF) [152]. Information published by TDAQ to the IS or OH is summed up by the Gatherer. Data quality flag is assigned by the DQMF, using in addition the information on the ATLAS detector components status from the Conditions Data Base, and published back to the IS and Run Control. 215

B.2. Convention for the Data Quality Monitoring of High Level Trigger [150], the so-called HLT Steering file. Axis represent the chain names, first column is the summary information for the whole Level 2 or Event Filter. First row is the input number of events, and higher rows show the number events for a given step, where -1 represents end of the chain. Last two rows show the after the pre-scale and after the pass-through number of events. From this input rates are calculated in the TriP. 216
B.3. Trigger Presenter (TriP) classes implementation for Level 1, Level 2 and Event Filter trigger information, HLT PC farm and global information. 217
B.4. Trigger Presenter (TriP) main panel. 218
B.6. Trigger Presenter (TriP) Level 2 and Event Filter details. 218
B.5. Trigger Presenter (TriP) Level 1 details. 219
B.7. Trigger Presenter (TriP) HLT farm details. 219

List of Tables

2.1. Standard Model particle content [39]. Fermions are matter particles which have a spin 1/2, and have corresponding antiparticles. They can be quarks, which interact in the strong, electromagnetic and weak interactions, and fermions, which interact in electromagnetic and weak interaction, where nearly massless neutrinos interact only weakly. Three generations of fermions differ in mass. Gauge bosons are interaction mediators, where electromagnetic interaction is mediated by γ, electroweak by $W^{\pm}$ and Z^0, and strong by g. Particles acquire mass via Higgs mechanism, and a quanta of the Higgs field is the Higgs particle. Uncertainties on e and μ mass are not shown in the table due to their high level of accuracy. 6

2.2. ATLAS and CMS Higgs mass measurements in the $H \to \gamma\gamma$ and $H \to ZZ^* \to 4l$ channels, and their combination. The measurements are presented with statistical and systematic uncertainty respectively. 18

3.1. MSSM particle content, given for chiral and gauge supermultiplets. The Q_i and L_i represent the supermultiplets containing $SU(2)_L$ doublets, and $\bar{U}_i, \bar{D}_i$ and $\bar{E}_i$ are the corresponding conjugate right-handed singlets [63]. The mass eigenstates are obtained by mixing. 32

6.1. Performance goals for the ATLAS detector [14]. High requirement on the resolution and η coverage for the reconstruction of tracks, electrons, photons, jets and muons. The units for E and p_T are in GeV. 58

9.1. NUHMG point $m^2_{H_1} = 2.8$ TeV^2, $m_{1/2} = 450$ GeV (C region) mass spectrum and branching ratios. Higher chargino and neutralino decays are relevant only for the direct gaugino production. $\tilde{q}$ and $\tilde{l}$ masses are given for the average of the first two generations, as they are almost degenerate. ($\tan\beta = 10$, $m_0 = 0$, $m^2_{H_2} = 0$, $A_0 < 0$, sign(μ) $>$ 0, l = (e,μ), q = (u,d,c,s), $\tilde{l} = (\tilde{e}\ ,\tilde{\mu}\ )$, $\tilde{q} = (\tilde{u},\tilde{d},\tilde{c},\tilde{s})$.) 110

9.2. NUHMG decay chains (from left to right) and final states for a point in the region C. Strong production has 2-4 light jets and $E_{\mathrm{T}}^{\mathrm{miss}}$, and similarly strong production with third generation has 2-4 b-jets, 0-4 W and $E_{\mathrm{T}}^{\mathrm{miss}}$. The gaugino production has 2 W, 2 Z or 2 h and $E_{\mathrm{T}}^{\mathrm{miss}}$. All final states in addition can have more soft l,τ or jets. l = (e,μ), q = (u,d,c,s), $\tilde{l} = (\tilde{e}\ ,\tilde{\mu})$. 113

10.1. NUHMG grid parameters. Grid is prepared in $m^2_{H_1}$ vs $m_{1/2}$ parameter space for given fixed parameters. $\tilde{\nu}_\tau$ NLSP and LEP limit [39] checks performed, together with the Higgs mass constrain [222]. . . 117

11.1. Details of the SM background MC simulation samples used in the analysis [31]. The MC generator, order of α_s of cross-section calculation, tune used for the underlying event and PDF sets are shown. Samples marked with (•) are used for the systematic uncertainty evaluation. For the γ+jets process the LO cross-section is taken directly form the MC generator. Where it is leading order (LO), next-to-leading order (NLO), next-to-next-to-leading order (NNLO), next-to-next-to-leading logarithm (NNLL). 131

11.2. Triggers used in the analysis. Trigger dedicated to SR uses 1 jet and $E_{\mathrm{T}}^{\mathrm{miss}}$, CRY uses a trigger with a photon, and VRZ, CRW, CRT use selections with a lepton or muon. The CRQ uses triggers with at least one jet, and the average trigger prescale over the full data sample is shown. However, the QCD estimation procedure uses average prescale for each trigger per data taking period [227]. . . . 135

11.3. NUHMG model baseline points used for optimization. Points with (*) are excluded or very close to the observed exclusion line using standard 0-lepton setup with 20.3 fb^{-1} [223]. Improvement is viable for a coverage of more than 3 NUHMG points from this list. 145

11.4. Extensive list of interesting variable combinations obtained with TMVA optimization. 2430 variable combinations were tested using $E_{\mathrm{T}}^{\mathrm{miss}}$, $E_{\mathrm{T}}^{\mathrm{miss}}/m_{\mathrm{eff}}^{\mathrm{excl}}$, $m_{\mathrm{eff}}^{\mathrm{incl}}$, H_{T} , $E_{\mathrm{T}}^{\mathrm{miss}}/\sqrt{H_T}$, $\Delta\phi(j_{1,2,3}, E_{\mathrm{T}}^{\mathrm{miss}})$, $\Delta\phi(j_{i>3}, E_{\mathrm{T}}^{\mathrm{miss}})$ and S_{T} variables with an OR for strongly correlated variables to reduce the number of combinations, using inclusive 4, 5 or 6 jet channels. Each variable combination was tested for maximum significance and then the scan was run for different TMVA testing signal efficiencies. In addition, cut flow for each efficiency was read out. There were 2 sets of criteria, first for $\mathrm{Z}_A \geq 5$ and second for $\mathrm{Z}_A \geq 3$ assuming 30% background uncertainty. Improvement compared to the standard 0-lepton searches would be reached for a coverage of more than 3 NUHMG points. Good performing candidates considered in this analysis are marked with (*). 147

11.5. Signal region optimization using the fit. Pre-cuts on the jet p_T, $E_{\mathrm{T}}^{\mathrm{miss}}$ and $\Delta\phi(j_{1,2,3}, E_{\mathrm{T}}^{\mathrm{miss}})$ were applied on the 6-jet selection and fit was run for a combination of cuts on $\Delta\phi(j_{i>3}, E_{\mathrm{T}}^{\mathrm{miss}})$, $m_{\mathrm{eff}}^{\mathrm{incl}}$, $E_{\mathrm{T}}^{\mathrm{miss}}$ $/m_{\mathrm{eff}}^{\mathrm{excl}}$ and S_{T} . Best for fit optimization combination of cuts was selected for further optimization. The removal of the $E_{\mathrm{T}}^{\mathrm{miss}}$ $/m_{\mathrm{eff}}^{\mathrm{excl}} > 0.05$ did not change the result, so it was not considered further in the analysis. The S_{T} was further removed as this did not change significantly the expected exclusion. This allowed for a higher cut on $m_{\mathrm{eff}}^{\mathrm{incl}}$, shown as 'improved' result in the table. As similar expected exclusion was obtained for low cut on $E_{\mathrm{T}}^{\mathrm{miss}}$ $/m_{\mathrm{eff}}^{\mathrm{excl}}$ and low cut on $\Delta\phi(j_{i>3}, E_{\mathrm{T}}^{\mathrm{miss}})$ this selection was chosen as the 'final' selection. 153

11.6. Selection criteria used in the analysis with a lepton veto ($p_T > 10$ GeV) [31]. The signal regions are named after the jet multiplicity selection, and labeled 2j, 3j, 4j, 5j or 6j. In addition, according to the level of signal efficiency of 'very loose', 'loose', 'medium', 'tight' and 'very tight', the extension 'l-', 'l', 'm', 't' or 't+' is added. In addition, the SR 2jW and SR 4jW have a requirement of 60 GeV $< m(W_{\mathrm{cand}}) <$ 100 GeV used for resolved and unresolved W bosons. The $E_{\mathrm{T}}^{\mathrm{miss}}$ $/m_{\mathrm{eff}}^{\mathrm{excl}}$ cut uses a value constructed from the leading N jets, but the $m_{\mathrm{eff}}^{\mathrm{incl}}$ cut includes all jets with $p_{\mathrm{T}} > 40$ GeV. 160

11.7. Cut flow for the 6jt+ SR for three NUHMG parameter-space points normalized to 20.3 fb^{-1}. Absolute efficiency in brackets (%). 161

11.8. Details of control regions used in the analysis [31]. For each control region the targeted background in the SR, the process in the CR and the selection in the CR are shown. The high-purity leptons (photons) in the CR have a 25 (130) GeV threshold. 162

11.9. Details on systematic uncertainties used in the likelihood fit. They are included as nuisance parameters in the fit, and can be treated as uncorrelated and partially or fully correlated per physics sample and selection region [227]. 175

11.10. SR6jt+ background fit results for the CRW, CRT, CRY, CRQ and SR regions, for an integrated luminosity of 20.3 fb^{-1} fb^{-1} [227]. Nominal MC expectations (normalized to MC cross-sections) are given for comparison. The errors shown for CRs are the statistical plus systematic, while for the SR they are systematic uncertainties only. 178

11.11. Scaling factors in the 6jt+ channel for Z+jets, W+jets, $t\bar{t}$ and multi-jet background obtained by the background-only fit. 178

11.12. Difference of number of events observed in data and SM MC expectations obtained by the fit, divided by the total uncertainty of the prediction ('pull'), in relevant VRs for the 6jt+ channel [31]. . . . 182

11.13. Breakdown of the dominant systematic uncertainties on background estimates obtained by the fit, in the SR 6jt+. Uncertainties relative to the expected total background yield are shown in parenthesis. 'CR stats' labels the uncertainties arising from a statistical uncertainty of a dedicated CR for a given physics process. Note that the individual uncertainties can be correlated, and do not necessarily add up quadratically to the total background uncertainty [31]. 183
11.14. Number of events observed in the signal region 6jt+ and background expectations shown for MC estimates and normalized by the fit [31]. The uncertainty on the total background yield is quoted symmetric. The 95% CL upper limits on the visible cross-section ($\langle\epsilon\sigma\rangle^{95}_{\text{obs}}$), the observed number of signal events (S^{95}_{obs}) and the number of signal events (S^{95}_{exp}) given the expected number (and $\pm1\sigma$ excursions on the expectation) of background events are given using 5000 MC pseudo-experiments and asymptotic formulae. The quoted p-value (p_0) is given for the background-only hypothesis, and the equivalent Gaussian significance (Z) is given in the brackets. 186
11.15. Selection criteria for the single-lepton SRs aimed for the $\tilde{q}$ or $\tilde{g}$ pair production. There are two sets of requirements using the single-bin and binned signal regions, where the selection for the binned case is in brackets. Electron and muon channels are targeted independently, see more details in [38]. 190
11.16. Single lepton analysis upper limits using the model independent fit, for 95% CL upper limit on the visible cross-section ($\langle\epsilon\sigma\rangle^{95}_{\text{obs}}$) and number of signal events (S^{95}_{obs}). 95% CL upper limit in the expected number of signal events S^{95}_{exp}, confidence level observed for the background-only hypothesis CL_B, and the discovery p-value ($p(s=0)$, for less observed events than expected p(s=0) = 0.5) [38]. 191

A.1. RNS NUHM and NUHM grid scan parameters. Grid is prepared in μ vs $m_{1/2}$ parameter space. In the scans the $\tilde{\chi}^0_1$ LSP and LEP limits [39] checks were performed, together with the Higgs mass constrain [222]. 203
A.2. NUHM point μ = 300 GeV, $m_{1/2}$ = 300 GeV mass spectrum and branching ratios. Direct gluino, squark and slepton production suppressed due to their high masses. Only direct gaugino production and decays are relevant for this grid at 8 TeV searches. Squark, slepton and sneutrino masses given for the average of the first two generations respectively, as they are almost degenerate. l = (e,μ), q = (u,d,c,s). 204

A.3. Signal region selection used in the 2, 3 and 4 lepton statistical combination analysis. One best expected signal region for 2 lepton analysis is used, and all listed 3 and 4 lepton signal regions. More details about samples, control and validation region selection, and individual analyses results can be found in [275–277]. DF, SF and SFOS denote different flavor, same flavor and same flavor opposite sign, respectively. 210

Acknowledgments

I would like to thank my group leader at the INN 'Vinča', Belgrade, Prof. Dr. Ivanka Božović-Jelisavčić, for introducing me into the wonderful world of high energy physics (HEP), and for sharing her endless passion for present and future colliders. My deepest gratitude and admiration goes to my supervisor PD Dr. Klaus Mönig in DESY, who had patience and constant support, from the very first until the very last day of my work towards the PhD thesis. With his sharp eye and subtle humor, he thought me how to quickly understand physics results, he forced me to develop and learn how to think for myself as a physicist, and challenged me to pose creative solutions. Due to his excellent knowledge in all fields of HEP, none of the physics topics were unknown to him, and he could help me with any question that I had. In my future work, I will always be followed by his suggestions and ways of thinking, and I feel very lucky to have been able to learn from such an exceptional physicist. I would also like to thank Prof. Dr. Hermann Kolanoski, who has guided me in understanding aspects of particle detection, and his sparkly and playful interest in new physics topics. I will always remember the numerous meetings in DESY, where Hermann would be on my left, and Klaus on the right.

The work in the filed of Supersymmetry would have never been possible without the wonderful comments and suggestions from Sabine Kraml, Monica D'Onofrio, Renaud Bruneliere, Marija Vranješ-Milosavljević, Nikola Makovec, Zoltan Gecse, Serhan Mete, Sascha Glazov, the friendly 0-lepton analysis team, and the combinations team in the electroweak searches. The work on the Trigger Peresenter was a wonderful achievement and it was a pleasure to work with Serguei Kolos, Andrea Dotti and wonderful Monitoring Working Group and TDAQ.

When working in DESY and CERN, new friendships are made in the office, at lunch time, in the control room, at the conferences, and it becomes very difficult to distinguish where the friendship begins and where the professional collaboration starts. In this light, I would like to thank my friends and colleagues Sophio Pataraia, Marcello Barisonzi, Regina Kwee and Marina Marinković, who proof-read my thesis and gave me suggestions on how to improve it, but at the same time were wonderful friends and great support in this work. Also, I would like to thank Sami Kama, Brinick Simmons, Estel Perez, Gabriella Sciolla, Paul Nilsson, Snežana Nektarijević and Kilian Rosbach, who were wonderful friends, chatting partners, office mates, but at the same time excellent experts on whose help I could rely. Finally, I would like to thank my sister Kornelija Mamužić, my brother in law Aleksandar Ružanović, my mother Julija Mamužić and, equally present, father Ivan Mamužić, for their persistent and endless love and support. On the way towards completing my PhD thesis, there were moments when their help was crucial.

Publications

- G. Aad et al. (ATLAS Collaboration). Search for the electroweak production of supersymmetric particles in $\sqrt{s}$=8 TeV pp collisions with the ATLAS detector. September 2015. Accepted by PRD, arXiv:1509.07152

- G. Aad et al. (ATLAS Collaboration). Search for squarks and gluinos with the ATLAS detector in final states with jets and missing transverse momentum and 20.3 fb^{-1} of $\sqrt{s}$=8TeV proton-proton collision data. May 2014. Published in JHEP 1409 (2014) 176, arXiv:1405.7875

- G. Aad et al. (ATLAS Collaboration). Search for squarks and gluinos with the ATLAS detector in final states with jets and missing transverse momentum and 20.3 fb^{-1} of $\sqrt{s}$=8 TeV proton-proton collision data. May 2013. ATLAS-CONF-2013-047, ATLAS-COM-CONF-2013-049

- Expected Performance of the ATLAS Experiment - Detector, Trigger and Physics. ATLAS Collaboration (G. Aad et al.). Jan 2009. 1852 pp., The Trigger for Early Running (pg. 550 - 564). SLAC-R-980, CERN-OPEN-2008-020, arXiv:0901.0512 [hep-ex]

- G. Aad et al. (ATLAS Collaboration). The ATLAS Experiment at the CERN Large Hadron Collider. Data acquisition system and high-level trigger (pg.242 - 256). Published in JINST 3 (2008) S08003, DOI: 10.1088/1748-0221/3/08/S08003

- T. Behnke et al. (ILC Collaboration). ILC Reference Design Report Volume 4 - Detectors. Dec 2007. FERMILAB-DESIGN-2007-02, arXiv:0712.2356 [physics.ins-det]

Selbständigkeitserklärung

Ich erkläre, dass ich die vorliegende Arbeit selbständig und nur unter Verwendung der angegebenen Literatur und Hilfsmittel angefertigt habe.

Berlin, den 15. 07. 2015. Judita Mamužić

.....